REPORT SERIES IN AEROSOL SCIENCE
N:o 209 (2018)

OBSERVATIONAL INVESTIGATIONS ON AIR IONS IN THE LOWER TROPOSPHERE

XUEMENG CHEN

Institute for Atmospheric and Earth System Research (INAR)
Faculty of Science
University of Helsinki
Helsinki, Finland

Academic dissertation

To be presented, with the permission of the Faculty of Science of the University of Helsinki, for public criticism in auditorium CK112, Gustaf Hällströmin katu 2, on April 13th, 2018, at 12 o'clock noon.

Helsinki 2018

Author's Address: Institute for Atmospheric and Earth System Research (INAR)
P.O.Box 64
FI-00014 University of Helsinki
e-mail: xuemeng.chen@helsinki.fi

Supervisors: Professor Veli-Matti Kerminen, Ph.D.
Institute for Atmospheric and Earth System Research (INAR)
University of Helsinki

Academician, Professor Markku Kulmala, Ph.D.
Institute for Atmospheric and Earth System Research (INAR)
University of Helsinki

Professor Tuukka Petäjä, Ph.D.
Institute for Atmospheric and Earth System Research (INAR)
University of Helsinki

Dr. Jussi Paatero, Ph.D.
Finnish Meteorological Institute

Reviewers: Professor Jyrki Mäkelä, Ph.D.
Laboratory of Aerosol Physics
Tampere University of Technology

Professor Kari Lehtinen, Ph.D.
Department of Applied Physics
University of Eastern Finland

Opponent: Professor Erik Swietlicki, Ph.D.
Department of Physics
Lund University

ISBN 978-952-7091-99-9 (printed version)
ISSN 0784-3496
Helsinki 2018
Unigrafia Oy

ISBN 978-952-7276-00-6 (pdf version)
http://ethesis.helsinki.fi
Helsinki 2018
Helsingin yliopiston verkkojulkaisut

Acknowledgements

The research presented in this thesis was conducted at the Department of Physics, University of Helsinki. I am thankful to the current and former heads of the department, Prof. Hannu Koskinen and Prof. Juhani Keinonen, for providing me with the working facilities. I greatly appreciate the Division of Atmospheric Sciences and the Doctoral Programme in Atmospheric Sciences for the financial support during the course of this thesis work. It was my great fortune to be granted the opportunity to have my doctoral thesis work completed in the Division of Atmospheric Sciences.

I would like to express sincere gratitude to my supervisors, Prof. Veli-Matti Kerminen, Prof. Markku Kulmala, Prof. Tuukka Petäjä and Dr. Jussi Paatero. I gratefully appreciate the support and guidance that Prof. Kerminen provided me over the years. He has always been ready to offer his time to guide my work and read and comment on my texts. It was a privilege to work under his supervision and have fruitful scientific discussions with him. I would like to thank Prof. Kulmala for hosting me in a world leading research group. Busy as him, he was still willing to share his inspiring scientific viewpoints with me, which often have directed me to overcome the obstacles in my research. I am thankful to Prof. Petäjä for accepting me to start as a summer worker back in 2013. It was upon this opportunity, I got in contact with the frontier research activities in atmospheric aerosol sciences and acquired hands-on knowledge on instruments for air ion measurement. The last but not the least, I would like to acknowledge Dr. Jussi Paatero for teaching me about atmospheric radioactivity. Without Dr. Paatero's generous help and knowledge-transfer, this thesis work could not have been completed.

I am thankful to Prof. Jyrki Mäkelä and Prof. Kari Lehtinen for providing careful review of my thesis.

I would like to thank all my co-authors for the good collaborations and my colleagues for the comfortable and creative working atmosphere. Also I would like to express my thankfulness to all former and current Hyytiälä staff. All of you are essential for this thesis work being done efficiently and pleasurably. Especially I would like to acknowledge Dr. Pauli Paasonen, Dr. Aki Virkkula, Dr. Hanna Manninen and Doc. Antti Lauri. Pauli and Aki have shared with me their valuable scientific experiences in data analysis and interpretation. Antti opened a door for me to atmospheric aerosol studies and Hanna introduced this field to the naive me. Besides, I would like also to thank my former supervisor, Dr. Sónia Carabineiro, for directing me onto the scientific path initially.

My gratitude also goes to Julie and Ingrid and all my other friends, who are still living in or have left Finland, for their friendship coloured my life here during the past years.

Finally, I would like to express my special gratefulness to my parents and grandparents. It was them who gave me the confidence to come to Finland initially. Their understanding and encouragement also make me brave enough to pursue this far in the scientific path. With my whole heart, I appreciate them for offering me the best possible support!

Observational investigations on air ions in the lower troposphere

Xuemeng Chen

University of Helsinki, 2018

Abstract

Air ions are constantly generated throughout the atmosphere by natural ionising radiation and they participate in the formation and dynamic processes of atmospheric aerosol particles. Their flow in the atmosphere is the cause for the air conductivity. However, there is a gap in understanding how variations in ionising radiation levels are reflected in air ion properties. Besides, observations related to air ions have been conducted at many sites around the globe, but the knowledge on features in air ions in vapour-limited environments is missing. The work in this thesis is dedicated to fill in these voids in knowledge related to air ions using the observational approach.

Factors influencing natural radioactivity in the atmosphere in a boreal forest were identified at the Hyytiälä SMEAR II Station in Finland. We found that the diurnal and seasonal patterns in the natural ionising radiation level were mainly introduced by boundary layer dynamics as well as snow cover and soil conditions. Current instrumentations for measuring the number size distribution of air ions have a lower size limit of 0.8 nm in the Millikan mobility diameter. Based on our analysis, the concentrations of 0.8-1 nm ions were generally seen varying similarly to the natural ionising radiation level. We found a clear enhancement of ionising radiation on 0.8-1.7 nm ion production on atmospheric NPF event days but not on non-event days, which suggests that 0.8-1.7 nm ions undergo less dynamic modifications and are possibly formed over shorter time scale on NPF event days than on non-event days.

To study features in air ions under conditions of limited vapours, the Concordia Station at Dome C, Antarctica, was chosen as the measurement site. Air ion processes were found to be active at the Concordia Station, including atmospheric new particle formation (NPF), ion production and loss in relation to cloud formation and wind-induced ion formation.

Overall, these results advance our understanding on the ion processes in the atmosphere, which can assist obtaining further insights into atmospheric aerosol formation mechanisms and ultimately finding solutions to air pollution issues and understanding climate variability.

Keywords: air ions, ionising radiation, non-detectable ions, theory updates

Contents

List of publications

This thesis consists of an introductory review, followed by five research articles. In the introductory part, the papers are cited according to their roman numerals. Papers I and II are reproduced with permission granted by the publishers. Papers III and IV are reprinted under Creative Commons Attribution 3.0 and 4.0 License, respectively.

I Dubtsov, S., Ovchinnikova, T., Valiulin, S., **Chen, X.**, Manninen, H. E., Aalto, P. P. and Petäjä, T.: Laboratory verification of Aerosol Diffusion Spectrometer and the application to ambient measurements of new particle formation, *J. Aerosol Sci.,* 105,10-23, doi: 10.1016/j.jaerosci.2016.10.015, 2017.

II **Chen, X.**, Paatero, J., Kerminen, V.-M., Riuttanen, L., Hatakka, J., Hiltunen, V., Paasonen, P., Hirsikko, A., Franchin, A., Manninen, H. E., Petäjä, T., Viisanen, Y. and Kulmala, M.: Responses of the atmospheric concentration of radon-222 to the vertical mixing and spatial transportation, *Boreal Env. Res.,* 21, 299-318, 2016.

III **Chen, X.**, Kerminen, V.-M., Paatero, J., Paasonen, P., Manninen, H. E., Nieminen, T., Petäjä, T. and Kulmala, M.: How do air ions reflect variations in ionising radiation in the lower atmosphere in a boreal forest? *Atmos. Chem. Phys.,* 16, 14297-14315, doi: 10.5194/acp-16-14297-2016, 2016.

IV **Chen, X.**, Virkkula, A., Kerminen, V.-M., Manninen, H. E., Busetto, M., Lanconelli, C., Lupi, A., Vitale, V., Del Guasta, M., Grigioni, P., Väänänen, R., Duplissy, E.-M., Petäjä, T., and Kulmala, M.: Features in air ions measured by an air ion spectrometer (AIS) at Dome C, *Atmos. Chem. Phys.*, 17, 13783-13800, 10.5194/acp-17-13783-2017, 2017.

1. Introduction

Air ions are electrically-charged airborne substances that suspend naturally in the atmosphere. Their formation is initiated by ionising radiation that turns air molecules (i.e. nitrogen and oxygen in the earth atmosphere) into so-called primary ions (e.g. (Israël, 1970; Harrison and Tammet, 2008; Shuman et al., 2015)). Within the planetary boundary layer of the Earth, owing to the presence of vapours and aerosol particles, primary ions can either transfer their charges to existing clusters and aerosol particles, or be transformed into charged clusters and particles by participating in clustering and subsequent growth processes. The critical cluster size defines the size limit, after which condensational growth is thermodynamically favoured (Curtius et al., 2006). Clusters that grow beyond the critical cluster size become nanoparticles. A schematic demonstration of the evolution of primary ions to charged clusters or particles is given in Fig. 1. These processes may involve both chemical reactions and physical transitions.

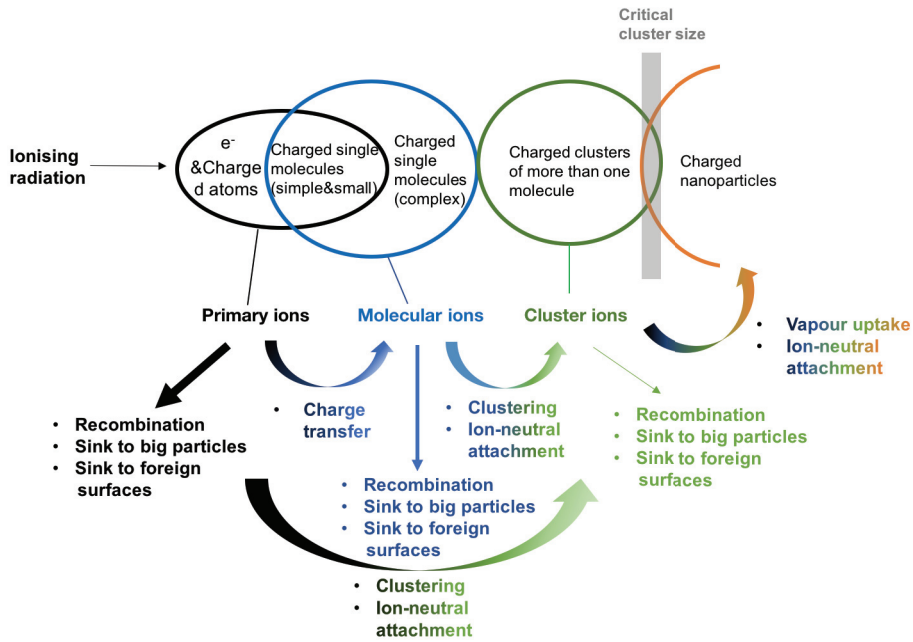

Figure 1. The evolution of primary ions to charged clusters or particles.

The drift of ions in the atmosphere makes air conductive. Air conductivity is one of the major electric properties of the atmosphere (e.g. (Israël, 1970)). To understand the origin of air conductivity had been the primary scientific focus in the discipline of the atmospheric electricity study until the late 19th century when air ion production was linked to the radioactive sources present in the atmosphere (Simpson, 1906; Herbert, 1997; Aplin et al., 2008). This advancement in understanding atmospheric electricity laid the foundation of the global electric circuit concept proposed by Charles Thomson Rees Wilson (Wilson, 1921,

1924). As air ions are one of the substantial components in the global electric circuit, motivations to understand the faith of air ions in the atmosphere continue in the atmospheric electricity discipline. Yet interests on air ions are not limited to the atmospheric electricity study. Being a naturally-occurring component in the Earth atmosphere, ions also attract scientists to investigate their chemical compositions and properties. Fred L. Eisele made the first attempt to make the mass spectrometric measurement of air ions at ground level (Perkins and Eisele, 1984), followed up by a series of studies by him and his group (e.g.(Perkins and Eisele, 1984; Eisele, 1986, 1988, 1989; Eisele and Tanner, 1990; Tanner and Eisele, 1991)).

Air ions are also a key constituent in atmospheric aerosol research. By definition, charged aerosol clusters or particles are air ions. The research discipline of atmospheric aerosols stems from the development of instrumentation for cloud and atmospheric electricity investigations ((Flagan, 1998; McMurry, 2000b), and references therein), with focuses oriented to understand the formation of atmospheric aerosol particles and their dynamics as well as involvement in cloud formation (Kulmala et al., 2004; Poschl, 2005; Arnold, 2008). Along with the rapid industrialisation during the 20th century at a global level, environmental crises started to manifest themselves in pollution, resource shortages and climatic anomalies (IPCC, 2014). Air pollution mitigation and evaluation of the climate variability urge the needs for understanding atmospheric aerosol formation and the roles aerosol particles play in the global radiation balance (Stanier et al., 2004; Poschl, 2005; Boucher et al., 2013).

Atmospheric aerosol particles consist of primary and secondary particles: primary aerosol particles are emitted to the atmosphere in the form of particulate matters, whereas secondary aerosol particles are formed in the atmosphere via phase transition from precursor vapours (Seinfeld and Pandis, 2006). Atmospheric new particle formation (NPF) has been observed all around the globe (Wiedensohler et al., 1996; Kulmala et al., 2004; Kanawade et al., 2012; Weller et al., 2015; Wang et al., 2017a). Newly-formed aerosol particles grow in size by various processes, mainly condensation (e.g. (Riipinen et al., 2012)), and may eventually reach climate-relevant sizes in the form of cloud condensation nuclei (CCN) (Dusek et al., 2006; Kerminen et al., 2012). These secondary aerosol particles are suggested to contribute to 40-70% of the CCN formation globally (Merikanto et al., 2009; Yu and Luo, 2009).

From C. T. R. Wilson's experimental works, ions are known to be capable of enhancing particle formation (Wilson, 1895, 1899). The participation of ions in atmospheric NPF has also been widely observed (Hõrrak et al., 1998; Virkkula et al., 2007; Enghoff et al., 2008; Enghoff and Svensmark, 2008; Manninen et al., 2010; Yu, 2010). Although ions have been demonstrated, based on simulations and experiments, to have an effective stabilising effect on clusters and particles, thereby promoting NPF (Curtius et al., 2006; Kirkby et al., 2011; Duplissy et al., 2016), their influences on atmospheric NPF seem to be minor (Kulmala et al., 2007). Recent studies from CERN CLOUD experiments suggest that some vapours are capable of stabilising small clusters and particles, suppressing the direct contribution of ions in NPF (Kürten et al., 2016; Lehtipalo et al., 2016). Yet, ions also contribute to NPF in neutral forms via ion-ion recombination (Yu, 2010). It is therefore crucial to investigate the

properties of air ions and ultimately reveal the role of air ions in atmospheric NPF to combat against air pollution and potential climate crisis.

In this thesis, air ions are studied using the observational approach, with the primary aim to elucidate the connection of air ion properties to ionising radiation and understand the role of air ions in the formation of atmospheric aerosol particles. The main processes covered by this doctoral work include ion production by ionising radiation (orange ellipse) and aerosol dynamics (green ellipse), as illustrated in Fig. 2. The specific objectives for the investigation of these processes are

a) to evaluate how comparable the features of new particle formation events are captured by different instruments (**Paper I**)
b) to reveal how air ions respond to variations in natural ionising radiation level (**Papers II & III**)
c) to characterise the features in air ions in an environment of limited vapour sources and their relations to new particle formation processes (**Paper IV**)

The following content of this thesis is organised into four different sections. Section 2 contains descriptions of the main instruments used in ambient observations and the measurement sites in this thesis work as well as a derived parameter – ionising capacity. In section 3, features in atmospheric NPF and air ions are presented. This section begins with an inter-comparison study of atmospheric NPF observations with different instruments to emphasize the necessity of combining different techniques in characterising atmospheric aerosols. Next, features in air ions in connection to variations in natural ionising radiation are discussed to demonstrate the influences of ionising radiation on air ion properties. This section is ended with an overview of features in air ions observed at Dome C, Antarctica to complete the global observation network of air ions. Finally, a review of publications and the author's contribution is presented in section 4 before moving to conclusion remarks and future outlook in section 5.

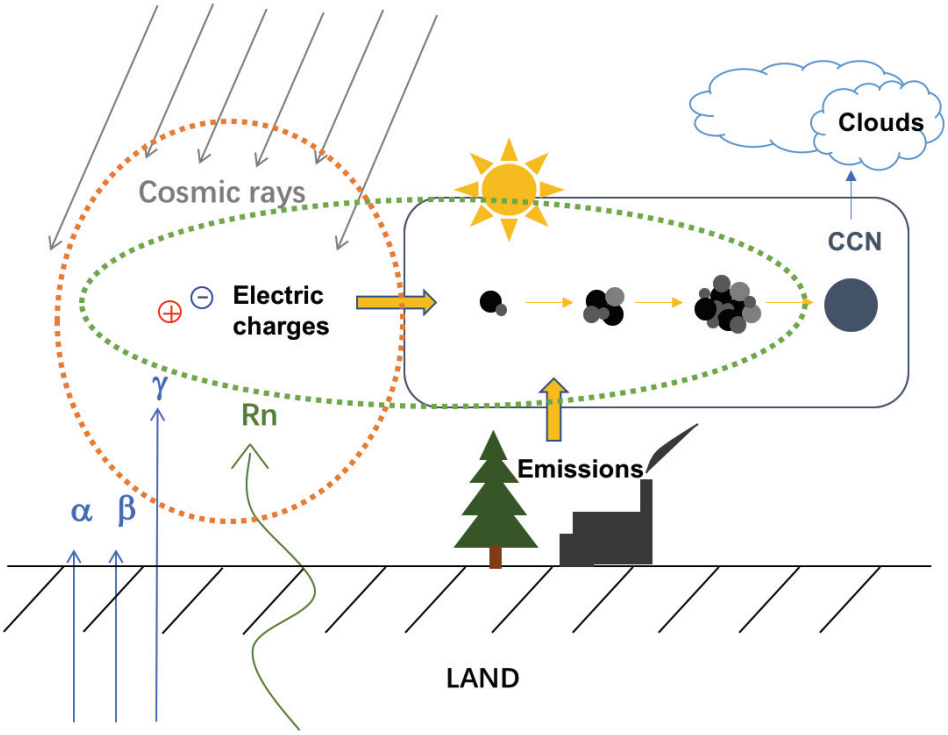

Figure 2. A schematic demonstration of atmospheric aerosol processes in connection to ion production by ionising radiation. The processes outlined in dashed ellipses are the main focuses in this thesis.

2. Materials and methods

Atmospheric aerosol particles vary in their concentration, size, shape and chemical compositions as well as in their charging properties (Seinfeld and Pandis, 2006). The characterisation of atmospheric aerosol particles therefore requires the application of instruments based on different measurement technologies (Kulkarni et al., 2011). Online measurements are typically preferred for field applications to probe the seasonality and long-term variability in aerosol properties. In the of work of this thesis, the concentration of aerosol particles is studied with size-segregated measurements for the investigation of the dynamical processes that modify the aerosol particle size distribution as well as charging properties.

2.1. Instrumentation and measurement sites

2.1.1. Online measurements of aerosol number size distribution

Atmospheric aerosol particles range from below 1 nm in Millikan mobility diameters (derived from the Stokes-Millikan equation (e.g. Hinds, 1999)) up to several hundreds of nanometres. The size segregation of aerosol particles in measurements can be based on their differences in electric mobility, penetration or vapour uptake. After size selection, particles can be detected online either electrically or optically (Flagan, 1998; McMurry, 2000a). Instrumentations employed in this thesis work include Differential Mobility Particle sizers (DMPS) (Aalto et al., 2001), an Aerosol Diffusion Spectrometer (ADS) (Dultsev et al., 2014), a Neutral and Air Ion Spectrometers (NAIS/AIS) (Mirme et al., 2007; Mirme and Mirme, 2013) and a Balanced Scanning Mobility Analyser (BSMA) (Tammet, 2006). Hereafter, the sizes of particles or ions are referred in Millikan mobility diameters, or shortly mobility diameters.

A DMPS measures the number size distribution of total aerosol particles, including both neutral and charged fractions. Before size segregation, the sampled aerosol particles are brought to a bipolar charging equilibrium by passing them through a bipolar diffusion charger. The size classification performed inside the DMPS system relies on the relationship between the particle sizes and electric mobility using one or two Differential Mobility Analysers (DMA). By step-wisely changing the voltage applied on the collecting electrode, particles of a certain electric mobility can be selected by the DMA. These particles are subsequently directed to a growth compartment typically hosted by a Condensational Particle Counter (CPC). Inside the CPC, particles grow in sizes to several microns by uptaking vapourised working fluid under slightly supersaturated conditions and are eventually detected optically. Depending on if a single-DMPS (**Paper IV**) or twin-DMPS (**Papers I and III**) design is used, the measurement size range of the system can be 9-550 nm or 3-1000 nm. For long-term ambient measurements, the sheath flow in the DMPS system is usually dried before being fed into the DMA.

An ADS (**Paper I**) can provide size-segregated concentration information of total aerosol particles in the size range of 3-200 nm. This instrument is composed of a screen-type diffusion battery (DB), a condensational particle magnifier (CPM) and an optically particle counter (OPC). The CPM and the OPC together are analogous to a CPC, but the working fluid in the CPM is dibuthylphthalate. The classification of aerosol particles based on their sizes occur in the DB section, which consists of screens organised into 8 stages. With the first screen stage being empty, the other 7 stages are composed of different numbers of meshes. For each measurement cycle, 8 number concentrations of particles are obtained, by varying the number of screen stages that aerosol particles pass through. The particle number size distribution is reconstructed based on a mathematical model describing the diffusional particle deposition on wire meshes proposed by Mavliev and Ankilov (1985).

The AIS and BSMA are ion spectrometers that provide the number size distribution information of air ions. In both instruments, air ions are classified according to their difference in electric mobility and detected by electrometers. In the BSMA (**Paper II**), two plain aspiration condensers are used for sizing air ions in positive and negative polarities, respectively. By scanning continuously through a voltage range on the repelling electrode, air ions are classified into 16 mobility channels. The condensers are in use for classification alternately. However, both condensers share a common electrometer for ion detection. In order to overcome the noise generation in the shared electrometer, a bridging circuit is used to balance the voltage supply on the repelling electrodes to establish induced electric currents on the collectors of an equal magnitude but of opposite polarity. In contrast, an AIS employs two cylindrical aspiration condensers, each of which is equipped with 21 electrometers. This design enables the AIS to simultaneously classify ions into 21 mobility channels with constant voltage supplies on the repelling electrodes in both positive and negative polarities. The BSMA has a measurement size range of 0.8-8 nm in the Millikan mobility diameter, while that of an AIS is typically 0.8-42 nm (but the AIS used in **Paper IV** had a measureable size range of 0.9-48 nm).

The NAIS (**Papers I**) is an upgraded version of the AIS, which can also measure total aerosol particles in the size range of 0.8-42 nm in addition to air ions. For measuring total aerosol particles, prior to entering the analysers, aerosol particles in the sample flow are brought into a unipolar charging equilibrium by passing them through a unipolar corona charger. The corona charger has the same polarity as the downstream analyser into which the conditioned sample flow is directed. However, due to the presence of charger ions in the conditioned sample flow, the records between 0.8- ~2.5 nm in the NAIS particle mode are subject to biased signals from the charger ions.

2.1.2. Ionising radiation measurements

Natural ionising radiation present in the atmosphere has either cosmic or terrestrial origins. Cosmic radiation contributes primarily to the ionisation in the upper atmosphere. The highest ionisation rate in the ambient air is found typically in the lower stratosphere (~10-

15 km) of around 15-35 $cm^{-3}s^{-1}$, which drops rapidly down to 2-3 $cm^{-3}s^{-1}$ at the sea level (Bazilevskaya et al., 2008). Radon and its short-lived progeny in the air and other radioactive nuclides of terrestrial origins are the main suppliers (~80%) of ionising energy for air ion production over continents in the lower troposphere (Harrison, 2004). Although solid radioactive nuclides in the ground undergo alpha, beta and gamma decays, only gamma radiation is able to escape from the ground and ionise in the atmosphere. The measurement system of ionising radiation used in this thesis work is composed of a radon monitor (Paatero et al., 1994) and a total gamma detector (Laakso et al., 2004; Hirsikko et al., 2007) (**Papers II&III**). The Finnish Meteorological Institute (FMI) is responsible for maintaining both instruments.

The radon monitor provides information on the activity concentration of atmospheric radon-222 based on detecting aerosol beta activities coming from decays of the short-lived progeny (lead-214 and bismuth-214) of radon-222. The device consists of two counters, each of which is made up of a Geiger-Müller (GM) tube wrapped around by a piece of filter shielded in lead casing. The sampled air is directed through one counter for 4 h for sample collection on the filter, while the other counter is closed for the collected radioactivity to decay. A 4-h effective collection period followed by a 4-h decay period makes up a full measurement cycle of 8 h for one counter. The two counters are in collection mode alternately. The pulses from each GM tube are counted by a ratemeter in 10-min time resolution and the 10-min counts are registered to a datalogger. The geometric configuration of the counters gives a counting efficiency of 0.96% and 4.3% for the beta emission from lead-214 and bismuth-214, respectively. Knowing these counting efficiencies, the sample flow rate and the registered cumulative counts in 10-min intervals over each 4-h collection period, the activity concentration of atmospheric radon-222 can be restored following the equations presented in **Paper II** and by Paatero et al. (1994). The radioactivity from the long-lived progeny of radon-220 and possible artificial contributions is eliminated from the radon-222 activity concentration determination by applying a basis line correction for each 8-h measurement cycle of a counter.

The total gamma detector records pulse height spectra of gamma radiation in the energy window of 100-3000 keV and provides total count rates in a 10-min time resolution. This instrument employs a piece of 76 mm × 76 mm NaI(Tl) (thallium-activated sodium iodide) crystal scintillator. A photomultiplier tube detects the light emissions from the interaction of incident gamma radiation with the detector material. The pulse height information is recorded with a multichannel analyser. By monitoring the gamma peak (1460 keV) of potassium-40, the total gain of the detecting system is kept constant. The count rates are converted into dose rates in the air ($\mu Sv\ h^{-1}$) using a calibration factor determined by comparing the total gamma detector to a pressurised ionisation chamber. The scintillator is encased in a glass-fiber box insulated with polyurethane foam to maintain a constant temperature in order to avoid variations in the light yield of the scintillator material and drifts in electronics.

2.1.3. Measurement sites

This thesis work was based on analysing ambient data collected from two measurement sites: SMEAR II station (**Papers I-III**) and Concordia station (**Paper IV**). The SMEAR II station (61°51' N, 24°17' E; 181 m above sea level) is located at Hyytiälä in Southern Finland (Hari and Kulmala, 2005). It sits in a boreal forest dominated by Scots pines (*Pinus sylvestris* L.), with an average age of 55 years. The average tree height is about16-18 m. The aerosol and ion measurements (except the PSM measurement) as well as the ionising radiation measurements belong to the long-term continuous observation network of the station. The PSM was deployed at this site during several campaigns (Kontkanen et al., 2017). The station also owns a 127-m measurement mast. Meteorological variables and trace gases are monitored continuously at eight different height levels on the mast.

The Concordia station (75°06' S, 123°23' E; 3220 m above sea level) is located at Dome C on the Antarctic plateau - the biggest frozen desert in the world. The nearest coast is at a distance of 1100 km from the station (Becagli et al., 2012). The ground is covered by ice glaciers and snow with a depth of more than 3000 m (Augustin et al., 2004). Aerosol and ion measurements were installed at a sampling site in the upwind direction of the prevailing winds, about 1 km southwest of the main station buildings. Northeasterly (10-90°) winds are suspected to be contaminated by local emissions from diesel generators and motor vehicles.

2.2. Determination of the ionising capacity

The ionisation rate in the ambient air is not directly measurable. However, theoretically the production rate of ion pairs can be approximated from ionising radiation measurements. For this purpose, a derived quantity, ionising capacity, is introduced in **Paper III**, which is defined as the potential maximum production rate of ion pairs upon ionisation in a unit volume per unit time. By knowing the activity concentration of atmospheric radon-222 (unit: Bq/m^3), it is possible to estimate the energy that can be released in a unit volume of air per unit time (F_{radon}) from the decays of radon-222 and its short-lived progeny (polonium-218, lead-214, bismuth-214, and polonium-214). The accounted decay modes and weighted average decay energy in the ionising capacity determination is listed in Table 1. The decay chain of radon-222 and its short-lived progeny also emits a small fraction of gamma radiation, which is assumed to be measurable by the total gamma detector. By multiplying with the air density (ρ_{air}), the gamma dose rates (DR, unit: $\mu Sv\ h^{-1}$) in air can be converted into energy absorbed in the air in a unit volume per unit time (F_{gamma}) (Eq. 1.1).

$$F_{\text{gamma}} = \text{DR} \cdot \rho_{air} \tag{1.1}$$

The air density can be determined using ambient temperature and pressure from the ideal gas law. Then with knowing the total available energy released into a unit air volume per unit time (F, unit: $J\ cm^{-3}\ s^{-1}$), i.e. F_{radon} or/and F_{gamma} in practice, the ionising capacity (Q,

unit: $cm^{-3}\ s^{-1}$) can be calculated based on the assumption that on average 34 eV of energy is used in forming an ion pair as follows

$$Q = \frac{F}{34\text{eV}}. \quad (1.2)$$

Table 1. Decay modes and energy of radon-222 and its short-lived progeny that are accounted in determining the ionising capacity. The data are from the National Nuclear Data Centre of Brookhaven National Laboratory (http://www.nndc.bnl.gov/chart/). Adapted from **Paper III**.

Nuclide	Decay mode	Weighted average decay energy [keV]
Radon-222	α (100%)	5589
Polonium-218	α (99.98%)	6001
Lead-214	β^- (100%)	225
Bismuth-214	β^- (100%)	642
Polonium-214	α (100%)	7687

3. Atmospheric observations

The pioneering observations of atmospheric aerosol particles began with interests in understanding the formation of clouds and atmospheric electricity. John Aitken investigated the condensation process of water and developed a prototype dust counter and a pocket dust counter during 1880-1891 based on growing dust particles by condensation (Aitken, 1880, 1888; McMurry, 2000b). Using these devices, he was the first to be able to count atmospheric aerosol particles. However, C.T.R. Wilson found out that condensation could also occur in dust-free air (Wilson, 1895). His research linked the formation of condensation nuclei with ions produced by ionising radiation and evidenced the enhancement of charges on the formation of aerosol particles (Wilson, 1895, 1899). Ever since, curiosities in the number concentrations of aerosol particles and their formation mechanisms and dynamics make investigations on atmospheric aerosol particles emerged into a research discipline of its own.

With improvements and developments in instrumentations, atmospheric observations of aerosol particles have been reported in different environments. The concentrations of atmospheric aerosol particles range from a few tens of particles cm^{-3} in clean Antarctic air (Samson et al., 1990; Koponen et al., 2003; Pant et al., 2011; Järvinen et al., 2013) to even more than 10^5 cm^{-3} in polluted urban regions (Zhu et al., 2002; Wehner, 2004; Mönkkönen et al., 2005; Wu et al., 2008). Polluted environments typically have higher condensation sinks (CS) than clean sites (Wu et al., 2008; Järvinen et al., 2013; Nie et al., 2014; Nieminen et al., 2014). The CS is a measure of the aerosol loading in the atmosphere, and it quantifies the uptake rate of vapours or small vapour-like substances (e.g. cluster ions) onto pre-existing aerosol particles. Air ion concentrations have also been reported from different sites around the globe. Concentrations of small ions (≈ cluster ions) vary typically from 200 to 2500 cm^{-3}, even up to 5000 cm^{-3} (Hirsikko et al., 2011).

Owing to the sizing power of modern instruments, the atmospheric NPF process and the subsequent particle growth can be depicted. Devices capable of measuring below 3 nm are especially valuable for providing crucial information on the initial steps of NPF (Kulmala et al., 2012; Kulmala et al., 2013). Atmospheric NPF has been observed to take place worldwide in different continents and climatic zones (Kulmala et al., 2004; Vakkari et al., 2011). NPF can occur in pristine Antarctic environments (Kyrö et al., 2013; Weller et al., 2015), in forests (Kulmala et al., 2013; Gonser et al., 2014), in coastal areas (Modini et al., 2009; Sipila et al., 2016), and also in heavily polluted megacities (Wu et al., 2007; Nie et al., 2014; Kulmala et al., 2016; Wang et al., 2017b).

3.1. Measurement of atmospheric new particle formation (NPF) using different instruments

The characterisation of atmospheric NPF involves extensively the application of mobility particle size spectrometer systems (e.g. (Wiedensohler et al., 1996; Aalto et al., 2001;

Vakkari et al., 2011; Kanawade et al., 2012; Järvinen et al., 2013; Fiebig et al., 2014; Weller et al., 2015)). Wiedensohler et al. (2012) pointed out the needs for, and provided recommendations to, standardising the design and operation of such instruments. A technical harmonisation is achievable for a type of instruments (e.g. (Wiedensohler et al., 2012)). However, there is no single reference device in measuring atmospheric aerosol particles. The study of atmospheric aerosol dynamics requires the employment of different types of instruments to cover the interested size range for investigation. To assess the performance of different types of instruments in measuring atmospheric aerosol particles, the only means is to conduct instrumental inter-comparisons.

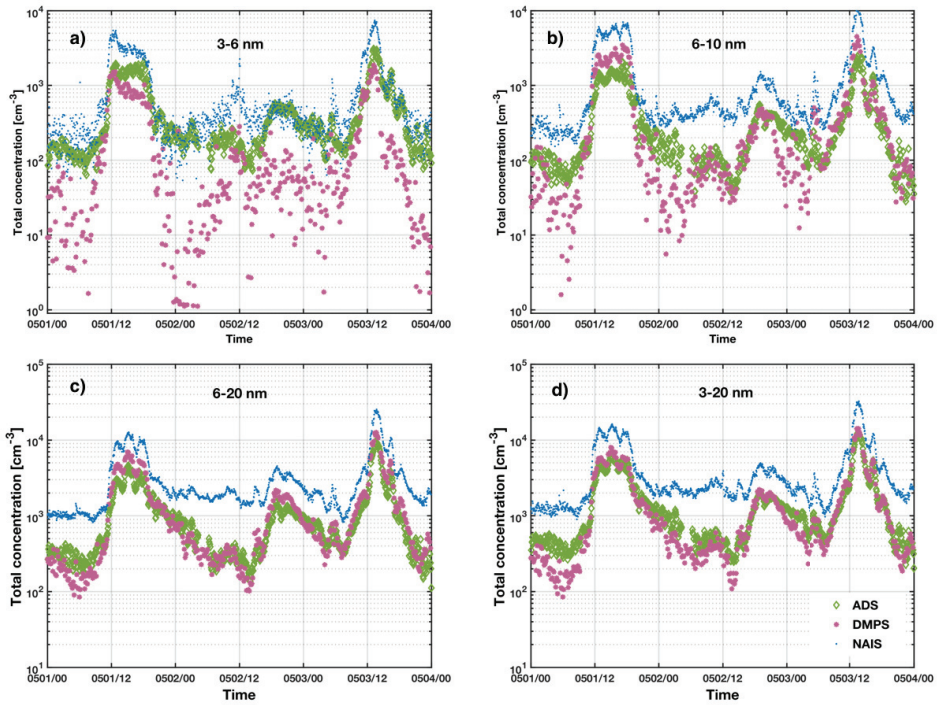

Figure 3. Comparisons between concentrations measured by the ADS (green diamonds), DMPS (pink stars) and NAIS (blue dots) in different size ranges for May 1-3, 2013. Except on May 2, 2013, daytime NPF process was observed. A nocturnal event occurred on the evening of May 2, 2013. The size range of 3-6 nm shown in a), 6-10 nm in b), 6-20 nm in c) and 3-20 nm in d). Adapted from **Paper I**.

During 29 April – 15 May, 2013, an ADS was inter-compared with a DMPS and a NAIS to evaluate its feasibility for ambient application in measuring atmospheric NPF at SMEAR II station in Hyytiälä (**Paper I**). Daytime NPF was observed on 1 and 3 May. Correspondingly,

concentration bursts of aerosol particles were seen in the measurements of the ADS, DMPS and NAIS (Fig. 3). In the size range of 3-6 nm, the ADS showed in general an agreement with the NAIS. The concentration measured by the DMPS, however, had the biggest deviation from those measured by the ADS and NAIS. This result implies the advantage of ADS over the DMPS in measuring small particles. The difference in concentrations between the DMPS and the ADS/NAIS was the smallest during NPF (Fig. 3a), i.e. the performance of the DMPS in 3-6 nm improved at high particle concentrations. This phenomenon suggests that this DMPS had a poor scheme accounting for diffusional losses of these small aerosol particles.

The agreement between the ADS and the DMPS improved as moving to larger sizes (Fig. 3b, c and d). The concentration level of 6-20 nm particles measured by the ADS and the DMPS almost overlapped with each other (Fig. 3c). But the NAIS consistently recorded higher concentrations of particles with sizes above 6 nm than the other two instruments (Fig. 3b, c and d). The reason comes most probably from the fact the ADS and DMPS shared a common sampling line, the inlet of which was on the top of the measurement cottage at 8 m, whereas the NAIS had a shorter inlet (~50 cm) that was located on the side of the cottage about 2.5 m above the ground level. Furthermore, the NAIS had a much higher sampling flow rate (60 l/min) compared with the DMPS (5 l/min) and the ADS (1 l/min).

3.2. Variations in the natural ionising radiation and the connection to air ions

The presence of radioactivity in the atmosphere induces air ion production. Tuomi (1989) observed an episode of significant high air conductivity at Helsinki-Vantaa airport in relation to Chernobyl nuclear accident. Although such introduction of radioactivity to the atmosphere via nuclear accidents and incidents is rare and temporal, natural radioactivity is present ubiquitously in the atmosphere. The production of air ions is inevitably influenced by variations in the natural radioactivity. Therefore, it is important to understand the seasonal and diurnal cycles in the natural ionising radiation. We used ionising radiation and air ion data collected from Hyytiälä SMEAR II station to investigate the variability in the natural ionising radiation and its connection to the observed air ions (**Papers II&III**).

The daily median radon and gamma fractions of the ionising capacity, derived from the measured ionising radiation using the method explained in section 2.2, exhibited different seasonality (Fig. 4a). The gamma ionising capacity had a relative constant level from May untill the end of the year of about 9-10 $cm^{-3}s^{-1}$. It showed, however, a gradual declination in the beginning of the year, which reached the minimum (below 5 $cm^{-3}s^{-1}$) in mid-March. This reduction in the gamma ionising capacity originated from the attenuation of terrestrial gamma radiation by the accumulation of snow during the winter season (**Paper III**). Once the snow thawing began, the gamma ionising capacity was quickly restored to its maximum level and retained there. More complicated patterns were observed in the variability of the

radon ionising capacity, because the atmospheric radon activity concentration is sensitive to the boundary layer development, soil conditions as well as transport schemes (**Paper II**). The low radon ionising capacity during the springtime (March-May) resulted from the prohibited radon exhalation from frozen or water saturated soils while being diluted in the enlarged mixing volume as the consequence of a prolonged daytime. In comparison, the high winter radon ionising capacity was due mainly to the shallow boundary layer.

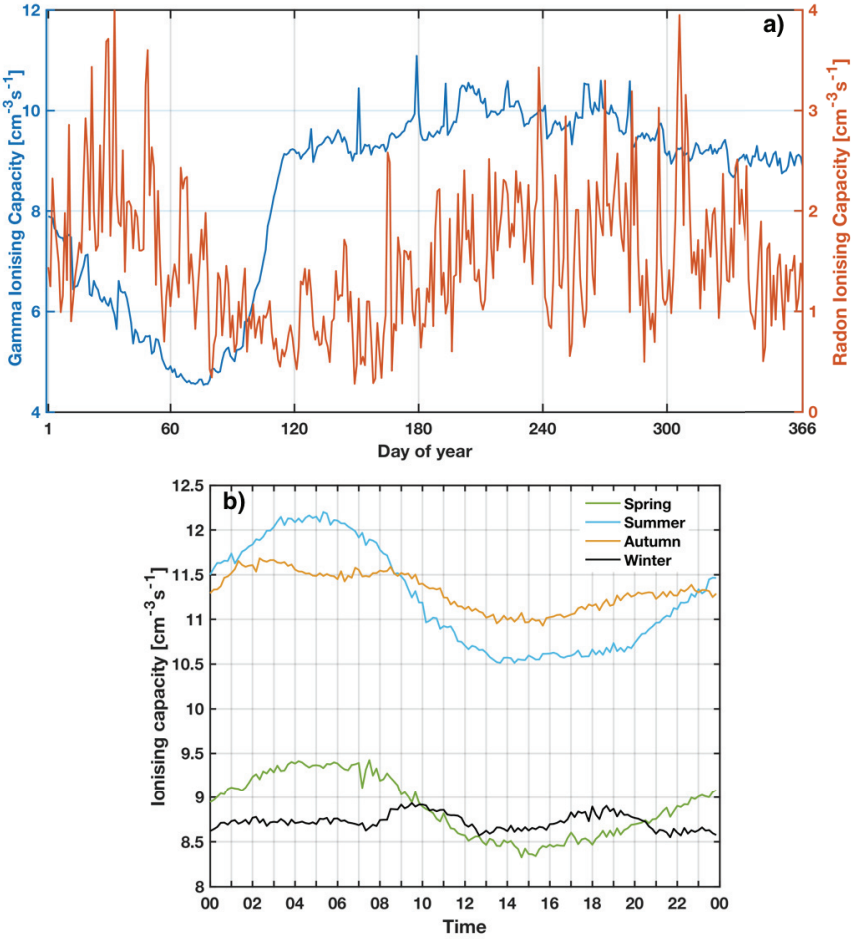

Figure 4. Seasonal and diurnal variability in the ionising capacity derived from the natural ionising radiation based on data measured in 2003-2006. a) Seasonal variations in the daily median gamma (left axis) and radon (right axis) ionising capacity. b) Diurnal variations in the median total ionising capacity in different seasons based on 10-min data. Spring: March-May, summer: June-August, autumn: September-November, winter: December-February. Data are presented in UTC+2:00. Adapted from **Paper III**.

Diurnal patterns in the median total ionising capacity were seen clearly in spring and summer, and to some extent in autumn (Fig. 4b). The diurnal variations in the total ionising

capacity were primarily caused by the response of atmospheric radon concentrations to the boundary layer dynamics. The radon ionising capacity was high in the early morning as a result of the accumulation of radon in the shallow nocturnal boundary layer. Along with the increased mixing due to the boundary layer thickening upon sunrise, the radon ionising capacity began to decline and reached its minimum in the afternoon when the boundary layer was fully developed. Afterwards, radon in the air was concentrated gradually as the mixing volume of the boundary layer shrank.

The total gamma radiation accounted for more than 80% of the ion pair production in the lower troposphere (**Paper III**). Once formed, ion pairs, i.e. primary ions, may undergo a series of dynamical processes and finally become charged nanoparticles. These processes deface easily the properties of charged nanoparticles in direct relation to the ionising radiation. Thus, by comparing the variability in the cluster (0.8-1.7 nm) ion concentration with that in the ionising capacity, only slight similarity could be identified (**Paper III**). However, ions in the size range of 0.8-1 nm followed the median variations in the ionising capacity in all the seasons except in winter (Fig. 5).

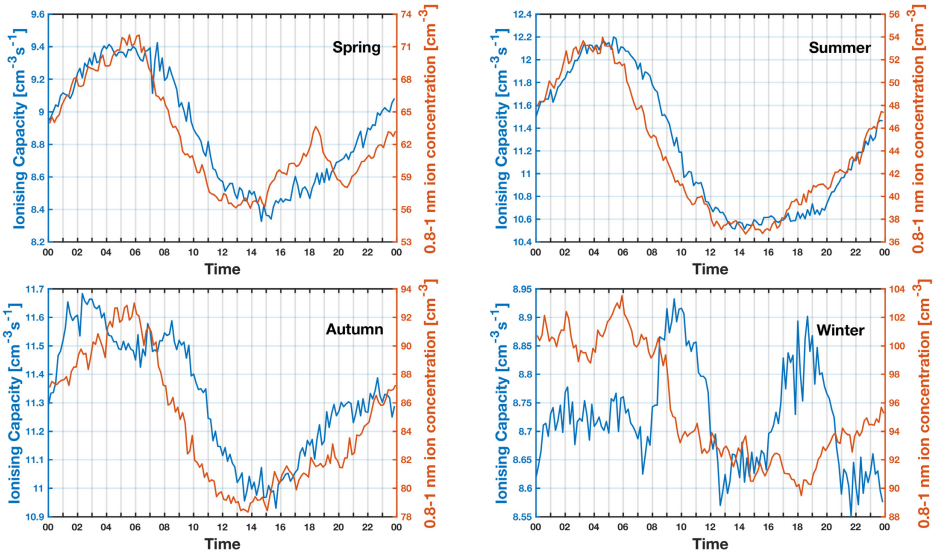

Figure 5. Diurnal patterns in the median 0.8-1 nm negative ion concentration and ionising capacity in different seasons based on 2003-2006 data.

By setting constraints on the cluster ion and ionising capacity data, a relationship between the concentration of all ions in the cluster size range (0.8-1.7 nm) and the ionising capacity became clear on NPF event days (Fig. 6). With the same set of constraints, however, no

such a clear pattern was seen on non-event days (**Paper III**). The influences from the diurnal and seasonal variability were minimised by choosing the time window of 0:00-3:00 and the months of September- December. Winds were constrained from the clean sector in 280°-30° to reduce the complication introduced by the transported radon from continental sources. The data were further restricted to low CS values (< 0.002 s^{-1}) and snow-free periods to avoid significant variations in the aerosol uptake of cluster ions and the snow attenuation of terrestrial gamma radiation. With such constraints, a clear enhancement of ionising radiation on the production of cluster ions was observed when the ionising capacity was below 11 cm^{-3} s^{-1}. However, with high ionising capacities (> 11 cm^{-3} s^{-1}), the cluster ion concentration levelled up. This observation indicated that the cluster formation process was unable to rescue charges efficiently from recombination in proportion to the infinite increase in the ionising capacity, possibly related to the limited availability of nucleating vapours. The fact that a better dependency of the cluster ion concentration on the ionising capacity was seen on NPF event days than on non-event days may suggest that cluster ions observed on NPF event days have undergone less transformations and are formed over shorter timescales than those on non-event days and consequently they can preserve features in relation to ionising radiation.

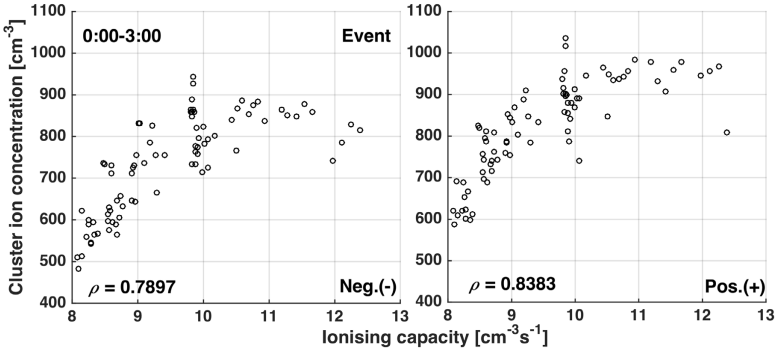

Figure 6. The cluster (0.8-1.7 nm) ion concentration as a function of the ionising capacity (radon ionising capacity + gamma ionising capacity) for selected data in the years 2003-2006, with Spearman's rank correlation coefficient (ρ). The data was constrained on event days in September-December between 0:00 and 3:00 with the wind direction between 280° and 30°, while the condensation sink (CS) was below 0.002 s^{-1}. No dependence of the cluster ion concentration on the CS or hour-of-day was identified. Also the snow season was screened out. Adapted from **Paper III**.

3.3. Features in air ions and their relation to aerosol dynamics

Participation of air ions in atmospheric NPF has been reported from many sites (e.g. (Virkkula et al., 2007; Manninen et al., 2010)). This phenomenon is typically characterised by a concentration burst of intermediate ions (1.7-7 nm) (Tammet et al., 2014; Leino et al., 2016). However, the production of intermediate ions is not limited to NPF processes. Observations of high ion concentrations in the intermediate size range near waterfalls and during rain episodes have been documented (Hõrrak et al., 2006; Laakso et al., 2007; Kolarz et al., 2012). These intermediate ions, however, differ from those formed during NPF, due to their shrinking rather than growing nature (Tammet et al., 2009). Air ion production has also been recorded in association with strong winds in cold environments (Virkkula et al., 2007; Manninen et al., 2010). Regardless of measurement locations and processes in air ion dynamics, there is always a pool of cluster ions present in the atmosphere (e.g. (Virkkula et al., 2007; Manninen et al., 2009)).

Ion processes are rich in the ambient air. The so-far reported observations of air ions are all from sites where there are available vapour sources that can potentially participate in clustering and the growth of aerosol particles. To add to the missing piece to the global air ion observations, an AIS was deployed at Concordia station on Dome C, Antarctica, during 22 December, 2010 – 16 November, 2011 for the investigation of the number and size properties of air ions (**Paper IV**). The high altitude and remote location of this measurement site provides a unique environment of a high exposure to cosmic radiation and very limited vapour sources. The high exposure means a high production rate of primary ions; but with limited vapours, the formation of larger ions is expected to be suppressed. However, in reality, atmospheric NPF processes were frequently observed during the Antarctica spring and autumn, even on consecutive days (Fig. 7a and b). Apart from regular NPF events occurring with only one mode (Fig. 7a), a number of multi-mode formation and growth events were observed (Fig. 7b).

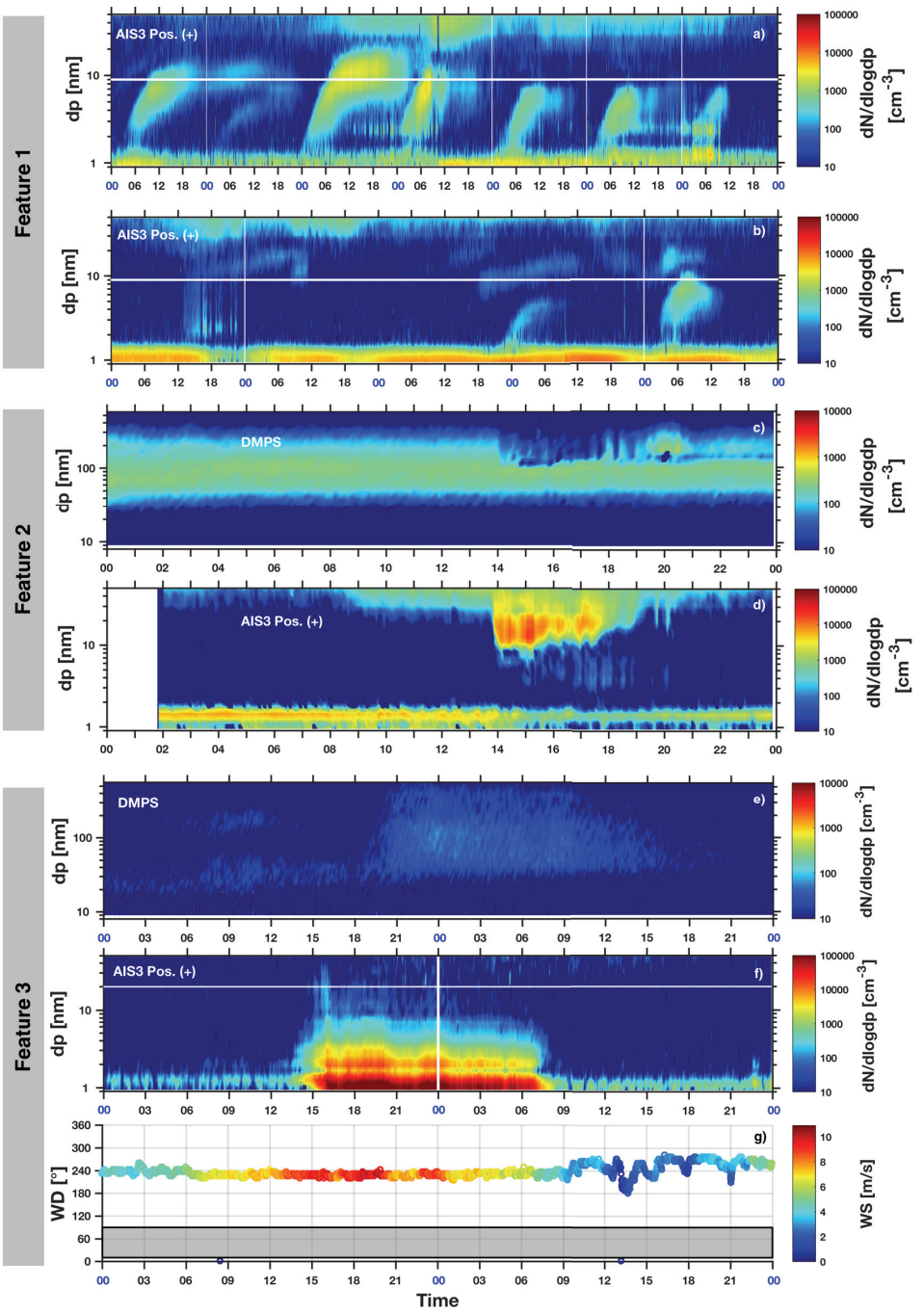

Figure 7. Ion processes measured by an AIS at Concordia station on Dome C, Antarctica. Feature 1 refers to atmospheric NPF: a) consecutive NPF events observed during 9-15 March 2011 by the AIS & b) consecutive multi-mode formation and growth events observed

during 12-16 February 2011 by the AIS; Feature 2 refers to the ion production in association with cloud formation on 20 January 2011: c) DMPS spectrum & d) AIS spectrum; and Feature 3 refers to wind-induced ion formation event observed on 3-4 July 2011: e) DMPS spectrum, f) AIS spectrum and g) wind directions (WD) and wind speeds (WS). Data are presented in UTC. The local time is UTC+8. Adapted from **Paper IV**.

In addition, during a cloud formation event (Fig. 7c), a reduction in the cluster ion concentration was seen along with an intensive production of ions larger than 8 nm. The reduction in cluster ion concentrations is known as a characteristic pattern in relation to cloud formation (Lihavainen et al., 2007). The ions with a size larger than 8 nm seen by the AIS might be multiply charged cloud droplets, but seen as singly-charged ions in the instrument. They could also be produced in the sampling line of the AIS as a result of the cloud droplet breakage under the high sampling rate and low temperature conditions. Moreover, ion production under strong wind conditions was also observed at the Concordia station (Fig. 7e-g). Unlike the feature reported from Jungfraujoch (Manninen et al., 2010), a fraction of the wind-induced ions was observed to grow to large sizes detectable by the DMPS at the Concordia station (Fig. 7e-g). Owing to the fact that the formation of ions occurred mostly below 7 nm, it is not likely that these ions were produced by mechanical pathways involving the shuttering of resuspended snowflakes and ice particles by turbulence, which in principle should lead to the formation of ions in all sizes. Rather, these wind-induced ions were probably formed via clustering of vapours released from the resuspension process via desorption and sublimation. The delay in the ion concentration burst from the onset of the wind intensification might be attributed to the needs of building-up atmospheric vapour concentrations for the clustering process to be detectable. Like being identified at Aboa (Virkkula et al., 2007), ion concentrations exhibited linear relationships with wind speeds (Fig. 8). The winds seemed to be more effective in air ion production at Concordia station than at Aboa.

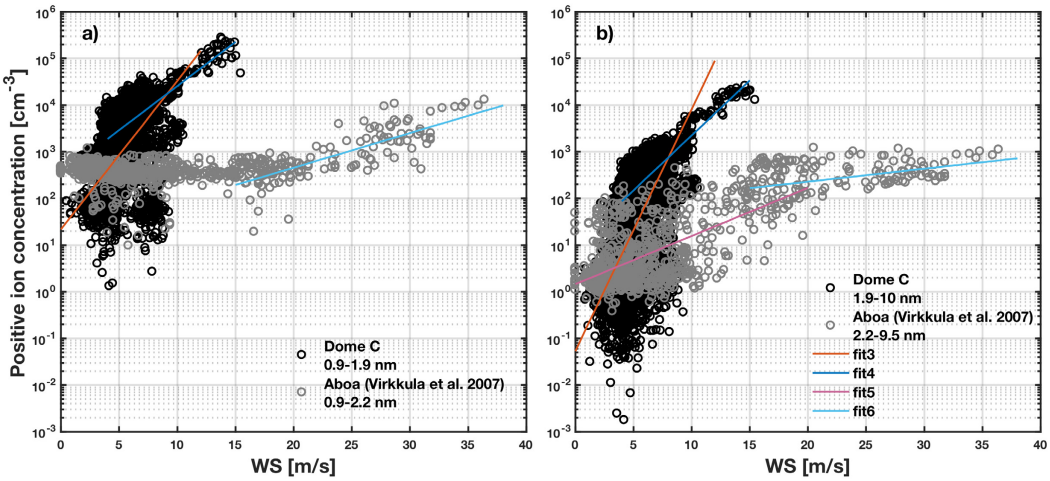

Figure 8. Ion concentrations as a function of wind speed. a) Ion concentration in the cluster size range: 0.9-1.9 nm for Dome C (black circles) and 0.9-2.2 nm for Aboa (grey circles, from Virkkula et al. (2007)). b) Ion concentration in the size range of 1.9-10 nm for Dome C (black circles) and in the intermediate size range of 2.2-9.5 nm for Aboa (grey circles, from Virkkula et al. (2007)). The Aboa ion data were reported in mass diameters. The size ranges referred here are reconverted from the measured electrical mobility channels in mobility diameters. A wind speed threshold of 17 m/s is used for characterising the 2-step linear feature at Aboa and 7 m/s for that at Concordia station. Adapted from **Paper IV**.

4. Review of papers and the author's contribution

Paper I verifies the performance of an Aerosol Diffusion Spectrometer (ADS) in laboratory and for measuring atmospheric new particle (NPF) formation at Hyytiälä SMEAR II station via an intercomparison with a Diffusion Mobility Particle Sizer (DMPS) and a Neutral and Air Ion Spectrometer (NAIS). Based on laboratory experiments, the ADS was found to have a good sizing ability and a reasonable accuracy for concentration measurement. It was also shown to be capable of depicting the features in atmospheric NPF. In this work, I analysed the ambient data for the instrumental intercomparison and participated in writing the manuscript.

Paper II identifies factors that introduce variability to the atmospheric radon activity concentration at the Hyytiälä SMEAR II station. The atmospheric radon activity concentration showed clear seasonal and diurnal variations. The diurnal patterns result mainly from the development of boundary layer. Seasonal variations are related primarily to seasonal changes in boundary layer heights, but also to snow cover and soil conditions. Low atmospheric radon activity concentrations were found in association with marine air masses, whereas high radon concentrations were observed with continental air masses. In this work, I performed all the data analysis and wrote most of the manuscript.

Paper III presents variations in natural ionising radiation that induces ionisation in the ambient air and their linkage to changes in air ion properties at Hyytiälä SMEAR II station. The diurnal features in ionising radiation came mainly from the response of atmospheric radon to boundary layer dynamics. The concentration of air ions in the size range of 0.8-1 nm was found to have a close relationship to the variability in ionising radiation. In general, our results suggest that 0.8-1.7 nm ions that have not undergone a very complicated dynamic process during their formation from primary ions tend to retain features in relation to variations in ionising radiation. In this work, I performed all the data analysis and wrote the manuscript.

Paper IV reports different features observed in air ions in an environment with high exposure to cosmic radiation and limited vapour sources. The results were obtained by analysing the first air ion dataset collected from the Concordia station located at Dome C, Antarctica. The main processes affecting the number size distribution of air ions at this site were identified, including atmospheric new particle formation, ion production or loss in relation to cloud formation and wind-induced ion formation. In this work, I performed substantially the data analysis and wrote most of the manuscript.

5. Conclusions and outlook

Air ions are initially produced by ionising radiation via the ionisation of air molecules and they modify the properties of atmospheric aerosol particles by providing stabilisation of newly formed clusters to enhance particle formation and participating in the dynamical processes of aerosol particles in the ambient air. Understanding the lifecycle of air ions in the atmosphere can ultimately deliver insights in the role of aerosol particles in air quality degradation and climate variability. This thesis brings advancement in understanding the connection of air ion properties to ionising radiation and air ion dynamic processes using the observational approach. The specific objectives listed in Section 1 are fulfilled by the following outcomes:

By intercomparing an Aerosol Diffusion Spectrometer (ADS), a Differential Mobility Particle Sizer (DMPS) and a Neutral and Air Ion Spectrometer (NAIS) in measuring size distributions during atmospheric new particle formation, we found that the general features depicted by these instruments were similar. The DMPS had a wide size range (3-1000 nm) for measurement. However, it underestimated the concentration of particles in 3-6 nm. The NAIS had the advantage in measuring small particles of 3-6 nm but was limited by an upper measureable size of 42 nm. The ADS provided number size distribution data of aerosol particles over the size range of 3-200 nm, and it turned out to be comparable to the NAIS for detecting relatively small particles and to the DMPS for detecting larger particles. These results reaffirm the importance of instrumental intercomparison for the verification of the applicability of instruments in ambient observations (**Paper I**).

Factors influencing the natural ionising radiation level in a boreal forest were identified. The diurnal pattern in ionising radiation was found mainly from changes in the atmospheric radon activity concentration as a result of boundary layer development and seasonality was primarily introduced by variations in boundary layer heights, snow cover depth and soil conditions. Air ions in the cluster size range of 0.8-1.7 nm exhibited connected patterns to, and dependency on, variations in the natural ionising radiation level. Dynamic processes modify the number size distributions of air ions. In general, the more aged the air ions were in the atmosphere, the less of their properties they could preserve in relation to the ionising radiation. Therefore, patterns in the 0.8-1 nm ion concentrations were found in a closer relationship to ionising radiation than larger ions in the cluster size range. With constraints on the data, a clear dependence of the production of 0.8-1.7 nm ions on ionising radiation was identifiable on NPF event days, but not on non-event days. This phenomenon likely implied a younger age of these ions on NPF event days than on non-event days (**Papers II& III**).

An Air Ion Spectrometer (AIS) was deployed on the Antarctic Plateau at Dome C for characterising air ion processes in a vapour-limited environment. Several features in air ions were identified, including atmospheric new particle formation (NPF), ion processes in relation to cloud formation as well as wind-induced ion production. Atmospheric NPF was

frequently observed during February, March, October and November. The onset time in the morning before noon of these observed NPF evidenced the involvement of photochemistry. Wind-induced ion production however was mainly seen in dark months. The features of the wind-induced ion formation process might likely imply that these ions were produced via clustering and growth processes rather than charging shattered products of snowflakes and ice crystals. The vapours were possibly released via resuspension from the surface snow during strong winds. A fraction of the wind-induced ions was found to be able to grow to a few hundred nm (**Paper IV**).

Overall, these results improve our understanding on how properties of air ions evolve through dynamic processes in the atmosphere after being produced by ionising radiation. Air ions are ubiquitously produced throughout the atmosphere and they modify constantly aerosol properties. The investigation of aerosol impacts on the global radiation budget requires knowledge on the contribution of secondary aerosol particles to the atmospheric aerosol loading. Therefrom, the formation mechanisms of aerosol particles from the gas phase and their destiny in the atmosphere need to be revealed, which can also benefit in seeking for solutions to combat air pollution. These, however, cannot be achieved without understanding the role of air ions. Moreover, air conductivity has been reported capable of acting as a proxy for air pollution (Retailis et al., 1991; Guo et al., 1996; Kamsali et al., 2009). Air ions, being the cause of air conductivity, are thus a key parameter in mitigating air pollution that is besetting many large and mega cities in the world.

Although observations of air ions have been conducted on short-term and long-term bases at many sites around the globe, their roles in the ambient air are far from being understood. Studies based on atmospheric observations show dominancy by the neutral pathway over the ion pathway in forming aerosol particles (Kulmala et al., 2007). However, theoretical simulations indicate that the involvement of ions in aerosol particle formation is thermodynamically favoured (Curtius et al., 2006). Recent chamber experiments suggest that some vapours are able to take over the role of ions in stabilising clusters to form nanoparticles (Kürten et al., 2016; Lehtipalo et al., 2016). However, to ultimately estimate the participation of ions in nanoparticle formation, we need to understand if ions can act also as catalysts in forming neutral clusters/particles and how significant are the three-body or multi-body recombination processes. Furthermore, the formation of clouds is one research focus in atmospheric aerosol studies. However, clouds are typically electrified and the charging mechanisms of clouds remain still ambiguous (Saunders, 2008), which is one research question to be solved in the atmospheric electricity discipline. There may exist an interconnection between the formation and charging mechanisms of clouds, which should be tackled with efforts of scientists from both the atmospheric electricity and atmospheric aerosol disciplines via collaboration. The interdisciplinary cooperation could also provide insights in ion closure assessment and ultimately elucidate the role of ions in the ambient air.

References

Aalto, P., Hämeri, K., Becker, E., Weber, R., Salm, J., MäKelä, J. M., Hoell, C., O'dowd, C. D., Karlsson, H., Hansson, H.-C., VäKevä, M., Koponen, I. K., Buzorius, G., and Kulmala, M.: Physical characterization of aerosol particles during nucleation events, Tellus, 53B, 344-358, 2001.

Aitken, J. A.: On Dust, Fogs, and Clouds, Trans. R. Soc. Edinburgh, XXX, 34-64, 1880.

Aitken, J. A.: On the Number of Dust Particles in the Atmosphere, Trans. R. Soc. Edinburgh, XXXV, 187-206, 1888.

Aplin, K. L., Harrison, R. G., and Rycroft, M. J.: Investigating Earth's Atmospheric Electricity: a Role Model for Planetary Studies, Space Sci. Rev., 137, 11-27, 10.1007/s11214-008-9372-x, 2008.

Arnold, F.: Atmospheric Ions and Aerosol Formation, Space Sci. Rev., 137, 225-239, 10.1007/s11214-008-9390-8, 2008.

Augustin, L., Barbante, C., Barnes, P. R. F., Barnola, J. M., Bigler, M., Castellano, E., Cattani, O., Chappellaz, J., Dahl-Jensen, D., Delmonte, B., Dreyfus, G., Durand, G., Falourd, S., Fischer, H., Flückiger, J., Hansson, M. E., Huybrechts, P., Jugie, G., Johnsen, S. J., Jouzel, J., Kaufmann, P., Kipfstuhl, J., Lambert, F., Lipenkov, V. Y., Littot, G. C., Longinelli, A., Lorrain, R., Maggi, V., Masson-Delmotte, V., Miller, H., Mulvaney, R., Oerlemans, J., Oerter, H., Orombelli, G., Parrenin, F., Peel, D. A., Petit, J.-R., Raynaud, D., Ritz, C., Ruth, U., Schwander, J., Siegenthaler, U., Souchez, R., Stauffer, B., Steffensen, J. P., Stenni, B., Stocker, T. F., Tabacco, I. E., Udisti, R., Wal, R. S. W. v. d., Broeke, M. v. d., Weiss, J., Wilhelms, F., Winther, J.-G., Wolff, E. W., and Zucchelli, M.: Eight glacial cycles from an Antarctic ice core, Nature, 429, 623-628, 2004.

Bazilevskaya, G. A., Usoskin, I. G., Flückiger, E. O., Harrison, R. G., Desorgher, L., Bütikofer, R., Krainev, M. B., Makhmutov, V. S., Stozhkov, Y. I., Svirzhevskaya, A. K., Svirzhevsky, N. S., and Kovaltsov, G. A.: Cosmic Ray Induced Ion Production in the Atmosphere, Space Sci. Rev., 137, 149–173, 10.1007/s11214-008-9339-y, 2008.

Becagli, S., Scarchilli, C., Traversi, R., Dayan, U., Severi, M., Frosini, D., Vitale, V., Mazzola, M., Lupi, A., Nava, S., and Udisti, R.: Study of present-day sources and transport processes affecting oxidised sulphur compounds in atmospheric aerosols at Dome C (Antarctica) from year-round sampling campaigns, Atmos. Environ., 52, 98-108, 10.1016/j.atmosenv.2011.07.053, 2012.

Boucher, O., Randall, D., Artaxo, P., Bretherton, C., Feingold, G., Forster, P., Kerminen, V.-M., Kondo, Y., Liao, H., Lohmann, U., Rasch, P., Satheesh, S. K., Sherwood, S., Stevens, B., and Zhang, X. Y.: Clouds and Aerosols, in: Climate Change 2013: The Physical Science Basis. Contribution of Working Group I to the Fifth Assessment Report of the Intergovernmental Panel on Climate Change . edited by: Stocker, T. F., Qin, D., Plattner, G.-K., Tignor, M., Allen, S. K., Boschung, J., Nauels, A., Xia, Y., Bex, V., and Midgley, P. M., Cambridge University Press, Cambridge, United Kingdom and New York, NY, USA., 2013.

Curtius, J., Lovejoy, E. R., and Froyd, K. D.: Atmospheric Ion-induced Aerosol Nucleation, Space Sci. Rev., 125, 159-167, 10.1007/s11214-006-9054-5, 2006.

Dultsev, F. N., Mik, I. A., Dubtsov, S. N., and Dultseva, G. G.: Identification of the functional groups on the surface of nanoparticles formed in photonucleation of aldehydes generated during forest fire events, 20th International Symposium on Atmospheric and Ocean Optics: Atmospheric Physics, Novosibirsk, Russian, 2014, 92922Q-92922Q-92927.

Duplissy, J., Merikanto, J., Franchin, A., Tsagkogeorgas, G., Kangasluoma, J., Wimmer, D., Vuollekoski, H., Schobesberger, S., Lehtipalo, K., Flagan, R. C., Brus, D., Donahue, N. M., Vehkamäki, H., Almeida, J., Amorim, A., Barmet, P., Bianchi, F., Breitenlechner, M., Dunne, E. M., Guida, R., Henschel, H., Junninen, H., Kirkby, J., Kürten, A., Kupc, A., Määttänen, A., Makhmutov, V., Mathot, S., Nieminen, T., Onnela, A., Praplan, A. P., Riccobono, F., Rondo, L., Steiner, G., Tome, A., Walther, H., Baltensperger, U., Carslaw, K. S., Dommen, J., Hansel, A., Petäjä, T., Sipilä, M., Stratmann, F., Vrtala, A., Wagner, P. E., Worsnop, D. R., Curtius, J., and Kulmala, M.: Effect of ions on sulfuric acid-water binary particle formation: 2. Experimental data and comparison with QC-normalized classical nucleation theory, J. Geophys. Res. Atmos., 121, 1752–1775, doi:10.1002/2015JD023539, 2016.

Dusek, U., Frank, G. P., Hildebrandt, L., Curtius, J., Schneider, J., Walter, S., Chand, D., Drewnick, F., Hings, S., Jung, D., Borrmann, S., and Andreae, M. O.: Size matters more than chemistry for cloud-nucleating ability of aerosol particles, Science, 312, 1375-1378, 10.1126/science.1125261, 2006.

Eisele, F. L.: Identification of tropospheric ions, J. Geophys. Res., 91, 7879-7906, 1986.

Eisele, F. L.: First tandem mass spectrometric measurement of tropospheric ions, J. Geophys. Res., 93, 716-724, 1988.

Eisele, F. L.: Natural and anthropogenic negative ions in the troposphere, J. Geophys. Res., 94, 2183-2196, 1989.

Eisele, F. L., and Tanner, D. J.: Identification of ions in continental air, J. Geophys. Res., 95, 20539-20550, 1990.

Enghoff, M. B., Pedersen, J. O. P., Bondo, T., Johnson, M. S., Paling, S., and Svensmark, H.: Evidence for the Role of Ions in Aerosol Nucleation, J. Phys. Chem. A, 112, 10305–10309, 2008.

Enghoff, M. B., and Svensmark, H.: The role of atmospheric ions in aerosol nucleation – a review, Atmos. Chem. Phys., 8, 4911–4923, 2008.

Fiebig, M., Hirdman, D., Lunder, C. R., Ogren, J. A., Solberg, S., Stohl, A., and Thompson, R. L.: Annual cycle of Antarctic baseline aerosol: controlled by photooxidation-limited aerosol formation, Atmos. Chem. Phys., 14, 3083–3093, 10.5194/acp-14-3083-2014, 2014.

Flagan, R. C.: History of electrical aerosol measurements, Aerosol Sci. Technol., 28, 301-380, 10.1080/02786829808965530, 1998.

Gonser, S. G., Klein, F., Birmili, W., Größ, J., Kulmala, M., Manninen, H. E., Wiedensohler, A., and Held, A.: Ion – particle interactions during particle formation and growth at a coniferous forest site in central Europe, Atmos. Chem. Phys., 14, 10547-10563, 10.5194/acp-14-10547-2014, 2014.

Guo, Y., Barthakur, N. N., and Bhartendu, S.: Using atmospheric electrical conductivity as an urban air pollution indicator, J. Geophys. Res.: Atmos., 101, 9197-9203, 10.1029/95jd02904, 1996.

Hari, P., and Kulmala, M.: Station for measuring ecosystem-atmosphere relations (SMEAR II), Boreal Environ. Res., 10, 315-322, 2005.

Harrison, R. G.: The global atmospheric electrical circuit and climate, Surv. Geophys., 25, 441–484, 2004.

Harrison, R. G., and Tammet, H.: Ions in the Terrestrial Atmosphere and Other Solar System Atmospheres, Space Sci. Rev., 137, 107-118, 10.1007/s11214-008-9356-x, 2008.

Herbert, K. B. H.: John Canton - Pioneer investigator of atmospheric electricity, Weather, 52, 286-290, 1997.

Hinds, W. C.: Aerosol technology: Properties, behavior, and measurement of airborne particles, 2 ed., Wiley-Interscience, New York, 1999.

Hirsikko, A., Paatero, J., Hatakka, J., and Kulmala, M.: The ^{222}Rn activity concentration, external radiation dose and air ion production rates in a boreal forest in Finalnd between March 2000 and June 2006, Boreal Env. Res., 12, 265 - 278, 2007.

Hirsikko, A., Nieminen, T., Gagné, S., Lehtipalo, K., Manninen, H. E., Ehn, M., Hõrrak, U., Kerminen, V. M., Laakso, L., McMurry, P. H., Mirme, A., Mirme, S., Petäjä, T., Tammet, H., Vakkari, V., Vana, M., and Kulmala, M.: Atmospheric ions and nucleation: a review of observations, Atmos. Chem. Phys., 11, 767-798, 10.5194/acp-11-767-2011, 2011.

Hõrrak, U., Salm, J., and Tammet, H.: Bursts of intermediate ions in atmospheric air, J. Geophys. Res.: Atmos., 103, 13909-13915, 10.1029/97jd01570, 1998.

Hõrrak, U., Tammet, H., Aalto, P. P., Vana, M., Hirsikko, A., Laakso, L., and Kulmala, M.: Formation of Charged Nanometer Aerosol Particles Associated with Rainfall: Atmospheric Measurements and Lab Experiment, Report Series in Aerosol Science, 80, 180-185, 2006.

IPCC: Fifth assessment report, 2014.

Israël, H.: Atmospheric electricity, Vol. I, Israel Program for Scientific Translations, Jerusalem, 1970.

Järvinen, E., Virkkula, A., Nieminen, T., Aalto, P. P., Asmi, E., Lanconelli, C., Busetto, M., Lupi, A., Schioppo, R., Vitale, V., Mazzola, M., Petäjä, T., Kerminen, V. M., and Kulmala, M.: Seasonal cycle and modal structure of particle number size distribution at Dome C, Antarctica, Atmos. Chem. Phys., 13, 7473-7487, 10.5194/acp-13-7473-2013, 2013.

Kamsali, N., Prasad, B. S. N., and Datta, J.: Atmospheric electrical conductivity measurements and modeling for application to air pollution studies, Adv. Space Res., 44, 1067-1078, 10.1016/j.asr.2009.05.020, 2009.

Kanawade, V. P., Benson, D. R., and Lee, S.-H.: Statistical analysis of 4-year observations of aerosol sizes in a semi-rural continental environment, Atmos. Environ., 59, 30-38, 10.1016/j.atmosenv.2012.05.047, 2012.

Kerminen, V.-M., Paramonov, M., Anttila, T., Riipinen, I., Fountoukis, C., Korhonen, H., Asmi, E., Laakso, L., Lihavainen, H., Swietlicki, E., Svenningsson, B., Asmi, A., Pandis, S. N., Kulmala, M., and Petäjä, T.: Cloud condensation nuclei production associated with atmospheric nucleation: a synthesis based on existing literature and new results, Atmos. Chem. Phys., 12, 12037–12059, 10.5194/acp-12-12037-2012, 2012.

Kirkby, J., Curtius, J., Almeida, J., Dunne, E., Duplissy, J., Ehrhart, S., Franchin, A., Gagne, S., Ickes, L., Kurten, A., Kupc, A., Metzger, A., Riccobono, F., Rondo, L., Schobesberger,

S., Tsagkogeorgas, G., Wimmer, D., Amorim, A., Bianchi, F., Breitenlechner, M., David, A., Dommen, J., Downard, A., Ehn, M., Flagan, R. C., Haider, S., Hansel, A., Hauser, D., Jud, W., Junninen, H., Kreissl, F., Kvashin, A., Laaksonen, A., Lehtipalo, K., Lima, J., Lovejoy, E. R., Makhmutov, V., Mathot, S., Mikkila, J., Minginette, P., Mogo, S., Nieminen, T., Onnela, A., Pereira, P., Petaja, T., Schnitzhofer, R., Seinfeld, J. H., Sipila, M., Stozhkov, Y., Stratmann, F., Tome, A., Vanhanen, J., Viisanen, Y., Vrtala, A., Wagner, P. E., Walther, H., Weingartner, E., Wex, H., Winkler, P. M., Carslaw, K. S., Worsnop, D. R., Baltensperger, U., and Kulmala, M.: Role of sulphuric acid, ammonia and galactic cosmic rays in atmospheric aerosol nucleation, Nature, 476, 429-433, 10.1038/nature10343, 2011.

Kolarz, P., Gaisberger, M., Madl, P., Hofmann, W., Ritter, M., and Hartl, A.: Characterization of ions at Alpine waterfalls, Atmos. Chem. Phys., 12, 3687-3697, 10.5194/acp-12-3687-2012, 2012.

Kontkanen, J., Lehtipalo, K., Ahonen, L., Kangasluoma, J., Manninen, H. E., Hakala, J., Rose, C., Sellegri, K., Xiao, S., Wang, L., Qi, X., Nie, W., Ding, A., Yu, H., Lee, S., Kerminen, V.-M., Petäjä, T., and Kulmala, M.: Measurements of sub-3 nm particles using a particle size magnifier in different environments: from clean mountain top to polluted megacities, Atmos. Chem. Phys., 17, 2163-2187, 10.5194/acp-17-2163-2017, 2017.

Koponen, I. K., Virkkula, A., Hillamo, R., Kerminen, V.-M., and Kulmala, M.: Number size distributions and concentrations of the continental summer aerosols in Queen Maud Land, Antarctica, J. Geophys. Res., 108, 10.1029/2003jd003614, 2003.

Kulkarni, P., Baron, P. A., and Willeke, K.: Aerosol measurement: principles, techniques, and applications, 3 ed., John Wiley and Sons, Inc, New York, Chichester, Weinheim, Brisbane, Singapore, Toronto, 2011.

Kulmala, M., Vehkamäki, H., Petäjä, T., Dal Maso, M., Lauri, A., Kerminen, V. M., Birmili, W., and McMurry, P. H.: Formation and growth rates of ultrafine atmospheric particles: a review of observations, J. Aerosol Sci., 35, 143-176, 10.1016/j.jaerosci.2003.10.003, 2004.

Kulmala, M., Riipinen, I., Sipila, M., Manninen, H. E., Petaja, T., Junninen, H., Maso, M. D., Mordas, G., Mirme, A., Vana, M., Hirsikko, A., Laakso, L., Harrison, R. M., Hanson, I., Leung, C., Lehtinen, K. E., and Kerminen, V.-M.: Toward direct measurement of atmospheric nucleation, Science, 318, 89-92, 10.1126/science.1144124, 2007.

Kulmala, M., Petaja, T., Nieminen, T., Sipila, M., Manninen, H. E., Lehtipalo, K., Maso, M. D., Aalto, P. P., Junninen, H., Paasonen, P., Riipinen, I., Lehtinen, K. E., Laaksonen, A., and Kerminen, V.-M.: Measurement of the nucleation of atmospheric aerosol particles, Nat. Protoc., 7, 1651-1667, 10.1038/nprot.2012.091, 2012.

Kulmala, M., Kontkanen, J., Junninen, H., Lehtipalo, K., Manninen, H. E., Nieminen, T., Petaja, T., Sipila, M., Schobesberger, S., Rantala, P., Franchin, A., Jokinen, T., Jarvinen, E., Aijala, M., Kangasluoma, J., Hakala, J., Aalto, P. P., Paasonen, P., Mikkila, J., Vanhanen, J., Aalto, J., Hakola, H., Makkonen, U., Ruuskanen, T., Mauldin, R. L., 3rd, Duplissy, J., Vehkamaki, H., Back, J., Kortelainen, A., Riipinen, I., Kurten, T., Johnston, M. V., Smith, J. N., Ehn, M., Mentel, T. F., Lehtinen, K. E., Laaksonen, A., Kerminen, V.-M., and Worsnop, D. R.: Direct observations of atmospheric aerosol nucleation, Science, 339, 943-946, 10.1126/science.1227385, 2013.

Kulmala, M., Petäjä, T., Kerminen, V.-M., Kujansuu, J., Ruuskanen, T., Ding, A., Nie, W., Hu, M., Wang, Z., Wu, Z., Wang, L., and Worsnop, D. R.: On secondary new particle formation in China, Front. Environ. Sci. Eng., 10, 8, 10.1007/s11783-016-0850-1, 2016.

Kürten, A., Bianchi, F., Almeida, J., Kupiainen-Määttä, O., Dunne, E. M., Duplissy, J., Williamson, C., Barmet, P., Breitenlechner, M., Dommen, J., Donahue, N. M., Flagan, R. C., Franchin, A., Gordon, H., Hakala, J., Hansel, A., Heinritzi, M., Ickes, L., Jokinen, T., Kangasluoma, J., Kim, J., Kirkby, J., Kupc, A., Lehtipalo, K., Leiminger, M., Makhmutov, V., Onnela, A., Ortega, I. K., Petäjä, T., Praplan, A. P., Riccobono, F., Rissanen, M. P., Rondo, L., Schnitzhofer, R., Schobesberger, S., Smith, J. N., Steiner, G., Stozhkov, Y., Tomé, A. n., Tröstl, J., Tsagkogeorgas, G., Wagner, P. E., Wimmer, D., Ye, P., Baltensperger, U., Carslaw, K., Kulmala, M., and Curtius, J.: Experimental particle formation rates spanning tropospheric sulfuric acid and ammonia abundances, ion production rates, and temperatures, J. Geophys. Res.: Atmos, 121, 12377-12400, 10.1002/, 2016.

Kyrö, E. M., Kerminen, V. M., Virkkula, A., Dal Maso, M., Parshintsev, J., Ruíz-Jimenez, J., Forsström, L., Manninen, H. E., Riekkola, M. L., Heinonen, P., and Kulmala, M.: Antarctic new particle formation from continental biogenic precursors, Atmos. Chem. Phys., 13, 3527-3546, 10.5194/acp-13-3527-2013, 2013.

Laakso, L., Petäjä, T., Lehtinen, K. E. J., Kulmala, M., Paatero, J., Hõrrak, U., Tammet, H., and Joutsensaari, J.: Ion production rate in a boreal forest based on ion, particle and radiation measurements, Atmos. Chem. Phys., 4, 1933–1943, 2004.

Laakso, L., Hirsikko, A., Grönholm, T., Kulmala, M., Luts, A., and Parts, T.-E.: Waterfalls as sources of small charged aerosol particles, Atmos. Chem. Phys., 7, 2271–2275, 2007.

Lehtipalo, K., Rondo, L., Kontkanen, J., Schobesberger, S., Jokinen, T., Sarnela, N., Kurten, A., Ehrhart, S., Franchin, A., Nieminen, T., Riccobono, F., Sipila, M., Yli-Juuti, T., Duplissy, J., Adamov, A., Ahlm, L., Almeida, J., Amorim, A., Bianchi, F., Breitenlechner, M., Dommen, J., Downard, A. J., Dunne, E. M., Flagan, R. C., Guida, R., Hakala, J., Hansel, A., Jud, W., Kangasluoma, J., Kerminen, V. M., Keskinen, H., Kim, J., Kirkby, J., Kupc, A., Kupiainen-Maatta, O., Laaksonen, A., Lawler, M. J., Leiminger, M., Mathot, S., Olenius, T., Ortega, I. K., Onnela, A., Petaja, T., Praplan, A., Rissanen, M. P., Ruuskanen, T., Santos, F. D., Schallhart, S., Schnitzhofer, R., Simon, M., Smith, J. N., Trostl, J., Tsagkogeorgas, G., Tome, A., Vaattovaara, P., Vehkamaki, H., Vrtala, A. E., Wagner, P. E., Williamson, C., Wimmer, D., Winkler, P. M., Virtanen, A., Donahue, N. M., Carslaw, K. S., Baltensperger, U., Riipinen, I., Curtius, J., Worsnop, D. R., and Kulmala, M.: The effect of acid-base clustering and ions on the growth of atmospheric nano-particles, Nat. Commun., 7, 11594, 10.1038/ncomms11594, 2016.

Leino, K., Nieminen, T., Manninen, H. E., Petäjä, T., Kerminen, V.-M., and Kulmala, M.: Intermediate ions as a strong indicator of new particle formation bursts in a boreal forest, Boreal Env. Res., 21, 274-286, 2016.

Lihavainen, H., Komppula, M., Kerminen, V.-M., Järvinen, H., Viisanen, Y., Lehtinen, K., Vana, M., and Kulmala, M.: Size distributions of atmospheric ions inside clouds and in cloud-free air at a remote continental site, Boreal Env. Res., 12, 337-344, 2007.

Manninen, H. E., Petäjä, T., Asmi, E., Riipinen, I., Niemnen, T., Mikkilä, J., Hõrrak, U., Mirme, A., Mirme, S., Laakso, L., Kerminen, V.-M., and Kulmala, M.: Long-time field

measurements of charged and neutral clusters using Neutral cluster and Air Ion Spectrometer (NAIS) Boreal Env. Res., 14, 591-605, 2009.

Manninen, H. E., Nieminen, T., Asmi, E., Gagné, S., Häkkinen, S., Lehtipalo, K., Aalto, P. P., Vana, M., Mirme, A., Mirme, S., Hõrrak, U., Plass-Dülmer, C., Stange, G., Kiss, G., Hoffer, A., Törő, N., Moerman, M., Henzing, B., Leeuw, G. d., Brinkenberg, M., Kouvarakis, G. N., Bougiatioti, A., Mihalopoulos, N., O'Dowd, C., Ceburnis, D., Arneth, A., Svenningsson, B., Swietlicki, E., Tarozzi, L., Decesari, S., Facchini, M. C., Birmili, W., Sonntag, A., Wiedensohler, A., Boulon, J., Sellegri, K., Laj, P., Gysel, M., Bukowiecki, N., Weingartner, E., Wehrle, G., Laaksonen, A., Hamed, A., Joutsensaari, J., Petäjä, T., Kerminen, V. M., and Kulmala, M.: EUCAARI ion spectrometer measurements at 12 European sites – analysis of new particle formation events, Atmos. Chem. Phys., 10, 7907-7927, 10.5194/acp-10-7907-2010, 2010.

Mavliev, R. A., and Ankilov, A. N.: Methods for the treatment of data for a netlike diffusion battery Kolloidn. Zhurn. (in Russian), 47, 523 – 530, 1985.

McMurry, P. H.: A review of atmospheric aerosol measurements, Atmos. Environ., 34, 1959-1999, 2000a.

McMurry, P. H.: The History of Condensation Nucleus Counters, Aerosol Science and Technology, 33, 297-322, 10.1080/02786820050121512, 2000b.

Merikanto, J., Spracklen, D. V., Mann, G. W., Pickering, S. J., and Carslaw, K. S.: Impact of nucleation on global CCN, Atmos. Chem. Phys., 9, 8601-8616, 2009.

Mirme, A., Tamm, E., Mordas, G., Vana, M., Uin, H., Mirme, S., Bernotas, T., Laakso, L., Hirsikko, A., and Kulmala, M.: A wide-range multi-channel Air Ion Spectrometer, Boreal Env. Res., 12, 247-264, 2007.

Mirme, S., and Mirme, A.: The mathematical principles and design of the NAIS – a spectrometer for the measurement of cluster ion and nanometer aerosol size distributions, Atmos. Meas. Tech., 6, 1061-1071, 10.5194/amt-6-1061-2013, 2013.

Modini, R. L., Ristovski, Z. D., Johnson, G. R., He, C., Surawski, N., Morawska, L., Suni, T., and Kulmala, M.: New particle formation and growth at a remote, sub-tropical coastal location, Atmos. Chem. Phys., 9, 7607-7621, 2009.

Mönkkönen, P., Koponen, I. K., Lehtinen, K. E. J., Hämeri, K., Uma, R., and Kulmala, M.: Measurements in a highly polluted Asian mega city: observations of aerosol number size distribution, modal parameters and nucleation events, Atmos. Chem. Phys., 5, 57–66, 2005.

Nie, W., Ding, A., Wang, T., Kerminen, V. M., George, C., Xue, L., Wang, W., Zhang, Q., Petaja, T., Qi, X., Gao, X., Wang, X., Yang, X., Fu, C., and Kulmala, M.: Polluted dust promotes new particle formation and growth, Sci. Rep., 4, 6634, 10.1038/srep06634, 2014.

Nieminen, T., Asmi, A., Maso, M. D., Aalto, P. P., Keronen, P., Petäjä, T., Kulmala, M., and Kerminen, V.-M.: Trends in atmospheric new-particle formation: 16 years of observations in a boreal-forest environment, Boreal Env. Res., 19 191–214, 2014.

Paatero, J., Hatakka, J., Mattsson, R., and Lehtinen, I.: A comprehensive station for monitoring atmospheric radioactivity, Radiat. Prot. Dosim., 54, 33-39, 1994.

Pant, V., Siingh, D., and Kamra, A. K.: Size distribution of atmospheric aerosols at Maitri, Antarctica, Atmos. Environ., 45, 5138-5149, 10.1016/j.atmosenv.2011.06.028, 2011.

Perkins, M. D., and Eisele, F. L.: First Mass Spectrometric Measurements of Atmospheric Ions at Ground Level, J. Geophys. Res., 89, 9649-9657, 1984.

Poschl, U.: Atmospheric aerosols: composition, transformation, climate and health effects, Angew. Chem., 44, 7520-7540, 10.1002/anie.200501122, 2005.

Retailis, D., Pitta, A., and Psallidas, P.: The Conductivity of the Air and Other Electrical Parameters in Relation to Meteorological Elements and Air Pollution in Athens, Meteorol. Atmos. Phys., 46, 197-204, 1991.

Riipinen, I., Yli-Juuti, T., Pierce, J. R., Petaja, T., Worsnop, D. R., Kulmala, M., and Donahue, N. M.: The contribution of organics to atmospheric nanoparticle growth, Nature Geosci, 5, 453-458, 2012.

Samson, J. A., Barnard, S. C., Obremski, J. S., Riley, D. C., Black, J. J., and Hogan, A. W.: On the systematic variation In surface aerosol concentration at the South Pole, Atmos. Res., 25, 385-396, 1990.

Saunders, C.: Charge Separation Mechanisms in Clouds, Space Sci. Rev., 137, 335-353, 10.1007/s11214-008-9345-0, 2008.

Seinfeld, J. H., and Pandis, S. N.: Atmospheric chemistry and physics from air pollution to climate change, 2 ed., John Wiley & Sons, Inc., Hoboken, New Jersey, United States, 2006.

Shuman, N. S., Hunton, D. E., and Viggiano, A. A.: Ambient and modified atmospheric ion chemistry: from top to bottom, Chem. Rev., 115, 4542-4570, 10.1021/cr5003479, 2015.

Simpson, G. C.: Atmospheric Electricity, Mon. Weather Rev., 34, 16-17, 1906.

Sipila, M., Sarnela, N., Jokinen, T., Henschel, H., Junninen, H., Kontkanen, J., Richters, S., Kangasluoma, J., Franchin, A., Perakyla, O., Rissanen, M. P., Ehn, M., Vehkamaki, H., Kurten, T., Berndt, T., Petaja, T., Worsnop, D., Ceburnis, D., Kerminen, V. M., Kulmala, M., and O'Dowd, C.: Molecular-scale evidence of aerosol particle formation via sequential addition of HIO3, Nature, 537, 532-534, 10.1038/nature19314, 2016.

Stanier, C. O., Khlystov, A. Y., and Pandis, S. N.: Ambient aerosol size distributions and number concentrations measured during the Pittsburgh Air Quality Study (PAQS), Atmos. Environ., 38, 3275-3284, 10.1016/j.atmosenv.2004.03.020, 2004.

Tammet, H.: Continuous scanning of the mobility and size distribution of charged clusters and nanometer particles in atmospheric air and the Balanced Scanning Mobility Analyzer BSMA, Atmos. Res., 82, 523-535, 10.1016/j.atmosres.2006.02.009, 2006.

Tammet, H., Hõrrak, U., and Kulmala, M.: Negatively charged nanoparticles produced by splashing of water, Atmos. Chem. Phys., 9, 357–367, 2009.

Tammet, H., Komsaare, K., and Hõrrak, U.: Intermediate ions in the atmosphere, Atmos. Res., 135-136, 263-273, 10.1016/j.atmosres.2012.09.009, 2014.

Tanner, D. J., and Eisele, F. L.: Ions in oceanic and continental air masses, J. Geophys. Res., 96, 1023-1031, 1991.

Tuomi, T. J.: Ten year summary 1977-1986 of Atmospheric Electricity Measured at Helsinki-Vantaa Airport, Finland, Geophysica, 25, 1-20, 1989.

Vakkari, V., Laakso, H., Kulmala, M., Laaksonen, A., Mabaso, D., Molefe, M., Kgabi, N., and Laakso, L.: New particle formation events in semi-clean South African savannah, Atmos. Chem. Phys., 11, 3333-3346, 10.5194/acp-11-3333-2011, 2011.

Virkkula, A., Hirsikko, A., Vana, M., Aalto, P. P., Hillamo, R., and Kulmala, M.: charged particle size distributions and analysis of particle formation events at the Finnish antarctic research station aboa, Boreal Env. Res., 12, 397–408, 2007.

Wang, Z., Wu, Z., Yue, D., Shang, D., Guo, S., Sun, J., Ding, A., Wang, L., Jiang, J., Guo, H., Gao, J., Cheung, H. C., Morawska, L., Keywood, M., and Hu, M.: New particle formation in China: Current knowledge and further directions, Sci. Total Environ, 577, 258-266, 10.1016/j.scitotenv.2016.10.177, 2017a.

Wang, Z., Wu, Z., Yue, D., Shang, D., Guo, S., Sun, J., Ding, A., Wang, L., Jiang, J., Guo, H., Gao, J., Cheung, H. C., Morawska, L., Keywood, M., and Hu, M.: New particle formation in China: Current knowledge and further directions., Sci. Total Environ., 577, 258-266, doi: 10.1016/j.scitotenv.2016.10.177, 2017b.

Wehner, B.: Variability of the aerosol number size distribution in Beijing, China: New particle formation, dust storms, and high continental background, Geophys. Res. Lett., 31, 10.1029/2004gl021596, 2004.

Weller, R., Schmidt, K., Teinilä, K., and Hillamo, R.: Natural new particle formation at the coastal Antarctic site Neumayer, Atmos. Chem. Phys., 15, 11399-11410, 10.5194/acp-15-11399-2015, 2015.

Wiedensohler, A., Covert, D. S., Swietlicki, E., Aalto, P., Heintzenberg, J., and Leck, C.: Occurrence of an ultrfine particle mode less than 20 nm in diameter in the marine boundary layer during Arctic summer and autumn, Tellus, 48B, 213-222, 1996.

Wiedensohler, A., Birmili, W., Nowak, A., Sonntag, A., Weinhold, K., Merkel, M., Wehner, B., Tuch, T., Pfeifer, S., Fiebig, M., Fjäraa, A. M., Asmi, E., Sellegri, K., Depuy, R., Venzac, H., Villani, P., Laj, P., Aalto, P., Ogren, J. A., Swietlicki, E., Williams, P., Roldin, P., Quincey, P., Hüglin, C., Fierz-Schmidhauser, R., Gysel, M., Weingartner, E., Riccobono, F., Santos, S., Grüning, C., Faloon, K., Beddows, D., Harrison, R., Monahan, C., Jennings, S. G., O'Dowd, C. D., Marinoni, A., Horn, H. G., Keck, L., Jiang, J., Scheckman, J., McMurry, P. H., Deng, Z., Zhao, C. S., Moerman, M., Henzing, B., Leeuw, G. d., Löschau, G., and Bastian, S.: Mobility particle size spectrometers: harmonization of technical standards and data structure to facilitate high quality long-term observations of atmospheric particle number size distributions, Atmos. Meas. Tech., 5, 657-685, 10.5194/amt-5-657-2012, 2012.

Wilson, C. T. R.: The effect of rontgen's rays on cloudy condensation, Proc. R. Soc. Lond., 59, 338-339, 1895.

Wilson, C. T. R.: On the condensation nuclei produced in gases by the action of rontgen rays, uranium rays, ultra-violet light, and other agents, Philos. T. R. Soc. Lond., Series A, 192, 403-453, 1899.

Wilson, C. T. R.: Investigations on lightning discharges and on the electric field of thunderstorms, Philos. Trans. R. Soc. London A., 221, 73-115, 1921.

Wilson, C. T. R.: The electric field of a thundercloud and some of its effects Proc. Phys. Soc. London, 37, 1924.

Wu, Z., Hu, M., Liu, S., Wehner, B., Bauer, S., Ma ßling, A., Wiedensohler, A., Petäjä, T., Dal Maso, M., and Kulmala, M.: New particle formation in Beijing, China: Statistical analysis of a 1-year data set, J. Geophys. Res., 112, 10.1029/2006jd007406, 2007.

Wu, Z., Hu, M., Lin, P., Liu, S., Wehner, B., and Wiedensohler, A.: Particle number size distribution in the urban atmosphere of Beijing, China, Atmos. Environ., 42, 7967-7980, 10.1016/j.atmosenv.2008.06.022, 2008.

Yu, F., and Luo, G.: Simulation of particle size distribution with a global aerosol model: contribution of nucleation to aerosol and CCN number concentrations, Atmos. Chem. Phys., 9, 7691-7710, 2009.

Yu, F.: Ion-mediated nucleation in the atmosphere: Key controlling parameters, implications, and look-up table, J. Geophys. Res., 115, 10.1029/2009jd012630, 2010.

Zhu, Y., Hinds, W. C., Kim, S., and Sioutas, C.: Concentration and Size Distribution of Ultrafine Particles Near a Major Highway, J. Air Waste Manag. Assoc., 52, 1032-1042, 10.1080/10473289.2002.10470842, 2002.

Paper I

Journal of Aerosol Science 105 (2017) 10–23

Contents lists available at ScienceDirect

Journal of Aerosol Science

journal homepage: www.elsevier.com/locate/jaerosci

Laboratory verification of Aerosol Diffusion Spectrometer and the application to ambient measurements of new particle formation

S. Dubtsov[a], T. Ovchinnikova[b], S. Valiulin[a,c], X. Chen[d], H.E. Manninen[d], P.P. Aalto[d], T. Petäjä[d,*]

[a] Voevodsky Institute of Chemical Kinetics and Combustion SB RAS, Institutskaya str., 3, 630090 Novosibirsk, Russia
[b] Institute for Water and Environmental Problems SB RAS, Morskoi avenue., 2, 630090 Novosibirsk, Russia
[c] Novosibirsk State Pedagogical University, Viluiskaya str., 28, 630126 Novosibirsk, Russia
[d] Department of Physics, University of Helsinki, P.O.Box 64 (Gustaf Hällstrømin katu 2a) FI-00014, Finland

ARTICLE INFO

Keywords:
Aerosol Diffusion Spectrometer
Differential Mobility Particle Sizer
Neutral cluster and Air Ion Spectrometer
new particle formation

ABSTRACT

Information on the ambient aerosol number size distribution is essential to address various scientific questions related to aerosol particles in the atmosphere. However, due to the wide size and concentrations ranges of ambient aerosol particles, no single instrument alone is capable of measuring them all. Instruments based on different measurement principles are engaged in the measurement of atmospheric aerosols. Intercomparison of such instruments is necessary to cross-validate the reliability of obtained data. In this study, a verification of a Novosibirsk Aerosol Diffusion Spectrometer (ADS) in the size classification of aerosol particles was carried out in laboratory and via a field intercomparison with a Differential Mobility Particle Sizer (DMPS) and a Neutral cluster and Air Ion Spectrometer (NAIS). The laboratory experiments affirmed the good accuracy of the ADS on sizing and concentration measurement. The ADS was satisfactorily comparable with the DMPS and the NAIS for the measurement of ambient aerosols within the size range 3–200 nm. The differences between condensation sinks derived from the ADS and DMPS measurements were smaller on days with new particle formation (NPF) than on non-NPF days. Similar formation rates and growth rates were acquired based on the DMPS, NAIS and ADS measurements, proving a reasonable ability of the ADS in measuring the concentrations and size distribution of nucleation-mode particles.

1. Introduction

Atmospheric aerosol particles have regional and global effects on climate, cloud formation, air quality, visibility and human health (Clarke et al., 2011; Collaud Coen et al., 2013; Dusek et al., 2006; Fountoukis et al., 2014; Jimenez et al., 2009; Kerminen, Lihavainen, Komppula, Viisanen & Kulmala, 2005; Pöschl, 2005; von Klot et al., 2005). The ambient aerosol number size distribution is of the key variables, in addition to the chemical composition, that are required to address these effects (Asmi et al., 2011; Freutel et al., 2013). The aerosol number size distribution spans from 1 nm up to 10 μm (Jiang et al., 2011; Kulmala et al., 2013; Kulmala et al., 2007; Laakso et al., 2003), while the total number concentration varies from 10^2 cm^{-3} in clean remote areas (Koponen, Virkkula, Hillamo, Kerminen & Kulmala, 2003) to 10^6 cm^{-3} in polluted urban mega-cities and in intense pollution plumes (Mönkkönen et al., 2005).

The challenge in measuring ambient aerosol number size distributions goes hand in hand with the wide range of particle sizes

* Corresponding author.
E-mail address: tuukka.petaja@helsinki.fi (T. Petäjä).

http://dx.doi.org/10.1016/j.jaerosci.2016.10.015
Received 4 December 2015; Received in revised form 15 June 2016; Accepted 27 October 2016
Available online 08 November 2016
0021-8502/

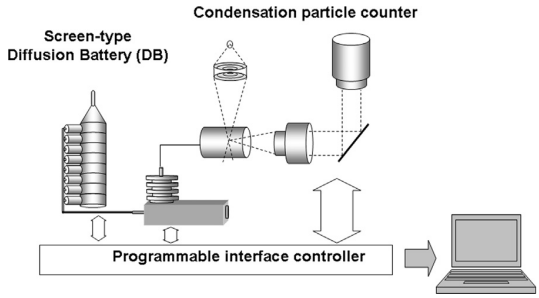

Fig. 1. A schematic sketch of the Aerosol Diffusion Spectrometer (ADS) and its major components.

and concentrations. Therefore, the full size or concentration range observed in the atmosphere cannot be covered completely with the help of a single instrument (McMurry, 2000). On the one hand, to capture the features of atmospheric particles, one has to rely on the synergy of different measurement techniques and instruments (Kulkarni, Baron & Willeke, 2011). On the other hand, the suite of instruments relying on different physical parameters in e.g. size classification needs to be intercompared to verify the performance of the instruments (Wiedensohler et al., 2012) in order to provide the crucial information on ambient aerosol number size distributions that is required to address various scientific questions related to these aerosol particles.

The aim of this study is to provide a technical description of Novosibirsk Aerosol Diffusion Spectrometer (ADS) and to verify its comparability with other aerosol measurement techniques addressing ambient aerosol properties. We summarize the measurement principles as well as the mathematical procedures required for the derivation of aerosol number size distributions within diameter range 3–200 nm. We present laboratory verification of the ADS with artificially generated monodisperse aerosol. Furthermore, we operated the ADS in parallel with aerosol and ion instruments at the Station for Measuring Ecosystem – Atmosphere Relations (SMEAR II) at Hyytiälä in southern Finland (Hari & Kulmala, 2005), which provided a benchmark data for the aerosol number size distributions.

2. Methods

2.1. Technical description of Aerosol Diffusion Spectrometer (ADS)

The ADS is used for measuring the number size distribution of nanoparticles. The technical design and operating characteristics are similar to that described by Dultsev, Mik, Dubtsov, and Dultseva (2014). Its major units include a diffusion battery (DB), a condensation particle magnifier (CPM), an optical particle counter (OPC), and an interface controller (IC). A schematic sketch of the ADS is presented in Fig. 1. Briefly, after passing consecutively through a certain number of screen stages (sets of meshes) in the DB, the sampled aerosol are delivered through the manifold to the condensation chamber of a mixing-type CPM, where they are enlarged to about 0.8 μm in diameter. The concentration of these enlarged particles is subsequently measured with an OPC. This procedure is repeated; the number of screen stages, through which aerosol particles pass in the DB, is decreased by one at a time (from 7 to 0).

The DB consists altogether of 8 consecutively connected screen stages. Seven of these stages contain meshes, with the first one being empty. The number of meshes in each screen stage and the cross-section of the corresponding DB compartment are presented in Table 1. The aerosol flow is switched between the sections of the DB with the help of a set of electromagnetic valves. The volumetric flow rate through the DB is set to be 1 l/min. The subsequent CPM has a similar design to that described by Fuchs and Sutugin (1965), where the particles are grown by the condensation of dibuthylphthalate (DBP). The saturator of the CPM is made from a 270-mm long copper tube with a diameter of 20 nm. It is filled with silica gel that is impregnated with DBP. The saturator is heated to 80 ± 0.3 °C, through which passes an air flow of 1 l/min, free of aerosol particles (purified with a HEPA filter). This air flow becomes saturated with DBP vapors after the saturator section, which is then mixed with the aerosol flow in the turbulent-type condensation chamber of the CPM, where the condensational growth of aerosol particles by supersaturated DBP vapors occurs. This growth continues in the enlargement tube (460 mm long, with an outer diameter of 20 mm), so that aerosol particles eventually gain a diameter of about 0.8 μm. The total flow after the CPM (2 l/min) is split into two: one (0.33 l/min) goes to the OPC for

Table 1
A summary of technical parameters of the Diffusion Battery (ADS). Nylon meshes – 50 μm fiber diameter, grid pitch - 172 μm; stainless meshes - 300 μm fiber diameter and grid pitch – 800 μm.

Section number	1	2	3	4	5	6	7	8
Cross-section, mm	8	11	30	50	50	50	50	50
Number of nylon meshes	0	6	3	3	7	15	29	53
Number of stainless steel meshes	0	2	2	2	2	2	2	2

concentration determination and the other (1.67 l/min) is discharged to the atmosphere through a HEPA filter. The measurable range of aerosol particle concentrations without dilution is from 10 to 2×10^5 cm^{-3}.

From each measurement cycle, we obtain 8 measured aerosol particle concentrations, n_i (i = 0–7), where i indicates the number of screen stages in the DB that the aerosol flow passes through. For example, n_0 is the concentration of particles passing through only the 1st screen stage (without meshes) and n_7 is the concentration of particles through all stages. In each cycle, it takes about 4 min as the minimal total time for the actual measurement and the subsequent size distribution reconstruction using the algorithm described below.

The particle size distribution is reconstructed in the range from 3 to 200 nm, based on the model of diffusional particle deposition on wire meshes, suggested by Mavliev and Ankilov (1985). Within this model, the penetration $\boldsymbol{P(R)}$ of monodisperse particles with a radius $\boldsymbol{R}$ through a set containing $\boldsymbol{s}$ meshes is described as

$$\boldsymbol{P}(\boldsymbol{R}) = \exp(-\boldsymbol{A}\boldsymbol{s}\boldsymbol{P}\boldsymbol{e}^{-2/3}), \quad \boldsymbol{A} = 6.35\boldsymbol{d}_s/\boldsymbol{h}_s \tag{1}$$

where $\boldsymbol{Pe}$ is Peclet number, equal to $\boldsymbol{d_f U/D(R)}$; $\boldsymbol{U}$ is the velocity of the aerosol flow; $\boldsymbol{d_f}$ is the wire diameter; $\boldsymbol{h_s}$ is the grid pitch; and $\boldsymbol{D(R)}$ is the diffusion coefficient of particles with the radius $\boldsymbol{R}$, equal to

$$\boldsymbol{B_1/R} + \boldsymbol{B_2/R^2} \tag{2}$$

where $\boldsymbol{B_1}$=8.53×10^{-9} and $\boldsymbol{B_2}$=1.27×10^{-6} [m^2/s] ($\boldsymbol{R}$ is expressed in nm). Cheng and Yeh (1980) have suggested a similar equation for penetration,

$$\boldsymbol{P} = \exp(-\boldsymbol{SN}\eta), \quad \boldsymbol{S} = 4\alpha\boldsymbol{h}/\pi(1-\alpha)\boldsymbol{d_f}, \quad \eta = 2.7\boldsymbol{Pe}^{-2/3} \tag{3}$$

where α is the solid volume fraction, $\boldsymbol{h}$ is the mesh thickness and $\boldsymbol{d_f}$ is the mesh fibre diameter.

Ichitsubo, Hashimoto, Alonso, and Kousaka (1996) showed experimentally that the penetration of uncharged and charged particles with sizes down to about 2 nm is reasonably well described by the model suggested by Cheng and Yeh (1980). For a set of equal meshes, the penetration of monodisperse particles with the same diffusion coefficient calculated according to Eq. (1), differs by 5–10% from that according to Eq. (3). This difference may arise from the usage of empirical parameters (6.35 in Eq. (1) and 2.7 in Eq. (2)). For a fixed value of $\boldsymbol{P(R)}$ through the screen stages of the DB (e.g. 0.4), the $\boldsymbol{D(R)}$ values calculated according to Eqs. (1) and (3) differ from each other by 7–10%. If these values are then converted into particle diameters using two combinations of equations - (1 and 2) and (3 and CMD correlation) (Friedlander, S. K. ,2000), the calculated particle diameters will differ by 4 – 7%. This is within the typical error of experimental measurements. Therefore, we used the combination of Eqs. (1) and (2) in our data inversion procedure. The detailed discussion on the theory of diffusion batteries is presented by Knutson (1999).

2.2. Data inversion algorithm

Measurement data obtained using a diffusion battery consist of m count values, c_i; here m is the total number of battery sections. The particle size distribution, $f(r)$, satisfies the system of integral equations (Ankilov, 1993; Eremenko & Ankilov ,1995).

$$c_i + e_i = \int_{r\,\min}^{r\,\max} f(r)p_i(r)dr\ , \quad i = 1\ldots m, \tag{4}$$

where e_i is the unknown measurement error, and $p_i(r)$ is the penetration function for the ith section of the battery. Supposing diffusion to be the only mechanism of particle precipitation on the surface of the DB screens, the probability, p, that a particle with a radius, r, passes through s screen stages of the DB can be approximated as

$$p(r, s) = \exp\left(-s\cdot C_b\left(\frac{B_1}{r} + \frac{B_2}{r^2}\right)^{2/3}\right). \tag{5}$$

Here B_1andB_2 are constants depending on the gas media and temperature; C_b is a constant determined by the diffusion battery configuration, such as the screen size, the diameter of the mesh wire, the grid pitch and the flow rate. For example, under normal atmospheric conditions (temperature T=20 °C) with the particle radius expressed in nm, $8.53\cdot10^{-5}$ and $1.27\cdot10^{-2}$. The coefficient C_b is proportional to the flow rate to the power of 2/3. Penetration functions for different values of s are presented in Fig. 2.

On the basis of the analysis and processing of measurement data, one can determine the size distribution of aerosol particles and some additional secondary characteristics (the average diameter D_m, the average volumetric diameterD_{mv} and the geometric mean diameter D_{mg}). We propose a method for solving the Eq. (4) based on a specially developed technique of averaging multiple solutions.

It is obvious that the solution of Eq. (4) cannot be a unique distribution of a single allocation. There is a convex continuum of distributions within measurement errors, matching the system, depicted by Eq. (1). Different distributions can be obtained by using different methods in solving Eq. (4) to match Eq. (1). In our approach, the solution is found by averaging multiple distributions using appropriate statistical weights. The basic idea for calculating these weights is that the most probable state (corresponding to the maximum entropy) is a state of "thermal equilibrium" (Yee, 1989). It is assumed that there is no significantly rapid change in the aerosol concentration and size distribution during the time of a measurement cycle (about 4 min).

Then the particle size range [r_{min} , r_{max}]is divided into n intervals ($n > m$), with the width of these intervals $\Delta_j = [r_j\ ,\ r_{j+1}]$ being logarithmically uniform and we get a system of linear equations in the matrix form. In the present work, we have neglected the measurement error, **e**, because of its minor contribution (< 5%).

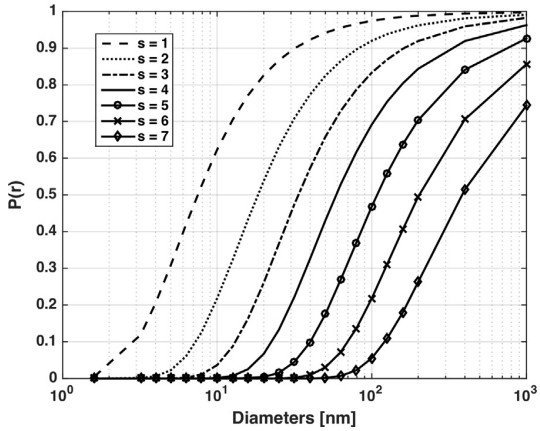

Fig. 2. An example of the penetration as a function of particle sizes for passing through different numbers of screen stages.

$$\mathbf{A}\cdot\mathbf{x} = \mathbf{b} + \mathbf{e}\ ,\quad A_{ij} = p_i(r_j)/\delta_i\ ;\quad x_j = f(r_j)\ ;\quad b_i = c_i/\delta_i\ ;\ i = 1\dots m\ ;\ j = 1\dots n. \tag{6}$$

The solution is found by minimizing the error functional (the Euclidean norm of the error vector) $\Phi = \|\mathbf{A}\cdot\mathbf{x} - \mathbf{c}\|$ (Rosen, 1960). The obtained size distribution is considered as a set of N discrete elements of equal weights, W. The number of elements should be large enough to reduce the discretization error.

$$d_j = x_j/W,\quad \sum_{j=1}^{n} x_j = N\ W. \tag{7}$$

If we let each element randomly change its index (i.e. diffuse along the set of sizes) and set the probability of a transition in such a way that the mean value of the error functional will stay close to the expected value (which is equivalent to the temperature), the system will gradually shift to a state of balance and then fluctuate around the equilibrium position. The statistical weight of each distribution is $P = N!/\prod k_j$ and can be evaluated automatically.

The final solution is obtained by averaging over sufficient distributions that occur during these fluctuations, so that the change of the solution is negligible.

Based on the obtained distribution, we find the average characteristics: the average diameter D_m, the average volumetric diameter D_{mv} and the geometric mean diameter (the value indicating the location of the point of the maximum distribution):

$$D_m = \frac{\sum_{j=1}^{n} r_j x_j}{S}; \tag{8}$$

$$D_{mv} = \left(\frac{\sum_{j=1}^{n} r_j^3 x_j}{S}\right)^{1/3}; \tag{9}$$

$$D_{mg} = r_k + d_1\,(r_{k+1} - r_k); \tag{10}$$

$$k = [d];\quad d_1 = \left\{\frac{d}{S}\right\};\quad d = \sum_{j=1}^{n} j\ x_j.$$

Here $S = \sum_{j=1}^{n} x_j$, $[z]$ is the integer part of z, $\{\ z\ \}$ is the fractional part of z.

An **e**xample of the algorithm application is presented in Fig. 3.

2.3. Field experiments

During the field campaign (April 29 - May 15, 2013) at Hyytiälä SMEAR II station, the ADS was primarily compared with a Differential Mobility Particle Sizer (DMPS) for the ambient measurement of atmospheric aerosol particles. Also a Neutral cluster and Air Ion Spectrometer (NAIS) was used to verify the performance of the ADS in capturing new particle formation (NPF).

The DMPS measures the number size distribution of aerosol particles between 3 and 1000 nm in mobility diameter. It consists of a drier, a radioactive bipolar charger, two Hauke-type Differential Mobility Analyzers (DMAs) with different dimensions and two Condensation Particle Counters (CPCs). By increasing the voltages applied on the DMAs stepwise, aerosol particles are size segregated and then counted in the CPCs (Kulmala et al., 2012; Wiedensohler et al., 2012). The sheath flow passes through a diffusion drier before entering into the DMAs to assist sizing of aerosol particles. Therefrom, a reduced moisture content in the

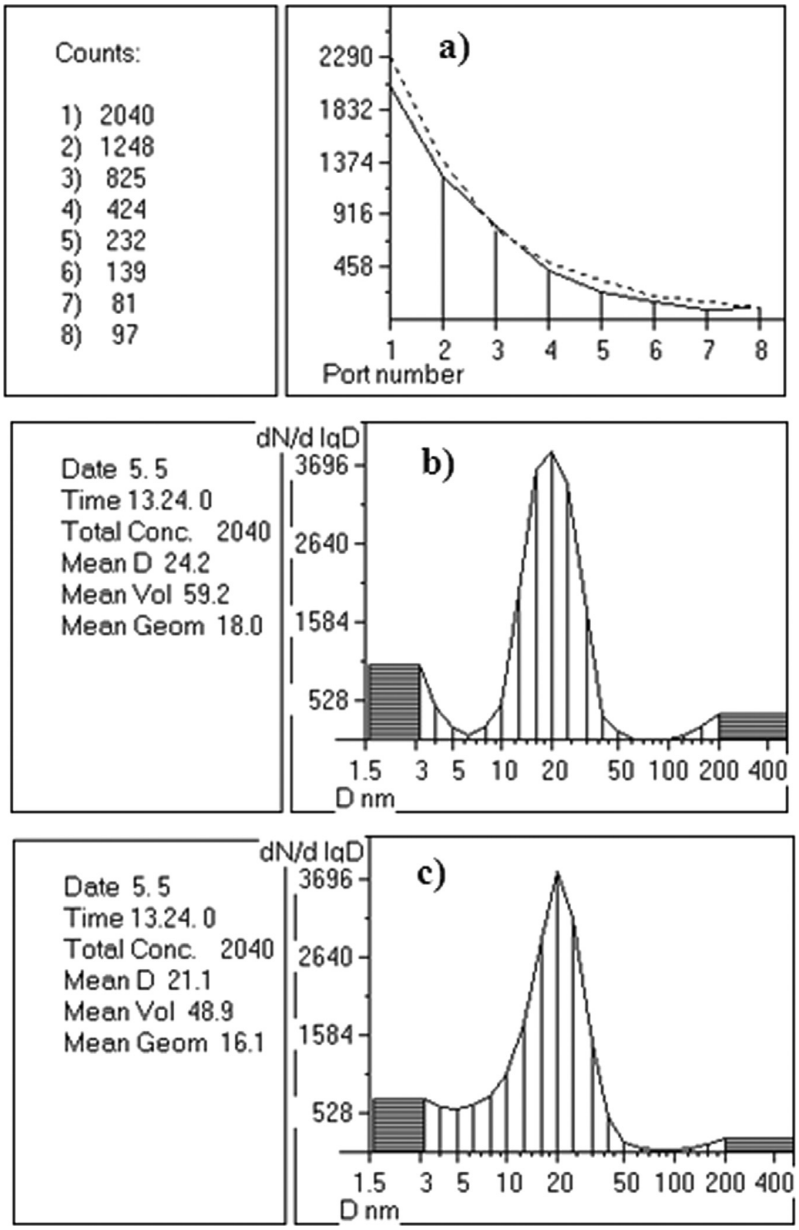

Fig. 3. Examples of the size distribution reconstruction using the proposed algorithm. Counts are shown in a) (dashed line corresponds to data restored from obtained distributions). The distribution b) is obtained by averaging of 4 solutions. The distribution c) is obtained by averaging of 32 solutions.

DMAs can be expected, leading to shrinkage of sampled particles (Yli-Juuti et al., 2011). Accordingly, the hygroscopic effect was taken into consideration in the data analysis of this work following the method described by Laakso et al. (2004). The parameterization represents well the aerosol in Hyytiälä as it is dominated by organic compounds with only a quite low hygroscopic growth factor (e.g. Zieger et al., 2015).

The NAIS gives number size distribution information both on aerosol particles and on air ions. Unipolar corona chargers are employed in the NAIS. It measures negative and positive polarities separately. The NAIS is composed of a set of precharger and prefilter, a set of main charger and filter and a set of cylindrical DMAs. Twenty one electrometers are integrated with each analyzer as detectors. Usually it is operated in three different modes: offset mode, ion mode and particle mode. Background signals of the electrometers are registered in the offset mode by turning on the prechargers and prefilters, which are used in correcting the currents

received in the ion and particle modes. Both pre and main sets of charger and filter are off when measuring air ions. For the classification of aerosol particles, main chargers and filters are in use (Manninen et al., 2009; Mirme & Mirme, 2013). Since the purpose of this comparison is to prove the ability of the ADS for NPF measurement, only particle data from the NAIS were used. The NAIS measures the mobility size distribution of aerosol particles (Manninen et al., 2010; Manninen et al., 2009). The ADS primarily provides sizing information based on diffusion diameter, which is equivalent to the mobility diameter (Lange, Fissan & Schmidt-Ott, 1996) for singly-charged particles.

All the instruments were placed inside a cottage. The DMPS is part of the long-term measurement system at the station. The ADS shared the same sampling line as the DMPS, which sampled from the top of the cottage. The NAIS had its own inlet on the side of the cottage due to its high flowrate requirement (60 l/min) for sampling (Manninen et al., 2009; Mirme & Mirme, 2013). The DMPS has a sample flow of 5 l/min (Kulmala et al., 2012), and the ADS has a sample flow of 1 l/min.

To quantify the NPF, the overall methodology of Kulmala et al. (2012) was used. Condensation sink (CS) and formation rate (J) were determined based on the parameterization suggested in Kulmala et al. (2004) and vapour source rate (Q) following the equation given by Kulmala et al. (2001) and Dal Maso et al. (2002). Yli-Juuti et al. (2011) tested two methods for growth rate determination for the nucleation mode particles: maximum concentrations and mode fitting. They found that the two methods gave similar results, and their results suggested a size dependence of the particle growth rate. Both these methods were applied in this work: the growth rate calculation from the DMPS and ADS followed the mode fitting method and that from the NAIS followed the method of maximum concentrations.

3. Results and discussion

3.1. Laboratory verification on the aerosol number size distribution of the ADS

The prototype of the ADS (ADB) was compared with various aerosol-measuring instruments during an international workshop at the Institute for Experimental Physics of the University of Vienna, Austria (Ankilov et al., 2002).

The accuracy of the particle size measurement by the ADS was estimated using monodisperse polystyrene latex (PSL) particles of different sizes (41, 73, 100, and 140 nm). Typical examples of the measured size distributions for such particles are presented in Fig. 4. The mean diameters for the tested PSL particles measured by the ADS varied within ± 10% of the specification provided by the manufacturers. And the accuracy of the measurement of the particle number concentration by the ADS was within ± 15% in the concentration range from about 10^3 to 10^5 cm^{-3}. An additional comparison of the ADS with TEM (LIBRA 120) was carried out using polydisperse ($\sigma_g \approx 1.45$) Ag and NaCl aerosol particles. One example is presented in Fig. 5. The diameter of Ag nanoparticles was calculated from TEM images by the following means: the image of an individual particle was approximated by a circle, so that its diameter was maximally close to the visible perimeter of the particle. A special software was used for this purpose (Glotov, 2008). The calculated circle diameter was assigned to the particle diameter.

The theoretical analysis of the DB size resolution was performed earlier (Eremenko, Caldow Baklanov, Havlicek & Sem G, 1995; Eremenko & Ankilov, 1995). Laboratory studies and numerical experiments showed that two modes could be resolved for the mixture of monodisperse PSL particles, if their diameters differed by a factor of two (Fig. 6a). Additional experiments were carried out to test size resolution of the ADS. Mixtures of nanoparticles with different mean diameters were prepared using a hot-wire generator, similar to that described by Kangasluoma et al. (2015) and a photochemical aerosol generator (Dubtsov & Baklanov, 1996). Fig. 6b shows the size distribution reconstruction for a mixture of 5 nm WO_x and 25 nm organic nanoparticles. In general, these experiments showed that the ADS can resolve two modes of polydisperse particles if their modal diameters differ by a factor of

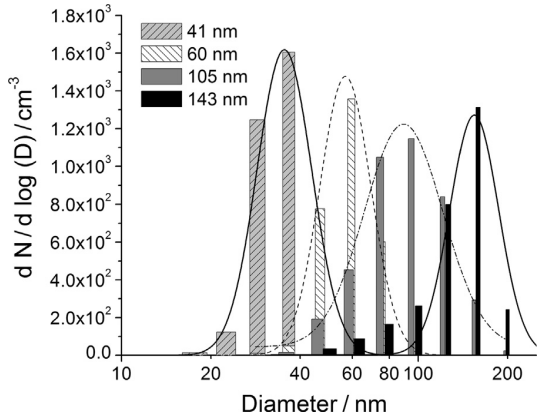

Fig. 4. Examples on particle size distributions of monodispersed polystyrene latex (PSL) particles measured with the ADS. Bars are experimentally measured size distributions and lines are log-normal fits to the observational data. The mean diameters for the PSL particles were 41 ± 3 nm, 60 ± 4 nm, 105 ± 6 nm and 143 ± 8 nm according to the specifications given by the manufacturers. The reconstructed ADS mean diameters were 39 ± 3 nm, 65 ± 4 nm, 98 ± 6 nm and 158 ± 13 nm, respectively.

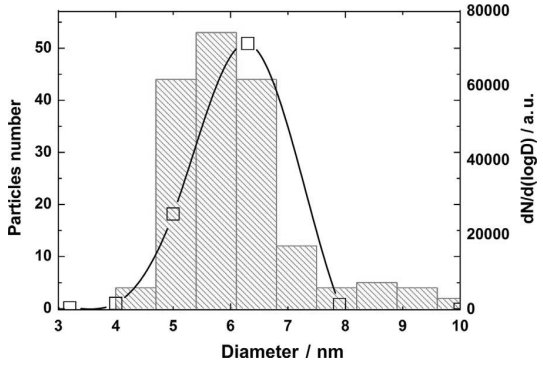

Fig. 5. A comparison of the size distributions of Ag nanoparticles, measured with the ADS and TEM. Bars for the TEM derived sizes and lines for the ADS size distribution.

3 - 4. Some more results of these experiments are presented by Valiulin et al. (2014).

3.2. Comparison of aerosol number size distribution from the ADS, DMPS and NAIS

During the field campaign at Hyytiälä SMEAR II station in the period of April 29 – May 15, 2013, the ADS was intercompared with a DMPS and a NAIS. The size distribution ranges given by the ADS, DMPS, and NAIS are 3–200 nm, 3–1000 nm and 3–42 nm, respectively. Because the sheath flow in the DMPS system passes through a diffusion drier, the distribution of aerosol particles measured by the DMPS is considered as the dry size distribution (Yli-Juuti et al., 2011). Thus, a hygroscopic correction was applied

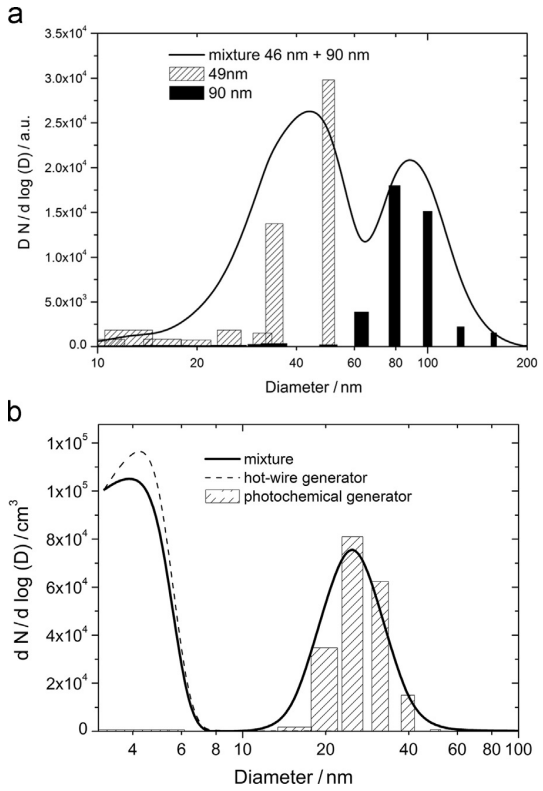

Fig. 6. a). Experimentally measured size distributions for 46 nm, 90 nm PSL particles and their mixture. Bars are measured size distributions for individual 46 and 90 nm PSL particles and the line indicating the size distribution of their mixture. b) Size distributions of organic particles (dashed line), WO_x particles (bars) and their mixture (solid line) measured by the ADS.

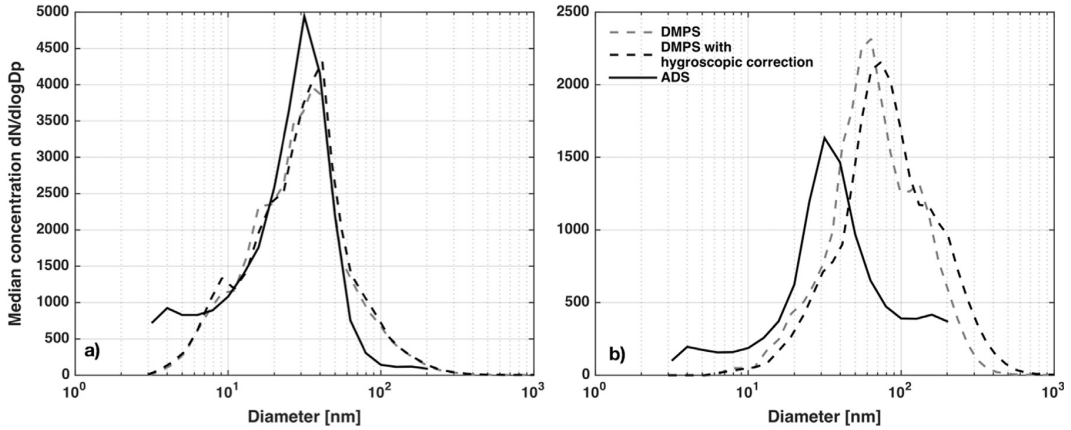

Fig. 7. Median particle number size distributions measured by the ADS and the DMPS a) on a NPF event day (May 3, 2013) and b) on a non-event day (May 5, 2013). DMPS with hygroscopic correction (black dashed line) and DMPS without hygroscopic correction (grey dashed line) in 3–1000 nm, and ADS (dotted line) in 3–200 nm.

to the DMPS data according to Laakso et al. (2004). This correct has little effect on the median number size distribution of measured aerosol particles by the DMPS on May 3, 2013 - a NPF event day (Fig. 7a). However, the median DMPS number size distribution showed a clear shift towards larger sizes on May 5, 2013 - a non-event day (Fig. 7b). On the non-event day, a shoulder at around 30–40 nm was observed on the median DMPS number size distribution curve, when the hygroscopic correction was applied, which approximately coincided with the location of the peak seen in the ADS curve. Such a connection in median number size distributions of the ADS and the DMPS was not visible without the hygroscopic correction.

The spectra of all the three instruments on the NPF-event day (May 3, 2013) resembled each other within the measurement size range of the NAIS (Fig. 8a). Above this limit, similar spectral features could still be captured by the ADS compared to the DMPS. The pattern on the non-event day (May 5, 2013), displayed in Fig. 8b, showed also no marked difference from each other, except for the strip in the NAIS spectrum at above 20 nm, which came from the deficiency in the NAIS data inversion accounting for multiply charged particles.

The number size distributions measured by the ADS and DMPS manifested similar features on the NPF-event day at above 6 nm (Fig. 7a). However, the ADS detected more aerosol particles than the DMPS on the NPF-event day in the size range of 20–40 nm, and slightly less above 40 nm. On the non-event day (Fig. 7b), the median number size distribution of the ADS peaked at a smaller size and did not attain clearly the shoulder appearing at around 150 nm in the DMPS plot.

The mean diameters derived from the DMPS and ADS measurements and the correlation between them on both the NPF event day and the non-event day are illustrated in Figs. 9 and 10, respectively. Diurnal variations were observed in the mean diameters, and they exhibited different profiles on event and non-event days. Particles on the non-event day were larger than those detected on the event day, as shown in Fig. 9. The smallest diameters were observed during the NPF event around noon on May 3, 2013. On the

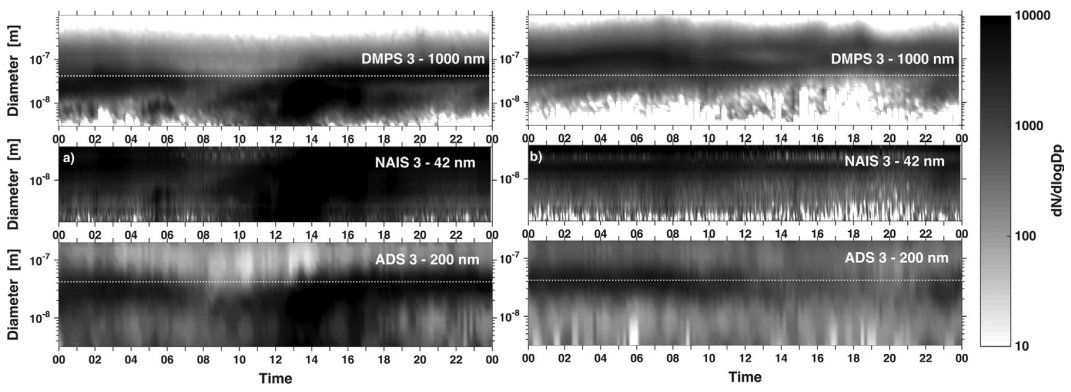

Fig. 8. Contour plots of the number size distributions obtained by the ADS, the DMPS and the NAIS: the left column (a) shows a NPF event on May 3, 2013 and the right column (b) a non-NPF event on May 5, 2013. From upper to lower panel: DMPS spectra in the size range of 3–1000 nm, NAIS spectra in the size range of 3–42 nm and ADS spectra in the size range of 3–200 nm. The dotted black line indicates the upper measurement limit (42 nm in mobility diameter) of the NAIS. The hygroscopic correction was applied to the DMPS data.

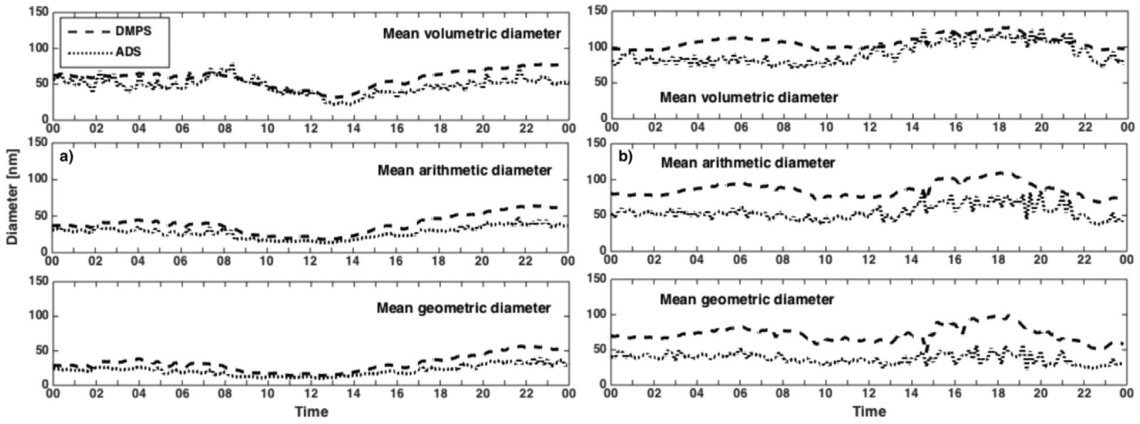

Fig. 9. The mean volumetric, arithmetic and geometric diameters obtained from the number size distribution measurements of the DMPS and the ADS on May 3, 2013 a) and May 5, 2013 b). The hygroscopic correction was taken into account for the DMPS data.

contrary, a bump could be seen on May 5, 2013 in the afternoon. These distinct phenomena resulted concurrently with the boundary layer development together with particle scavenging and growth processes. The difference between the sizes derived from the DMPS and ADS was smaller on the event day whereas more notable on the non-event day. Arithmetic and geometric diameters of the DMPS and ADS measurements on the event day matched better with each other than in the case of the volumetric diameter. However, on May 5, 2013, the non-event day, the correlation coefficient for the volumetric diameter was the highest. The overall behavior was that the ADS tended to marginally underestimate the size of the aerosol particles compared with the DMPS, especially on the non-NPF day.

As for the concentration demonstrated in Fig. 12, the two bursts in the particle concentration occurred around noon on May 1 and May 3, 2013 were due to the NPF processes. Another distinguishable increase during the evening of May 2, 2013 was a nocturnal NPF event. In the size range of 2.9 – 6 nm, the ADS detected a higher concentration of aerosol particles than the DMPS, which however, was similar to that given by the NAIS. The congruity in the concentration recorded by the ADS and DMPS emerged as moving to larger sizes, while the distinction from the concentration level measured by the NAIS intensified. Nevertheless, upon

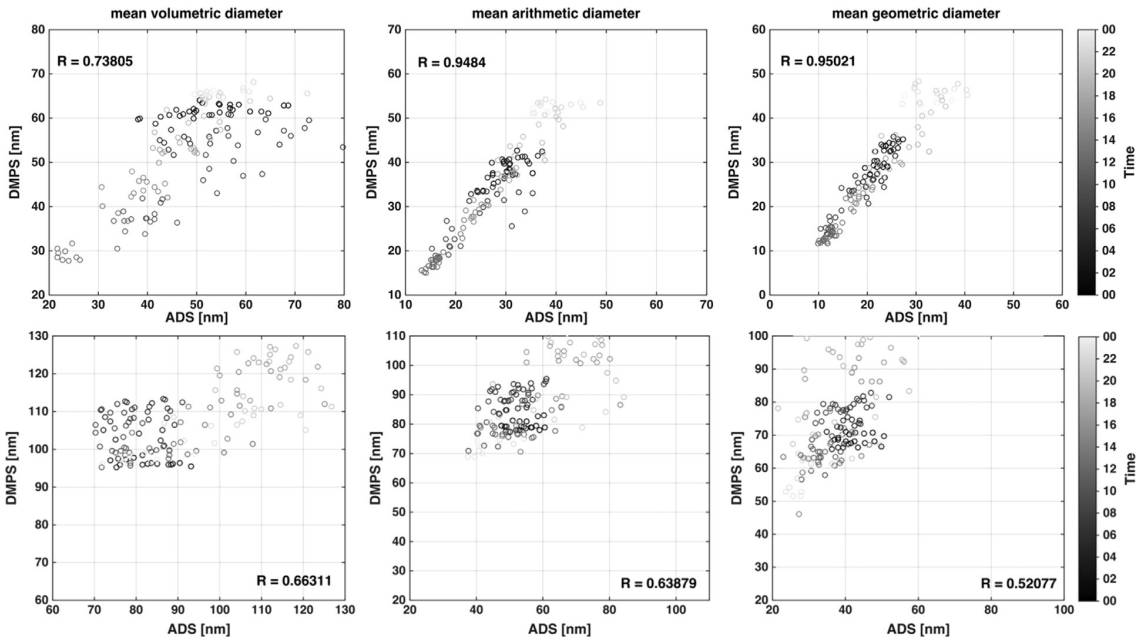

Fig. 10. Correlations between volumetric diameters, arithmetic diameters and geometric diameters derived from the DMPS and the ADS. Upper panel: a NPF day on May 3, 2013. Lower panel: a non-NPF day on May 5, 2013. The hygroscopic correction was taken into account for the DMPS data.

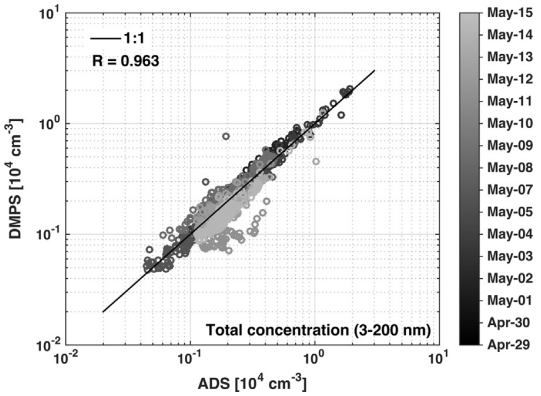

Fig. 11. Correlations between measured total concentrations by the DMPS and the ADS in the size range of 3–200 nm. Each color corresponds to a measurement day with the corresponding correlation coefficient (*R*). Improper function of the ADS was observed on May 9–12. The ADS was not in operation on May 6. The hygroscopic correction was taken into account for the DMPS data.

the occurrence of the NPF, the divergence between the NAIS and DMPS or ADS diminished and tended to retain at its minimum during the event. However, outside the NPF, the disagreement was especially noticeable. The ADS showed a better agreement with the NAIS for the concentration of particles with sizes below 6 nm, suggesting the advantage of the ADS over the DMPS in counting small particles. A good correlation between the total concentrations measured by the ADS and DMPS in the size range of 3–200 nm

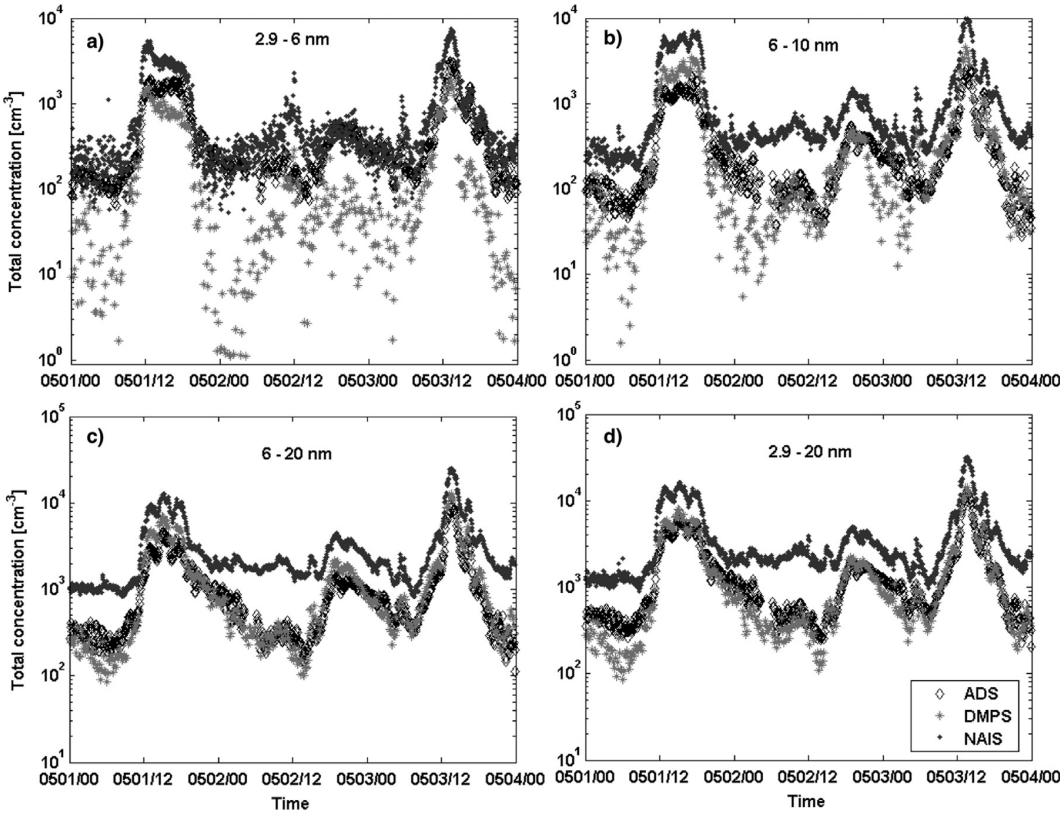

Fig. 12. Comparisons between concentrations measured by the ADS (diamonds), the DMPS (stars) and the NAIS (dots) in different size ranges for May 1–3, 2013. Except on May 2, 2013, daytime NPF process was observed. A nocturnal event occurred on the evening of May 2, 2013. The size range of 2.9–6 nm shown in a), 6–10 nm in b), 6–20 nm in c) and 2.9–20 nm in d). The hygroscopic correction was taken into account for the DMPS data.

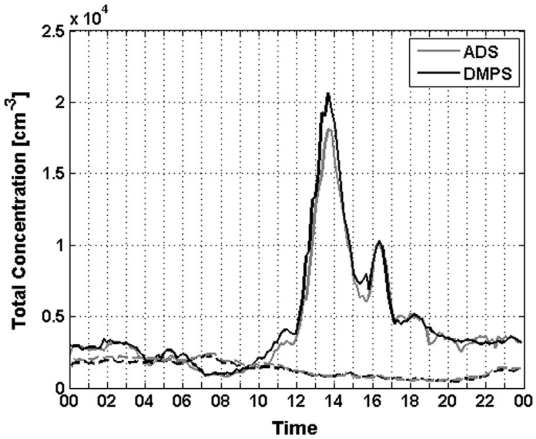

Fig. 13. Diurnal profiles of ambient aerosol particle concentrations in the size range of 3 - 200 nm on the event-day May 3, 2013 (solid line) and on the non-event-day May 5, 2013 (dashed line). The hygroscopic correction was taken into account for the DMPS data.

was found during this field campaign in general (Fig. 11), apart from the days with ADS malfunction. The ADS tended to underestimate the particle concentration at larger sizes near its cut-off (Fig. 7). The similar particle concentration measured by the ADS to that by the DMPS could therefore result from compensation to the underestimated concentration of bigger particles by the higher concentration of smaller particles given by the ADS.

3.3. Measurements of new particle formation with ADS

Diurnal variations were observed in the total concentration of aerosol particles. On the NPF event day, a sudden rise in the total particle concentration could be seen at around noon after a slight concave at around 8 o'clock in the morning (Fig. 13). Upon sunrise, a rapid vertical mixing resulting from boundary layer development enhanced the dilution and sink of aerosol particles. Consequently, the number concentration of particles dropped to its minimum. At the same time photochemical processes intensified producing vapors driving the new particle formation and subsequent growth (Kulmala et al. 2013; Ehn et al., 2014). As a consequence, a sharp rise in the total particle concentration, as shown in Fig. 13, was observed. Discriminatively, an opposite trend was found on the non-event day. A mild concentration increase occurred in the morning hours (8:00–10:00), which was followed by a decline with the minimum reached in the late afternoon. The slight morning increase of the total particle concentration could be related to the expansion of the mixing volume as a result of boundary layer development, which imposes a dilution on particle number concentration leading to a reduction in the sink of vapor sources by condensation.

The condensation sink (CS) accounts for the loss rate of vapors by condensation onto aerosol particles and NPF events are favored on low-CS days (Dal Maso et al., 2005). During our campaign, lower condensation sinks were observed on NPF days, where differences between the condensation sinks derived from the ADS and DMPS were also the smallest (Fig. 14). On clear and strong NPF event days, the ratio between the CS derived from the ADS and DMPS were primarily found in between 1:1.5 and 1:5 when the full size range of the instrumentations were taken into consideration (Fig. 14a). However, when inspecting only the common size range (3–200 nm), most data laid between the bounds of 1:1 and 1:2 (Fig. 14d). The reason for the bigger ratio than unity can be attributed to the decreasing detection efficiency of the ADS towards the upper limit in its measurement size range. For all NPF event days, the upper bound of the CS ratio derived from the common size range for most data was enlarged to 1:3 whereas the lower bound fell slightly below unity (Fig. 14e). Even when non-event days were considered, apart from minor shifts in the upper and lower bounds, no significant deviation in the relation between the CS derived from the ADS and DMPS was seen from the pattern of NPF event days (Fig. 14f). On both NPF event and non-event days, the ratio between condensation sinks derived from the common size range was smaller than those derived from the whole measurement size range of the instrumentations. Yet, more remarkable difference in the CS ratio was observed on non-event days than on NPF event days (Fig. 14b & e and c & f).

Due to the relatively poor sizing of the ADS at above 100 nm, the derived sinks from its measurement data could be biased by uncertainties. Lower sinks were obtained from the ADS data compared to those from the DMPS measurement (Fig. 14 and Table 2). Other relevant parameters for characterizing NPF processes include growth rates (GR) and formation rates (J) (Kulmala et al., 2012). GR depicts the rate of bulk particle growth due to vapor uptake in terms of the diameter change and J quantifies the source rate of particles of a certain size. J rates are typically calculated for particles in certain size ranges and the formation rate of 3–25 nm particles, often denoted as J_3, is known to be a representative measure for nucleation mode particles (Nieminen et al., 2014). Similar GRs were acquired based on the DMPS, NAIS and ADS measurements (Table 2). J_3 values obtained from the DMPS and ADS for 3–25 nm particles were also comparable with each other.

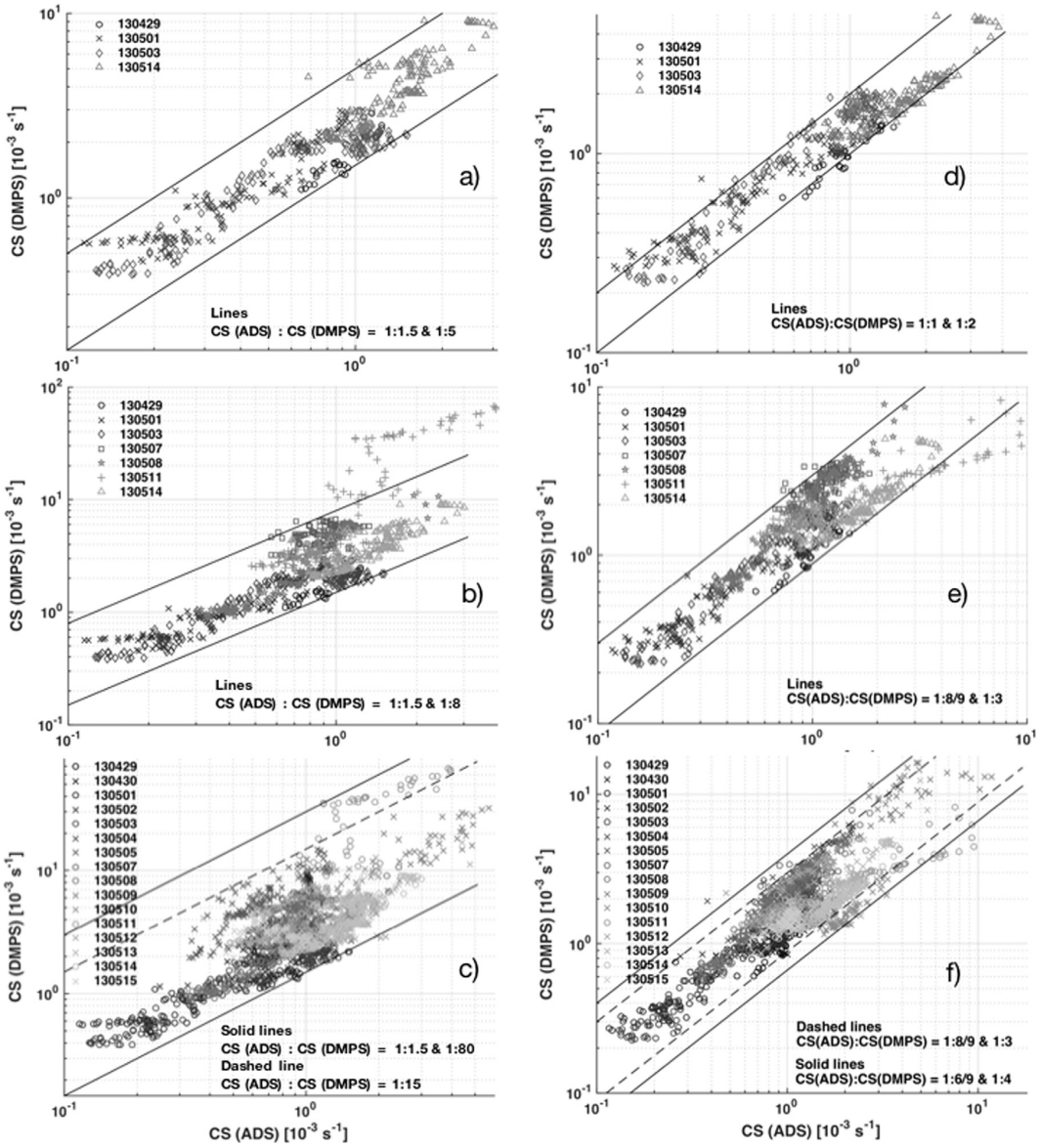

Fig. 14. Condensation sinks derived from the DMPS vs. condensation sinks derived from the ADS. Left column: DMPS (3–1000 nm) and ADS (3–200 nm). Right column: DMPS (3–200 nm) and ADS (3–200 nm). Upper panel: on selected NPF event days, middle panel: on all NPF event days and lower panel: on all the days (NPF event days are marked with circles and non-events with crosses). A hygroscopic correction was applied to the DMPS data. The event days selected in Fig. 7a and d were observed with strong and clear NPF events. Improper function of the ADS was observed on May 9–12. The ADS was not in operation on May 6.

4. Summary and conclusions

A technical description of the Novosibirsk Aerosol Diffusion Spectrometer (ADS) was presented, including measurement principles as well as mathematical procedures for the reconstruction of aerosol number size distributions within the diameter range of 3–200 nm. The size segregation of the ADS was verified with artificially generated monodisperse aerosols and their mixtures in the laboratory. In addition, the ADS was intercompared with aerosol and ion instruments in the Station for Measuring Ecosystem – Atmosphere Relations (SMEAR-II) at Hyytiälä in southern Finland, assuring the competence of the ADS for the classification of ambient aerosol particles.

The laboratory verification based on measurements of monodisperse particles showed that the particle sizing of the ADS was in good agreement (± 10%) with the specifications provided by the manufacturers of the PSL particles. For the concentration range of

Table 2
NPF event parameters determined from the ADS, NAIS and DMPS data: growth rate (GR), condensation sink (CS), formation rate of 3–25 nm particles (J_3) and vapour source rate (Q). The CS, J_3 and Q were determined for the size range of 3–200 nm for both the ADS and DMPS.

Parameters	May 1, 2013			May 3, 2013		
Instruments	ADS	NAIS	DMPS	ADS	NAIS	DMPS
GR [nm/h]	4.1	4.4	4.2	6.4	6.2	5.3
CS [10^{-3} s^{-1}]	0.4	–	0.6	0.8	–	1.4
J_3 [cm^{-3} s^{-1}]	0.3	–	0.4	2.1	–	2.5
Q [10^4 cm^{-3} s^{-1}]	3.2	–	4.4	6.6	–	8.8
Parameters	May 8, 2013			May 14, 2013		
Instruments	ADS	NAIS	ADS	NAIS	ADS	NAIS
GR [nm/h]	6.0	6.4	6.0	6.4	6.0	6.4
CS [10^{-3} s^{-1}]	0.9	–	0.9	–	0.9	–
J_3 [cm^{-3} s^{-1}]	0.07	–	0.07	–	0.07	–
Q [10^4 cm^{-3} s^{-1}]	7.7	–	7.7	–	7.7	–

10^3–10^5 cm^{-3}, only a ± 15% uncertainty was found in the resolved number concentration measured by the ADS.

The performance of the ADS during the field campaign was satisfactorily comparable with the DMPS and the NAIS for measuring ambient aerosol particles in the size range of 3–200 nm. Good correlations between number concentrations measured by the ADS and the DMPS were observed. Lower condensation sinks were obtained from the ADS data compared with those from the DMPS. The differences between the sinks were smaller on NPF event days than on non-NPF days. -Similar formation rates and growth rates were acquired based on the DMPS, NAIS and ADS measurements, proving a reasonable capability of the ADS in measuring nucleation mode particles during NPF.

Acknowledgements

This work is supported by Academy of Finland via Finnish Center of Excellence (No. 272041) and European Commission via ACTRIS (654109), ACTRIS2 and PEGASOS projects (FP7-ENV-2010-265148).

References

Ankilov, A. N. (1993). The way for accuracy of size measurements estimation of diffusion batteries. *Journal of Aerosol Science*, 24, 237–238.
Ankilov, A., Baklanov, A., Colhoun, M., Enderle, K.-H., Gras, J., Julanov, Y. Zagaynov, V. A. (2002). Intercomparison of number concentration measurements by various aerosol particle counters. *Atmospheric Research*, 62, 177–207.
Asmi, A., Wiedensohler, A., Laj, P., Fjaeraa, A. M., Sellegri, K., Birmili, W. Kulmala, M. (2011). Number size distributions and seasonality of submicron particles in Europe 2008–2009. *Atmospheric Chemistry and Physics*, 11, 5505–5538.
Cheng, Y. S., & Yeh, H. C. (1980). Theory of a screen-type diffusion battery. *Journal of Aerosol Science*, 313–320.
Clarke, N., Fischer, R., de Vries, W., Lundin, L., Papale, D., Vesala, T. Paoletti, E. (2011). Availability, accessibility, quality and comparability of monitoring data for European forests for use in air pollution and climate change science. *iForest, Biogeosciences and Forestry*, 4, 162–166.
Collaud Coen, M., Andrews, E., Asmi, A., Baltensperger, U., Bukowiecki, N., Day, D. Laj, P. (2013). Aerosol decadal trends – Part 1: In-situ optical measurements at GAW and IMPROVE stations. *Atmospheric Chemistry and Physics*, 13, 869–894.
Dal Maso, M., Kulmala, M., Lehtinen, K. E. J., Mäkelä, J. M., Aalto, P., & O'Dowd, C. D. (2002). Condensation and coagulation sinks and formation of nucleation mode particles in coastal and boreal forest boundary layers. *Journal of Geophysics Research*, 107, 8097. http://dx.doi.org/10.1029/2001jd001053.
Dal Maso, M., Kulmala, M., Riipinen, I., Wagner, R., Hussein, T., Aalto, P. P., & Lehtinen, K. E. J. (2005). Formation and growth of fresh atmospheric aerosols: Eight years of aerosol size distribution data from SMEAR II, Hyytiälä, Finland. *Boreal Environment Research*, 10, 323–336.
Dubtsov, S. N., & Baklanov, A. M. (1996). Design and testing of a photochemical aerosol generator for calibrating aerosol measuring instruments in submicrometer region. Aerosol Science *and Technology*, 25, 67–72.
Dultsev, F. N., Mik, I. A., Dubtsov, S. N., & Dultseva, G. G. (2014). Identification of the functional groups on the surface of nanoparticles formed in photonucleation of aldehydes generated during forest fire events.Paper presented at In Proceedings of the 20th International Symposium on Atmospheric and Ocean Optics: Atmospheric Physics, Novosibirsk, Russia
Dusek, U., Frank, G. P., Hildebrandt, L., Curtius, J., Schneider, J., Walter, S. Andreae, M. O. (2006). Size matters more than chemistry for cloud-nucleating ability of aerosol particles. *Science*, 312, 1375–1378.
Ehn, M., Thornton, J. A., Kleist, E., Sipilä, M., Junninen, H., Pullinen, I., Springer, M., Rubach, F., Tillmann, R., Lee, B., Lopez-Hilfiker, F., Andres, S., Acir, I.-H., Rissanen, M., Jokinen, T., Schobesberger, S., Kontkanen, J., Nieminen, T., Kurtén, T., Nielsen, L. B., Jørgensen, S., Kjaergaard, H. G., Canagaratna, M., Dal Maso, M., Berndt, T., Petäjä, T., Wahner, A., Kerminen, V.-M., Kulmala, M., Worsnop, D. R., Wildt, J., & Mentel, T. F. (2014). A large source of low-volatility secondary organic aerosol. *Nature*, 506, 476–479.
Eremenko, S. I., Caldow, R., Baklanov, A. M., Havlicek, M., & Sem, G. (1995). Diffusion battery particle sizing system based on the MSA data conversion algorithm: Experimental examination. *Journal of Aerosol Science*, 26, S741–S748.
Eremenko, S. I., & Ankilov, A. N. (1995). Conversion of the diffusion battery data to particle size distribution: Multiple solutions averaging algorithm (MSA). *Journal of Aerosol Science*, 26, S749–S750.
Fountoukis, C., Megaritis, A. G., Skyllakou, K., Charalampidis, P. E., Pilinis, C., Denier van der Gon, H. A. C. Pandis, S. N. (2014). Organic aerosol concentration and composition over Europe: Insights from comparison of regional model predictions with aerosol mass spectrometer factor analysis. *Atmospheric Chemistry and Physics*, *14*, 9061–9076.
Freutel, F., Schneider, J., Drewnick, F., von der Weiden-Reinmüller, S. L., Crippa, M., Prévôt, A. S. H. Borrmann, S. (2013). Aerosol particle measurements at three stationary sites in the megacity of Paris during summer 2009: Meteorology and air mass origin dominate aerosol particle composition and size distribution. *Atmospheric Chemistry and Physics*, *13*, 933–959.
Friedlander, S. K. (2000). *Smoke, dust, and haze. Fundamentals of aerosol dynamic* Oxford: Oxford University Press.
Fuchs, N. A., & Sutugin, A. G. (1965). Coagulation rate of highly dispersed aerosols. *Journal of Colloid Science*, 20, 492–500.
Glotov, O. G. (2008). Image processing of the fractal aggregates composed of nanoparticles. Russian *Journal of Physical Chemistry A*, 82(13), 2213–2218.

Hari, P., & Kulmala, M. (2005). Station for measuring ecosystem-atmosphere relations (SMEAR II). *Boreal Environment Research*, 10, 315–322.
Ichitsubo, H., Hashimoto, T., Alonso, M., & Kousaka, Y. (1996). Penetration of ultrafine particles and ion clusters throuogh wire screens. *Aerosol Science and Technology*, *24*, 119–127.
Jiang, J., Zhao, J., Chen, M., Eisele, F. L., Scheckman, J., Williams, B. J. McMurry, P. H. (2011). First measurements of neutral atmospheric cluster and 1–2 nm particle number size distributions during nucleation events. *Aerosol Science and Technology*, *45*. http://dx.doi.org/10.1080/02786826.2010.546817.
Jimenez, J. L., Canagaratna, M. R., Donahue, N. M., Prevot, A. S., Zhang, Q., Kroll, J. H. Worsnop, D. R. (2009). Evolution of organic aerosols in the atmosphere. *Science*, *326*, 1525–1529.
Kangasluoma, J., Attoi, M., Junninen, H., Lehtipalo, K., Samodurov, A., Korhonen, F. Petäjä, T. (2015). Sizing of neutral sub 3 nm tungsten oxide clusters using Airmodus Particle Size Magnifier. *J Aerosol Sci*, 87, 53–62.
Kerminen, V.-M., Lihavainen, H., Komppula, M., Viisanen, Y., & Kulmala, M. (2005). Direct observational evidence linking atmospheric aerosol formation and cloud droplet activation. *Geophysical Research Letters*, 32, L14803. http://dx.doi.org/10.1029/2005gl023130.
Knutson, E. O. (1999). History of diffusion batteries in aerosol measurements. *Aerosol Science and Technology*, 31, 83–1128.
Koponen, I. K., Virkkula, A., Hillamo, R., Kerminen, V.-M., & Kulmala, M. (2003). Number size distributions and concentrations of the continental summer aerosols in Queen Maud Land, Antarctica. *Journal of Geophysical Research*, 108, 4587. http://dx.doi.org/10.1029/2003jd003614.
Kulkarni, P., Baron, P. A., & Willeke, K. (2011). *Aerosol measurement: Principles, techniques, and applications* (3 ed.) New York, Chichester, Weinheim, Brisbane, Singapore: Toronto: John Wiley and Sons, Inc.
Kulmala, M., Kontkanen, J., Junninen, H., Lehtipalo, K., Manninen, H. E., Nieminen, T. Worsnop, D. R. (2013). Direct observations of atmospheric aerosol nucleation. *Science*, *339*, 943–946.
Kulmala, M., Dal Maso, M., Mäkelä, J. M., Pirjola, L., Väkevä, M., Aalto, P., Hämeri, K. O'Dowd, C. D. (2001). On the formation, growth and composition of nucleation mode particles. *Tellus*, *53B*, 479–490.
Kulmala, M., Petäjä, T., Nieminen, T., Sipilä, M., Manninen, H. E., Lehtipalo, K. Kerminen, V.-M. (2012). Measurement of the nucleation of atmospheric aerosol particles. *Natural Protocols*, *7*, 1651–1667.
Kulmala, M., Riipinen, I., Sipilä, M., Manninen, H. E., Petäjä, T., Junninen, H. Kerminen, V.-M. (2007). Towards direct measurement of atmospheric nucleation. *Science*, *318*, 89–92.
Kulmala, M., Vehkamäki, H., Petäjä, T., Dal Maso, M., Lauri, A., Kerminen, V. M. McMurry, P. H. (2004). Formation and growth rates of ultrafine atmospheric particles: A review of observations. *J Aerosol Sci*, 35, 143–176.
Laakso, L., Hussein, T., Aarnio, P., Komppula, M., Hiltunen, V., Viisanen, Y., & Kulmala, M. (2003). Diurnal and annual characteristics of particle mass and number concentrations in urban, rural and Arctic environments in Finland. *Atmospheric Environment*, *37*, 2629–2641.
Laakso, L., Petäjä, T., Lehtinen, K. E. J., Kulmala, M., Paatero, J., Hõrrak, U. Joutsensaari, J. (2004). Ion production rate in a boreal forest based on ion, particle and radiation measurements. *Atmospheric Chemistry and Physics*, 4, 1933–1943.
Lange, R., Fissan, H., & Schmidt-Ott, A. (1996). Determination of equivalent diameters of agglomerates. *Journal of Aerosol Science*, *29*, S417–S418.
Manninen, H. E., Petäjä, T., Asmi, E., Riipinen, I., Nieminen, T., Mikkilä, J. Kulmala, M. (2009). Long-time field measurements of charged and neutral clusters using Neutral cluster and Air Ion Spectrometer (NAIS). *Boreal Environment Research*, *14*, 591–605.
Manninen, H. E., Nieminen, T., Asmi, E., Gagné, S., Häkkinen, S., Lehtipalo, K. Kulmala, M. (2010). EUCAARI ion spectrometer measurements at 12 European sites – analysis of new particle formation events. *Atmospheric* Measurement *Techniques*, *10*, 7907–7927.
Mavliev, R. A., & Ankilov, A. N. (1985). Methods for the treatment of data for a netlike diffusion battery Kolloidn. *Zhurn (in Russian)*, *47*, 523–530.
McMurry, P. H. (2000). A review of atmospheric aerosol measurements. *Atmospheric Environment*, *34*, 1959–1999.
Mirme, S., & Mirme, A. (2013). The mathematical principles and design of the NAIS – a spectrometer for the measurement of cluster ion and nanometer aerosol size distributions. ***Atmospheric Measurement Technology***, *6*, 1061–1071.
Mönkkönen, P., Koponen, I. K., Lehtinen, K. E. J., Hämeri, K., Uma, R., & Kulmala, M. (2005). Measurements in a highly polluted Asian mega city: Observations of aerosol number size distribution, modal parameters and nucleation events. *Atmospheric Chemistry and Physics*, *5*, 57–66.
Nieminen, T., Asmi, A., Dal Maso, M., Aalto, P. P., Keronen, P., Petäjä, T. Kerminen, V.-M. (2014). Trends in atmospheric new-particle formation: 16 years of observations in a boreal-forest environment. *Boreal Environment Research*, 19B, 191–214.
Pöschl, U. (2005). Atmospheric aerosols: Composition, transformation, climate and health effects. *Angewandte Chemie International Edition in English*, *44*, 7520–7540.
Rosen, J. B. (1960). *The gradient projection method for nonlinear programming, Part 1 – Linear constraints*. SIAM, 8.
Valiulin, S. V., Vosel, S. V., Karasev, V. V., Onischuk, A. A., Baklanov, A. M., & Purtov, P. A. (2014). Study of sulfur heterogeneous nucleation from supersaturated vapor on tungsten oxide and sodium chloride seed particles. Determination of contact angle of critical sulfur nuclei. *Colloid Journal*, *76*, 271–284.
von Klot, S., Peters, A., Aalto, P., Bellander, T., Berglind, N., D'Ippoliti, D. Health Effects of Particles on Susceptible Subpopulations Study, G. (2005). Ambient air pollution is associated with increased risk of hospital cardiac readmissions of myocardial infarction survivors in five European cities. *Circulation*, *112*, 3073–3079.
Wiedensohler, A., Birmili, W., Nowak, A., Sonntag, A., Weinhold, K., Merkel, M. Bastian, S. (2012). Mobility particle size spectrometers: Harmonization of technical standards and data structure to facilitate high quality long-term observations of atmospheric particle number size distributions. *Atmospheric Measurement Techniques*, 5, 657–685.
Yee, E. (1989). On the interpretation of diffusion battery data. *Journal of Aerosol Science*, 20, 797–812.
Yli-Juuti, T., Nieminen, T., Hirsikko, A., Aalto, P. P., Asmi, E., Hõrrak, U. Riipinen, I. (2011). Growth rates of nucleation mode particles in Hyytiälä during 2003–2009: Variation with particle size, season, data analysis method and ambient conditions. *Atmospheric Chemistry and Physics*, 11, 12865–12886.
Zieger, P., Aalto, P. P., Aaltonen, V., Äijälä, M., Backman, J., Hong, J. Petäjä, T. (2015). Low hygroscopic scattering enhancement of boreal aerosol and the implications for a columnar optical closure study. *Atmospheric Chemistry and Physics*, 15, 7247–7267.

Paper II

BOREAL ENVIRONMENT RESEARCH 21: 299–318
ISSN 1239-6095 (print) ISSN 1797-2469 (online)

Helsinki 2016

Responses of the atmospheric concentration of radon-222 to the vertical mixing and spatial transportation

Xuemeng Chen[1)]*, Jussi Paatero[2)], Veli-Matti Kerminen[1)], Laura Riuttanen[1)], Juha Hatakka[2)], Veijo Hiltunen[1)], Pauli Paasonen[1)], Anne Hirsikko[2)], Alessandro Franchin[1)], Hanna E. Manninen[1)], Tuukka Petäjä[1)], Yrjö Viisanen[2)] and Markku Kulmala[1)]

[1)] *Department of Physics, P.O. Box 64, FI-00014 University of Helsinki, Finland (*corresponding author's e-mail: xuemeng.chen@helsinki.fi)*
[2)] *Finnish Meteorological Institute, P.O. Box 503, FI-00101 Helsinki, Finland*

Received 28 April 2015, final version received 10 Nov. 2015, accepted 11 Nov. 2015

Chen X., Paatero J., Kerminen V.-M., Riuttanen L., Hatakka J., Hiltunen V., Paasonen P., Hirsikko A., Franchin A., Manninen H.E., Petäjä T., Viisanen Y. & Kulmala M. 2016: Responses of the atmospheric concentration of radon-222 to the vertical mixing and spatial transportation. *Boreal Env. Res.* 21: 299–318.

Radon-222 (^{222}Rn) has traditionally been used as an atmospheric tracer for studying air masses and planetary boundary-layer evolution. However, there are various factors that influence its atmospheric concentration. Therefore, we investigated the variability of the atmospheric radon concentration in response to the vertical air mixing and spatial transport in a boreal forest environment in northern Europe. Long-term ^{222}Rn data collected at the SMEAR II station in southern Finland during 2000–2006 were analysed along with meteorological data, mixing layer height retrievals and air-mass back trajectory information. The daily mean atmospheric radon concentration followed a log-normal distribution within the range < 0.1–11 Bq m^{-3}, with the geometric mean of 2.5 Bq m^{-3} and a geometric standard deviation of 1.7 Bq m^{-3}. In spring, summer, autumn and winter, the daily mean concentrations were 1.7, 2.7, 2.8 and 2.7 Bq m^{-3}, respectively. The low, spring radon concentration was especially attributed to the joint effect of enhanced vertical mixing due to the increasing solar irradiance and inhibited local emissions due to snow thawing. The lowest atmospheric radon concentration was observed with northwesterly winds and high radon concentrations with southeasterly winds, which were associated with the marine and continental origins of air masses, respectively. The atmospheric radon concentration was in general inversely proportional to the mixing layer height. However, the ambient temperature and small-scale turbulent mixing were observed to disturb this relationship. The evolution of turbulence within the mixing layer was expected to be a key explanation for the delay in the response of the atmospheric radon concentration to the changes in the mixing layer thickness. Radon is a valuable naturally-occurring tracer for studying boundary layer mixing processes and transport patterns, especially when the mixing layer is fully developed. However, complementing information, provided by understanding the variability of the atmospheric radon concentration, is of high necessity to be taken into consideration for realistically interpreting the evolution of air masses or planetary boundary layer.

Editor in charge of this article: Hannele Korhonen

Introduction

Radon-222 (^{222}Rn) is a radioactive noble gas with a half-life of about 3.8 days, which is naturally exhaled from soil into the atmosphere (e.g. Pal *et al*. 2015). It originates from the spontaneous decay series of ^{238}U in the Earth's crust. Owing to the long half-life, monatomic radon gas can migrate through the soil and enter the atmosphere before lost in the radioactive decay. The concentration of radon in the atmosphere is directly related to the exhalation rate of radon from soils (Escobar *et al*. 1999). This exhalation process is affected by several factors, including the concentration of its parent nuclide (radium-226), internal structure of radium-containing mineral grain, soil type, moisture and temperature; and also the changing ambient air pressure has influences on the exhalation rate (Clements and Wilkening 1974, Stranden *et al*. 1984, Schery 1989, Markkanen and Arvela 1992, Nazaroff 1992, Ashok *et al*. 2011). Typically, radon is formed from radium decay inside the mineral grains of soil, and therefore, it has to first escape into pores in between the grains before being transported to the atmosphere by diffusion and convection (Porstendörfer 1994). The transport mechanisms of radon from soil to the atmosphere have been elucidated by Nazaroff (1992).

The dynamics of the planetary boundary layer (PBL) has crucial effects on the surface-atmosphere exchanges of energy, moisture, momentum and pollutants (Seidel *et al*. 2010, Behrendt *et al*. 2011, Pal and Devara 2012, Lac *et al*. 2013, McGrath-Spangler and Denning 2013, Lee *et al*. 2015). Therefore, the atmospheric concentration of radon is inevitably dependent on the vertical mixing through transport and changes in a dispersion volume in the PBL. According to Stull (1998), the PBL has a well-defined structure in high-pressure regions over land, which evolves with time: a very turbulent daytime mixed layer dies out after sunset, forming a residual layer and a relatively stable nocturnal boundary layer. Mixing due to turbulence can, to some extent, take place in the nocturnal boundary layer (Stull 1998). There is an increasing number of observational studies showing that boundary layer mixing can have distinct characteristics in different environments (e.g. Barlow *et al*. 2011, Schween *et al*. 2014, Vakkari *et al*. 2015). Accordingly, a mixing layer (ML) is preferably used to denote the layer with complete or incomplete mixing process in the PBL (Beyrich 1997, Seibert *et al*. 1999).

Owing to the facts that radon is chemically inert and its removal from the atmosphere depends only on the radioactive decay process, radon has long been regarded as a useful tracer in studying the vertical mixing in the ML (Jacobi and André 1963, Guedalia *et al*. 1980, Kritz 1983, Sesana *et al*. 2003, Grossi *et al*. 2012, Pal 2014). Pal *et al*. (2015) studied the variability of the atmospheric boundary layer using radon and recently Griffiths *et al*. (2013) reported the use of radon data to improve the determination of the ML height from lidar backscatter profiles. Radon is also the favoured choice for testing and developing climate and chemical transport models (Jocab and Prather 1990, Forster *et al*. 2007, Zhang *et al*. 2008), as reviewed by Zahorowski *et al*. (2004). Several applications involving radon as the atmospheric tracer have also been summarised by Williams *et al*. (2011). However, these studies were mostly based on relatively short-term study periods varying from a few weeks to a year, and therefore, they lack long-term statistical reliability on the diurnal and seasonal variability of the atmospheric radon concentration in responses to vertical and spatial mixings. If a biased observation on the intrinsic features in the variability of the atmospheric radon concentration were made, the scarcity would probably be propagated into the subsequent applications. Hence, data sets based on long-term comprehensive measurements are essential.

In this paper, we analysed the variability of the atmospheric radon concentration in response to the vertical mixing and spatial transport of air at the SMEAR II station (61°51´N, 24°17´E, 181 m a.s.l.) in a boreal forest environment at Hyytiälä of southern Finland (*see* Hari and Kulmala 2005). The investigation was based on data sets of radon and meteorological variables collected during 2000–2006. Mixing-layer height estimates and back-trajectory calculations were used to assist the interpretation of the ambient data. The main goal of this study was, by using long-term data sets with aids of meteorological

data, modelled mixing layer height and trajectory statistics, to elucidate how the mixing layer development and air mass motions affect the observed variability in the atmospheric radon concentration in the boreal forest environment of northern Europe.

Material and methods

The radon measurement at the SMEAR II station was deployed by the Finnish Meteorological Institute (FMI) and has been integrated into the long-term measurement system of the station. The atmospheric concentration of ^{222}Rn was resolved from the measurement of beta activity on atmospheric aerosol particles by a radon monitor. The meteorological data on wind and air temperature were obtained from mast measurements. The mast at the SMEAR II station had a height of 73 m, and continuous measurements during 2000–2006 were carried out at seven heights. The mast was later extended to 127 m and three more measurement heights were added. The air temperature data were taken from 4.2 m and 67.2 m, and the data on wind speed and wind direction from 8.4 m of the mast measurements. For a thorough investigation of the relation between the variations in the atmospheric radon concentration and vertical and spatial mixing, also the mixing layer (ML) height obtained from the European Centre for Medium-Range Weather Forecasts (ECMWF) Meteorological Archival and Retrieval System (MARS) and trajectory information calculated from the FLEXible TRAjectories (FLEXTRA) model (Stohl *et al*. 1995) were analysed in this work. The data are presented for UTC + 2.

Radon measurement

The radon measurements were carried out by a filter-based radon monitor and the design details of the instrument are described in Paatero *et al*. (1994). Here, we briefly present the measurement procedures and focus on resolving the atmospheric concentration of ^{222}Rn from recorded count rates. The inlet of this monitor is kept at 6 m above the ground. The device comprises primarily a pair of cylindrical Geiger-Müller counters housed in lead shields for beta particle detection and a mass flow meter for measuring the air stream. Both counters have an effective time of 4 h for sample collection, and while one of the counters is sampling, the other one is closed for the radioactivity on the filter to decay. The airflow contains aerosol particles carrying daughter nuclides of radon. While passing through the device, these aerosol particles are collected on the filter wrapping the effective counter. The beta particles released from them are registered cumulatively in 10-min intervals. For the geometric configuration of this device, counting efficiencies of 0.96% and 4.3% are achieved for beta emissions from ^{214}Pb and ^{214}Bi, respectively. A rough estimation of the 1-σ counting statistics is ±20% for a presumed stable ^{222}Rn concentration of 1 Bq m^{-3}.

A full cycle of each counter takes 8 h before being effective for the next collection period. Ideally, counts in either counter drop to the base level at the end of the 8-h period, provided that the activity comes solely from the short-lived radon progeny, i.e. daughter nuclides of ^{222}Rn. In practice, however, long-lived radioactivity in the air may affect measurements. This long-lived radioactivity is comprised mainly of ^{220}Rn progeny and, to a lesser extent, of artificial radionuclides (for example, ^{137}Cs from nuclear tests and accidents, e.g. Chernobyl). The long-lived radioactivity can elevate the base level for the next collection period. These contributions were excluded in this study by subtracting the base level from the beta activity registered in the concerned collection period. If the background activity at the beginning of an 8-h cycle was lower than that at the end of this cycle, it indicates that the long-lived radioactivity came from the first 4-h collection period during this cycle. The base level was, therefore, determined by a linear interpolation between the activities recorded at the beginning and at the end of an 8-h cycle for 4 h. Otherwise, the base level was obtained from a linear interpolation over 8 h.

The atmospheric concentration of ^{222}Rn can be approximated by the concentration (C) of ^{218}Po in the atmosphere, which is resolvable from the registered activity according to the following equation (Paatero *et al*. 1994):

$$C = \frac{R}{\varepsilon_1 V\left(\frac{S_1}{\lambda_1}+\frac{S_2}{\lambda_2}\right)+\varepsilon_2 V\left(\frac{S_3}{\lambda_1}+\frac{S_4}{\lambda_2}+\frac{S_5}{\lambda_3}\right)}. \quad (1)$$

Here, it is assumed that the recorded radioactivity originates only from the decay of ^{222}Rn and the first three daughter nuclides of radon (^{218}Po, ^{214}Pb and ^{214}Bi) have an equal concentration. Based on the studies carried out in Helsinki, Mattsson (1984) reported that ^{218}Po, ^{214}Pb and ^{214}Bi remained mostly in equilibrium with unity ratio among them, regardless of weather conditions. No significant sources of artificial radioactivity existed during the study period. Consequently, artificial radioactive sources could be neglected, and the recorded radioactivity could be attributed to the decay of ^{222}Rn only. In Eq. 1, R is the newly-collected activity during 10 minutes corrected for the left-over activity present on the filter, V is the volumetric flow rate of the air stream passing through the filter, λ is the decay constant with subscripts 1 to 3 referring to ^{218}Po, ^{214}Pb and ^{214}Bi, and ε_1 and ε_2 are the counting efficiencies of the beta particles emitted in the decay processes of ^{214}Pb and ^{214}Bi, respectively. The term S_i was derived from Bateman equations (Bateman 1910) which quantify the abundances of nuclides in the decay chain and take the following forms:

$$S_1 = 1-\frac{\lambda_2}{\lambda_2-\lambda_1}e^{-\lambda_1 t}-\frac{\lambda_1}{\lambda_1-\lambda_2}e^{-\lambda_2 t}, \quad (2)$$

$$S_2 = 1-e^{-\lambda_2 t}, \quad (3)$$

$$S_3 = 1-\frac{\lambda_2}{\lambda_2-\lambda_1}\frac{\lambda_3}{\lambda_3-\lambda_1}e^{-\lambda_1 t} - \frac{\lambda_1}{\lambda_1-\lambda_2}\frac{\lambda_3}{\lambda_3-\lambda_2}e^{-\lambda_2 t} - \frac{\lambda_1}{\lambda_1-\lambda_3}\frac{\lambda_2}{\lambda_2-\lambda_3}e^{-\lambda_3 t}, \quad (4)$$

$$S_4 = 1-\frac{\lambda_3}{\lambda_3-\lambda_2}e^{-\lambda_2 t}-\frac{\lambda_2}{\lambda_2-\lambda_3}e^{-\lambda_3 t}, \quad (5)$$

$$S_5 = 1-e^{-\lambda_3 t}. \quad (6)$$

Meteorological measurements

The ambient air temperature (T) used in this study was measured at 4.2 m and 67.2 m. It was measured with PT-100 sensors mounted on the mast. These sensors were protected from solar radiation and ventilated by fans. Based on the comparison with a reference mercury thermometer, the bias of these measurements was within ±0.2 °C.

Before 4 September 2003, the wind speed (WS) at the 8.4-m height was measured with a cup anemometer (A101M/L, Vector Instruments, Rhyl, Clwyd, UK; threshold 0.15 m s^{-1}), and as of 5 September 2003, with an ultrasonic anemometer (Ultrasonic anemometer 2D, Adolf Thies GmbH, Göttingen, Germany; accuracy ±1 m s^{-1}). The information on the wind direction (WD) at this height was also obtained with the ultrasonic anemometer (accuracy ±1°).

Mixing layer (ML) height model

The ML height estimates were obtained from the European Centre for Medium-Range Weather Forecasts (ECMWF, www.ecmwf.int) Meteorological Archival and Retrieval System (MARS). The boundary Layer Height (BLH) parameter (i.e. ML) was retrieved from the operative forecast model in use at the time (http://www.ecmwf.int/en/forecasts/documentation-and-support/changes-ecmwf-model). Determination of the BLH in the model is based on the parcel-lifting method: the parcel is lifted from the surface layer up to the level where a critical bulk Richardson number is reached (ECMWF 2001). Even though the mixing layer heights retrieved from the forecast data are only approximations, they have been shown to represent the diurnal and seasonal cycles of the ML height reasonably well (Seidel *et al*. 2012). ML heights can be derived from various measurements (e.g. Cimini *et al*. 2013, Pal 2014, Schween *et al*. 2014, Vakkari *et al*. 2015). Korhonen *et al*. (2014) compared three data sets of modelled ML heights for a South African site derived from different models with ML heights calculated from radiosonde and lidar backscatter measurements and found the best agreement for the ECMWF model with the lidar measurement, showing only a mean relative difference of 15.4%. Kouznetsov *et al*. (2012) did similar comparisons for Helsinki, Finland between modelled ML heights and Sodar data.

Although the ECMFW ML heights did not show the best agreement with the measurement among tested models, the measured and ECMWF ML heights were found comparable.

FLEXTRA trajectory and data analysis

Air mass back trajectories arriving at Hyytiälä on the 950-hPa pressure level were calculated with the FLEXTRA kinematic trajectory model (ver. 3.3) (Stohl *et al*. 1995). For this study, 120-h back trajectories were calculated in 3-h intervals. Analysed meteorological fields from the European Centre for Medium-Range Weather Forecasts (ECMWF) numerical weather forecast model were used as a model input.

The trajectory data were analysed based on the method proposed by Riuttanen *et al*. (2013), which takes into account the horizontal uncertainties associated with the atmospheric transport model used for generating the air mass trajectories. By comparing the distance between receptor cells and calculated trajectory with the distance being travelled along the trajectory to the measurement site, weighing factors were assigned to the receptor cells. According to Stohl and Seibert (1998), the horizontal uncertainty in the trajectory calculated from the FLEXTRA model, with the analysed meteorological field input from the ECMWF numerical weather forecast model, is less than 20% of the travel distance after 120-h travel time. Similar horizontal bias has also been reported for the computed trajectories when compared with manned balloon tracks (Baumann and Stohl 1997). Accordingly, if an adjacent cell (cell 1 in Fig. 1) fell in between 10% and 20% of the travelling distance by the trajectory (d) before reaching the SMEAR II station, it was given a weighing factor of 0.3 ('near' case), and if the distance between the cell (cell 2) and the trajectory was shorter than d_2, it received a weighing factor of 0.7 ('close' case). Cells outside the 20% boundary were assumed to receive no influence from the contents carried by the air mass travelling along the trajectory.

Because the resolved radon concentration was log-normally distributed (Fig. 2), the geometric mean value of the weighed concentrations accumulated in each cell was used to construct

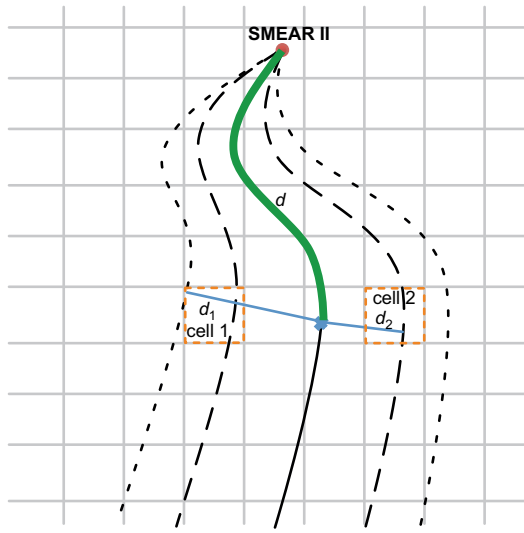

Fig. 1. A schematic demonstration of the trajectory analysis. Here $d_1 = 0.2 \times d$ and $d_2 = 0.1 \times d$, where d represents the distance being travelled by the trajectory before reaching the SMEAR II station.

the concentration field following Eq. 7, which was then normalised by the median values of the data set in this study to generate a relative concentration field.

$$C_{ij} = \exp\left[\frac{\sum_{n=1}^{K}\ln(C_n)w_k + \sum_{n=1}^{L}\ln(C_n)w_l}{\sum_{n=1}^{K}w_k + \sum_{n=1}^{L}w_l}\right]_{ij}, \quad (7)$$

where, i and j are the indices for the geographical coordinates of a receptor cell, n is the index of the trajectory, and w represents the weighing factor, with k and l indicting the 'close' and 'near' cases, respectively. According to Riuttanen *et al*. (2013), Eq. 7 is applicable only when the number of trajectory hits within each cell grid is greater than 10.

Mass balance analysis of the evolution of radon concentration with time and ML height

A mass balance approach, based on the Eulerian box model (Seinfeld and Pandis 2006), can be written to depict the temporal evolution of the atmospheric radon concentration with time by presuming that an equilibrium state is always established in the ML right after any change in

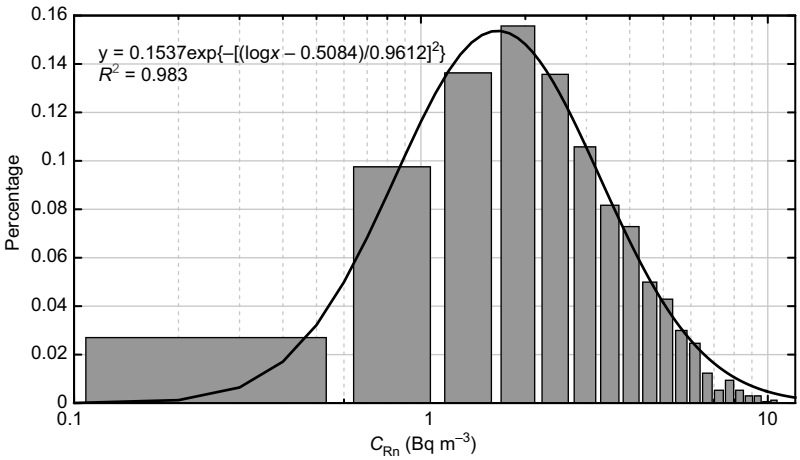

Fig. 2. Statistical distribution of the daily mean atmospheric radon concentration, C_{Rn}, for 2000–2006 with a log-normal fitting (solid line).

the system. The atmospheric radon concentration in this equilibrium state is expressed as C_{eq}. Furthermore, the distribution of radon in the ML is assumed to be homogeneous and therefore C_{eq} equals to the concentration derived from the measurement.

When the studied column is narrow enough, the horizontal transport of radon into the concerned volume can be roughly cancelled by the out-going fraction carried out by air masses from the volume. When averages of long-term data are considered, the effect of the horizontal transport on the column concentration can also be neglected, because the motion of air masses is not restricted into a single direction.

The primary source of radon is due to exhalation. Radon typically vanishes within the volume by spontaneous decay. The application of a mass balance approach is straightforward when this volume is constant. In the atmosphere, the ML depth changes with time, typically being low during night and early morning hours followed by a growth after sunrise with the maximum reached in the afternoon (e.g. Schween *et al*. 2014, Pal *et al*. 2015). When the ML expands, air above the ML containing radon gas (with concentration marked as C_0) gets mixed into the volume, which dilutes the radon content in it, yet being an additional source of radon. C_0, however, becomes equal to C_{eq}, once the maximum mixing depth is reached. As a result, the balance equation can be written as:

$$dC_{eq}/dt = \text{Exhalation} + \text{Dilutiuon} + \text{Decay}, \quad (8)$$

where the exhalation term can be expressed as the exhalation rate (ExR) over the ML height (H), ExR/H. By assuming that the radon concentration in the ML is in equilibrium, the decay term can be written as

$$dC_{eq}/dt_{Decay} = -\lambda C_{eq}, \quad (9)$$

where λ is the decay constant of ^{222}Rn. The dilution term has two different forms depending on the dynamics of the ML: for ML expansion,

$$\frac{dC_{eq}}{dt_{Dilution}} = \frac{dH}{dt}\left[\frac{1}{H}\left(C_0 - C_{eq}\right)\right], \quad (10)$$

and for ML shrinking, as $C_0 = C_{eq}$,

$$dC_{eq}/dt_{Dilution} = 0. \quad (11)$$

According to Eq. 10, the change rate of radon concentration is related to the expansion rate of the ML. This relationship has been illustrated by Pal *et al*. (2015), showing that the faster the ML grows, the faster radon concentration decreases.

Results and discussion

General patterns in the atmospheric radon concentration

At the SMEAR II station, daily mean atmospheric concentrations of ^{222}Rn ranged between < 0.1 and 11 Bq m^{-3} (the lower end of this range is restricted by the detection limit of the radon

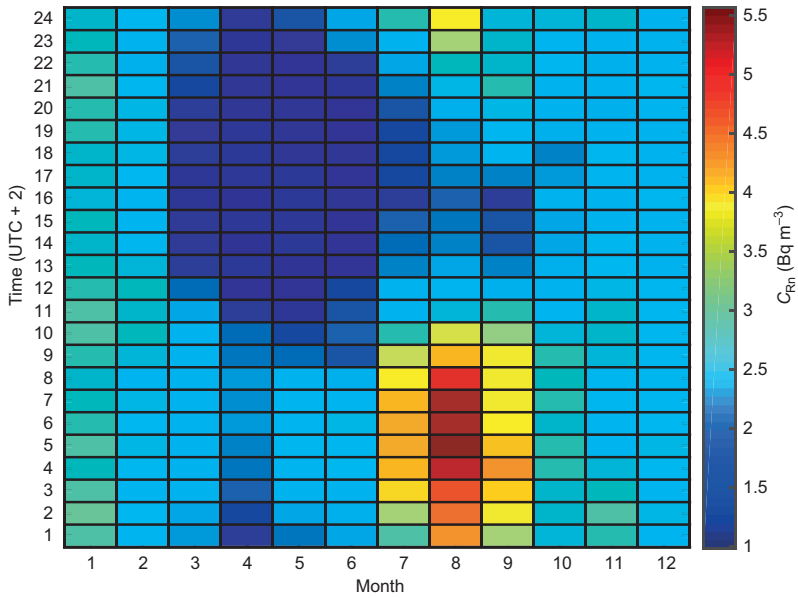

Fig. 3. Patterns in the hourly-median atmospheric radon concentration (C_{Rn}) in different months in 2000–2006. First, hourly medians were calculated for the whole measurement period from the 10-minute measurement data. From these data, median values for each month as a vector of hour of the day were then calculated.

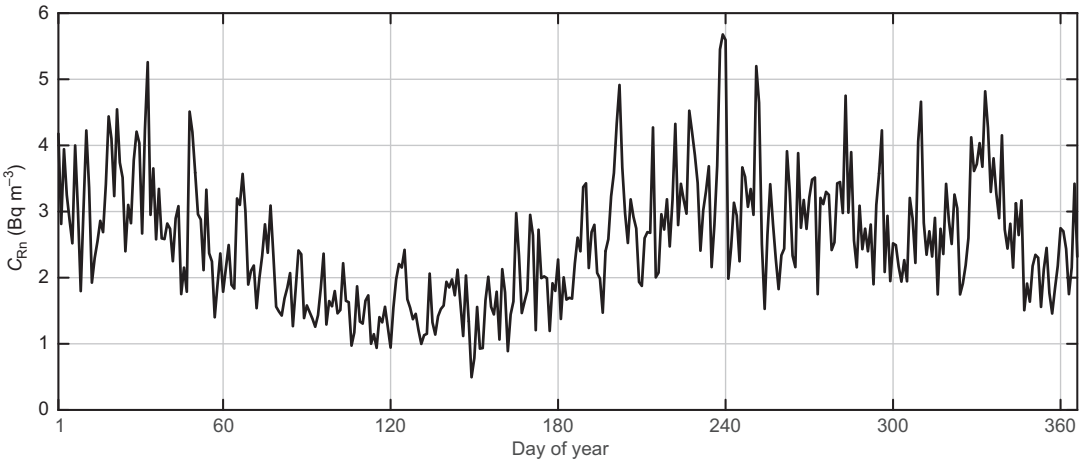

Fig. 4. Seasonal variation in the daily median atmospheric radon concentration (C_{Rn}) on the day-of-year basis for the years 2000–2006. First, hourly medians were calculated for the whole measurement period from the 10-minute measurement data. From these data, a median value for each day of the year was calculated.

monitor) during the years 2000–2006. They followed a log-normal distribution with a geometric mean of 2.5 Bq m^{-3} and a geometric standard deviation of 1.7 Bq m^{-3} (Fig. 2). The geometric mean of the daily mean radon concentration in each year fell in between 2.3 and 2.6 Bq m^{-3}, implying little inter-annual variability. A similar distribution pattern was also observed in daily medians of radon concentration, the geometric mean of which, however, got a slightly smaller value of 2.3 Bq m^{-3} with a geometric standard deviation of 1.8 Bq m^{-3}.

For the years 2000–2006, both the hourly medians for monthly periods and the daily medians on the day-of-year basis of the atmospheric radon concentration varied roughly between 1 and 5 Bq m^{-3} (Figs. 3 and 4). Similar to observations by Pal *et al*. (2015) in central Europe, a clear diurnal cycle in the atmospheric radon concentration, with a maximum in the early

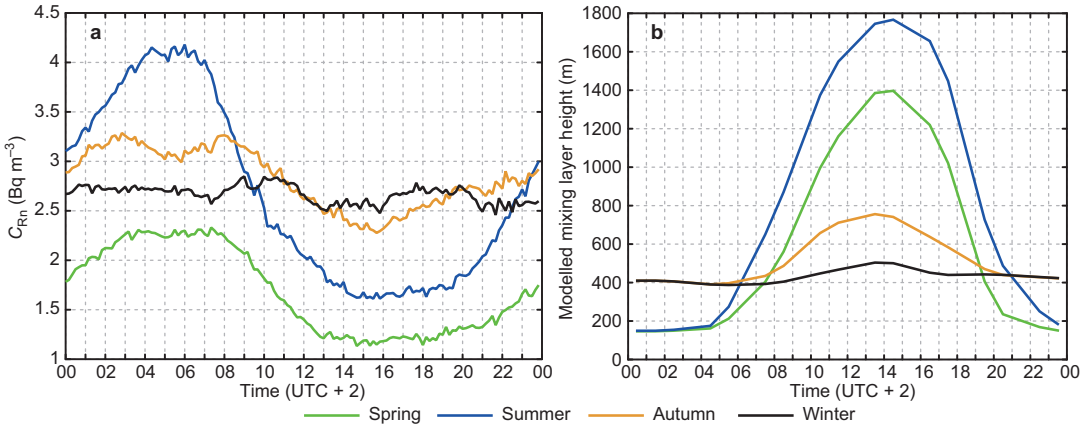

Fig. 5. Diurnal variations in different seasons in (*a*) median radon concentrations (C_{Rn}) in 10-min resolution for the years 2000–2006, and (**b**) modelled mixing layer heights processed as hourly medians for the years 2003–2006. The seasons are: spring (March–May), summer (June–August), autumn (September–November) and winter (December–February).

morning and minimum in the afternoon, was found for March–October. During these months, the average length of a period within a day with a low atmospheric radon concentration first increased until the end of May, after which an opposite behaviour was seen until September. During the other months, the atmospheric radon concentration showed little diurnal variation. The high radon concentration observed between midnight and 9:00 (UTC + 2) in the morning in late summer can be ascribed to the increase in local emission due to the optimal combination of the temperature and soil moisture condition for radon exhalation, together with the frequent occurrence of nocturnal inversion.

As for the seasonal cycle (Fig. 4), a relatively high median radon concentration was found in winter. A decline in the daily median radon concentration during the spring lasted until April. Thereafter, a recovery of concentration prevailed during the summer. The median radon concentration fluctuated around a relatively high level throughout the rest of the year, even though a slight decrease was seen in autumn. This observation is comparable to the pattern shown by Mattsson (1970), who also reported that ^{214}Bi, the short-lived progeny of ^{222}Rn, possessed a concentration in the range of about 25–125 pCi m^{-3} (1–5 Bq m^{-3}) in Finland. A joint effect of soil moisture and mixing layer development, which will be discussed later in the text, resulted in the minimum median radon concentration observed in April. The high atmospheric concentration of radon in autumn and winter was typically related to the persistent surface inversion.

Clear diurnal cycles in the median radon concentration based on the 10-min data were identifiable in all seasons, with the exception of winter (Fig. 5a). The largest amplitude in the diurnal variation was observed in the summer (June–August), with the maximum median radon concentration at around 06:00 and minimum at around 16:00. Comparable daily mean atmospheric concentrations of ^{222}Rn were observed in summer (2.7 Bq m^{-3}), autumn (September–November, 2.8 Bq m^{-3}) and winter (December–February, 2.7 Bq m^{-3}), whereas the concentration was clearly lower in spring (March–May, 1.7 Bq m^{-3}). Our findings are similar to the results obtained for a French site (Pal *et al.* 2015), where, however, no obvious low radon concentration was observed in spring and more pronounced diurnal variation was observed in autumn as compared with the patterns in other seasons.

Vertical mixing, horizontal transportation and local emissions affect atmospheric radon concentration. In summer, autumn and winter, the dilution due to vertical mixing, contribution from horizontal transportation and changes in local emissions were assumed to maintain the atmospheric radon concentration around a rela-

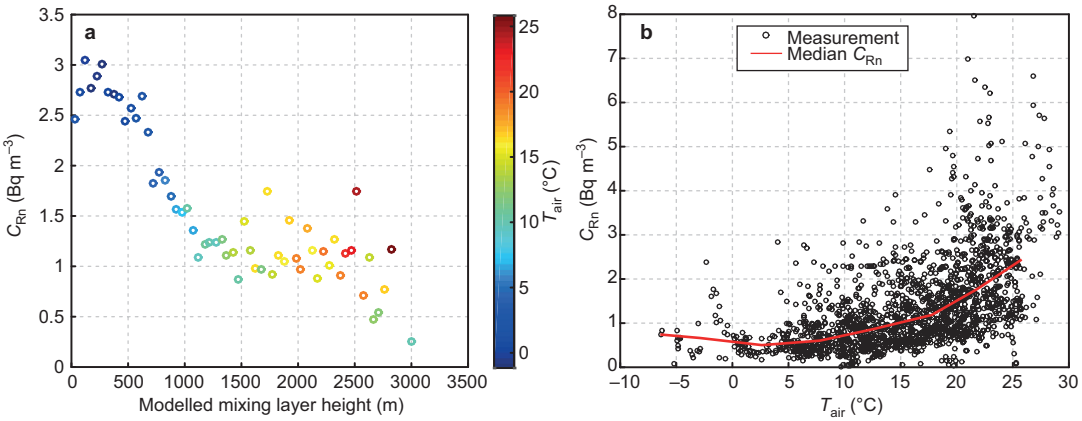

Fig. 6. The atmospheric radon concentration (C_{Rn}) during 2003–2006 as a function of (**a**) the modelled mixing layer height and (**b**) air temperature (T_{Air}). The colour scale indicates air temperature measured at the 4.2 m height. In **a**, median radon concentrations were calculated from all the data in binned mixing layer heights with a coequal interval of 50 m. In **b**, hourly median radon concentrations within the mixing layer height range of 1500–2500 m were taken into account. Median radon concentrations in 5 °C intervals in the selected mixing layer range were plotted in red.

tive stable median level (Fig. 5a). However, the dilution effect of vertical mixing and the reduction in local radon exhalation due to water blockage from snow thawing are especially prominent in spring, consequently leading to a remarkably low atmospheric concentration of radon..

The response of the atmospheric radon concentration to the development of ML

The seasonal and diurnal variations in the atmospheric radon concentration were linked to the vertical mixing in the atmosphere. The mixing layer (ML) was typically the deepest in the afternoon at around 14:00 (Fig. 5b), which corresponded to the time of observation of low radon concentration (Fig. 5a). The magnitude of the diurnal variation in the atmospheric radon concentration was connected to the development of the ML: the deeper the ML expanded, the more pronounced diurnal cycles in the radon concentration were observed. Along with an air temperature increase, the median radon concentration first decreased almost linearly in response to the expansion of the ML up to a median height of 1500 m (Fig. 6a). With further warming, however, the concentration levelled at around 1 Bq m^{-3}, when the median modelled ML height resided between 1500 and 2500 m. This observation indicates that there was enrichment in the atmospheric radon concentration in relation to the high air temperature, which overcame the dilution due to the thickening of the ML. The increase in the atmospheric radon concentration can be attributed to both local sources and transport. Owing to its 3.8-day half-life, transportation of ^{222}Rn in the atmosphere is possible over considerable distances.

The local radon source is primarily dependent on the availability of radon gas in the soil, which is determined by the emanation rate. In addition, it is also determined by the exhalation of the radon gas from soil, which weakly depends on the temperature (Stranden *et al*. 1984). Nazaroff (1992) elucidated that once radon atoms get released to soil pores from soil grains, they can be in three different phases: the sorbed phase on soil grain, gaseous phase and aqueous phase. The sorption process, while abated by a temperature increase, is less relevant in ambient conditions owing to the involvement of moisture (Stranden *et al*. 1984, Nazaroff 1992). However, the temperature affects the partitioning between the other two phases, because radon is weakly soluble in water and its solubility decreases with an increasing temperature (Lewis *et al*. 1987). Furthermore, the transport of radon from soil pores to the atmosphere is governed by another temperature-dependent process, diffusion, under ambient con-

ditions (Nazaroff 1992). Accordingly, an increase in the air temperature heats the surface layer of the soil, which subsequently contributes to the growth in atmospheric radon concentration by reducing the solubility of radon in moisture contained in soil pores and enhancing the diffusion of the radon gas through the soil.

Compared with the temperature, the moisture has been shown to have a stronger influence on radon exhalation (Stranden *et al*. 1984, Nazaroff 1992). Typically the moisture plays opposite roles in affecting radon emanation and diffusion. The moisture reduces significantly the diffusion coefficient of radon in soil (Nazaroff 1992), whereas it enhances the emanation of radon from soil grains to soil pores (Markkanen and Arvela 1992), possibly due to the lower recoil range of radon in water than that in air (Nazaroff 1992). The overall effect of these two processes is that the maximum exhalation rate of radon appears at an optimal moisture concentration depending on the soil type, as shown by Stranden *et al*. (1984). The high soil moisture content during the snow-thawing period hindered radon exhalation, which contributed to the occurrence of the minimum radon concentration in April (Figs. 3–4). Yet, an over-dry condition brings no incentive either. Therefore, the ground-water level has been coherently found as an indicator of radon exhalation (Mattsson 1970). During warm periods, the surface air dries up the topsoil, which favours the diffusive transport of radon through the ground surface to the atmosphere, yet possibly without disrupting the radon emanation from ores containing the parent nuclides of radon. As a consequence, the plateau in Fig. 6a was most likely caused, in addition to the transported source, by the combination of the opposite effects of enhanced radon exhalation from soil and vertical dilution in the atmosphere. This means that the effect of the intensified radon exhalation resulting from increasing air temperature was counterbalanced by the enhanced dilution as the ML height grew from 1500 m to 2500 m (Fig. 6a). In support of this, an exponential relationship was identified between air temperature and atmospheric radon concentration within the ML height range between 1500 and 2500 m based on hourly data (Fig. 6b). Such an increase in the atmospheric radon concentration with an increasing air temperature was also evident beyond this ML range, when air temperature was above 5 °C.

For the ML height higher than about 2500 m, the median radon concentration tended to decrease further with an increasing ML height, and the median air temperature dropped from about 15 °C to slightly below 10 °C (Fig. 6a). Days with such a thick ML and moderate air temperature occurred typically in late spring and early summer.

We observed clear diurnal patterns in the median radon concentration as a function of the temperature difference between the 67.2 m and 4.2 m heights in spring, summer and autumn (Fig. 7). Apart from the winter season, a stable layer near the surface with a positive temperature difference (inversion) was observed during the night, which lasted the longest in summer, followed by spring and autumn. The positive temperature difference was prominent in winter, yet no clear pattern in the evolution of this parameter with time could be identified in relation to the atmospheric radon concentration during this season. During other seasons, the median radon concentration increased over the night when the positive temperature inversion prevailed, and ultimately led to the maximum median radon concentration at around 06:00 in the morning (Fig. 5a). Hereafter, the enhanced vertical mixing due to expanding ML after sunrise diminished the temperature inversion. Eventually, a reduction in the median radon concentration occurred in the unstable atmosphere when the dilution became predominant on average. This process was intensified along with the further development of the ML until the maximum depth was reached at around 14:00, when the median radon concentration nearly dropped to its minimum. Thereafter, especially in summer and autumn following some latency, a slow increase in the median radon concentration emerged along with the gradual shrinkage of the ML.

The effect of wind on the atmospheric radon concentration

Wind affects the observed variability in the concentrations of trace components in the atmosphere (e.g. Pal *et al*. 2014). High median wind

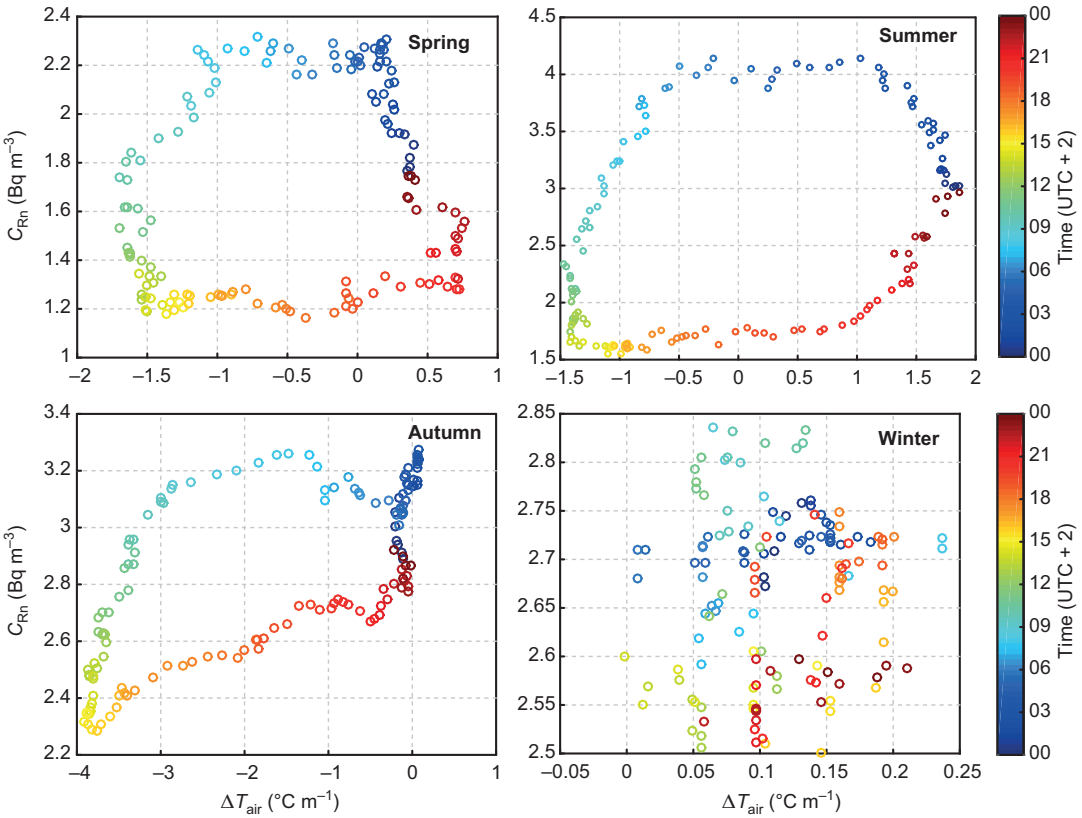

Fig. 7. Median atmospheric radon concentration (C_{Rn}) as a function of the temperature difference between the 67.2 m and 4.2 m heights, ΔT_{Air}, for different seasons in the years 2000–2006. Time is shown on the colour scale. Positive values of ΔT indicate stable conditions and negative ones an unstable atmosphere. All the data were processed seasonally as 10-min medians for the years 2000–2006.

speeds were typically seen at around midday, which corresponded to the full development of the ML in an unstable atmosphere (Fig. 8). The low-wind-speed condition was, however, associated with a shallow ML and stable atmosphere in the evening. These features, however, were unidentifiable in the wintertime. Nonetheless, an inverse relationship with a linear proportionality was found between the wind-speed bins with coequal interval of 0.5 m s^{-1} and the corresponding median radon concentration in these bins (Fig. 9).

The ML started to shrink after reaching the maximum height at about 14:00 (Fig. 5b), after which the atmospheric radon concentration recovered with some time lag (Figs. 5, 7 and 8). A delay was seen in the early morning as well, when the high radon concentration lasted for a while after the clear increase in the ML height. While similar features have been pointed out by Guedalia *et al*. (1980) and Chambers *et al*. (2011), the reason for such a phenomenon has not been clearly attributed to the processes taking place in the atmosphere. Here an improved mechanism related to turbulent mixing is proposed for these observations based on a mass balance analysis (Eqs. 8–11).

Since ^{222}Rn stems from the decay chain of ^{238}U that originates from the ground, free troposphere is expected to have a low radon concentration. According to Galeriu *et al*. (2011), a difference of one to three orders of magnitude exists between the radon concentration in the free troposphere and that near the ground surface. However, the residual layer preserves the remnant radon from the ML of the previous day. As the ML rises, it swallows in radon from the residual layer only, provided that the ML

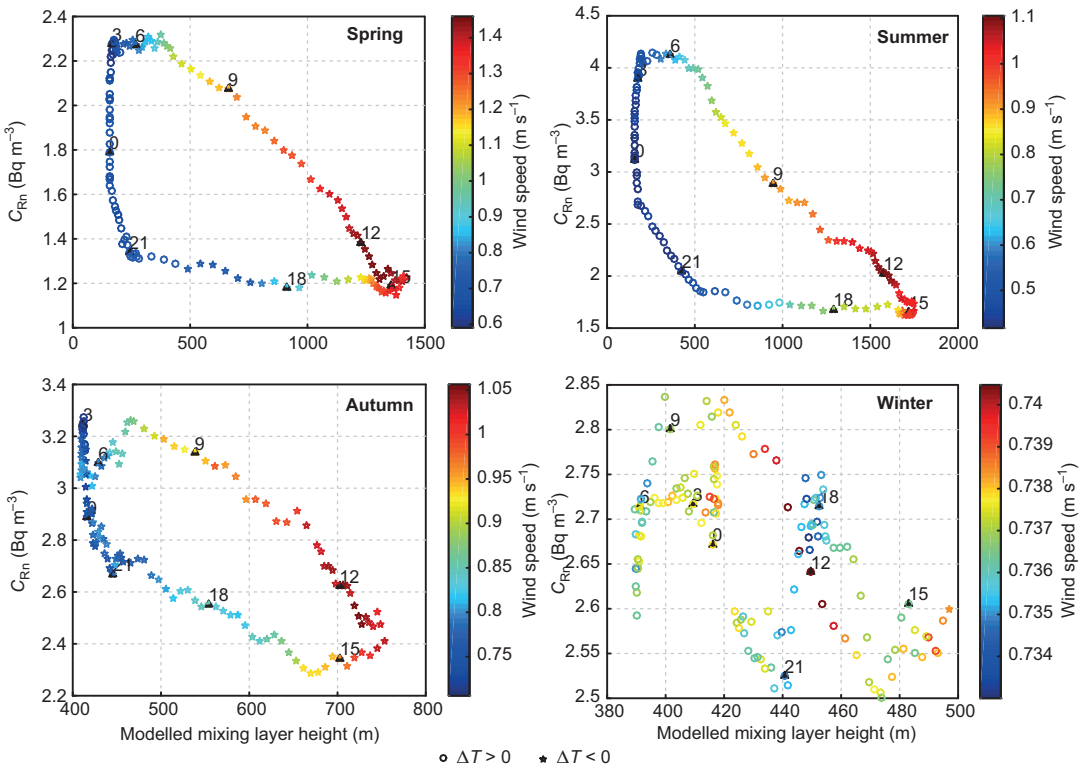

Fig. 8. Median atmospheric radon concentration (2000–2006), C_{Rn}, as function of the modelled mixing layer height (2003–2006) during the four seasons. The colour scale indicates the median wind speed (2000–2006). The filled black triangles indicate the observation time in 3-h intervals. The circles correspond to the positive (negative) temperature difference between the heights 67.2 m and 4.2 m. All the data were processed seasonally as 10-min medians.

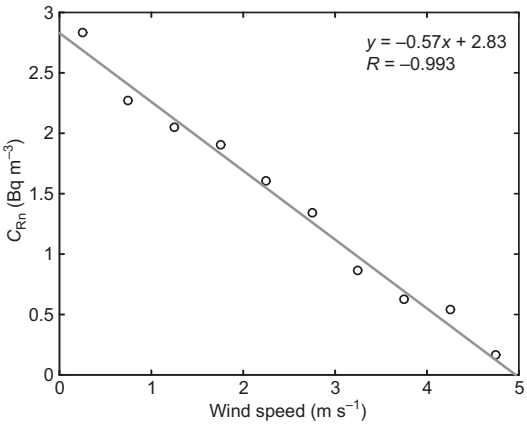

Fig. 9. The relation between the median atmospheric radon concentration (C_{Rn}) and median wind speed measured at the 8.4 m height for the years 2000–2006. Median radon concentrations were calculated in wind-speed bins with a coequal interval of 0.5 m s^{-1}.

height does not exceed that of the previous day. Otherwise, the nearly radon-free air from the free troposphere would significantly reduce the radon concentration in the ML. An example of the behaviours of the dilution and decay terms in the mass balance for the radon in the ML (Eqs. 8–11) is present in Fig. 10. This analysis was carried out using the median radon concentration and the median modelled ML height of the diurnal data from the summers of 2000–2006. As the ML typically is deepest in summer (McGrath-Spangler and Denning 2013) and tends to deepen towards the end of summer (Leventidou *et al.* 2013), the air from the free troposphere has the greater effect on the dilution at this time of the year. In addition, the sum of the dilution and decay terms should be negative, since there is another source, the exhalation term, in the

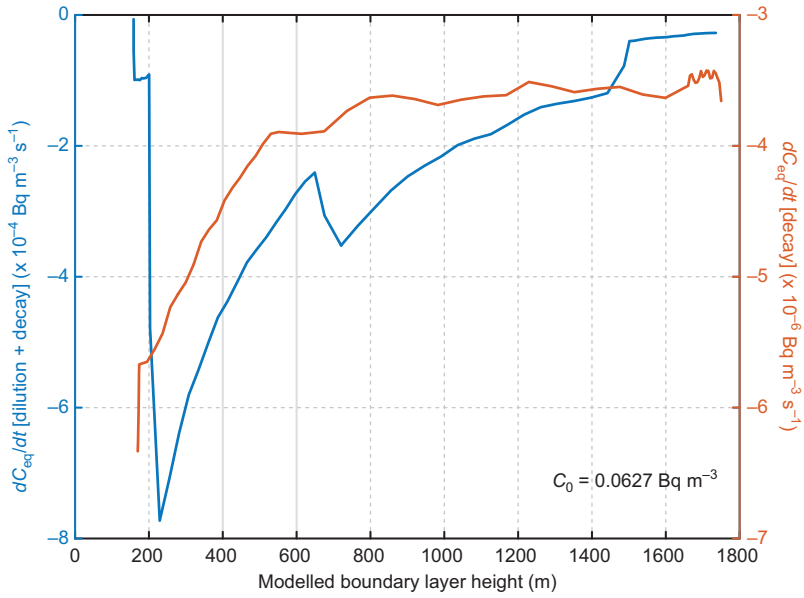

Fig. 10. The contribution of the dilution and decay terms in Eq. 8. The dilution term for the period of ML expansion was determined by assuming a constant radon concentration of 0.0627 Bq m^{-3} in the air above the ML. The change rate of atmospheric radon concentration during ML expansion is shown in blue on the left-hand-side axis and that during ML shrinkage in red on the right-hand-side axis. The analysis was carried out under the assumption of a homogeneous distribution of radon through the mixing layer.

balance equation. Accordingly, the atmospheric radon concentration above the ML, when assuming C_0 to be constant, should be smaller than 0.0627 Bq m^{-3}. The position and shape of the curves in Fig. 10 are insensitive to small variations in C_0.

The relatively-stable nocturnal boundary layer had a depth slightly below 200 m in summer (Fig. 5b). At around 04:30 in the morning, the ML started to expand and the atmospheric radon concentration reached its maximum (Fig. 5a). An increase in the ML height reduces the exhalation term in Eq. 8. In addition, the sum of the dilution and decay terms possessed negative values, even though this sum exhibited an exponential increase with an increase in the ML height (Fig. 10). Thus, in principle, the atmospheric radon concentration should drop simultaneously, which however, showed a delay by about 2 h. This observation could be related to the low turbulence in summer before 06:30 (Fig. 8): the solar radiation induced shear-driven turbulence in the top layer of the ML first and the gradual transport of this mixing to the measurement level retarded the instantaneous decrease in radon concentration. Using six years of data, Lapworth (2006) showed, that the downward transportation of turbulence is primarily responsible for warming up the surface layer. The surface heating enables the transition from shear-driven to convective mixing in the morning, but the warming of the surface layer comes mostly from the entrainment above due to the mechanical turbulence (Angevine 2001). The end of the morning transition occurs typically at the maximum extension rate of the ML depth, which is the onset of ML growth after the stable boundary layer is eroded (Pal *et al*. 2012, Pal *et al*. 2013), when the dilution effect on atmospheric radon concentration due to vertical mixing becomes pronounced. As for the shrinkage of the ML, the dilution term was zero, i.e. exhalation was the only source term in the mass balance equation. The turbulence was gradually discharged in the beginning of the ML thinning (Fig. 8) and such decay in turbulence is typically initialised in the top layer of the ML (Darbieu *et al*. 2014). Correspondingly, only a gentle increase in the median radon concentration was observed (Fig. 5a). When the turbulence diminished, the accumulation of radon became predominant near the ground surface and a clear recovery in the atmospheric radon concentration eventually emerged after 19:00 (Fig. 5a). Once such a relatively stable condition was encountered, especially in spring and summer, the accumulation of radon near the ground surface continued until turbulence was introduced again in the following morning.

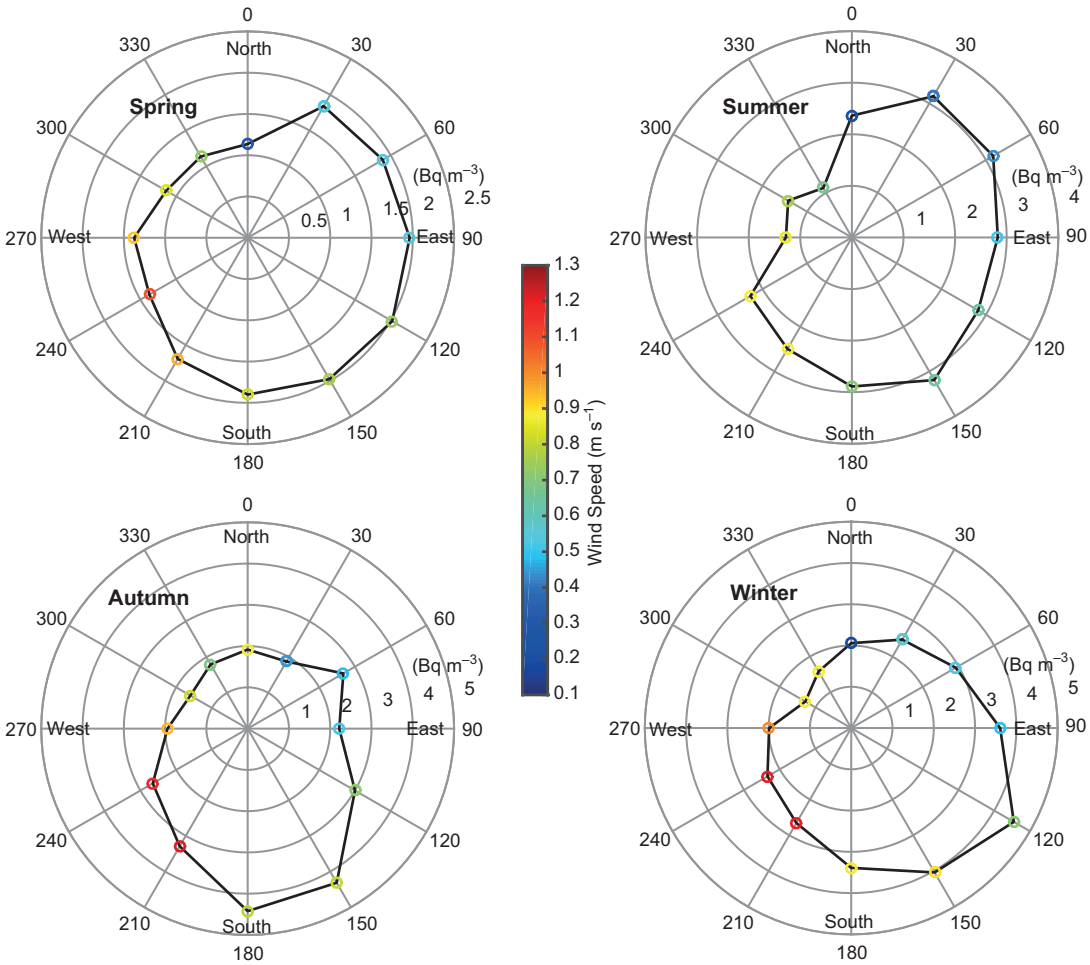

Fig. 11. Variations in the median atmospheric radon concentration, expressed as the distance form the origin, in relation to the wind direction and speed measured at the 8.4-m height in different seasons of the years 2003–2006. The median wind speed is shown on the colour scale. Radon concentration and wind speed data were processed as medians over 30° sectors of wind direction.

Apart from the convective transport of radon gas in the ML, the advective motion of air masses brings also variations in the atmospheric radon concentration. As ^{222}Rn has a half-life of 3.8 days, sources originating far away from the SMEAR II station may be detected at this site after a long journey guided by the movement of air masses in the atmosphere.

The lowest median radon concentrations at the SMEAR II station were typically observed when the wind blew from the northwest regardless of the wind speed. Such winds are expected to bring air masses of marine origins to the measurement site (Fig. 11). Because the role of the oceans as a radon source is negligible, these marine air masses, which originate typically from the Atlantic Ocean, carry only small amounts of radon, resulting in the observation of the lowest radon concentration. Relatively high median radon concentrations, especially in spring and summer, were observed with the lowest median wind speeds from the northeast. This phenomenon might be ascribed to situations, where under certain combinations of the locations of high and low pressure systems, air masses arriving at the SMEAR II station from the northeast actually originate from continental areas of eastern Europe or Russia rather than from marine regions. In the springtime, high median radon concentrations generally span over the wind directions of

30°–180°, with the maximum found with southeasterly winds associated with the continental air masses. Such a pattern existed in summer as well, however, with the maximum observed with both southeasterly and northeasterly winds. Although high median radon concentrations were also associated with southeasterly winds in autumn and winter seasons, in contrast to the warmer seasons, median radon concentrations remained at relatively low levels when the wind came from the northeast. The southwesterly winds were strongest in all seasons, but brought, on average, only moderate amounts of radon, possibly due to the mixing in of clean marine air masses from the Atlantic Ocean, because air masses coming to Finland from the west have more mid-latitude weather system activity than air masses coming from the east (Hoskins and Hodges 2002, Sinclair *et al*. 2012).

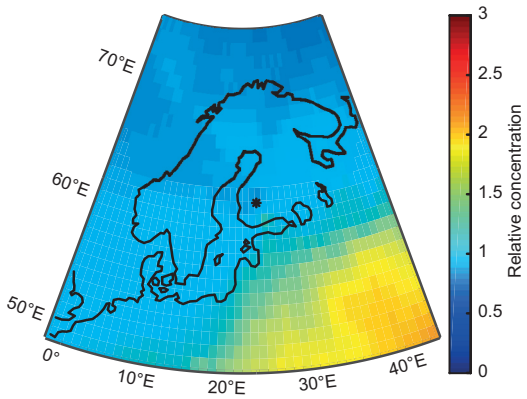

Fig. 12. Trajectory statistics of the relative atmospheric radon concentration (to the observed concentration at SMEAR II station) over 2000–2006. A radon concentration field was obtained by following Eq. 7, which was then normalised by the median concentration to generate the relative concentration field. The asterisk represents the SMEAR II station.

Trajectory analysis

The highest wind speed was measured between 12:00 and 15:00 (Fig. 8). In order to minimise the perturbation from local radon sources, radon data in this time window were used in the trajectory analysis. Overall, the relative concentration (*see* Fig. 12) suggested that the high radon relative concentration came substantially from the southeast. This observation aligns with the outcomes obtained from the exploration of the atmospheric radon concentration in relation to winds (Fig. 11) and also agrees with the results for ^{210}Pb, a daughter nuclide of ^{222}Rn, shown by Paatero and Hatakka (2000) based on samples collected at Sodankylä station (67°22´N, 26°39´E) in Finland. Riuttanen *et al*. (2013) showed that the potential source areas of aerosol particles located in the eastern Europe and Russia, which coincide with the hotspots depicted in Fig. 12 for radon, indicating the consistency in air mass transport. According to Wilkening and Clements (1975), the exhalation rate of ^{222}Rn over ocean is less than 2% of that over the continental areas. Oceanic air masses, therefore, share practically no contribution to the observed atmospheric radon concentration at the SMEAR II station whereas air masses passed over continental land take part in the transportation of radon gas originating from locations other than the measurement site. Consequently, in the annual trajectory statistics, hotspots of radon were observed over the continent in the southeast (Fig. 12). Besides, high relative concentration of radon was identified on the southern coast of Finland around Helsinki, coincident with the pattern shown by Szegvary *et al*. (2009) and the high concentration regions shown on the indoor radon map published by the Finnish Radiation and Nuclear Safety Authority (STUK 2014) and on the European indoor radon map (Tollefsen *et al*. 2014).

The transport pattern of radon, however, showed distinct seasonal features (Fig. 13). The continental air masses from the southeast brought especially large portion of radon to the SMEAR II station in spring and autumn, compared with the other two seasons. Sources of radon could be seen in northern Sweden all year round except in autumn. With the exception of winter, southern Sweden and Norway typically had slightly higher radon concentrations. An interesting spot was found for summer in southern Norway near the border with Sweden, which was probably due to the dilution by marine air masses over the surrounding regions. This region has been reported to have relatively high indoor radon concentrations (Tollefsen *et al*. 2014). The low concentration region over the continental Europe in the summer could also be attrib-

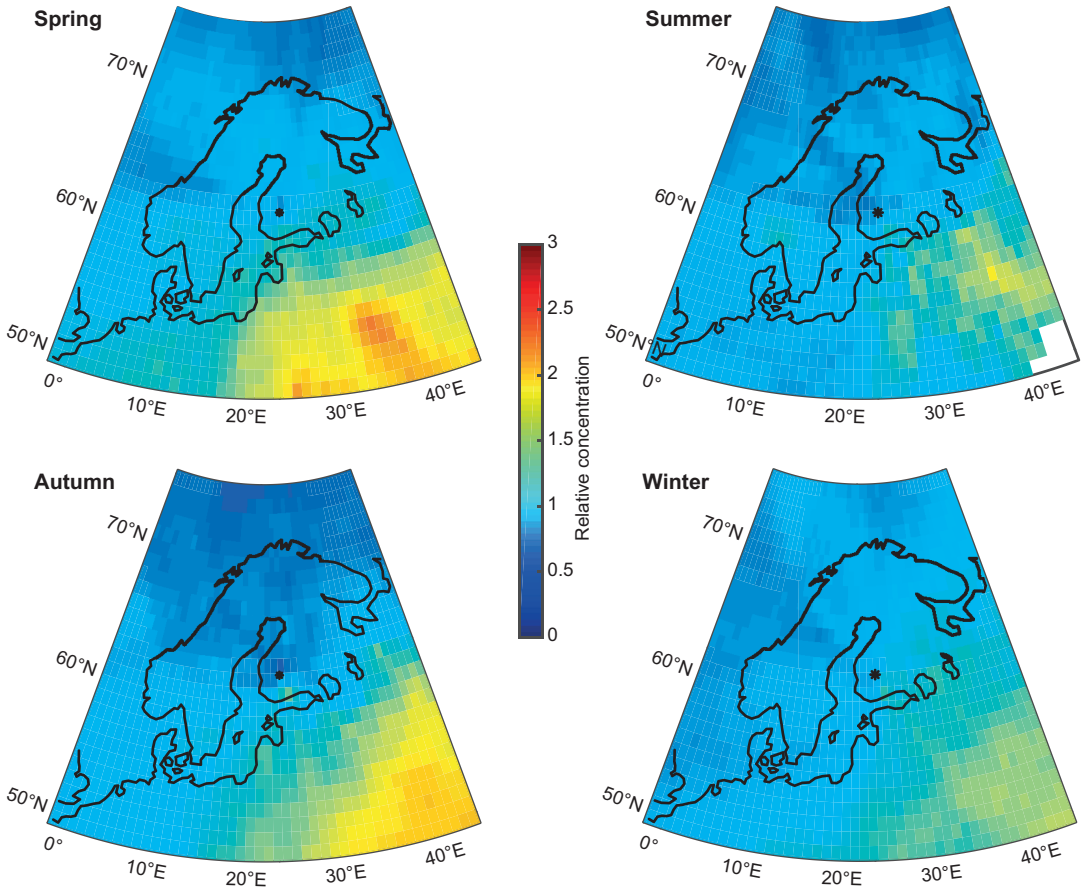

Fig. 13. Trajectory statistics of the relative atmospheric radon concentration (to the observed concentration at the SMEAR II station) in different seasons of 2000–2006. A radon concentration field was obtained by following Eq. 7, which was then normalised by the median concentration to generate the relative concentration field. The asterisk represents SMEAR II station.

uted to the mixing-in of clean air masses from the ocean and increased precipitation. The high radon concentration in winter was found mainly over the continental areas, though the long-range transport from North America may contribute to the observation of radon over the North Atlantic Ocean (Rummukainen *et al*. 1996, Paatero and Hatakka 2000).

Summary and conclusions

Long-term radon data collected during 2000–2006 at the SMEAR II station in a Finnish boreal forest were analysed along with meteorological data and trajectory information for the exploration of the variability of the atmospheric ^{222}Rn concentration in response to the vertical mixing and spatial transportation. No distinct inter-annual variation in the atmospheric radon concentration was found. The daily mean radon concentration followed a log-normal distribution ranging between < 0.1 and 11 Bq m^{-3}, with the geometric mean of 2.5 Bq m^{-3} and a geometric standard deviation of 1.7 Bq m^{-3}. A similar distribution also existed in the daily median concentrations. In general, the lowest atmospheric radon concentration was found in spring, most likely because of the joint effect of the enhanced vertical mixing and the reduced local emissions due to snow thawing. Clear diurnal variations in hourly median radon concentration were discernible from March to October, with a maximum at around 06:00 and a minimum at around 16:00.

In general, the median radon concentration was inversely related to the depth of the mixing layer (ML) height. However, a plateau was observed for the ML heights between 1500 and 2500 m, which coincided with an increased air temperature. This situation resulted from both the enhanced radon exhalation from soil due to the increasing temperature and the promoted dilution as the consequence of the thickening of the ML. During the winter months, the ^{222}Rn concentration was relatively high with very little diurnal variation. Radon was accumulated near the surface as a consequence of the absence of solar radiation and subsequently reduced vertical mixing of the air. Later in the spring the concentration level decreased, when the mixing was intensified as the amount of solar radiation increased. The minimum concentrations was observed in the late spring when daytime convective movements of the air diluted the radon content of the air to a bigger volume and the flux of radon from the ground to the atmosphere was at its seasonal minimum due to the high moisture content in the soil due to snow thawing. In the late summer, the diurnal variation of atmospheric radon concentration was at its maximum due to frequent nocturnal surface inversions and the simultaneous high radon flux from the ground to the atmosphere. The latter factor, in turn, is related to the low soil moisture content, especially in the surface layer.

The lowest radon concentration was related to clean marine air masses arriving at the SMEAR II station from the northwest, and high radon concentrations were typically found during southeasterly winds of continental origins. These observations were confirmed by the trajectory analysis. A reduction in the atmospheric radon concentration was observed in response to the intensification of wind speed. In addition, the downward transportation of turbulence from the top of the ML layer in the early morning led to a delayed response in the atmospheric radon concentration to the expansion of the ML. Similarly, the discharge of residual turbulence in the shrinking ML retarded the immediate recovery of the atmospheric radon concentration.

The features in the variability of the atmospheric radon concentration found here in relation to the development of the mixing volume and the spatial transportation are important characteristics of radon in the atmosphere. In general, the variation in atmospheric radon concentration can capture the vertical mixing height well. However, as shown in this paper, the changes in atmospheric radon concentration do not instantly follow the start of ML growth and shrinkage. This information is of paramount importance when determining the ML height or parameterising the PBL mixing processes from radon data. In addition, our results imply that radon is a suitable candidate for studying the evolution of the turbulence during morning and evening transitions in the boundary mixing processes. Nevertheless, it is also crucial to take into account the effect of the horizontal transportation on the atmospheric radon concentration. Wind either potentially carries more radon to the site or dilutes locally-emitted atmospheric radon. Such information can be typically obtained by studying the trajectories of air masses arriving at the measurement site, without which biases may be introduced when comparing similar vertical mixing processes of different days by using radon. Moreover, as an inert and long-lived gas, radon is useful in evaluating transport models, which can be applied to other trace components or pollutants in the atmosphere. Yet, to improve the accuracy of the transport pattern, it is important to be cautious about the variations in atmospheric radon concentration introduced by the boundary layer dynamics along the air-mass trajectories.

Acknowledgements: This study was supported by the Academy of Finland Centre of Excellence (projects 272041 and 1118615). The authors acknowledge the funding provided by the CRAICC (Cryosphere–atmosphere interactions in a changing Arctic climate) project within the Nordforsk Top-level Research Initiative Programme 'Interaction between climate change and the cryosphere. This study also received funding from the European Union's Horizon 2020 Research and Innovation Programme (grant no. 654109) as well as the European Union Seventh Framework Programme (FP7/2007-2013) (grant no. 262254). Valuable communications and suggestions from Dr. Aki Virkkula were thankfully appreciated.

References

Angevine W.M. 2001. Observations of the morning transition

of the convective boundary layer. *Bound.-Layer Meteor.* 101: 209–227.

Ashok G.V., Nagaiah N., Shiva Prasad N.G. & Ambika M.R. 2011. Study of radon exhalation rate from soil, Bangalore, south India. *Radiat. Protect. Environ.* 34: 235–239.

Barlow J.F., Dunbar T.M., Nemitz E.G., Wood C.R., Gallagher M.W., Davies F., O'Connor E. & Harrison R.M. 2011. Boundary layer dynamics over London, UK, as observed using Doppler lidar during REPARTEE-II. *Atmos. Chem. Phys.* 11: 2111–2125.

Bateman H. 1910. Ther solution of a system of differential equations occurring in the theory of radio-active transformations. *Proceedings of the Cambridge Philosophical Society, Mathematical and Physical Sciences* 15: 423.

Baumann K. & Stohl A. 1997. Validation of a long-range trajectory model using gas balloon tracks from the Gordon Bennett Cup 95. *J. Appl. Meteorol.* 36: 711–720.

Behrendt A., Pal S., Wulfmeyer V., Valdebenito B.Á.M. & Lammel G. 2011. A novel approach for the characterization of transport and optical properties of aerosol particles near sources — Part I: Measurement of particle backscatter coefficient maps with a scanning UV lidar. *Atmos. Environ.* 45: 2795–2802.

Beyrich F. 1997. Mixing height estimation from sodar data — a critical discussion. *Atmos. Environ.* 31: 3941–3953.

Chambers S., Williams A.G., Zahorowski W., Griffiths A. & Crawford J. 2011. Separating remote fetch and local mixing influences on vertical radon measurements in the lower atmosphere. *Tellus* 63B: 843–859.

Clements W.E. & Wilkening M.H. 1974. Atmospheric pressure effects on ^{222}Rn transport across the earth–air interface. *J. Geophys. Res.* 79: 5025–5029.

Darbieu C., Lohou F., Lothon M., Vilà-Guerau de Arellano J., Couvreux F., Durand P., Pino D., G. Patton E., Nilsson E., Blay-Carreras E. & Gioli B. 2014. Turbulence vertical structure of the boundary layer during the afternoon transition. *Atmos. Chem. Phys. Discuss.* 14: 32491–32533.

ECMWF 2001. *Newsletter No. 90.* Shinfield Park, Reading, UK.

Escobar V.G., Tomé F.V. & Lozano J.C. 1999. Procedures for the determination of ^{222}Rn exhalation and effective ^{226}Ra activity in soil samples. *Appl. Radiat. Isot.* 50: 1039–1047.

Forster C., Stohl A. & Seibert P. 2007. Parameterization of convective transport in a lagrangian particle dispersion model and its evaluation. *J. Appl. Meteor. Climatol.* 46: 403–422.

Galeriu D., Melintescu A., Stochioiu A., Nicolae D. & Balin I. 2011. Radon, as a tracer for mixing height dynamics — an overview and rado perspectives. *Rom. Rep. Phys.* 63: 115–127.

Griffiths A.D., Parkes S.D., Chambers S.D., McCabe M.F. & Williams A.G. 2013. Improved mixing height monitoring through a combination of lidar and radon measurements. *Atmos. Meas. Tech.* 6: 207–218.

Grossi C., Arnold D., Adame J.A., López-Coto I., Bolívar J.P., de la Morena B.A. & Vargas A. 2012. Atmospheric ^{222}Rn concentration and source term at El Arenosillo 100 m meteorological tower in southwest Spain. *Radiat. Meas.* 47: 149–162.

Guedalia D., Ntsila A., Druilhet A. & Fontan J. 1980. Monitoring of the atmospheric stability above an urban and suburban site using sodar and radon measurements. *J. Appl. Meteorol.* 19: 839–848.

Hari P. & Kulmala M. 2005. Station for measuring ecosystem-atmosphere relations (SMEAR II). *Boreal Env. Res.* 10: 315–322.

Hoskins B.J. & Hodges K.I. 2002. New perspectives on the northern hemisphere winter storm tracks. *J. Atmos. Sci.* 59: 1041–1061.

Jacobi W. & André K. 1963. The vertical distribution of radon 222, radon 220 and their decay products in the atmosphere. *J. Geophys. Res.* 68: 3799–3814.

Jocab D.J. & Prather M.J. 1990. Radon-222 as a test of convective transport in a general circulation model. *Tellus* 42B: 118–134.

Korhonen K., Giannakaki E., Mielonen T., Pfüller A., Laakso L., Vakkari V., Baars H., Engelmann R., Beukes J.P., Van Zyl P.G., Ramandh A., Ntsangwane L., Josipovic M., Tiitta P., Fourie G., Ngwana I., Chiloane K. & Komppula M. 2014. Atmospheric boundary layer top height in South Africa: measurements with lidar and radiosonde compared to three atmospheric models. *Atmos. Chem. Phys.* 14: 4263–4278.

Kouznetsov R., Wood C., Sofiev M., Soares J., Karppinen A. & Fortelius C. 2012. Sodar verification of boundary-layer height schemes for the output of meteorological models. In: *16th International Symposium for the Advancement of Boundary-Layer Remote Sensing, 5–8 June 2012, Boulder, Colorado*, Steering Committee of the 16th International Symposium for the Advancement of Boundary-Layer Remote Sensing, pp. 138–141. [Also available at http://www.esrl.noaa.gov/psd/events/2012/isars/pdf/isars2012-abstractVolume.pdf].

Kritz M.A. 1983. Use of long-lived radon daughters as indicators of exchange between the free troposphere and the marine boundary layer. *J. Geophys. Res.* 88: 8569–8573.

Lac C., Donnelly R.P., Masson V., Pal S., Riette S., Donier S., Queguiner S., Tanguy G., Ammoura L. & Xueref-Remy I. 2013. CO_2 dispersion modelling over Paris region within the CO_2-MEGAPARIS project. *Atmos. Chem. Phys.* 13: 4941–4961.

Lapworth A. 2006. The morning transition of the nocturnal boundary layer. *Bound.-Layer Meteor.* 119: 501–526.

Lee T.R., De Wekker S.F.J., Pal S., Andrews A.E. & Kofler J. 2015. Meteorological controls on the diurnal variability of carbon monoxide mixing ratio at a mountaintop monitoring site in the Appalachian Mountains. *Tellus* 67B, 25659, doi:10.3402/tellusb.v67.25659.

Leventidou E., Zanis P., Balis D., Giannakaki E., Pytharoulis I. & Amiridis V. 2013. Factors affecting the comparisons of planetary boundary layer height retrievals from CALIPSO, ECMWF and radiosondes over Thessaloniki, Greece. *Atmos. Environ.* 74: 360–366.

Lewis C., Hopke P.K. & Stukelt J.J. 1987. Solubility of radon in selected perfluorocarbon compounds and water *Ind. Eng. Chem. Res.* 26: 356–359.

Markkanen M. & Arvela H. 1992. Radon emanation from soils. *Radiat. Prot. Dosim.* 45: 269–272.

Mattsson R. 1970. Seasonal variations of short-lived radon

progeny, ^{210}Pb and ^{210}Po in ground level air in Finland. *J. Geophys. Res.* 75: 1741–1744.

Mattsson R. 1984. *Observations of radioactivity 1982*. Finnish Meteorological Institue, Helsinki.

McGrath-Spangler E.L. & Denning A.S. 2013. Global seasonal variations of midday planetary boundary layer depth from CALIPSO space-borne LIDAR. *J. Geophys. Res. Atmos.* 118: 1226–1233.

Nazaroff W.W. 1992. Radon transport from soil to air. *Rev. Geophys.* 30: 137–160.

Paatero J. & Hatakka J. 2000. Source areas of airborne ^{7}Be and ^{210}Pb measured in northern Finland. *Health Phys.* 79: 691–696.

Paatero J., Hatakka J., Mattsson R. & Lehtinen I. 1994. A comprehensive station for monitoring atmospheric radioactivity. *Radiat. Prot. Dosim.* 54: 33–39.

Pal S. 2014. Monitoring depth of shallow atmospheric boundary layer to complement LiDAR measurements affected by partial overlap. *Remote Sens.* 6: 8468–8493.

Pal S. & Devara P.C.S. 2012. A wavelet-based spectral analysis of long-term time series of optical properties of aerosols obtained by lidar and radiometer measurements over an urban station in western India. *J. Atmos. Sol.-Terr. Phy.* 84–85: 75–87.

Pal S., Haeffelin M. & Batchvarova E. 2013. Exploring a geophysical process-based attribution technique for the determination of the atmospheric boundary layer depth using aerosol lidar and near-surface meteorological measurements. *J. Geophys. Res. Atmos.* 118: 9277–9295.

Pal S., Lee T.R., Phelps S. & De Wekker S.F. 2014. Impact of atmospheric boundary layer depth variability and wind reversal on the diurnal variability of aerosol concentration at a valley site. *Sci. Total. Environ.* 496: 424–434.

Pal S., Lopez M., Schmidt M., Ramonet M., Gibert F., Xueref-Remy I. & Ciais P. 2015. Investigation of the atmospheric boundary layer depth variability and its impact on the ^{222}Rn concentration at a rural site in France. *J. Geophys. Res. Atmos.* 120: 623–643.

Pal S., Xueref-Remy I., Ammoura L., Chazette P., Gibert F., Royer P., Dieudonné E., Dupont J.C., Haeffelin M., Lac C., Lopez M., Morille Y. & Ravetta F. 2012. Spatio-temporal variability of the atmospheric boundary layer depth over the Paris agglomeration: an assessment of the impact of the urban heat island intensity. *Atmos. Environ.* 63: 261–275.

Porstendörfer J. 1994. Properties and behaviour of radon and thoron and their decay products in the air. *J. Aerosol Sci.* 25: 219–263.

Riuttanen L., Hulkkonen M., Dal Maso M., Junninen H. & Kulmala M. 2013. Trajectory analysis of atmospheric transport of fine particles, SO_2, NO_x and O_3 to the SMEAR II station in Finland in 1996–2008. *Atmos. Chem. Phys.* 13: 2153–2164.

Rummukainen M., Laurila T. & Kivi R. 1996. Yearly cycle of lower tropospheric ozone at the arctic circle. *Atmos. Environ.* 30: 1875–1885.

Schery S.D. 1989. The flux of radon and thoron from Australian soils. *J. Geophys. Res.* 94: 8567–8576.

Schween J.H., Hirsikko A., Löhnert U. & Crewell S. 2014. Mixing-layer height retrieval with ceilometer and Doppler lidar: from case studies to long-term assessment. *Atmos. Meas. Tech.* 7: 3685–3704.

Seibert P., Beyrich F., Gryning S.-E., Joffre S., Rasmussen A. & Tercier P. 1999. Review and intercomparison of operational methods for the determination of the mixing height. *Atmos. Environ.* 34: 1001–1027.

Seidel D.J., Ao C.O. & Li K. 2010. Estimating climatological planetary boundary layer heights from radiosonde observations: comparison of methods and uncertainty analysis. *J. Geophys. Res.* 115: D16113, doi:10.1029/2009JD013680.

Seidel D.J., Zhang Y., Beljaars A., Golaz J.-C., Jacobson A.R. & Medeiros B. 2012. Climatology of the planetary boundary layer over the continental United States and Europe. *J. Geophys. Res. Atmos.* 117, D17106, doi:10.1029/2012JD018143.

Seinfeld J.H. & Pandis S.N. 2006. *Atmospheric chemistry and physics from air pollution to climate change*, 2nd ed. John Wiley & Sons, Inc., Hoboken, NJ.

Sesana L., Caprioli E. & Marcazzan G.M. 2003. Long period study of outdoor radon concentration in Milan and correlation between its temporal variations and dispersion properties of atmosphere. *J. Environ. Radioact.* 65: 147–160.

Sinclair V.A., Niemelä S. & Leskinen M. 2012. Structure of a narrow cold front in the boundary layer: observations versus model simulation. *Mon. Weather Rev.* 140: 2497–2519.

Stohl A. & Seibert P. 1998. Accuracy of trajectories as determined from the conservation of meteorological tracers. *Q. J. R. Meteorol. Soc.* 124: 1465–1484.

Stohl A., Wotawa G., Seibert P. & Kromp-Kolb H. 1995. Interpolation errors in wind fields as a function of spatial and temporal resolution and their impact on different types of kinematic trajectories. *J. Appl. Meteorol.* 34: 2149–2165.

Stranden E., Kolstad A.K. & Lind B. 1984. The influence of moisture and temperature on radon exhalation. *Radiat. Prot. Dosim.* 7: 55–58.

STUK 2014. *Surveillance of environmental radiation in Finland. Annual report 2013*. STUK, Helsinki.

Stull R.B. 1998. *An introduction to boundary layer meteorology*. Kluwer Academic Publishers, Dordrecht, Boston, London.

Szegvary T., Conen F. & Ciais P. 2009. European ^{222}Rn inventory for applied atmospheric studies. *Atmos. Environ.* 43: 1536–1539.

Tollefsen T., Cinelli G., Bossew P., Gruber V. & De Cort M. 2014. From the European indoor radon map towards an atlas of natural radiation. *Radiat. Prot. Dosim.* 162: 129–134.

Vakkari V., O'Connor E.J., Nisantzi A., Mamouri R.E. & Hadjimitsis D.G. 2015. Low-level mixing height detection in coastal locations with a scanning Doppler lidar. *Atmos. Meas. Tech.* 8: 1875–1885.

Wilkening M.H. & Clements W.E. 1975. Radon 222 from the ocean surface. *J. Geophys. Res.* 80: 3828–3830.

Williams A.G., Zahorowski W., Chambers S., Griffiths A., Hacker J.M., Element A. & Werczynski S. 2011. The

vertical distribution of radon in clear and cloudy daytime terrestrial boundary layers. *J. Atmos. Sci.* 68: 155–174.

Zahorowski W., Chambers S.D. & Henderson-Sellers A. 2004. Ground based radon-222 observations and their application to atmospheric studies. *J. Environ. Radioact.* 76: 3–33.

Zhang K., Wan H., Zhang M. & Wang B. 2008. Evaluation of the atmospheric transport in a GCM using radon measurements: sensitivity to cumulus convection parameterization. *Atmos. Chem. Phys.* 8: 2811–2832.

Paper III

Atmos. Chem. Phys., 17, 13783–13800, 2017
https://doi.org/10.5194/acp-17-13783-2017

Atmospheric Chemistry and Physics
Open Access
EGU

Features in air ions measured by an air ion spectrometer (AIS) at Dome C

Xuemeng Chen[1], Aki Virkkula[1,2], Veli-Matti Kerminen[1], Hanna E. Manninen[1,3], Maurizio Busetto[4], Christian Lanconelli[4], Angelo Lupi[4], Vito Vitale[4], Massimo Del Guasta[5], Paolo Grigioni[6], Riikka Väänänen[1], Ella-Maria Duplissy[1], Tuukka Petäjä[1], and Markku Kulmala[1]

[1]Department of Physics, University of Helsinki, P.O. Box 64, 00014 Helsinki, Finland
[2]Finnish Meteorological Institute, Air Quality Research, P.O. Box 503, 00101 Helsinki, Finland
[3]CERN, 1211 Geneva, Switzerland
[4]Institute of Atmospheric Sciences and Climate, Italian National Research Council, 40129 Bologna, Italy
[5]Istituto Nazionale di Ottica, INO-CNR, 50019 Sesto Fiorentino (FI), Italy
[6]ENEA Laboratory for Observations and Analyses of Earth and Climate, C.R. Casaccia, 00123 S. Maria di Galeria (RM), Italy

Correspondence to: Xuemeng Chen (xuemeng.chen@helsinki.fi)

Received: 4 April 2017 – Discussion started: 20 April 2017
Revised: 25 September 2017 – Accepted: 4 October 2017 – Published: 20 November 2017

Abstract. An air ion spectrometer (AIS) was deployed for the first time at the Concordia station at Dome C (75°06′ S, 123°23′ E; 3220 m a.s.l.), Antarctica during the period 22 December 2010–16 November 2011 for measuring the number size distribution of air ions. In this work, we present results obtained from this air ion data set together with aerosol particle and meteorological data. The main processes that modify the number size distribution of air ions during the measurement period at this high-altitude site included new particle formation (NPF, observed on 85 days), wind-induced ion formation (observed on 36 days), and ion production and loss associated with cloud/fog formation (observed on 2 days). For the subset of days when none of these processes seemed to operate, the concentrations of cluster ions (0.9–1.9 nm) exhibited a clear seasonality, with high concentrations in the warm months and low concentrations in the cold. Compared to event-free days, days with NPF were observed with higher cluster ion concentrations. A number of NPF events were observed with restricted growth below 10 nm, which were termed as suppressed NPF. There was another distinct feature, namely a simultaneous presence of two or three separate NPF and subsequent growth events, which were named as multi-mode NPF events. Growth rates (GRs) were determined using two methods: the appearance time method and the mode fitting method. The former method seemed to have advantages in characterizing NPF events with a fast GR, whereas the latter method is more suitable when the GR was slow. The formation rate of 2 nm positive ions (J_2^+) was calculated for all the NPF events for which a GR in the 2–3 nm size range could be determined. On average, J_2^+ was about 0.014 cm^{-3} s^{-1}. The ion production in relation to cloud/fog formation in the size range of 8–42 nm seemed to be a unique feature at Dome C, which has not been reported elsewhere. These ions may, however, either be multiply charged particles but detected as singly charged in the AIS, or be produced inside the instrument, due to the breakage of cloud condensation nuclei (CCN), possibly related to the instrumental behaviour under the extremely cold condition. For the wind-induced ion formation, our observations suggest that the ions originated more likely from atmospheric nucleation of vapours released from the snow than from mechanical charging of shattered snow flakes and ice crystals.

1 Introduction

Air ions, also known as atmospheric ions, are electric charge carriers in the atmosphere, ranging from primary ions (most have a mobility diameter smaller than 0.8–1 nm) to charged aerosol particles (with a mobility diameter up to several hun-

dred nanometres) (e.g. Harrison and Tammet, 2008; Hirsikko et al., 2011; Chen et al., 2016). Scientific interest in air ions has persisted for over a century. Air ions have a primary role in the discipline of atmospheric electricity, because their motion in the atmosphere is integral to the air conductivity (Wilson, 1924; Israël, 1970; Tinsley, 2008). Air ions have also raised the interest of aerosol scientists because of their participation in atmospheric aerosol formation and thus they have influence on air quality, human health, and climate (Gunn, 1954; Bricard et al., 1968; Hõrrak et al., 1998; Yu and Turco, 2008; Manninen et al., 2010; Waring and Siegel, 2011).

Upon the ionization of air molecules by ionizing radiation, electric charges are created. After undergoing a series of chemical and dynamic processes with trace gases and preexisting aerosol particles, electric charges that survive the initial recombination and other loss mechanisms are stabilized in the form of charged aerosol particles (Chen et al., 2016). Charged nanoparticles in the mobility size range of 1.7–7 nm are typically observed during new particle formation (NPF) events (Manninen et al., 2009; Hirsikko et al., 2011; Leino et al., 2016). NPF is an important source of atmospheric aerosol particles (Kulmala et al., 2004; Poschl, 2005) and, under favourable conditions, of cloud condensation nuclei (CCN; Kerminen et al., 2012; Dunne et al., 2016). In this way, aerosol particles originating from NPF have a potential to influence many cloud properties and thus climate (Boucher et al., 2013; Dunne et al., 2016).

Carslaw et al. (2013) suggested that aerosol-related uncertainties in global models could be best reduced through the study of natural aerosols in environments with negligible anthropogenic influence. Antarctica is such an environment. Long-term time series of particle number concentrations have been published both from the coastal Antarctica, including the Neumayer station (Weller et al., 2011), and from the upper plateau including the South Pole (e.g. Samson et al., 1990). Number size distributions of aerosol particles have been measured during short-term campaigns, mainly at coastal stations (e.g. Ito, 1993; Koponen et al., 2003; Virkkula et al., 2007; Asmi et al., 2010; Pant et al., 2011; Belosi et al., 2012; Kyrö et al., 2013; Weller et al., 2015), but also on the upper plateau at the South Pole (e.g. Park et al., 2004). Hara et al. (2011) presented particle number size distributions measured on the coast of Queen Maud Land at the Japanese station Syowa in the period 2003–2005. At the Norwegian Troll station in the inner region of Queen Maud Land, particle number size distributions in the size range 30–800 nm have been measured over several years (Fiebig et al., 2014). Järvinen et al. (2013) presented a 2-year record of particle number size distributions in the size range of 10–600 nm measured at the Italian–French Concordia station at Dome C on the upper Antarctic Plateau, and observed clear signs of atmospheric NPF. However, since their measurement size range started at 10 nm particle diameter, there was no information on the initial step of the NPF, which is expected to take place at diameters below 2 nm (Kulmala et al., 2013). In particular, the question of the role of air ions in NPF remained open. Air ion number size distributions in the size range from < 1 nm up to about 40 nm have been measured at Aboa in the coastal Antarctica during several summer campaigns (Virkkula et al., 2007; Asmi et al., 2010; Kyrö et al., 2013), but not on the upper plateau. The high altitude of Dome C means that the Concordia station is more exposed to cosmic radiation than the coastal sites in Antarctica. Also, stronger cosmic ray ionization can be expected at polar regions than at mid-latitudes (Kazil et al., 2006; Bazilevskaya et al., 2008). However, the inland location of Dome C represents a pristine environment with very limited source of vapours essential for clustering and subsequent nanoparticle formation. Therefore, it is worthwhile to investigate the synergic impact of high cosmic-ray ionization and low precursor vapours on the properties of air ions at this Antarctic site.

In this work, we present a first set of results on air ion observation at Dome C. Our aims are to characterize the key features of air ions at this Antarctic site, including the seasonality of their concentrations, and to analyse the variability of air ions in relation to NPF. Previously, particle growth during NPF processes has been studied in terms of growth rates (GRs) using two methods: the appearance time method (Lehtipalo et al., 2014) and the mode-fitting method (Dal Maso et al., 2005). Here we compare GRs determined using these two methods.

2 Methods

The analyses in this work were based on ambient data collected from the Concordia station (75°06′ S, 123°23′ E) at Dome C in Antarctica during 22 December 2010–16 November 2011. The station is located on the Antarctic Plateau at an altitude of 3220 m a.s.l. and a minimum distance of 1100 km from the coastline (Becagli et al., 2012). Measurements were taken at the same sampling site used by Järvinen et al. (2013) and Becagli et al. (2012), located upwind in the direction of the prevailing wind at a distance of about 1 km southwest of the main station buildings. The northeastern direction is therefore considered as the contaminated sector (10–90°), due to local emissions from diesel generators and motor vehicles. All the data are presented in UTC.

2.1 Air ion and total aerosol particle measurements

2.1.1 Air ion measurement

The number size distribution of air ions was measured with an air ion spectrometer (AIS) during the campaign period. The AIS employs two cylindrical multi-channel aspiration-type analysers and a high sample flowrate (60 L min^{-1}). Such design enables it to measure negative and positive ions simultaneously down to sizes of below 1 nm (Mirme et al., 2007).

The air sampled in the AIS is split into two equal streams. On the way to the analyser, each stream passes through

a sample preconditioner, i.e. a corona charger coupled with an electrical filter. Sample preconditioners are turned on only during the measurement of background signals, where corona chargers produce charger ions of an opposite polarity to the subsequent analysers, so that clusters and particles in each sample stream are either neutralized or assigned an opposite polarity to the analyser and therefore generate no signal in the detection system. During the campaign, each AIS measurement cycle was composed of 1 min background probing and 4 min ambient sampling. Preconditioners are turned off for ambient sampling. Sample streams pass directly into the respective analysers, where air ions are segregated based on their electrical mobility into different channels. The analyser used in the AIS is a variant of the differential mobility analyser (DMA). Unlike common cylindrical DMA, in which ions are collected at the inner electrode and, via altering the voltage applied on the electrodes, ions of different mobility are measured (Hinds, 1999), the outer electrode in the AIS analyser serves the collecting role and ions of different mobility are collected simultaneously by different channels. The operation of the AIS analyser is based on electrical repulsion. The sample flow is introduced near the inner electrode and sheath flow near the outer one. The outer electrode of the AIS analyser is divided into 21 insulated sections, each of which is connected to an electrometer as the detector. Coupling the outer electrode design with a specially shaped inner electrode, which comprises several cylindrical sections biased at different potentials, the analyser is able to perform a concurrent classification of ions into the 21 measuring channels. More detailed technical descriptions of the instrument are presented by Mirme et al. (2007) and Mirme and Mirme (2013).

The AIS assumes the normal temperature and pressure (NTP) condition and has a total sample flowrate of $60\,\mathrm{L\,min^{-1}}$ and a sheath flowrate of $60\,\mathrm{L\,min^{-1}}$ in each analyser at NTP. A single blower controls the whole flow system. Although sample, sheath and total exhaust flowrates are monitored by Venturi flowmeters to balance the flow system in the AIS, only the total exhaust flowrate, equivalent to the total sample flowrate, is recorded. Owing to the distinct ambient condition at Dome C in relation to NTP, a flow correction was applied to the recorded data to retrieve the actual number concentration of ions. In a Venturi system, the volumetric flowrate (Q) is expressed as

$$Q = C\sqrt{\frac{2\Delta P}{\rho}}\frac{A_a}{\sqrt{\left(\frac{A_a}{A_b}\right)^2 - 1}}, \tag{1}$$

where C is the discharge coefficient which takes into account the viscosity of fluids, ΔP is the pressure difference across the Venturi tube, ρ is the density of the fluid, and A_a and A_b are the cross sections of the Venturi tube at the two locations between which the pressure difference is determined. In the case of air, the density can be derived from the ideal gas law

$$\rho = \frac{PM}{RT}, \tag{2}$$

where P is pressure in pascal, T is temperature in kelvin, R is the gas constant, and M is the molar mass of air. Since the AIS measurement is based on the NTP assumption, the corrected sample flowrate ($Q_{\mathrm{s,\,cor}}$) can be obtained by adding an additional multiplier, $\sqrt{\frac{T_{\mathrm{atm}}}{P_{\mathrm{atm}}}\frac{P_{\mathrm{NTP}}}{T_{\mathrm{NTP}}}}$, to Eq. (1) as follows:

$$Q_{\mathrm{s,\,cor}} = C\sqrt{2\Delta P}\sqrt{\frac{RT_{\mathrm{NTP}}}{P_{\mathrm{NTP}}M}}\frac{A_a}{\sqrt{\left(\frac{A_a}{A_b}\right)^2 - 1}}\sqrt{\frac{T_{\mathrm{atm}}}{P_{\mathrm{atm}}}\frac{P_{\mathrm{NTP}}}{T_{\mathrm{NTP}}}}, \tag{3}$$

where P_{NTP} and T_{NTP} are pressure and temperature at the NTP condition, and P_{atm} and T_{atm} are at ambient atmospheric conditions. Equation (3) can be simplified to the following form:

$$Q_{\mathrm{s,\,cor}} = Q_{\mathrm{s,\,meas}}\sqrt{\frac{T}{P}\frac{P_{\mathrm{NTP}}}{T_{\mathrm{NTP}}}}, \tag{4}$$

where $Q_{\mathrm{s,\,meas}}$ denotes the recorded sample flowrate by the AIS. Then, the number concentration of ions measured in each mobility range (N_i) is corrected by

$$N_{i,\mathrm{cor}} = N_{i,\mathrm{meas}} \cdot \frac{Q_{\mathrm{s,\,meas}}}{Q_{\mathrm{s,\,cor}}}. \tag{5}$$

In addition to the number concentration, the flowrates in the AIS influence the upper and lower limits of mobility ranges (Mirme et al., 2010; Mirme and Mirme, 2013). The lower and upper limiting mobility are proportional to the sheath flowrate (Q_{sh}) and the sum of sample and sheath flowrates, respectively. Therefore, the corrected lower and upper limiting mobility can be expressed as

$$Z_{i,\mathrm{L,cor}} = Z_{i,\mathrm{L,meas}} \cdot \frac{Q_{\mathrm{sh,\,cor}}}{Q_{\mathrm{sh,\,meas}}} \quad \text{and}$$
$$Z_{i,\mathrm{U,cor}} = Z_{i,\mathrm{U,meas}} \cdot \frac{Q_{\mathrm{sh,\,cor}} + Q_{\mathrm{s,\,cor}}}{Q_{\mathrm{sh,\,meas}} + Q_{\mathrm{s,\,meas}}}, \tag{6}$$

where $Z_{i,\mathrm{L}}$ and $Z_{i,\mathrm{U}}$ represent lower and upper limiting mobility in the mobility range, i.

In this work, to be comparable with particle data, air ion data are presented in Millikan mobility diameters. The conversion of electrical mobility to sizes is based on the Stokes–Millikan equation (e.g. Hinds, 1999), using measured ambient temperature and pressure. After the flow correction, the AIS has a measurable mobility size range of 0.9–48 nm. The deployed AIS had a separate 30 cm long inlet that extended outside the measurement cabin. The inlet tube had an inner diameter of 16 mm. However, since we had no measurement of the temperature profile of the inlet, a correction for the inlet diffusional loss is not feasible. Therefore, we report the

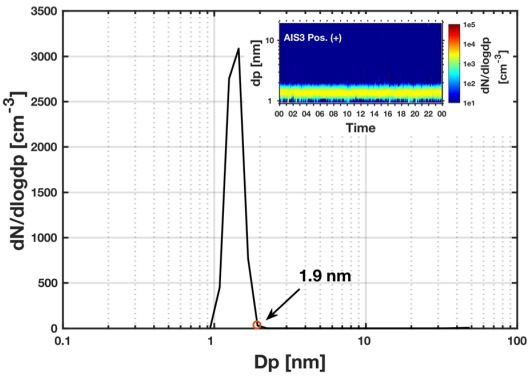

Figure 1. The median size distribution of positive ions measured by the AIS on an event-free day (16 January 2011). The measured number size distribution of this day is shown in the contour plot.

number size distribution data of air ions without the inlet diffusional loss correction.

The primary feature of an ambient AIS spectrum contains a persistent band of high ion concentrations at lowest sizes (Fig. 1), which is typically known as the cluster ion band. The upper boundary of this band typically lies at around 1.7 nm in the mobility diameter ($\sim$ 1.3 nm in the mass diameter; Mirme et al., 2007) under mid-latitude ambient conditions, representing critical cluster sizes (Kulmala et al., 2013; Chen et al., 2016). After applying the flow and ambient condition correction to the AIS data, the cluster ion size range at Dome C was found to be between 0.9 and 1.9 nm in the positive polarity (Fig. 1). However, the upper boundary of the cluster size range in the recorded negative AIS spectra was shifted down to around 1 nm (Fig. S1 in the Supplement), likely caused by the establishment of an ill-shaped electric field inside the analyser due to the malfunctioning of grounding or insulation. Such an anomaly is indicative of a low reliability of the negative ion data. Thus, only positive ion data from the AIS measurement are reported in this work.

2.1.2 Total aerosol particle measurement

A differential mobility particle sizer (DMPS), the same used by Järvinen et al. (2013), was responsible for recording the number size information of total aerosol particles. The DMPS classifies particles of mobility sizes between 9 and 550 nm. It consists mainly of a medium-size Hauke-type DMA for classifying particles and a TSI 3010 condensation particle counter (CPC) for detection. Prior to the classifying and detecting sections, the sampled air passes through a bipolar radioactive charger (Ni-63), where aerosol particles in the sample attain a Boltzmann equilibrium charge distribution. These aerosol particles then enter the DMA. Particles of different electrical mobility are selected from the sample by changing the high voltage applied on the DMA inner electrode step-wisely. The mobility-segregated particles are subsequently grown by vapour condensation and detected optically in the CPC. Each measurement cycle takes 10 min. The number size distribution of the measured aerosol particles was derived from the recorded mobility distribution via an inversion procedure described in detail by Aalto et al. (2001). The sizes of aerosol particles are presented in Millikan mobility diameters. Hereafter, unless otherwise specified, the particle and ion sizes refer to their Millikan mobility diameters.

2.2 Meteorological and lidar data

The ambient air temperature (T), relative humidity (RH), wind speed (WS), and wind direction (WD) data were from the routine meteorological observation records at Station Concordia as part of the IPEV/PNRA Project – a collaborative project between "Programma Nazionale di Ricerche in Antartide" (PNRA) and Institut Polaire Français Paul–Emile Victor (IPEV) (www.climantartide.it).

An automatic depolarization lidar (532 nm) has operated at Dome C since 2008 (http://lidarmax.altervista.org/englidar/_Antarctic%20LIDAR.php). The lidar is sensitive to large aerosols and cloud particles, whose presence can be detected from a few metres above ground to 7000 m. The discrimination between liquid and solid relies on the aerosol-induced depolarization of linearly polarized laser light.

2.3 Derived quantities

To assist our analyses, GRs, condensation sinks (CS), and formation rates of ions were determined from the measured air ion and total aerosol particle spectra. The GR characterizes how rapidly particles enlarge in size due to condensational growth and coagulation, which typically has a unit of nm h^{-1} (Dal Maso et al., 2005; Kulmala et al., 2012). The CS describes the loss rate of condensable vapours onto aerosol particles and is expressed in s^{-1} (Pirjola et al., 1998; Dal Maso et al., 2002). The formation rate of ions quantifies the rate at which ions in a certain size range are formed and has a unit of cm^{-3} s^{-1} (Nieminen et al., 2011; Kulmala et al., 2012).

2.3.1 GR determination

The concentration of ions/aerosol particles evolves in both time and particle size. We used two approaches in determining GRs: the mode-fitting method (Dal Maso et al., 2005) and the appearance time method (Lehtipalo et al., 2014). The mode-fitting method follows the concentration change in the time dimension and the appearance time method follows the change in the size dimension.

In the mode-fitting method, at each time stamp of the measurement, the representative size of the aerosol population is determined by fitting a normal distribution to the measured

concentration distribution along the logarithm of sizes with a base of 10. The mode of the fitted curve is transcribed back to linear scale and taken as the representative size of the particle population measured at this moment (a more detailed description of the method has been presented by Dal Maso et al., 2015). In contrast, in the appearance time method, for each size (the geometric mean size of a measurement size bin), one determines the time (the appearance time) at which the particle population is considered to reach this size, based on the measured concentration evolution in time (Lehtipalo et al., 2014). This procedure is repeated for each measurement size bin. In this study, we defined the moment at which the concentration rises to 75 % of the maximum as the appearance time for each size. The GR was then calculated as the slope of a linear fit to the size data as a function of time. In addition, we also determined the instantaneous GR ($\mathrm{d}dp/\mathrm{d}t$) as the change in sizes within the interval of two adjacent time stamps to support the analysis of the GR dependence on sizes.

2.3.2 CS determination

Sulfuric acid is a key chemical species in forming aerosol particles in the ambient air (Kulmala et al., 2014). We determined CS for sulfuric acid vapours from the number size distribution measured by the DMPS, based on the method described by Pirjola et al. (1998) and Dal Maso et al. (2002), using the following equation:

$$\mathrm{CS} = 2\pi D \int d_\mathrm{p} \beta \left(d_\mathrm{p}\right) n \left(d_\mathrm{p}\right) \mathrm{d}d_\mathrm{p}. \quad (7)$$

Here D is the diffusion coefficient of condensing vapour molecules, d_p is the diameter of aerosol particles, n is the concentration, and β is a transitional correction factor (Fuchs and Sutugin, 1971), which is a function of the mass accommodation coefficient (α) and Knudsen number (Kn). In most applications, α is assumed to be unity while Kn can be connected to D via the mean free path of vapour molecules (λ_v) using the mean free-path theory (Mason and McDaniel, 1988; Pirjola et al., 1998).

The diffusion coefficient of vapour molecules is determined using the Fuller's model (Poling et al., 2004; Tang et al., 2014), which describes a binary gas system of species A diffusing in B:

$$D = \frac{0.00143 \cdot T^{1.75}}{\left[P/10^5 : \mathrm{bar}\right] \cdot M_\mathrm{AB}^{1/2} \left[(\Sigma_\mathrm{v})_\mathrm{A}^{1/3} + (\Sigma_\mathrm{v})_\mathrm{B}^{1/3} \right]^2},$$

$$\text{with} \quad M_\mathrm{AB} = \frac{2}{1/M_\mathrm{A} + 1/M_\mathrm{B}}. \quad (8)$$

Here, $(\Sigma_\mathrm{v})_\mathrm{A}$ and $(\Sigma_\mathrm{v})_\mathrm{B}$ are the diffusion volumes of species A and B, respectively, and M_A and M_B are the corresponding molar masses. For the system of sulfuric acid diffusing in air, $\Sigma_{v,\,\mathrm{H_2SO_4}} = 51.96$ and $\Sigma_{v,\,\mathrm{air}} = 19.7$. The measured ambient temperature and pressure were used in the CS determination.

2.3.3 Formation rate of 2 nm ions ($J_2^{\pm}$)

The formation rates of 2 nm ions ($J_2^{\pm}$) was determined based on the following equation:

$$J_2^{\pm} = \frac{\mathrm{d}n_{2-3}^{\pm}}{\mathrm{d}t} + \mathrm{CoagS}_2 n_{2-3}^{\pm} + \frac{\mathrm{GR}_{2-3}}{1\,\mathrm{nm}} n_{2-3}^{\pm} + \alpha n_{2-3}^{\pm^2}, \quad (9)$$

where $n_{2-3}^{\pm}$ is the ion concentration in the 2–3 nm size range, GR_{2-3} is the GR of 2–3 nm ions, and α is the ion–ion recombination coefficient ($\alpha = 1.6 \times 10^{-6}\,\mathrm{cm^3\,s^{-1}}$). CoagS_2 stands for the coagulation sink for 2 nm ions and it was determined using particle data measured by the DMPS based on the method described by Kulmala et al. (2001). Owing to the malfunction of the negative analyser in our AIS, the ion formation rates in this study were determined only for the positive polarity, based on the assumption that the negative ion concentration is equal to the positive ion concentration.

3 Results and discussions

3.1 Overview of features observed in air ions

During the campaign period (330 days in total), there were 287 days with valid air ion measurements, i.e. valid air ion data were collected on nearly 87 % of the measurement days. We were able to identify NPF, wind-induced ion formation, and cloud activation events from the valid measurements. Altogether, NPF events were observed on 32 days, wind-induced ion formations on 36 days, and cloud activations on 7 days with two certain cases. For the NPF events, 20 cases were classified as suppressed NPF events, which were characterized by no clear particle growth beyond 10 nm. Cases with two or more separate, yet simultaneous, NPF events with subsequent growth, i.e. multi-mode NPF events, were seen on 12 NPF days. Additionally, 85 days were recognized as event-free days, during which no above-mentioned events, contamination, or other unexplainable processes disturbing the cluster ion band (0.9–1.9 nm) were observed.

A clear seasonality was found on these event-free days in the cluster ion concentration (Fig. 2a). The cluster ion concentration was highest during the warm months, with a maximum in February. The median cluster ion concentration was typically below $100\,\mathrm{cm^{-3}}$ during the winter. This seasonality is related to variations in the natural ionizing radiation, which produces initial charge carriers via the ionization of air molecules, as well as to the availability of vapours capable of forming cluster ions (Chen et al., 2016). The variability in the ionizing radiation originates, in general, from changes in the atmospheric radon concentration, terrestrial gamma, and cosmic radiation (Chen et al., 2016). Owing to the presence of the thick ice and snowpack (over 3000 m in depth; Augustin et al., 2004), the contribution of radon exhalation or terrestrial gamma emissions from ground at Dome C to the ionization of air molecules can be neglected. Also, atmo-

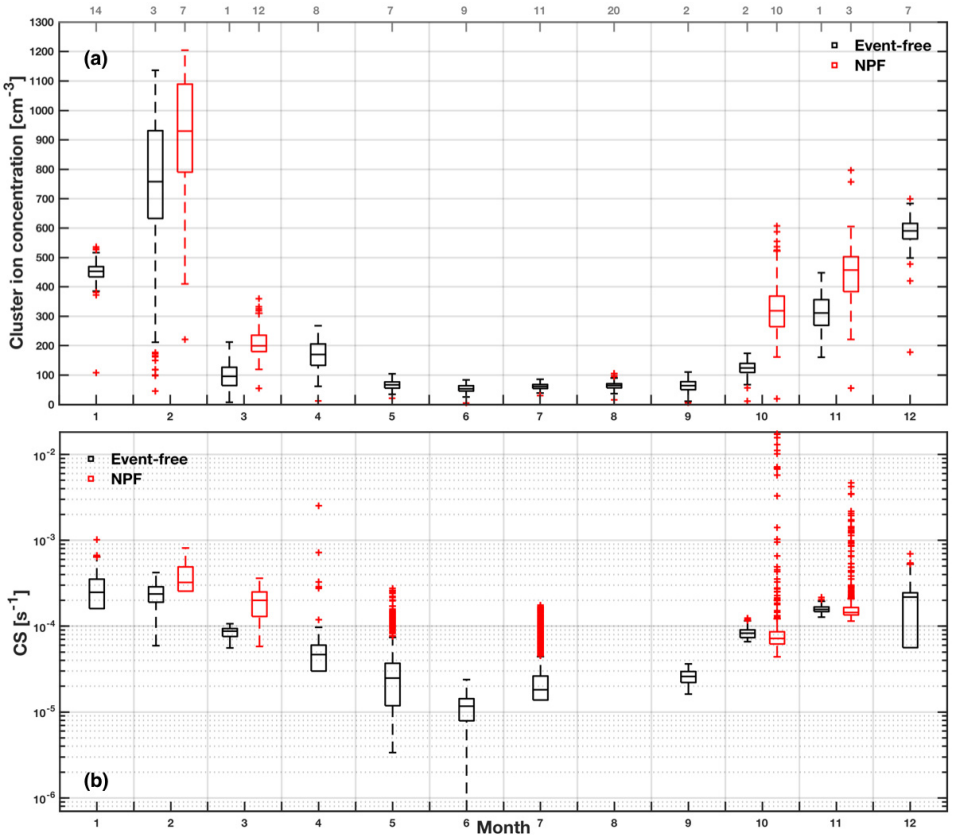

Figure 2. Seasonality in the median **(a)** cluster ion (0.9–1.9 nm) concentration and **(b)** condensation sink (CS). Tops and bottoms of the boxes are the 75th and 25th percentiles of the median daily values in 10 min time resolution, with bars in the middle showing the 50th percentiles. Whiskers represent spans of the interquartile ranges multiplied by 1.5. Cluster ion concentrations or CS on NPF days shown in red and on event-free days in black. Event-free conditions were restricted to days on which there was no NPF, cloud activation, wind-induced events, or contamination as well as other anomalies altering the ion concentration in the cluster band. The numbers of days classified as either event-free or NPF are displayed at the top of panel **(a)** in grey. No CS was obtained in August due to the lack of measured temperature and pressure data from the station database.

spheric radon emitted from the coastal areas or other remote regions may hardly reach Dome C by wind transportation. Therefore, the only major ionization source of air molecules comes from cosmic radiation. The cosmic ray intensity is mainly modulated by the solar activity and therefore can be considered invariable in the short term. Muons are the main cosmic ray component responsible for the ionization in the lower atmosphere (Goldhagen, 2000). The intensity of the muon flux in Antarctica has been found to have a weak seasonality and to be related to the stratospheric temperature, being low in winter and high in summer, and the temperature modulation has been reported to be ±8 % on an annual basis (IceCube Collaboration, 2011). Although the seasonal cycle in the cluster ion concentration corresponded to the seasonality in the muon flux, the influence of the variation in the ionizing radiation alone is insufficient to account for the difference of more than 30 % in the cluster ion concentration between summer and winter (Fig. 2a). Thus, most probably the low winter cluster ion concentration was additionally affected by the limited source of vapours that can participate in cluster ion formation due to the inhibited photochemistry under the reign of polar-night darkness. The development of the planetary boundary layer may additionally influence the concentration of cluster ions by imposing either a dilution or concentration effect. The longer day length in February than in March or October may result in the development of a deeper mixed layer, which could dilute the cluster ions within the mixing volume. However, the high-

est cluster ion concentration was found in February. Also, polar nights would cause the formation of only a very shallow and stable boundary layer in winter months. The mixing volume in winter is therefore expected to be much smaller than in other seasons, but no concentration effect on cluster ion concentration can be identified. Consequently, even if the seasonal change of boundary layer heights has an influence on the seasonality in cluster ion concentrations, this effect is likely to be minor.

The daily-median cluster ion concentration at Dome C was observed to be higher on NPF event days compared with event-free days. A similar phenomenon was also seen in a boreal forest environment at SMEAR II station in southern Finland (Fig. S2). Such a connection between cluster ion concentrations and NPF occurrences may imply that compared with event-free days, NPF event days probably had higher concentrations of vapours that are able to contribute to both cluster ion formation and NPF. In the Antarctic autumn (February and March), the value of CS tended to be higher on NPF days compared with event-free days (Fig. 2b). Since a large CS is indicative of a higher atmospheric sink for low-volatility vapours, this observation suggests a particularly strong source rate of such vapours during this time of the year, especially on NPF days. Interestingly, the opposite pattern in CS was seen in the Antarctic spring (October and November, Fig. 2b).

3.2 NPF and growth

3.2.1 NPF events

One of the major features observed in the AIS spectra at Dome C was the process of NPF and subsequent growth of newly formed charged clusters/particles. The smooth growth that lasts for several hours can imply a homogeneous condition in the sampled air (Hirsikko et al., 2007; Manninen et al., 2010). Seven clear NPF events were seen on consecutive days during the period 9–15 March 2011, with the initial step traceable down to the cluster ion band (Fig. 3b). All these NPF events occurred during westerly winds, apart from the first one on 9 March (Fig. 3e). This NPF event was associated with winds from the contaminated sector (10–90°) and possibly affected by the diesel generator of the station and motor vehicle pathways (Järvinen et al., 2013). These NPF events occurred after sunrise between about 00:00 and 06:00 UTC (between 08:00 and 14:00 in the local UTC + 8:00 time zone), which is in line with the proposed importance of photochemistry in NPF events and particle growths (Kulmala and Kerminen, 2008; Ehn et al., 2014; Kulmala et al., 2014). Except for the weak NPF event on 10 March, the newly formed particles of 9–12 March reached sizes larger than 10 nm and could be captured by both AIS and DMPS (Fig. 3a and b). Sudden increases in the concentration of 10–100 nm total particles corresponded to these NPF events (Fig. 3c). However, the NPF events seen during 13–15 March were restricted to sizes below 10 nm and showed no traces in the DMPS spectra (Fig. 3a and b). Consistently, no elevated concentrations were observed for particles in the size range of 10–100 nm for these events (Fig. 3c). Such differences result likely from the availability of vapours that sustain the growth. We could see slight concentration increases in the cluster ion size range at the time when NPF events were initiated, but no systemic features in relation to NPF events were identifiable in the total concentration of particles larger than 100 nm (Fig. 3c). The CS varied in a similar way to the total concentration of particles larger than 100 nm, ranging between 10^{-4} and 4×10^{-4} s^{-1}, in line with the values of CS reported at Dome C during NPF events (Järvinen et al., 2013).

Figure 4 shows examples of multi-mode NPF events that were observed during 12–16 February 2011. One of them (14 to 15 February) had three concurrent NPF and growth events. The first of them was initially captured by the DMPS at around 03:00 UTC, and at a size of around 15 nm, but it showed no clear traces in the AIS measurements before 12:00 UTC. While the particles formed during this first event were still growing in size, a second NPF event started from a size of 9 nm at 18:00 UTC and was detected almost simultaneously by both AIS and DMPS. About 4 h after the onset of the second NPF event, and during the growth stages of both the first and second events, a third NPF event was observed in the AIS starting from the cluster size range. The growth of particles originating from this last NPF event ceased at around 6 nm and was therefore not seen by the DMPS. A similar multi-mode NPF event was also observed on the following day, 16 February (Fig. 4). On 12 February at 06:00 UTC, a NPF event was observed by the DMPS at an initial size of 10 nm, and the same event was observed by the AIS after around 13:00 UTC. This event lasted until the noon of 13 February. Over the consecutive 5 days of 12–16 February, a slowly growing (GR ≈ 1.4 nm h^{-1}) population of 40–200 nm particles could be observed in the background, with their initial formation traceable back to 06:00 UTC on 12 February. Interestingly, apart from the particles initiated at 10 and 40 nm, a third mode of particles with sizes larger than 100 nm was recognizable on the morning of 12 February. This particle mode grew approximately from 100 to 300 nm during 12–13 February, and then gradually merged with the mode initiated at 40 nm at the end of 16 February. These multi-mode NPF events were associated with 2 times higher values of CS than the events presented in Fig. 3, owing to the presence of higher concentrations of background particles (Figs. 3c, 4c and d).

3.2.2 GR comparisons

The GRs determined by the appearance time method tended to be higher than those determined by the mode-fitting method (Fig. 5). This difference probably originates from the foundations that these two methods rest on. Both methods were developed to treat the measured number size dis-

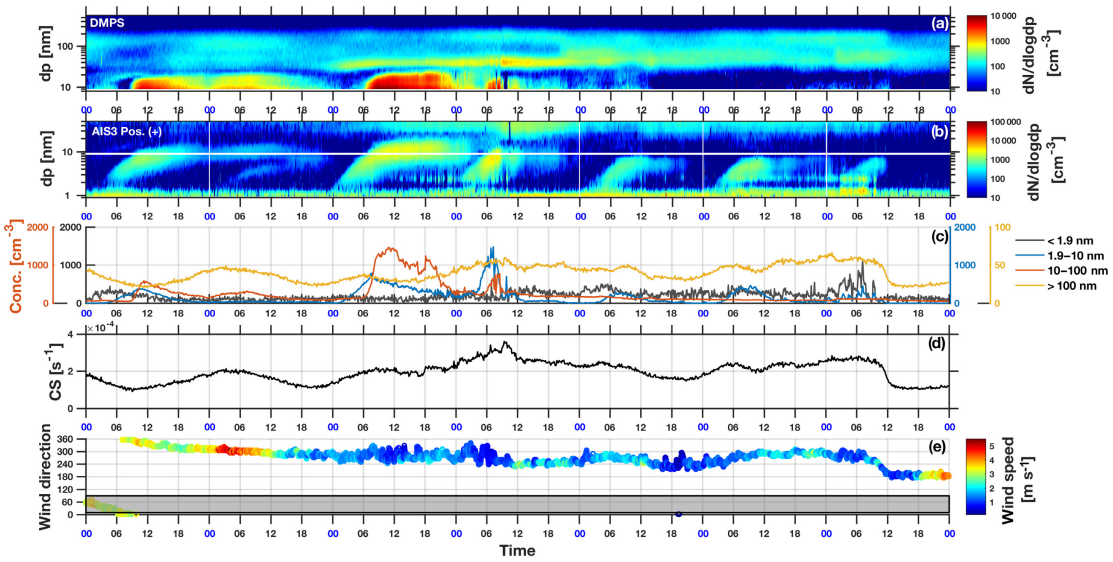

Figure 3. Consecutive NPF events observed during the period 9–15 March 2011. **(a)** DMPS spectra; **(b)** AIS positive polarity spectra; **(c)** ion and particle concentrations in four different size ranges: 0.9–1.9 nm (ions), 1.9–10 nm (ions), 10–100 nm (total particles), and total particles of diameters above 100 nm; **(d)** CS; and **(e)** wind direction, colour-coded for wind speed. The white line in **(b)** indicates the lower limit of the DMPS size range. The grey band in **(e)** represents the contaminated wind sector. Data are presented in UTC.

tribution data of ions/particles that vary in time, size, and ion/particle number concentrations. The appearance time method follows the concentration change as a function of time along the particle size dimension, whereas the mode-fitting method tracks the concentration change as a function of particle size along the time dimension. Accordingly, the appearance time method is able to preserve the growth features related to particle size, whereas the mode-fitting method characterizes better the evolution of particle growth with time.

The NPF event that occurred on 12 March between 00:00 and 06:00 UTC had clearly two simultaneously growing modes, with corresponding particle GRs marked by GR_6 and GR_7 in Fig. 5a and b. For this NPF event, although higher uncertainties were associated with the GR determined by the appearance time method than with the mode-fitting method, the former method succeeded in tracking the growth following both modes while the latter failed (Fig. 5). For GR_1 and GR_4, both methods led to similar GR values based on linear fitting – however, with a slightly smaller uncertainty (root-mean-square error) obtained using the appearance time method. Apart from for the slow-growth cases, the appearance time method seems to present a narrower uncertainty range than the mode-fitting method.

Even though the GR is often calculated as the slope of a linear fit to the size data as a function of time (Yli-Juuti et al., 2011; Lehtipalo et al., 2014), like in Fig. 5, it is not always appropriate to express the change in sizes along time by a linear proportionality, e.g. GR_1 determined by the appearance time method in Fig. 5b and GR_2 determined by the mode-fitting method in Fig. 5a. Alternatively, the change in sizes within the interval of two adjacent time stamps, i.e. the instantaneous GR ($\mathrm{d}dp/\mathrm{d}t$), was used to investigate the size dependence of GR. We found that the instantaneous GR derived from the AIS measurements during the NPF events tended to increase with an increasing particle size (Fig. 6c and d). A similar feature has been reported at many other sites for the sub-20 nm size range (see Häkkinen et al., 2013, and references therein). The median instantaneous GRs given by the appearance time method were in the range of 0.5–25 nm h^{-1} and by the mode-fitting method in the range of 1–150 nm h^{-1}. The reported GRs of newly formed atmospheric aerosol particles are typically below a few tens of nm h^{-1} (Yli-Juuti et al., 2011; Järvinen et al., 2013; Wang et al., 2017). The instantaneous GRs determined using the former method fall in this range, while using the latter method resulted in larger instantaneous GRs. This feature could be ascribed to the higher uncertainties associated with the mode-fitting method. The mode-fitting method tracks the mode concentration corresponding to sizes based on curve fitting for each measurement cycle, and it could be that the sizes at which mode concentrations were identified differ significantly in two adjacent measurement cycles, i.e. over a short time interval. A large size difference over a small time in-

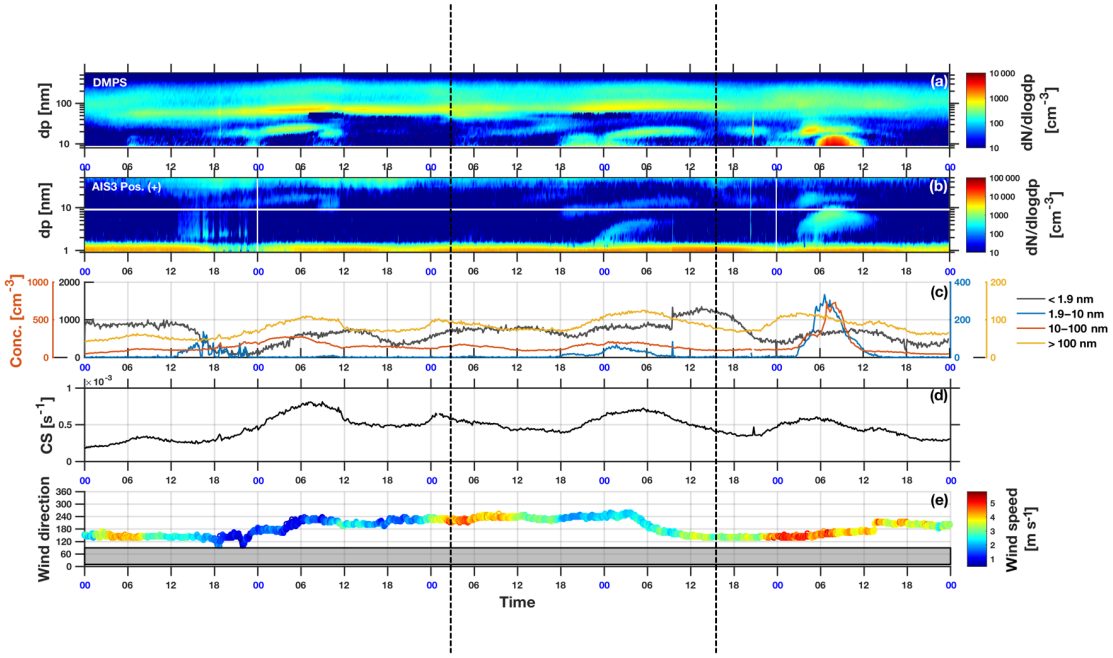

Figure 4. Consecutive multi-mode formation and growth events observed during 12–16 February 2011. **(a)** DMPS spectra; **(b)** AIS positive polarity spectra; **(c)** ion and particle concentrations in four different size ranges 0.9–1.9 nm (ions), 1.9–10 nm (ions), 10–100 nm (total particles), and total particles of diameters above 100 nm; **(d)** CS; and **(e)** wind direction, colour-coded with wind speed. The white line in **(b)** indicates the lower limit of the DMPS size range. The grey band in **(e)** represents the contaminated wind sector. The two vertical dashed lines outline the three NPF which occurred on 14–15 February 2011. Data are presented in UTC.

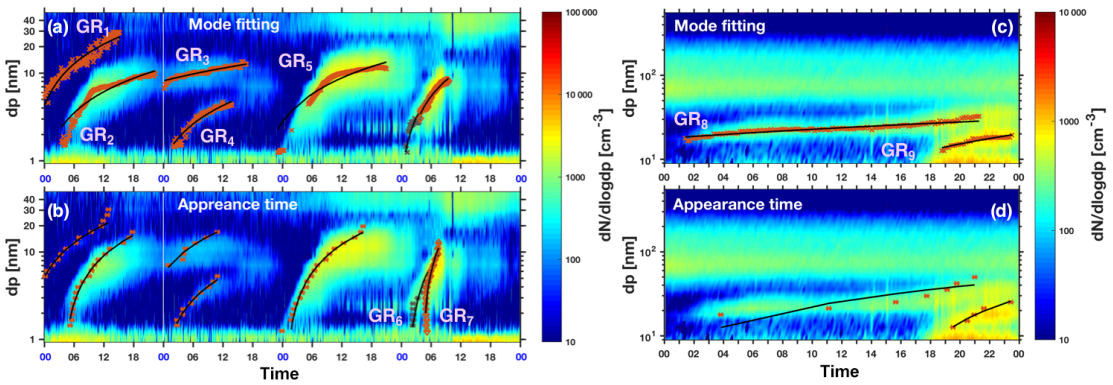

Figure 5. Comparison of GR for nine growth modes (GR_i, $i = 1, \ldots, 9$ in the figure) determined by the mode-fitting method **(a, c)** and by the appearance time method **(b, d)**, from the AIS measurement for 9–12 March 2011 (left-hand panels) and from the DMPS measurement for 25 February 2011 (right-hand panels). Growth rates estimated from linear fittings with root-mean-square errors expressed as uncertainties are shown in Table 1. The red or grey dots depict the estimated size evolution of ions/particles with respect to time determined by the mode-fitting or appearance time methods, with the linear fits to these size–time relationships shown as black lines.

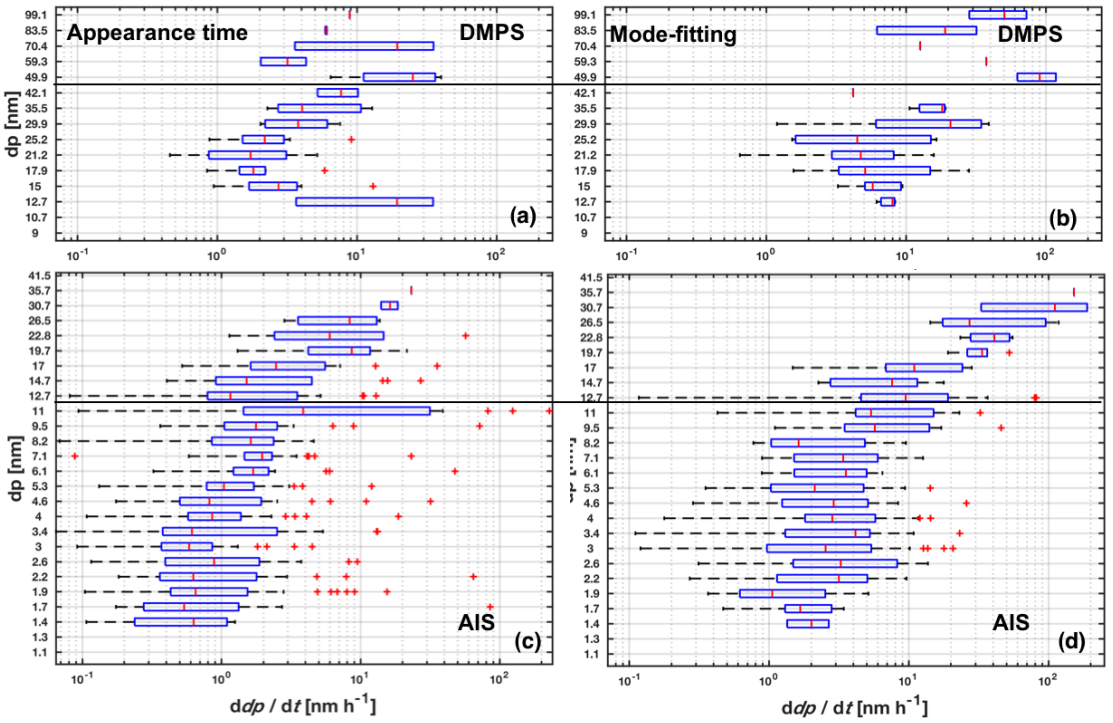

Figure 6. The GR dependence on size. Sizes are in mobility diameters and GRs of ions and particles are presented as discrete time derivatives of the change in mobility diameters (ddp/dt). GRs of aerosol particles measured by the DMPS are shown in the upper panels **(a, b)**, and GRs of ions measured by the AIS are shown in the lower panels **(c, d)**. GRs in the left-hand panels **(a, c)** are determined using the appearance time method and those in the right-hand panels **(b, d)** are determined using the mode-fitting method. The solid black lines indicate the overlapping size range of the DMPS and AIS measurements. The box was drawn with 25th and 75th percentiles of GRs determined at each size, with the median indicated as a right bar inside the box. The whiskers extend to the smallest and highest GR values within 1.5 times the interquartile range at each size. GRs beyond the 1.5 times interquartile range are marked by red crosses as outliers.

terval, therefore, would lead to a huge instantaneous GR. In contrast, the appearance time method is based on looking for the time stamp, when the concentration reaches 75 % of its maximum in the concentration vs. time space for each size channel of the instrument. Owing to the fact that aerosol and ion data have a higher resolution in the time dimension than in the size dimension, the appearance time method could pick up the time stamp more precisely for each size than the mode-fitting method could do the sizes for each measurement cycle. Consequently, the appearance time method presents GRs with smaller uncertainties (Fig. 5 and Table 1) and yields more representative instantaneous GRs. The instantaneous GRs derived from the DMPS measurement exhibit a rather vague pattern in connection to sizes (Fig. 6a and b); yet, a light increasing tendency might be still deducible. At large sizes in the overlapping size range (10–42 nm) of AIS and DMPS, the instantaneous GR derived from the AIS measurements tended to be larger than those from the DMPS measurements. This difference may result from the fact that the DMPS measures total particles, including both ions and neutral particles, whereas the AIS detects only charged particles. Also, the AIS measurements at sizes larger than 20 nm are subject to the uncertainties brought about by the detection of multiply charged particles as singly charged particles. At small sizes in the overlapping size range, the instantaneous GR derived from the DMPS exhibited a decreasing trend with increasing sizes, which, however, was not shown by the instantaneous GR derived from the AIS. This difference may again be attributed to the difference in the sampled particles targeted by the two instruments.

3.2.3 Formation rates of 2 nm positive ions (J_2^+)

The formation rate of 2 nm positive ions (J_2^+) was determined for 26 NPF event days, for which GRs in the 2–3 nm size range were obtained using the appearance time method. The average value of J_2^+ was 0.014 cm^{-3} s^{-1},

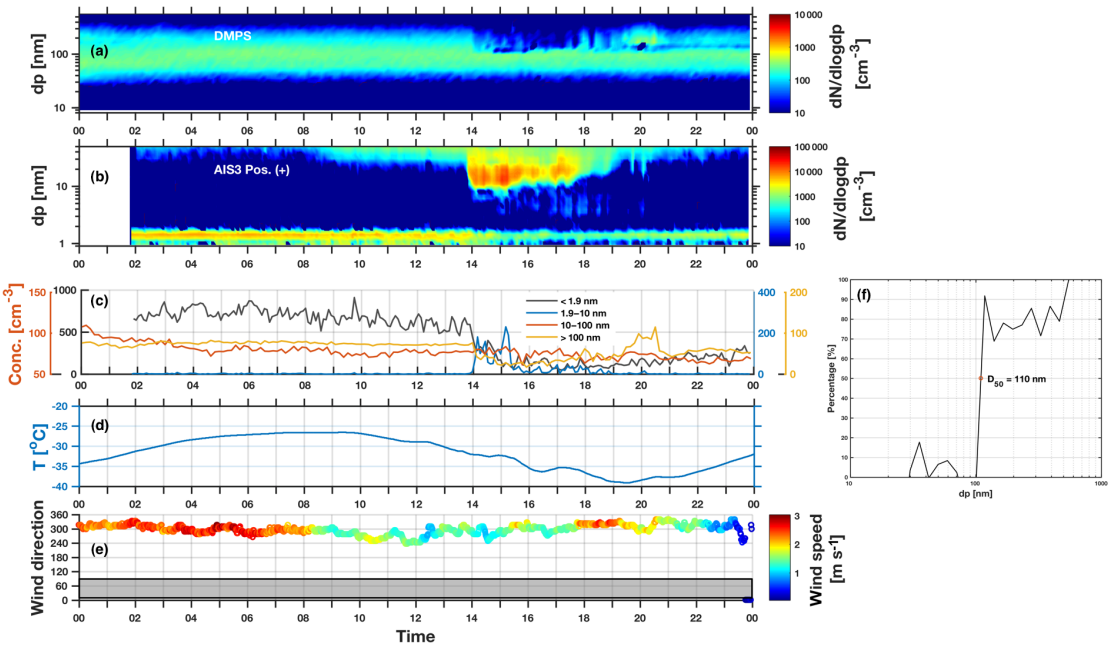

Figure 7. A cloud activation event observed on 20 January 2011. **(a)** DMPS spectra; **(b)** AIS positive polarity spectra; **(c)** ion and particle concentrations in four different size ranges: ions of diameters below 1.9 nm, ions of diameters between 1.9 and 10 nm, total particles of diameters between 10 and 100 nm, and total particles of diameters above 100 nm; **(d)** ambient air temperature (T); **(e)** wind direction, colour-coded with wind speed; and **(f)** activation diameter (D_{50}), determined based on the method described by Komppula et al. (2005). Data are presented in UTC.

Table 1. GRs estimated from linear fittings with root-mean-square errors expressed as uncertainties for the nine growth modes shown in Fig. 5. GR_{mf} stands for GRs determined by the mode-fitting method and GR_{apt} for those determined by the appearance time method. Normal text in the table corresponds to GRs determined from the AIS measurement (9–12 March 2011) and bold text to GRs determined from the DMPS measurement (25 February, 2011).

ID	GR_1	GR_2	GR_3	GR_4	GR_5	GR_6	GR_7	**GR_8**	**GR_9**
GR_{mf} (nm h^{-1})	1.4 ± 2.2	0.4 ± 0.7	0.3 ± 0.3	0.3 ± 0.3	0.5 ± 1.0	0.9 ± 0.3	0.9 ± 0.3	**0.5 ± 1.0**	**1.2 ± 0.7**
Size ranges (nm)	4.6–29	1.5–10	6.7–14	1.4–4.7	1.3–12	1.3–8.6	3.1–8.2	**1.7–12**	**10–17**
GR_{apt} (nm h^{-1})	1.3 ± 1.2	1.1 ± 0.5	1.1 ± 0.8	0.4 ± 0.2	1.1 ± 0.5	1.5 ± 1.2	3.5 ± 1.0	**1.6 ± 7.5**	**3.3 ± 1.2**
Size ranges (nm)	5.3–31	1.4–17	7.1–17	1.4–5.3	1.3–20	1.4–13	1.3–13	**1.7–17**	**11–20**

with a standard deviation of 0.020 cm^{-3} s^{-1}. An estimation of uncertainties in J_2^+ was made by assuming an underestimation of 15–30 % in the AIS measurement (Wagner et al., 2016), an uncertainty of ±10 % in the DMPS measurement in the whole size range (Wiedensohler et al., 2012), an error of ±1 C in the temperature measurement, and ±1 hPa in the pressure measurement. We calculated the maximum and minimum estimates of J_2^+ based on these assumptions and evaluated the deviations of J_2^+ from the mean values of the maximum and minimum estimates. We found that this deviation was smaller than 0.005 cm^{-3} s^{-1} (< 0.020 cm^{-3} s^{-1}) for more than 80 % (88 %) of the values of J_2^+. Other characteristic values for J_2^+ were as follows: 0.0005 cm^{-3} s^{-1} (minimum), 0.0024 cm^{-3} s^{-1} (first quartile), 0.0066 cm^{-3} s^{-1} (median), 0.015 cm^{-3} s^{-1} (third quartile), and 0.079 cm^{-3} s^{-1} (maximum). These ion formation rates are comparable to those reported for the SMEAR II station in Finland (Nieminen et al., 2011), as well as to those observed in several other sites in Europe (Manninen et al., 2010).

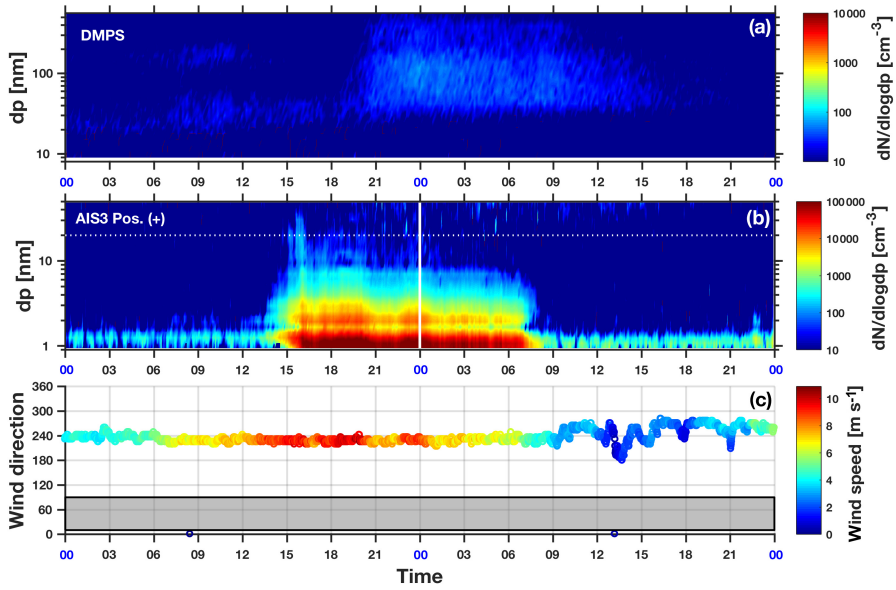

Figure 8. A wind-induced ion formation event observed on 3–4 July 2011. **(a)** DMPS spectra; **(b)** AIS positive polarity spectra; and **(c)** wind direction, colour-coded with wind speed. The white dotted line is a visual guide to outline the 20 nm location. The grey band in **(c)** represents the contaminated wind sector. Data are presented in UTC.

3.3 Other specific features

3.3.1 Influence of cloud/fog formation on aerosol particles and air ions

A cloud activation event initiated at around 14:00 UTC was observed on 20 January 2011 (Fig. 7). In general, such events are characterized by a disappearance of aerosol particles from the measured particle size range (Komppula et al., 2005; Kyrö et al., 2013). Additionally, a sudden drop in the cluster ion concentration has been reported as a feature for cloud activation events (Lihavainen et al., 2007). We observed similar connections between cluster ions and cloud activation at Dome C (Fig. 7a–c). Moreover, we found that the cloud activation event was accompanied by a burst of ions in the 8–42 nm size range measured by the AIS (Fig. 7b and c), yet not captured by the DMPS.

By following the approach introduced by Komppula et al. (2005) based on DMPS measurements, it can be estimated that particles larger than about 110 nm in diameter had been activated into cloud droplets during this cloud event (Fig. 7). This observation is well in line with the activation thresholds from < 50 nm up to about 200–300 nm for the "dry" particle diameter observed in real atmospheric clouds (see Henning et al., 2002, and references therein; Anttila et al., 2009; Kyrö et al., 2013; Portin et al., 2014; Leaitch et al., 2016). Cluster ions were efficiently lost onto the cloud droplets at Dome C. Because of their large sizes beyond the detection capability of the DMPS, cloud droplets could collect multiple charges via the uptake of cluster ions, which might then be detected by the AIS as singly charged particles in the size range of 8–42 nm. Additionally, these ions detected by the AIS might also be artificial products resulting from the cloud droplet cleavage inside the sampling line of the instrument, possibly related to the high sample flowrate and the low-temperature condition (Fig. 7d). This cloud activation was possibly a result of ground-level fog formation, as lidar observations showed no evidence of clouds above 40 m (Fig. S3a and b). A cloudy pattern appeared in the lidar spectra at the near-ground level after about 15:00 UTC (Fig. S3c and d). This 1 h delay compared with the aerosol instruments may be related to the fact that aerosol particles/cloud droplets cannot be captured by the lidar unless the aerosol/cloud layer is optically thick enough. It is very likely that the ground-level fog was initially very thin, yet observable with the DMPS system, and only later became thick enough for the lidar to capture it. The high depolarization indicates a high probability of the presence of ice particles. Some precipitation could be recognized (Fig. S3a and b), originating from cirrus clouds at heights between 2500 and 3000 m above ground between 16:00 and 18:00 UTC. Light precipitation might have reached the ground level after around 18:00 UTC (Fig. S3c and d), which perturbed the cloud activation and

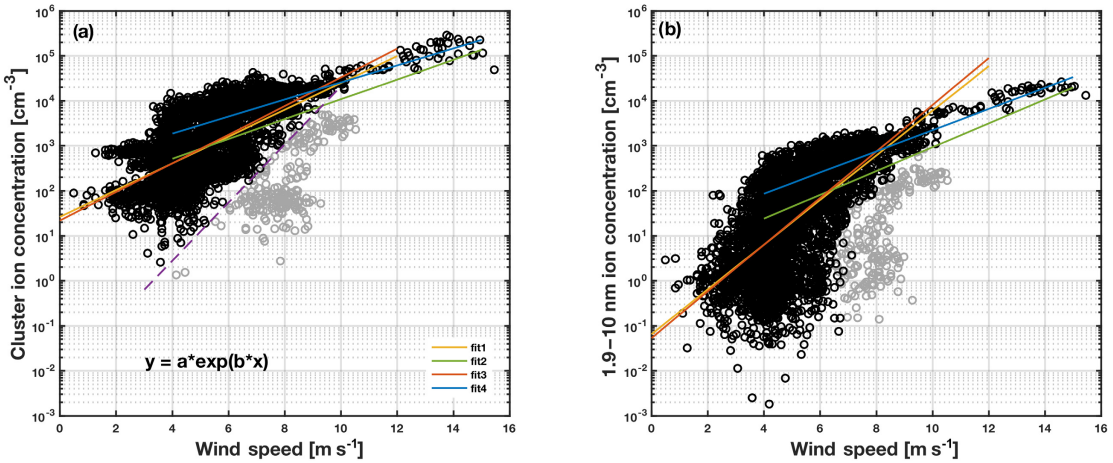

Figure 9. Ion concentrations as a function of wind speed: **(a)** ion concentration in the cluster size range (0.9–1.9 nm) and **(b)** ion concentration in the size range of 1.9–10 nm. The solid lines are linear fits to the data. Fits 1 and 3 are to data with a wind speed below the threshold wind speed (7 m s^{-1}) and fits 2 and 4 are to data above the threshold wind speed. Fits 1 and 2 are obtained based on all data below or above the wind speed threshold, respectively. The data points in grey colour, however, are not taken into account in determining the fitting coefficients for fits 3 and 4. These grey data points correspond to cluster ion concentration values below the purple dashed line ($y = 0.0074 \cdot e^{1.4855x}$). The coefficients of these fits as well as the 95 % confidence bounds of the coefficients and coefficient of determination measuring the goodness of fit are given in Table S1 in the Supplement.

impaired the effect of fog/cloud formation exerted on air ions (Fig. 7a–c).

3.3.2 Wind-induced ion formation

Ion formation events during strong wind episodes have been observed at Aboa in Antarctica (Virkkula et al., 2007), as well as at the high-altitude site on Jungfraujoch in Switzerland (Manninen et al., 2010). At Dome C, we observed wind-induced ion formation especially during the dark months (15 cases during May–August). An example of such an event, observed during 3–4 July 2011, illustrates the close connection between the ion formation and wind speed (Fig. 8): ions generated by a strong wind were mainly in the cluster ion size range, even though a large number of ions were also apparent in the 1.9–10 nm size range.

Under strong wind conditions, small snowflakes and ice crystals in the surface layer of the accumulated snow on the ground can be resuspended by turbulence and be shattered further by their collisions (Pomeroy and Jones, 1996). Vapours adsorbed on and trapped in these snowflakes and ice crystals can be released into the air to replenish vapours in the air that are capable of participating in cluster ion formation and possibly also NPF. This resuspension process also assists the escape of vapours trapped beneath the surface snow layer on the ground. Moreover, owing to the sudden drop of the surrounding vapour pressure, gaseous molecules of water and other trace species may also be freed from the resuspended particles by sublimation (Pomeroy and Jones, 1996). Ionizing radiation produces primary ions, which are either lost through ion–ion recombination or transformed into more stable air ions by nucleation or condensation (Chen et al., 2016). A small concentration of ions slightly larger than the cluster sizes could be observed in connection to the high wind speeds between 06:00 and 12:00 UTC (Fig. 8b and c). As the wind speed increased further after 12:00 UTC, the vapour replenishment was probably amplified, leading to an ion burst in the size range of 0.9–10 nm via nucleation, condensation, and coagulation. A fraction of these ions seems to be able to further undergo dynamic processes to form large aerosol particles with sizes of even 500 nm (Fig. 8a).

Turbulent conditions might enhance the collection of electric charges by the shattered snowflakes and ice particles via a charge transfer from initial charge carriers, contributing to the formation of an ion burst. In addition, the shattered particles might gain electric charges through friction charging. However, we think that these two pathways of ion formation are not likely to contribute to the ion burst captured by the AIS. In principle, the shattering of resuspended snowflakes and ice particles mechanically by turbulence results in the formation of particles of smaller but random sizes. If this mechanism had produced nano-sized particles that subsequently became electrically charged either by charge transfer or friction charging, our AIS should have detected some of them and have shown an unsystematic spectrum, i.e. ions of random sizes and concentrations. Yet, conversely, the AIS

showed high concentrations of ions of only small sizes, and hardly anything of sizes larger than 2–3 nm in diameter between 12:00 and 14:00 UTC during the intensification of the wind speed. Nevertheless, involvement of these processes cannot be ruled out completely based on our ambient observations. This kind of wind-induced ion formation warrants further experimental investigation, for example by releasing snow in a wind tunnel to disclose the true mechanisms governing the ion production.

Putting together all the 36 wind-induced ion formation events, the logarithm of the ion concentration exhibited linear relations to the wind speed (Fig. 9), as also observed at Aboa (Virkkula et al., 2007). For both cluster ions and ions in the size range of 1.9–10 nm, there seemed to be a two-step linear relation with a breakpoint at around $7\,\mathrm{m\,s^{-1}}$ (Fig. 9). Winds below this threshold value were less efficient in producing ions than winds with speeds of $> 7\,\mathrm{m\,s^{-1}}$. This feature could be also recognized in the Aboa data, but with the threshold in wind speeds lying at around $17\,\mathrm{m\,s^{-1}}$ (Fig. S4). The effect of wind on ions seemed to be stronger at Dome C than at Aboa (Table S1 and Fig. S4). The slopes for the logarithm of ion concentrations as a function of wind speeds differed by about an order of magnitude between Dome C and Aboa. This is so far the clearest and largest difference in the air ion processes at these two sites and deserves a more detailed study in the future.

4 Conclusions

Based on 1 year of air ion observations with an AIS at Dome C, Antarctica, we found that this site has a rich set of ion processes, especially when considering its inland location on the largest ice desert on the Earth – the Antarctic Plateau. NPF, wind-induced ion formation, and ion production and loss associated with cloud/fog formation were the main processes that were found to modify the number size distribution of air ions at this high-altitude site. On event-free days, i.e. on days without the above-mentioned processes or other anomalies, concentrations of cluster ions (0.9–1.9 nm) showed a clear seasonality, with high concentrations in the warm months and low concentrations in the cold season. Days with NPF events were characterized by higher cluster ion concentrations than event-free days. The specific features of the recorded air ion data allowed further classification of NPF into suppressed NPF and multi-mode NPF events. The former refers to NPF events during which the growth of newly formed particles hardly exceeds 10 nm, and the latter characterizes NPF events with two or three co-occurring NPF and growth events in different size ranges.

GRs determined using the mode-fitting method and appearance time method were used to characterize the NPF processes. Comparison between these two methods suggests that the GRs derived from the appearance time method work better in depicting the cases with a fast particle growth, whereas GRs determined from the mode-fitting method appeared to be more suitable for describing cases with a slow particle growth. We found that the change in particle diameters did not usually increase linearly with the time. Therefore, we derived the instantaneous GR ($\mathrm{d}dp/\mathrm{d}t$) as the change in sizes within the interval of two adjacent time stamps, and found that the GR tended to increase with an increasing particle size. The formation rate of 2 nm positive ions was found to be $0.014 \pm 0.020\,\mathrm{cm^{-3}\,s^{-1}}$ based on 26 NPF events.

Ion production in relation to cloud/fog formation in the size range of 8–42 nm was found uniquely at Dome C. These ions may be either multiply charged particles detected as singly charged in the AIS or splinters of cloud droplets formed inside the instrument related to the instrumental behaviour under the extremely cold conditions. Accordingly, it would be worthwhile to carefully characterize the instrumental behaviour of ion spectrometers under extremely low temperature conditions in relation to the presence of cloud droplets by conducting laboratory experiments. In addition, wind-induced ion formation was found to resemble new aerosol particle formation from vapours released from the snow, rather than being caused by mechanical charging of shattered snowflakes or ice crystals. The ion formation during strong wind episodes is a phenomenon of great interest. It is also worth mentioning that at this high-plateau site, wind-induced ion formation was approximately an order of magnitude stronger than at the low-altitude Antarctic site, Aboa, in which the same phenomenon has been observed earlier. The hidden mechanisms behind such processes need further investigation, which may reveal a new pathway of atmospheric NPF in dark wintertime conditions.

The air ion data used in this work were limited to the positive polarity due to a technical malfunctioning of the negative analyser. Further ambient measurements on air ions would be valuable to be carried out at Dome C and other sites on the Antarctic Plateau, not only to reveal possible differences between positive and negative ion properties and their connections to the ion and aerosol processes, but also to understand the mechanisms behind the ion formation related to the cloud/fog formation or wind episodes and to acquire a better characterization of atmospheric NPF in Antarctica. In the future in addition to air ions, the properties of neutral clusters and particles also need to be probed in order to understand the relative importance of ions and neutrals in atmospheric NPF at Dome C, and to characterize the comparability of the roles of ions and neutrals in atmospheric NPF observed at Dome C and at other sites around the globe.

Data availability. Data used in this work can be found via http://avaa.tdata.fi/openida/dl.jsp?pid=urn:nbn:fi:csc-ida.

The Supplement related to this article is available online at https://doi.org/10.5194/acp-17-13783-2017-supplement.

Competing interests. The authors declare that they have no conflict of interest.

Acknowledgements. This work received financial support from the Academy of Finland (project nos. 264375 and 264390), the NordForsk funded Nordic Centre of Excellence CRAICC (Cryosphere–atmosphere interactions in a changing Arctic climate, project no. 26060), and the Academy of Finland's Centre of Excellence Programme (Centre of Excellence in Atmospheric Science – From Molecular and Biological Processes to the Global Climate, project no. 272041). Funding for this research was also provided by Consiglio Nazionale delle Ricerche and PNRA (projects 2009/B.04 and 2010/A3.05). We appreciate the support of the IPEV/PNRA Project "Routine Meteorological Observation at Station Concordia", www.climantartide.it with the radiosounding data set. Xuemeng Chen acknowledges the Doctoral Programme in Atmospheric Sciences (ATM-DP, University of Helsinki) for financial support. Valuable advice from Sander Mirme is sincerely appreciated.

Edited by: Christopher Hoyle
Reviewed by: three anonymous referees

References

Aalto, P., Hämeri, K., Becker, E., Weber, R., Salm, J., MäKelä, J. M., Hoell, C., O'dowd, C. D., Karlsson, H., Hansson, H.-C., VäKevä, M., Koponen, I. K., Buzorius, G., and Kulmala, M.: Physical characterization of aerosol particles during nucleation events, Tellus B, 53, 344–358, 2001.

Anttila, T., Vaattovaara, P., Komppula, M., Hyvärinen, A.-P., Lihavainen, H., Kerminen, V.-M., and Laaksonen, A.: Size-dependent activation of aerosols into cloud droplets at a subarctic background site during the second Pallas Cloud Experiment (2nd PaCE): method development and data evaluation, Atmos. Chem. Phys., 9, 4841–4854, https://doi.org/10.5194/acp-9-4841-2009, 2009.

Asmi, E., Frey, A., Virkkula, A., Ehn, M., Manninen, H. E., Timonen, H., Tolonen-Kivimäki, O., Aurela, M., Hillamo, R., and Kulmala, M.: Hygroscopicity and chemical composition of Antarctic sub-micrometre aerosol particles and observations of new particle formation, Atmos. Chem. Phys., 10, 4253–4271, https://doi.org/10.5194/acp-10-4253-2010, 2010.

Augustin, L., Barbante, C., Barnes, P. R. F., Barnola, J. M., Bigler, M., Castellano, E., Cattani, O., Chappellaz, J., Dahl-Jensen, D., Delmonte, B., Dreyfus, G., Durand, G., Falourd, S., Fischer, H., Flückiger, J., Hansson, M. E., Huybrechts, P., Jugie, G., Johnsen, S. J., Jouzel, J., Kaufmann, P., Kipfstuhl, J., Lambert, F., Lipenkov, V. Y., Littot, G. C., Longinelli, A., Lorrain, R., Maggi, V., Masson-Delmotte, V., Miller, H., Mulvaney, R., Oerlemans, J., Oerter, H., Orombelli, G., Parrenin, F., Peel, D. A., Petit, J.-R., Raynaud, D., Ritz, C., Ruth, U., Schwander, J., Siegenthaler, U., Souchez, R., Stauffer, B., Steffensen, J. P., Stenni, B., Stocker, T. F., Tabacco, I. E., Udisti, R., van de Wal, R. S. W., van den Broeke, M., Weiss, J., Wilhelms, F., Winther, J.-G., Wolff, E. W., and Zucchelli, M.: Eight glacial cycles from an Antarctic ice core, Nature, 429, 623–628, 2004.

Bazilevskaya, G. A., Usoskin, I. G., Flückiger, E. O., Harrison, R. G., Desorgher, L., Bütikofer, R., Krainev, M. B., Makhmutov, V. S., Stozhkov, Y. I., Svirzhevskaya, A. K., Svirzhevsky, N. S., and Kovaltsov, G. A.: Cosmic ray induced ion production in the atmosphere, Space Sci. Rev., 137, 149–173, https://doi.org/10.1007/s11214-008-9339-y, 2008.

Becagli, S., Scarchilli, C., Traversi, R., Dayan, U., Severi, M., Frosini, D., Vitale, V., Mazzola, M., Lupi, A., Nava, S., and Udisti, R.: Study of present-day sources and transport processes affecting oxidised sulphur compounds in atmospheric aerosols at Dome C (Antarctica) from year-round sampling campaigns, Atmos. Environ., 52, 98–108, https://doi.org/10.1016/j.atmosenv.2011.07.053, 2012.

Belosi, F., Contini, D., Donateo, A., Santachiara, G., and Prodi, F.: Aerosol size distribution at Nansen Ice Sheet Antarctica, Atmos. Res., 107, 42–50, https://doi.org/10.1016/j.atmosres.2011.12.007, 2012.

Boucher, O., Randall, D., Artaxo, P., Bretherton, C., Feingold, G., Forster, P., Kerminen, V.-M., Kondo, Y., Liao, H., Lohmann, U., Rasch, P., Satheesh, S. K., Sherwood, S., Stevens, B., and Zhang, X. Y.: Clouds and Aerosols, in: Climate Change 2013: The Physical Science Basis. Contribution of Working Group I to the Fifth Assessment Report of the Intergovernmental Panel on Climate Change, edited by: Stocker, T. F., Qin, D., Plattner, G.-K., Tignor, M., Allen, S. K., Boschung, J., Nauels, A., Xia, Y., Bex, V., Midgley, P. M., Cambridge University Press, Cambridge, UK and New York, NY, USA, 2013.

Bricard, J., Billard, F., and Madelaine, G.: Formation and evolution of nuclei of condensation that appear in air initially free of aerosols, J. Geophys. Res., 73, 4487–4496, https://doi.org/10.1029/JB073i014p04487, 1968.

Carslaw, K. S., Lee, L. A., Reddington, C. L., Pringle, K. J., Rap, A., Forster, P. M., Mann, G. W., Spracklen, D. V., Woodhouse, M. T., Regayre, L. A., and Pierce, J. R.: Large contribution of natural aerosols to uncertainty in indirect forcing, Nature, 503, 67–71, https://doi.org/10.1038/nature12674, 2013.

Chen, X., Kerminen, V.-M., Paatero, J., Paasonen, P., Manninen, H. E., Nieminen, T., Petäjä, T., and Kulmala, M.: How do air ions reflect variations in ionising radiation in the lower atmosphere in a boreal forest?, Atmos. Chem. Phys., 16, 14297–14315, https://doi.org/10.5194/acp-16-14297-2016, 2016.

Dal Maso, M., Kulmala, M., Lehtinen, K. E. J., Mäkelä, J. M., Aalto, P., and O'Dowd, C. D.: Condensation and coagulation sinks and formation of nucleation mode particles in coastal and boreal forest boundary layers, J. Geophys. Res.-Atmos., 107, D19, https://doi.org/10.1029/2001jd001053, 2002.

Dal Maso, M., Kulmala, M., Riipinen, I., Wagner, R., Hussein, T., Aalto, P. P., and Lehtinen, K. E. J.: Formation and growth of fresh atmospheric aerosols: eight years of aerosol size distribution data from SMEAR II, Hyytiälä, Finland, Boreal Environ. Res., 10, 323–336, 2005.

Dunne, E. M., Gordon, H., Kürten, A., Almeida, J., Duplissy, J., Williamson, C., Ortega, I. K., Pringle, K. J., Adamov, A., Baltensperger, U., Barmet, P., Benduhn, F., Bianchi, F., Breitenlechner, M., Clarke, A., Curtius, J., Dommen, J., Donahue, N. M., Ehrhart, S., Flagan, R. C., Franchin, A., Guida, R., Hakala, J., Hansel, A., Heinritzi, M., Jokinen, T., Kangasluoma, J., Kirkby, J., Kulmala, M., Kupc, A., Lawler, M. J., Lehtipalo, K., Makhmutov, V., Mann, G., Mathot, S., Merikanto, J.,

Miettinen, P., Nenes, A., Onnela, A., Rap, A., Reddington, C. L. S., Riccobono, F., Richards, N. A. D., Rissanen, M. P., Rondo, L., Sarnela, N., Schobesberger, S., Sengupta, K., Simon, M., Sipilä, M., Smith, J. N., Stozkhov, Y., Tomé, A., Tröstl, J., Wagner, P. E., Wimmer, D., Winkler, P. M., Worsnop, D. R., and Carslaw, K. S.: Global atmospheric particle formation from CERN CLOUD measurements, Science, 354, 1119–1124, 2016.

Ehn, M., Thornton, J. A., Kleist, E., Sipila, M., Junninen, H., Pullinen, I., Springer, M., Rubach, F., Tillmann, R., Lee, B., Lopez-Hilfiker, F., Andres, S., Acir, I. H., Rissanen, M., Jokinen, T., Schobesberger, S., Kangasluoma, J., Kontkanen, J., Nieminen, T., Kurten, T., Nielsen, L. B., Jorgensen, S., Kjaergaard, H. G., Canagaratna, M., Maso, M. D., Berndt, T., Petaja, T., Wahner, A., Kerminen, V. M., Kulmala, M., Worsnop, D. R., Wildt, J., and Mentel, T. F.: A large source of low-volatility secondary organic aerosol, Nature, 506, 476–479, https://doi.org/10.1038/nature13032, 2014.

Fiebig, M., Hirdman, D., Lunder, C. R., Ogren, J. A., Solberg, S., Stohl, A., and Thompson, R. L.: Annual cycle of Antarctic baseline aerosol: controlled by photooxidation-limited aerosol formation, Atmos. Chem. Phys., 14, 3083–3093, https://doi.org/10.5194/acp-14-3083-2014, 2014.

Fuchs, N. and Sutugin, A.: Highly dispersed aerosol, in: Topics in Current Aerosol Research, edited by: Hidy, G., Brock, J., Pergamon, New York, 1971.

Goldhagen, P.: Overview of aircraft radiation exposure and recent er-2 measurements, Health Phys., 79, 526–544, 2000.

Gunn, R.: DIffusion charging of atmospheric droplets by ions, and the resulting combination coefficients, J. Meteorol., 11, 339–347, 1954.

Häkkinen, S. A. K., Manninen, H. E., Yli-Juuti, T., Merikanto, J., Kajos, M. K., Nieminen, T., D'Andrea, S. D., Asmi, A., Pierce, J. R., Kulmala, M., and Riipinen, I.: Semi-empirical parameterization of size-dependent atmospheric nanoparticle growth in continental environments, Atmos. Chem. Phys., 13, 7665–7682, https://doi.org/10.5194/acp-13-7665-2013, 2013.

Hara, K., Osada, K., Nishita-Hara, C., Yabuki, M., Hayashi, M., Yamanouchi, T., Wada, M., and Shiobara, M.: Seasonal features of ultrafine particle volatility in the coastal Antarctic troposphere, Atmos. Chem. Phys., 11, 9803–9812, https://doi.org/10.5194/acp-11-9803-2011, 2011.

Harrison, R. G. and Tammet, H.: Ions in the terrestrial atmosphere and other solar system atmospheres, Space Sci. Rev., 137, 107–118, https://doi.org/10.1007/s11214-008-9356-x, 2008.

Henning, S., Weingartner, E., Schmidt, S., Wendisch, M., Gäggeler, H. W., and Baltensperger, U.: Size-dependent aerosol activation at the high-alpine siteJungfraujoch (3580 m a.s.l.), Tellus B, 54, 82–95, 2002.

Hinds, W. C.: Aerosol Technology: Properties, Behavior, and Measurement of Airborne Particles, 2 ed., Wiley-Interscience, New York, 1999.

Hirsikko, A., Bergman, T., Laakso, L., Dal Maso, M., Riipinen, I., Hõrrak, U., and Kulmala, M.: Identification and classification of the formation of intermediate ions measured in boreal forest, Atmos. Chem. Phys., 7, 201–210, https://doi.org/10.5194/acp-7-201-2007, 2007.

Hirsikko, A., Nieminen, T., Gagné, S., Lehtipalo, K., Manninen, H. E., Ehn, M., Hõrrak, U., Kerminen, V.-M., Laakso, L., McMurry, P. H., Mirme, A., Mirme, S., Petäjä, T., Tammet, H., Vakkari, V., Vana, M., and Kulmala, M.: Atmospheric ions and nucleation: a review of observations, Atmos. Chem. Phys., 11, 767–798, https://doi.org/10.5194/acp-11-767-2011, 2011.

Hõrrak, U., Salm, J., and Tammet, H.: Bursts of intermediate ions in atmospheric air, J. Geophys. Res.-Atmos., 103, 13909–13915, https://doi.org/10.1029/97jd01570, 1998.

IceCube Collaboration: Seasonal Variations of High Energy Cosmic Ray Muons Observed by the IceCube Observatory as a Probe of Kaon/Pion Ratio, 32nd International Cosmic Ray Conference, Beijing, 2011.

Israël, H.: Atmospheric Electricity, Vol. I, Israel Program for Scientific Translations, Jerusalem, 1970.

Ito, T.: Size distribution of Antarctic submicron aerosols, Tellus, 45 B, 145–159, 1993.

Järvinen, E., Virkkula, A., Nieminen, T., Aalto, P. P., Asmi, E., Lanconelli, C., Busetto, M., Lupi, A., Schioppo, R., Vitale, V., Mazzola, M., Petäjä, T., Kerminen, V.-M., and Kulmala, M.: Seasonal cycle and modal structure of particle number size distribution at Dome C, Antarctica, Atmos. Chem. Phys., 13, 7473–7487, https://doi.org/10.5194/acp-13-7473-2013, 2013.

Kazil, J., Lovejoy, E. R., Barth, M. C., and O'Brien, K.: Aerosol nucleation over oceans and the role of galactic cosmic rays, Atmos. Chem. Phys., 6, 4905–4924, https://doi.org/10.5194/acp-6-4905-2006, 2006.

Kerminen, V.-M., Paramonov, M., Anttila, T., Riipinen, I., Fountoukis, C., Korhonen, H., Asmi, E., Laakso, L., Lihavainen, H., Swietlicki, E., Svenningsson, B., Asmi, A., Pandis, S. N., Kulmala, M., and Petäjä, T.: Cloud condensation nuclei production associated with atmospheric nucleation: a synthesis based on existing literature and new results, Atmos. Chem. Phys., 12, 12037–12059, https://doi.org/10.5194/acp-12-12037-2012, 2012.

Komppula, M., Lihavainen, H., Kerminen, V.-M., Kulmala, M., and Viisanen, Y.: Measurements of cloud droplet activation of aerosol particles at a clean subarctic background site, J. Geophys. Res.-Atmos., 110, D06204, https://doi.org/10.1029/2004jd005200, 2005.

Koponen, I. K., Virkkula, A., Hillamo, R., Kerminen, V.-M., and Kulmala, M.: Number size distributions and concentrations of the continental summer aerosols in Queen Maud Land, Antarctica, J. Geophys. Res.-Atmos., 108, 4587, https://doi.org/10.1029/2003jd003614, 2003.

Kulmala, M. and Kerminen, V.-M.: On the formation and growth of atmospheric nanoparticles, Atmos. Res., 90, 132–150, https://doi.org/10.1016/j.atmosres.2008.01.005, 2008.

Kulmala, M., Maso, M. D., Mäkelä, J. M., L. Pirjola, Väkevä, M., P. Aalto, Miikkulainen, P., Hämeri, K., and O' Dowd, C. D.: On the formation, growth and composition of nucleation mode particles, Tellus B, 53, 479–490, 2001.

Kulmala, M., Vehkamäki, H., Petäjä, T., Dal Maso, M., Lauri, A., Kerminen, V. M., Birmili, W., and McMurry, P. H.: Formation and growth rates of ultrafine atmospheric particles: a review of observations, J. Aerosol Sci., 35, 143–176, https://doi.org/10.1016/j.jaerosci.2003.10.003, 2004.

Kulmala, M., Petaja, T., Nieminen, T., Sipila, M., Manninen, H. E., Lehtipalo, K., Maso, M. D., Aalto, P. P., Junninen, H., Paasonen, P., Riipinen, I., Lehtinen, K. E., Laaksonen, A., and Kerminen, V.-M.: Measurement of the nucleation

of atmospheric aerosol particles, Nat. Protoc., 7, 1651–1667, https://doi.org/10.1038/nprot.2012.091, 2012.

Kulmala, M., Kontkanen, J., Junninen, H., Lehtipalo, K., Manninen, H. E., Nieminen, T., Petaja, T., Sipila, M., Schobesberger, S., Rantala, P., Franchin, A., Jokinen, T., Jarvinen, E., Aijala, M., Kangasluoma, J., Hakala, J., Aalto, P. P., Paasonen, P., Mikkila, J., Vanhanen, J., Aalto, J., Hakola, H., Makkonen, U., Ruuskanen, T., Mauldin, R. L., 3rd, Duplissy, J., Vehkamaki, H., Back, J., Kortelainen, A., Riipinen, I., Kurten, T., Johnston, M. V., Smith, J. N., Ehn, M., Mentel, T. F., Lehtinen, K. E., Laaksonen, A., Kerminen, V.-M., and Worsnop, D. R.: Direct observations of atmospheric aerosol nucleation, Science, 339, 943–946, https://doi.org/10.1126/science.1227385, 2013.

Kulmala, M., Petaja, T., Ehn, M., Thornton, J., Sipila, M., Worsnop, D. R., and Kerminen, V. M.: Chemistry of atmospheric nucleation: on the recent advances on precursor characterization and atmospheric cluster composition in connection with atmospheric new particle formation, Annu. Rev. Phys. Chem., 65, 21–37, https://doi.org/10.1146/annurev-physchem-040412-110014, 2014.

Kyrö, E.-M., Kerminen, V.-M., Virkkula, A., Dal Maso, M., Parshintsev, J., Ruíz-Jimenez, J., Forsström, L., Manninen, H. E., Riekkola, M.-L., Heinonen, P., and Kulmala, M.: Antarctic new particle formation from continental biogenic precursors, Atmos. Chem. Phys., 13, 3527–3546, https://doi.org/10.5194/acp-13-3527-2013, 2013.

Leaitch, W. R., Korolev, A., Aliabadi, A. A., Burkart, J., Willis, M. D., Abbatt, J. P. D., Bozem, H., Hoor, P., Köllner, F., Schneider, J., Herber, A., Konrad, C., and Brauner, R.: Effects of 20–100 nm particles on liquid clouds in the clean summertime Arctic, Atmos. Chem. Phys., 16, 11107–11124, https://doi.org/10.5194/acp-16-11107-2016, 2016.

Lehtipalo, K., Leppä, J., Kontkanen, J., Kangasluoma, J., Franchin, A., Wimmer, D., Schobesberger, S., Junninen, H., Petäjä, T., Sipilä, M., Mikkilä, J., Vanhanen, J., Worsnop, D. R., and Kulmala, M.: Methods for determining particle size distribution and growth rates between 1 and 3 nm using the Particle Size Magnifier, Boreal Environ. Res., 19 (suppl. B), 215–236, 2014.

Leino, K., Nieminen, T., Manninen, H. E., Petäjä, T., Kerminen, V.-M., and Kulmala, M.: Intermediate ions as a strong indicator of new particle formation bursts in a boreal forest, Boreal Environ. Res., 21, 274–286, 2016.

Lihavainen, H., Komppula, M., Kerminen, V.-M., Järvinen, H., Viisanen, Y., Lehtinen, K., Vana, M., and Kulmala, M.: Size distributions of atmospheric ions inside clouds and in cloud-free air at a remote continental site, Boreal Environ. Res., 12, 337–344, 2007.

Manninen, H. E., Petäjä, T., Asmi, E., Riipinen, I., Niemnen, T., Mikkilä, J., Hõrrak, U., Mirme, A., Mirme, S., Laakso, L., Kerminen, V.-M., and Kulmala, M.: Long-time field measurements of charged and neutral clusters using Neutral cluster and Air Ion Spectrometer (NAIS), Boreal Environ. Res., 14, 591–605, 2009.

Manninen, H. E., Nieminen, T., Asmi, E., Gagné, S., Häkkinen, S., Lehtipalo, K., Aalto, P., Vana, M., Mirme, A., Mirme, S., Hõrrak, U., Plass-Dülmer, C., Stange, G., Kiss, G., Hoffer, A., Törő, N., Moerman, M., Henzing, B., de Leeuw, G., Brinkenberg, M., Kouvarakis, G. N., Bougiatioti, A., Mihalopoulos, N., O'Dowd, C., Ceburnis, D., Arneth, A., Svenningsson, B., Swietlicki, E., Tarozzi, L., Decesari, S., Facchini, M. C., Birmili, W., Sonntag, A., Wiedensohler, A., Boulon, J., Sellegri, K., Laj, P., Gysel, M., Bukowiecki, N., Weingartner, E., Wehrle, G., Laaksonen, A., Hamed, A., Joutsensaari, J., Petäjä, T., Kerminen, V.-M., and Kulmala, M.: EUCAARI ion spectrometer measurements at 12 European sites – analysis of new particle formation events, Atmos. Chem. Phys., 10, 7907–7927, https://doi.org/10.5194/acp-10-7907-2010, 2010.

Mason, E. A. and McDaniel, E. W.: Transport Properties of Ions in Gases, John Wiley and Sons, New York, Chichester, Brisbane, Toronto, Singapore, 1988.

Mirme, A., Tamm, E., Mordas, G., Vana, M., Uin, H., Mirme, S., Bernotas, T., Laakso, L., Hirsikko, A., and Kulmala, M.: A wide-range multi-channel Air Ion Spectrometer, Boreal Environ. Res., 12, 247–264, 2007.

Mirme, S., Mirme, A., Minikin, A., Petzold, A., Hõrrak, U., Kerminen, V.-M., and Kulmala, M.: Atmospheric sub-3 nm particles at high altitudes, Atmos. Chem. Phys., 10, 437–451, https://doi.org/10.5194/acp-10-437-2010, 2010.

Mirme, S. and Mirme, A.: The mathematical principles and design of the NAIS – a spectrometer for the measurement of cluster ion and nanometer aerosol size distributions, Atmos. Meas. Tech., 6, 1061–1071, https://doi.org/10.5194/amt-6-1061-2013, 2013.

Nieminen, T., Paasonen, P., Manninen, H. E., Sellegri, K., Kerminen, V.-M., and Kulmala, M.: Parameterization of ion-induced nucleation rates based on ambient observations, Atmos. Chem. Phys., 11, 3393–3402, https://doi.org/10.5194/acp-11-3393-2011, 2011.

Pant, V., Siingh, D., and Kamra, A. K.: Size distribution of atmospheric aerosols at Maitri, Antarctica, Atmos. Environ., 45, 5138–5149, https://doi.org/10.1016/j.atmosenv.2011.06.028, 2011.

Park, J., Sakurai, H., Vollmers, K., and McMurry, P. H.: Aerosol size distributions measured at the South Pole during ISCAT, Atmos. Environ., 38, 5493–5500, https://doi.org/10.1016/j.atmosenv.2002.12.001, 2004.

Pirjola, L., Kulmala, M., Wilck, M., Bischoff, A., Stratmann, F., and Otto, E.: Formation of sulphuric acid aerosols and cloud condensation nuclei: an expression for significant nucleation and model comparison, J. Aerosol Sci., 30, 1079–1094, 1998.

Poling, B. R., Prausnitz, J. M., and O'Connell, J. P.: The Properties of Gas and Liquids, 5 ed., McGraw-Hill, New York, 2004.

Pomeroy, J. W. and Jones, H. G.: Wind-Blown Snow: Sublimation, Trransport and Changes to Polar Snow, Processes of Chemical Exchange between the Atmosphere and Polar Snow, NATO ASI Series, Berlin, 453–490, 1996.

Portin, H., Leskinen, A., Hao, L., Kortelainen, A., Miettinen, P., Jaatinen, A., Laaksonen, A., Lehtinen, K. E. J., Romakkaniemi, S., and Komppula, M.: The effect of local sources on particle size and chemical composition and their role in aerosol–cloud interactions at Puijo measurement station, Atmos. Chem. Phys., 14, 6021–6034, https://doi.org/10.5194/acp-14-6021-2014, 2014.

Poschl, U.: Atmospheric aerosols: composition, transformation, climate and health effects, Angew. Chem. Int. Edit., 44, 7520–7540, https://doi.org/10.1002/anie.200501122, 2005.

Samson, J. A., Barnard, S. C., Obremski, J. S., Riley, D. C., Black, J. J., and Hogan, A. W.: On the systematic variation In surface aerosol concentration at the South Pole, Atmos. Res., 25, 385–396, 1990.

Tang, M. J., Cox, R. A., and Kalberer, M.: Compilation and evaluation of gas phase diffusion coefficients of reactive trace gases in the atmosphere: volume 1. Inorganic compounds, Atmos. Chem. Phys., 14, 9233–9247, https://doi.org/10.5194/acp-14-9233-2014, 2014.

Tinsley, B. A.: The global atmospheric electric circuit and its effects on cloud microphysics, Rep. Prog. Phys., 71, 066801, https://doi.org/10.1088/0034-4885/71/6/066801, 2008.

Virkkula, A., Hirsikko, A., Vana, M., Aalto, P. P., Hillamo, R., and Kulmala, M.: Charged particle size distributions and analysis of particle formation events at the Finnish antarctic research station aboa, Boreal Environ. Res., 12, 397–408, 2007.

Wagner, R., Manninen, H. E., Franchin, A., Lehtipalo, K., Mirme, S., Steiner, G., Petäjä, T., and Kulmala, M.: On the accuracy of ion measurements using a Neutral cluster and Air Ion Spectrometer, Boreal Environ. Res., 21, 230–241, 2016.

Wang, Z., Wu, Z., Yue, D., Shang, D., Guo, S., Sun, J., Ding, A., Wang, L., Jiang, J., Guo, H., Gao, J., Cheung, H. C., Morawska, L., Keywood, M., and Hu, M.: New particle formation in China: current knowledge and further directions, Sci. Total Environ., 577, 258–266, https://doi.org/10.1016/j.scitotenv.2016.10.177, 2017.

Waring, M. S. and Siegel, J. A.: The effect of an ion generator on indoor air quality in a residential room, Indoor Air, 21, 267–276, https://doi.org/10.1111/j.1600-0668.2010.00696.x, 2011.

Weller, R., Minikin, A., Wagenbach, D., and Dreiling, V.: Characterization of the inter-annual, seasonal, and diurnal variations of condensation particle concentrations at Neumayer, Antarctica, Atmos. Chem. Phys., 11, 13243–13257, https://doi.org/10.5194/acp-11-13243-2011, 2011.

Weller, R., Schmidt, K., Teinilä, K., and Hillamo, R.: Natural new particle formation at the coastal Antarctic site Neumayer, Atmos. Chem. Phys., 15, 11399–11410, https://doi.org/10.5194/acp-15-11399-2015, 2015.

Wiedensohler, A., Birmili, W., Nowak, A., Sonntag, A., Weinhold, K., Merkel, M., Wehner, B., Tuch, T., Pfeifer, S., Fiebig, M., Fjäraa, A. M., Asmi, E., Sellegri, K., Depuy, R., Venzac, H., Villani, P., Laj, P., Aalto, P., Ogren, J. A., Swietlicki, E., Williams, P., Roldin, P., Quincey, P., Hüglin, C., Fierz-Schmidhauser, R., Gysel, M., Weingartner, E., Riccobono, F., Santos, S., Grüning, C., Faloon, K., Beddows, D., Harrison, R., Monahan, C., Jennings, S. G., O'Dowd, C. D., Marinoni, A., Horn, H.-G., Keck, L., Jiang, J., Scheckman, J., McMurry, P. H., Deng, Z., Zhao, C. S., Moerman, M., Henzing, B., de Leeuw, G., Löschau, G., and Bastian, S.: Mobility particle size spectrometers: harmonization of technical standards and data structure to facilitate high quality long-term observations of atmospheric particle number size distributions, Atmos. Meas. Tech., 5, 657–685, https://doi.org/10.5194/amt-5-657-2012, 2012.

Wilson, C. T. R.: The electric field of a thundercloud and some of its effects, Proc. Phys. Soc. London, 37, 32D, https://doi.org/10.1088/1478-7814/37/1/314, 1924.

Yli-Juuti, T., Nieminen, T., Hirsikko, A., Aalto, P. P., Asmi, E., Hõrrak, U., Manninen, H. E., Patokoski, J., Dal Maso, M., Petäjä, T., Rinne, J., Kulmala, M., and Riipinen, I.: Growth rates of nucleation mode particles in Hyytiälä during 2003–2009: variation with particle size, season, data analysis method and ambient conditions, Atmos. Chem. Phys., 11, 12865–12886, https://doi.org/10.5194/acp-11-12865-2011, 2011.

Yu, F. and Turco, R.: Case studies of particle formation events observed in boreal forests: implications for nucleation mechanisms, Atmos. Chem. Phys., 8, 6085–6102, https://doi.org/10.5194/acp-8-6085-2008, 2008.

Supplement of Atmos. Chem. Phys., 17, 13783–13800, 2017
https://doi.org/10.5194/acp-17-13783-2017-supplement

Atmospheric Chemistry and Physics Open Access EGU

Supplement of

Features in air ions measured by an air ion spectrometer (AIS) at Dome C

Xuemeng Chen et al.

Correspondence to: Xuemeng Chen (xuemeng.chen@helsinki.fi)

Table S1. Coefficients for the fittings ($y = a \cdot e^{b \cdot x}$) shown in Figs. 9 and S4. R^2 is the coefficient of determination measuring the goodness of fit, which denotes the fraction of the total variation in the data can be explained by the fit. For Dome C data shown in Fig. 9, fits 1 and 2 are obtained based on all data below or above the wind speed threshold (7 m/s), respectively. The grey data points in Fig. 9 are used in determining the fitting coefficients for fits 3 and 4. For Aboa data shown in Fig. S4, a wind speed threshold of 17 m/s is used.

DOME C (Figs. 9 & S4)	Cluster (0.9-1.9 nm) ion concentrations vs. wind speeds					
	Fits	*a*	*b*	95% conference interval for *a*	95% conference interval for *b*	R^2
	1	0.69	26.34	[0.65 0.73]	[21.62 32.10]	0.24
	2	0.51	68.64	[0.41 0.60]	[29.88 157.67]	0.12
	3	0.73	21.83	[0.69 0.77]	[18.02 26.44]	0.28
	4	0.44	327	[0.40 0.47]	[244.95 436.53]	0.52
	1.9-10 nm ion concentrations vs. wind speeds					
	Fits	*a*	*b*	95% conference interval for *a*	95% conference interval for *b*	R^2
	1	1.14	0.07	[1.08 1.2]	[0.05 0.09]	0.29
	2	0.61	2.1	[0.71 0.88]	[0.88 5.01]	0.15
	3	1.19	0.05	[1.25 0.04]	[0.04 0.07]	0.31
	4	0.54	9.87	[0.58 7.18]	[7.18 13.58]	0.58
ABOA (Fig. S4)	0.9-2.2 nm ion concentrations vs. wind speeds					
	Fits	*a*	*b*	95% conference interval for *a*	95% conference interval for *b*	R^2
	6	0.17	14.98	[0.15 0.19]	[9.02 24 88]	0.66
	2.2-9.5 nm ion concentrations vs. wind speeds					
	Fits	*a*	*b*	95% conference interval for *a*	95% conference interval for *b*	R^2
	5	0.24	1.45	[0.22 0.26]	[1.26 1.68]	0.35
	6	0.06	63.24	[0.04 0.09]	[34.72 115.18]	0.17

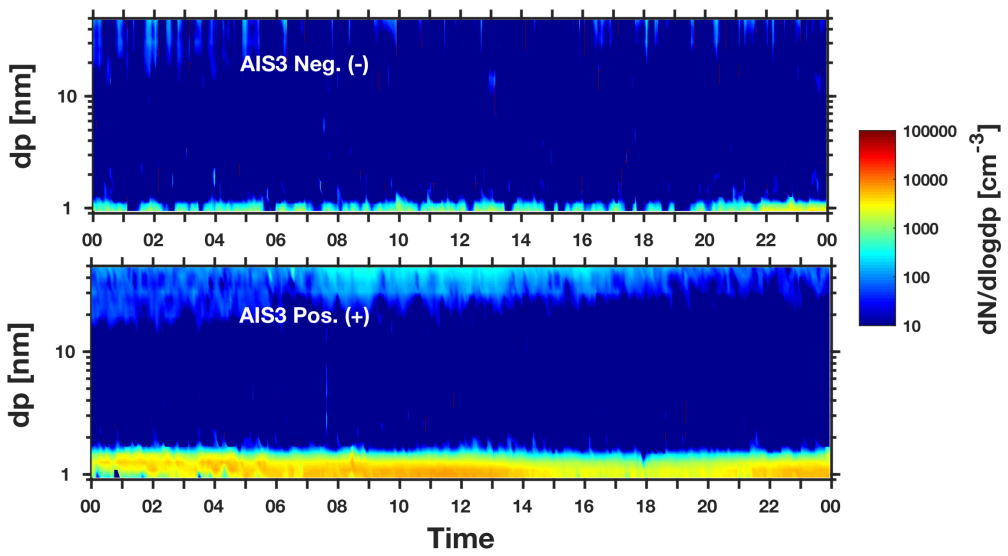

Figure S1. AIS spectra on Feb. 8, 2011. The negative polarity shown in the upper panel and the positive in the lower panel.

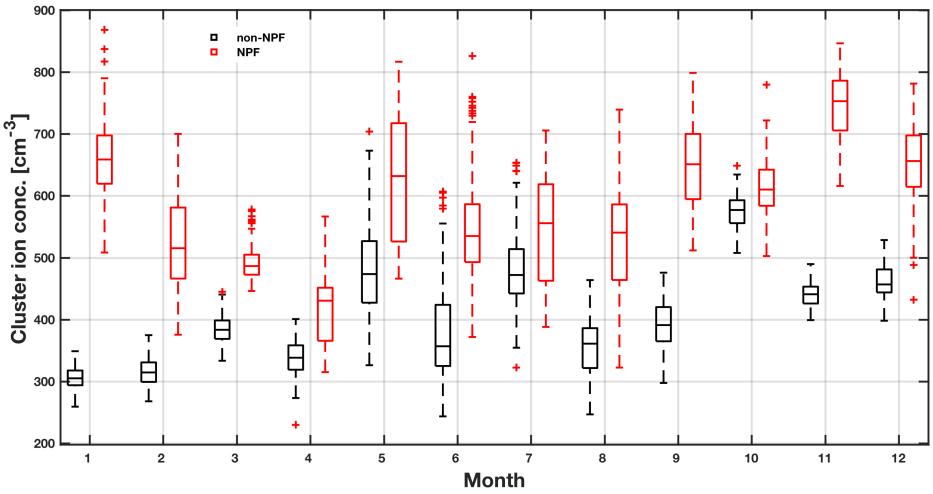

Figure S2. Seasonality in the median cluster ion (0.8-1.7 nm) concentration at SMEAR II station in southern Finland. Tops and bottoms of the boxes are the 75th and 25th percentiles of the median daily cluster ion concentrations in 10 min time resolution, with bars in the middle showing the 50th percentiles. Whiskers represent spans of the interquartile ranges multiplied by 1.5. Cluster ion concentrations on new particle formation (NPF) days shown in red and on non-event days in black. The event classification was based on the method described by Dal Maso et al. (2005).

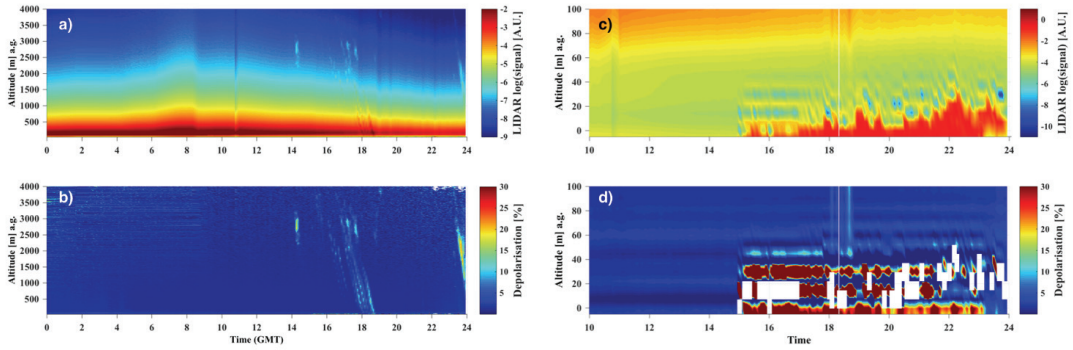

Figure S3. Left column: a) & b) Lidar observation on 20 January 2011 at Dome C. Right column: c) & d) zoom into the lowest heights (0-100 m) between 10:00 and 24:00 UTC. The lowest part of c) & d) (0-30 m) is a non-linear part in the LIDAR signal, and electrically induced noise bands are evident in d). The height information is also possibly subject to an uncertainty of ±5 m.

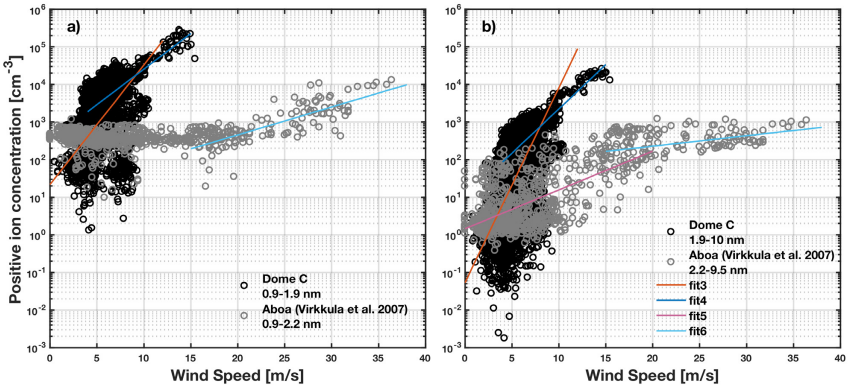

Figure S4. Ion concentrations as a function of wind speeds. a) Ion concentration in the cluster size range: 0.9-1.9 nm for Dome C (black circles) and 0.9-2.2 nm for Aboa (grey circles, from Virkkula et al. (2007)). b) Ion concentration in the size range of 1.9-10 nm for Dome C (black circles) and in the intermediate size range of 2.2-9.5 nm for Aboa (grey circles, from Virkkula et al. (2007)). The Aboa ion data were reported in mass diameters. The size ranges referred here are reconverted from the measured electrical mobility channels in mobility diameters. The solid lines are linear fits to the logarithm of the ion concentration data. The fitting parameters are given in Table S1. A wind speed threshold of 17 m/s is used for characterising the 2-step linear feature at Aboa and 7 m/s for that at Dome C.

Paper IV

Atmos. Chem. Phys., 16, 14297–14315, 2016
www.atmos-chem-phys.net/16/14297/2016/
doi:10.5194/acp-16-14297-2016

Atmospheric Chemistry and Physics Open Access EGU

How do air ions reflect variations in ionising radiation in the lower atmosphere in a boreal forest?

Xuemeng Chen[1], Veli-Matti Kerminen[1], Jussi Paatero[2], Pauli Paasonen[1], Hanna E. Manninen[1], Tuomo Nieminen[1,3], Tuukka Petäjä[1], and Markku Kulmala[1]

[1]Department of Physics, University of Helsinki, P.O. Box 64, 00014 Helsinki, Finland
[2]Finnish Meteorological Institute, Observation services, P.O. Box 503, 00101 Helsinki, Finland
[3]Department of Applied Physics, University of Eastern Finland, P.O. Box 1627, 70211 Kuopio, Finland

Correspondence to: Xuemeng Chen (xuemeng.chen@helsinki.fi)

Received: 23 May 2016 – Published in Atmos. Chem. Phys. Discuss.: 20 June 2016
Revised: 30 September 2016 – Accepted: 21 October 2016 – Published: 16 November 2016

Abstract. Most of the ion production in the atmosphere is attributed to ionising radiation. In the lower atmosphere, ionising radiation consists mainly of the decay emissions of radon and its progeny, gamma radiation of the terrestrial origin as well as photons and elementary particles of cosmic radiation. These types of radiation produce ion pairs via the ionisation of nitrogen and oxygen as well as trace species in the atmosphere, the rate of which is defined as the ionising capacity. Larger air ions are produced out of the initial charge carriers by processes such as clustering or attachment to preexisting aerosol particles. This study aimed (1) to identify the key factors responsible for the variability in ionising radiation and in the observed air ion concentrations, (2) to reveal the linkage between them and (3) to provide an in-depth analysis into the effects of ionising radiation on air ion formation, based on measurement data collected during 2003–2006 from a boreal forest site in southern Finland. In general, gamma radiation dominated the ion production in the lower atmosphere. Variations in the ionising capacity came from mixing layer dynamics, soil type and moisture content, meteorological conditions, long-distance transportation, snow cover attenuation and precipitation. Slightly similar diurnal patterns to variations in the ionising capacity were observed in air ion concentrations of the cluster size (0.8–1.7 nm in mobility diameters). However, features observed in the 0.8–1 nm ion concentration were in good connection to variations of the ionising capacity. Further, by carefully constraining perturbing variables, a strong dependency of the cluster ion concentration on the ionising capacity was identified, proving the functionality of ionising radiation in air ion production in the lower atmosphere. This relationship, however, was only clearly observed on new particle formation (NPF) days, possibly indicating that charges after being born underwent different processes on NPF days and non-event days and also that the transformation of newly formed charges to cluster ions occurred in a shorter timescale on NPF days than on non-event days.

1 Introduction

Ambient radioactivity in the lower atmosphere supplies ionising energy for the production of electric charges in the air. It consists of natural and anthropogenic radioactivity. The anthropogenic fraction comes mainly from routine and accidental emissions from nuclear power plants and related facilities as well as nuclear detonations. Minor emissions of natural radioactivity occur also in connection with various mining activities. Natural radioactivity is composed of the decay emissions of naturally occurring radionuclides and cosmic radiation. Alpha and beta particles as well as the associated gamma and X-ray photons constitute the ionising radiation from natural radionuclides. ^{222}Rn is a naturally occurring radioactive gas that is the daughter nuclide of ^{226}Ra, which is typically present in soil grains. Naturally two other isotopic forms of radon exist as well, ^{219}Rn and ^{220}Rn, but in trace quantities. Once formed, radon can diffuse through soil pores and eventually enter into the atmosphere (Chen et al., 2016; Nazaroff, 1992). Radon and its progeny undergo alpha and beta decay in the atmosphere and, together with the accom-

panying gamma radiation, supply the energy for ionisation. Apart from radon, gamma radiation from the Earth's crust as well as photons and elementary particles of cosmic radiation also contribute to the creation of electric charges in the lower atmosphere. In the case of cosmic radiation near the ground, most of the ionisation of air is due to muons, with minor contributions from neutrons, photons and electrons (Goldhagen, 2000). Typically, 32.5–35 eV is needed to produce an ion pair in the atmosphere (Krause et al., 2002), with an average expenditure of 34 eV per ion pair often accepted in the lower atmosphere (Jesse and Sadaukis, 1957; Laakso et al., 2004; Wilkening, 1981).

Due to the atmospheric abundance of nitrogen (N_2) and oxygen (O_2), their derivatives are the initial carriers of electric charges generated from the ionisation process. These initial charge carriers are known as primary ions, which can be an electron or simple atomic or molecular ions. Primary ions are consumed either directly or via the formation of more complex molecular ions by (1) ion–ion recombination, (2) clustering, (3) charge transfer to pre-existing aerosol particles (or clusters) or gaseous species in the atmosphere and (4) sink to foreign surfaces. These processes may involve both chemical reactions and physical transformations. The recombination and sink to foreign surfaces lead to a reduced amount of electric charges in the air, whereas the clustering and charge transfer result in either charged or neutral gaseous species, clusters and aerosol particles. The term "air ion" refers to all airborne substances that are electrically charged, ranging from primary ions to charged aerosol particles. The relationship between primary ions, molecular ions and cluster ions is illustrated in Fig. 1.

Air ions were historically concerned in the discipline of atmospheric electricity (Israël, 1970), because their flow in the electric field of the Earth–atmosphere system serves as the measurable conduction current in the atmosphere (Harrison and Carslaw, 2003; Tinsley, 2008; Wilson, 1921). The interest in atmospheric electricity could be traced back to the early 18th century, when thunderstorms were suggested to be electrical phenomena (Herbert, 1997). However, only after Benjamin Franklin proposed the idea to draw electricity down from lightning in 1752 was this theory confirmed, and the study of atmospheric electricity became popular (Herbert, 1997; Tinsley, 2008). Early efforts in this field were substantially invested in understanding lightning and electrification of clouds (e.g. Canton, 1753a, b; Franklin, 1751), even though there were reports on observations of atmospheric electricity under fair weather conditions (Bennett and Harrison, 2007; Canton, 1753b; Read, 1792). Why the air was conductive could not, however, be explained. Meanwhile, Charles-Augustin de Coulomb observed gradual discharge of a well-insulated electroscope around 1785 and he attributed his observation to the contact of suspending particles present in the air (De Angelis, 2014; Walter, 2012). This phenomenon was reproduced by Michael Faraday half a century later in 1835 (De Angelis, 2014). Thanks to the further improvement of the electroscope by William Thomson and Lord Kelvin (De Angelis, 2014; Flagan, 1998), Crookes (1878) found that the discharge rate of an electroscope decreases with a decreasing air pressure, suggesting that it is the air inside the instrument that manipulates the discharge. However, the reasoning remained undisclosed until the discovery of radioactivity by Wilhelm Röntgen, Henri Becquerel and Marie and Pierre Curie enabled Julius Elster and Hans Geitel from Germany and Charles Thomson Rees Wilson from Scotland to relate the spontaneous discharge of the electroscope to ionisation of the air by radioactive sources (Carlson and De Angelis, 2011; De Angelis, 2014; Wilson, 1895, 1899). Therefrom, the importance of air ions in the atmosphere emerged. Contemporaneously, the interest of Joseph John Thomson, director of the Cavendish Laboratory, in the charge carriers produced by ionising radiation motivated the development of instrumentations for measuring electrical charges in gases, leading to various valuable outcomes, e.g. the cloud chamber designed by C. T. R. Wilson, as well as techniques for measuring ion mobility by Ernest Rutherford and John Zeleny and for studying gaseous ion diffusion by John Sealy Townsend (Flagan, 1998; Robotti, 2006). These works laid the theoretical and instrumental foundation for later aerosol studies. The experimental results from C. T. R. Wilson's cloud chamber measurements in 1895 and 1899 on the influence of ionising radiation on the formation of cloud droplets brought interest in air ions to the atmospheric aerosol community. Inspired by these early works, advancements in atmospheric aerosol studies progressed both instrumentally and theoretically over the century (e.g. Aplin and Harrison, 2000; Hewitt, 1957; Hinds, 1999; Hogg, 1939; Mason and McDaniel, 1988; Millikan, 1923; Nolan, 1924; Reischl, 1991; Rosell-Llompart and Fernández de la Mora, 1993; Tammet, 1970, 1995, 2006).

Devices employed for ion studies comprise different types of aspiration condensers, ion mobility spectrometers (IMSs) and mass spectrometers (Cumeras et al., 2015; Hirsikko et al., 2011; Laskin et al., 2012; Tammet, 1970). Notably, modern key instruments for field observations of air ions are mainly aspiration contender-based devices and mass spectrometers, such as the Gerdien counter – an integral aspiration condenser (Aplin and Harrison, 2000; Gerdien, 1905; Vojtek et al., 2006) – ion spectrometers designed by Airel Ltd. – single or multiple channel aspiration condensers (Kulmala et al., 2016; Manninen et al., 2009; Mirme et al., 2007; Tammet, 2006, 2011) – and the atmospheric pressure interface time-of-flight mass spectrometer (APi-ToF) (Junninen et al., 2010). While aspiration condensers provide information on the concentration and mobility of charge carriers, mass spectrometers reveal mainly the chemical properties of them. The IMS, however, has a limited application in studying ambient ions due to difficulties in spectrum interpretation (Hirsikko et al., 2011). The purpose of these instrumentations is not only air ion or air conductivity observations but also

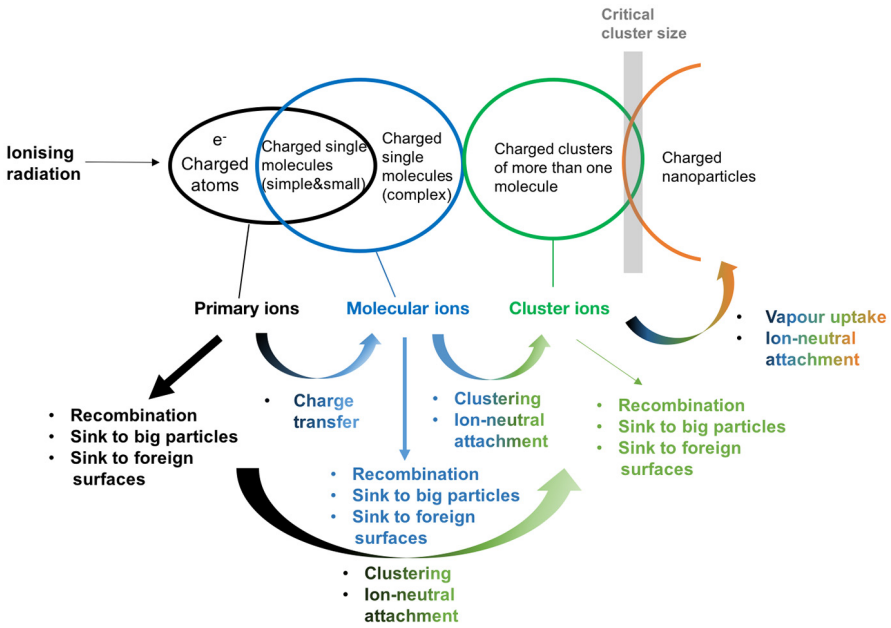

Figure 1. A schematic demonstration of the relationship between primary ions, molecular ions and cluster ions, as well as processes governing their formation and loss.

nano-material synthesis (Kruis et al., 1998) and the improvement of the fundamental understanding on the relationship between mobility, mass and size (Ku and Fernández de la Mora, 2009).

At present, the number size distribution of air ions can be measured down to about 0.8 nm in Millikan mobility size by using ion spectrometers (Manninen et al., 2009; Tammet, 2006, 2011). Most air ions concentrate at the lowest size band with a diameter of 0.8–1.7 nm (Manninen et al., 2009), which is generally known as the cluster size range (Tammet, 1995, 2012). In principle, this size range contains large molecular ions and clusters of molecular ions. Ions smaller than 0.8 nm comprise mostly relatively simple molecular ions, which are either primary ions or originate from the survived fraction of primary ions from recombination. The critical cluster size was found to be 1.5 ± 0.3 nm for atmospheric nucleation (Kulmala et al., 2013). Once the critical cluster size is reached, further growth of a cluster in size is energetically favoured (Vehkamäki, 2006). Air ions that have sizes larger than the critical cluster size are therefore typically viewed as nanoparticles, observable especially during new particle formation (NPF) events (Kulmala et al., 2012; Manninen et al., 2009). However, since the atmosphere is a vast pool full of clusters with different structures and compositions, the critical cluster size is rather a size range than a single size, as demonstrated in Fig. 1. As a consequence, a clear size separation exists neither between cluster ions and charged nanoparticles nor between molecular ions and cluster ions. Thus, although the size range of 0.8–1.7 nm may contain molecular ions, cluster ions and even charged nanoparticles, we hereafter refer ions in this size range as cluster ions, unless otherwise mentioned.

Although it is known that ionising radiation creates ion pairs via ionisation in the atmosphere (Flagan, 1998; Harrison and Carslaw, 2003; Israël, 1970), except for a few attempts (Hirsikko et al., 2007; Laakso et al., 2004), only minor efforts have been invested in understanding the connection between ionising radiation and observed air ions in the lower atmosphere. Moreover, there is a lack of quantification on the underlying processes. Such deficiencies prompt the motivation of this work to examine how variations in ionising radiation are reflected in observed air ions based on ambient measurement. The aims of this study are (1) to identify the key factors responsible for the variability in ionising radiation and in observed air ion concentrations, (2) to reveal the linkage of observed air ions to the variations in ionising radiation and (3) to provide an in-depth analysis on the effects of ionising radiation on air ion formation. We will first introduce factors that cause the seasonal and diurnal variability in ionising radiation and air ions and then exposit the connection of observed air ions to variations in ionising radiation and the influence of different atmospheric conditions on this relationship. To assist our analysis, we will determine theoretically the potential maximum production rate of ion pairs

by ionising radiation, based on our ionising radiation measurements and an assumed average energy expenditure of 34 eV for creating an ion pair, which is termed as the ionising capacity. The ionising capacity can be viewed as a measure of the theoretical maximum ionisation rate, which, however, may not well capture the true ionisation rate due to uncertainties in ionising radiation measurements, possible energy dissipation of ionising radiation in excitation and the invalidity concern associated with the use of 34 eV per production of an ion pair at near ground level in our calculation.

2 Materials and methods

The data presented in this work were collected from a boreal forest site, which is known as the SMEAR II station located at Hyytiälä, Southern Finland (61°51′ N, 24°17′ E; 181 m above sea level) (Hari and Kulmala, 2005), during 2003–2006. Monitoring devices for ionising radiation have been deployed to this site since 2000 and the air ion measurement was initialised in 2003. Both of these measurements have been integrated into the long-term monitoring system on the site. Other data used in this work included the condensation sink (CS; Kulmala et al., 2012) derived from the number size distribution of ambient aerosol particles, ambient relative humidity (RH), soil water content (SWC), soil temperature, snow cover depth and modelled mixing layer height (MLH). The estimates of MLH were retrieved from the European Centre for Medium-Range Weather Forecasts (ECMWF) Meteorological Archival and Retrieval System (MARS), Reading, UK (www.ecmwf.int).

2.1 Instrumentation and data processing

The ionising radiation measurement system consists of a radon monitor and a gamma spectrometer. Both devices are maintained by the Finnish Meteorological Institute (FMI). The air ion data were obtained by a Balanced Scanning Mobility Analyser (BSMA) (Tammet, 2006), which is part of the aerosol monitoring system at the station. A differential mobility particle sizer (DMPS) has been responsible for observing the ambient aerosol number size distribution on this site since 1996. For the study period of 2003–2006, the data availability for air ions, particles, radon and gamma was 91, 99, 71 and 76 %, respectively, allowing the coverage of every single day-of-year by each parameter. Data are presented in local winter time (UTC+02:00).

2.1.1 Ionising radiation measurement

The radon monitor is a dual fixed filter-based instrument and measures the aerosol beta activity. Its inlet is fixed at 6 m above the ground and this device has been described in detail by Paatero et al. (1994). Briefly, it is made up of two cylindrical Geiger–Müller counters covered with glass-fibre filters in lead shielding. A pump controller directs the airflow to each counter alternatively for a 4 h period, allowing the beta activity on the other counter to decay. The counting efficiency for beta particles is determined by the geometric configuration of the counting system together with the intrinsic detection efficiency of the GM tubes, which is 0.96 and 4.3 % for ^{214}Pb and ^{214}Bi beta particles, respectively. The cumulative counts are logged at 10 min intervals. The re-establishment of the radon activity concentration into Bq m^{-3} from the recorded count rates was achieved following the method and assumption given by Paatero et al. (1994) and Chen et al. (2016).

The gamma spectrometer is a scintillation-type detector using a piece of 76 mm × 76 mm NaI(Tl) crystal as the detection medium (Hirsikko et al., 2007; Laakso et al., 2004). It is kept at the height of 1.5 m above the ground in a temperature-controlled shelter. Pulse height spectra over the energy range of 100–3000 keV are recorded with a multichannel analyser and the total count rate within this energy range are registered with a time resolution of 10 min. The total gain of the detecting system is kept constant via digital spectrum stabilisation using the ^{40}K gamma peak (1460 keV) as the reference. For the determination of the ionising capacity in this work, the total count rate data were used instead of the spectral information. The recorded total count rates were converted into dose rates in the air (μSv h^{-1}) by a calibration factor obtained from an instrumental comparison to a pressurised ionisation chamber. Thus, the obtained dose rates take into account ionisation by both gamma radiation of terrestrial origins and from radon decays and cosmic ray constituents. However, a portion of high-energy cosmic ray muons may not be well detected by our counting system, possibly due to their weak interaction with the detector material or their light production leading to electrical pulses exceeding the dynamic range of the instrumentation.

2.1.2 Air ion measurement

The most state-of-the-art measurement techniques nowadays, usually employing a mass spectrometer as the detector, such as the APi-ToF (Junninen et al., 2010, 2016), are able to track air ions down to molecular sizes and characterise their chemical composition, but they lack the capability for providing information on the number concentration. Ion spectrometers are the most deployed type of devices for the study of air ion concentrations in segregated mobility channels (Hirsikko et al., 2011). The BSMA (Tammet, 2006) and the Neutral Cluster and Air Ion Spectrometer (NAIS) (Kulmala et al., 2007; Manninen et al., 2016; Mirme and Mirme, 2013) are examples in this category. The highest measurable mobility with these ion spectrometers is 3.2 cm^2 Vs^{-1} (Mirme and Mirme, 2013; Tammet, 2006, 2011), equivalent to a mobility diameter of about 0.8 nm based on the Stokes–Millikan equation. The mobility size of a particle may vary with the choice of a mobility diameter model as well as parameters and coefficients used therein (e.g. Ehn et al., 2011;

Tammet, 1995, 2011; Mäkelä et al., 1996; Fernandez-Garcia and Fernandez de la Mora, 2013) .

Ambient air ion data used in this work were measured by a BSMA. The inlet of this instrument was at a height of 1.5 m above the ground. The BSMA is an integral-type counter (Tammet, 1970), which offers air ion mobility spectra by a continuous voltage-scanning system. It is composed of two plain aspiration condensers, one for each polarity. An electrofilter is installed at the inlet of each condenser. The BSMA has a total flow rate of 2640 L min^{-1}, which is split into two streams at the inlet, supplying each condenser with a flow of 1320 L min^{-1}. For either condenser, only one-eighth of the air stream passing through the electrofilter contains air ions, which is taken as the sample flow, leaving the rest ion-free fraction as the sheath flow. After the electrofilter, there exists an electric field in each condenser, created between a grounded collecting electrode and a repelling electrode that is kept at a high potential, where the trajectories of sampled air ions are deflected towards the collecting electrode. A 33 mm long and 170 mm wide sensing unit is inlaid on the counter electrode of each polarity. Both sensing units share a common electrometer for counting the captured ions. A bridging circuit balances the voltage supply onto the repelling electrodes, so that the induced electric currents on the collectors during the voltage scanning are equal in magnitudes, but of opposite polarity. This design avoids the generation of noise in the common electrometer. The BSMA segregates air ions based on their mobility into 16 channels in the range of 0.032–3.2 cm^2 Vs^{-1}. A full measurement cycle scanning through the mobility range for both polarities takes 10 min. The air ion number concentration measured in the mobility domain was automatically processed into number size distributions by the recording programme, with the particle size expressed in Tammet's mass diameter (Tammet, 1995, 2006), which was subsequently converted to the mobility diameter based on the mobility size conversion model proposed by Tammet (1995) and the Stokes–Millikan equation. The core of the Tammet model lies on a modified Millikan equation, which approaches the Chapman–Enskog equation in the free molecular scale and the Millikan equation in the macroscopic scale. The equivalent mobility diameter range of the BSMA is 0.8–8 nm. In this work, particle sizes are always presented in mobility diameters.

2.1.3 Other instrumentation

A DMPS gives the information on the aerosol number size distribution (Wiedensohler et al., 2012). At the SMEAR II station, a twin-DMPS system is deployed, with one responsible for the mobility size range of 3–50 nm and the other for larger sizes (Aalto et al., 2001; Kulmala et al., 2012). Each DMPS consists primarily of a differential mobility analyser (DMA) and a condensation particle counter (CPC). The sample air passes through a common bipolar diffusion charger, where aerosol particles are brought to a thermal charge equilibrium. Subsequently, the sample stream is divided into two to be directed to individual DMPSs, where aerosol particles are size segregated in the DMA by changing the voltage stepwisely and then counted in the CPC. The DMPS covered 3–500 nm until December 2004, after which the size range was expanded to 3–1000 nm. The determination of the CS was conducted following the method presented by Kulmala et al. (2012). CS accounts for the loss rate of vapours due to condensational uptake by aerosol particles in the atmosphere (Kulmala et al., 2001).

The snow cover depth was measured manually on a weekly basis on seven different locations at the SMEAR II station. Measurements on soil temperature and soil volumetric water content were described by Pumpanen et al. (2003) and Ilvesniemi et al. (2010). Only the organic horizon data (5 cm depth, above the mineral layer; Pumpanen et al., 2003) were used in this work. The organic horizon is in direct contact with the atmosphere, the condition of which exerts the primary influence on radon exhalation. The ambient relative humidity and air temperature data were taken from the mast measurement at 16 and 4.2 m, respectively. More detailed description of the mast instrumentation can be found from the home page of the measurement site (http://www.atm.helsinki.fi/SMEAR/index.php/smear-ii/measurements).

2.2 Ionising capacity

The ionising capacity (Q) is defined as the potential maximum amount of ion pairs produced per unit time in a unit volume upon ionisation by ionising radiation in the atmosphere. The ionising capacity in this work was determined on the basis of the assumption that 34 eV is needed for the production of an ion pair in the air. The energy released by ^{222}Rn and its short-lived progeny during alpha and beta decay were taken into consideration. The contributions from actinon (^{219}Rn) and thoron (^{220}Rn) were excluded in our study, because they are present in trace amounts naturally and have remarkably shorter half-lives (3.96 s for actinon and 55.6 s for thoron) than ^{222}Rn, which hardly permit them enough time to migrate out of the ground, especially in the case of actinon. Frozen ground and snow cover could substantially cease the transportation of thoron to the atmosphere during cold months. Even the vegetation reduces the flux of thoron from the ground to the surface air (Mattsson et al., 1996). Besides, Laakso et al. (2004) found only little contribution by thoron in the SMEAR II station to the overall radon activity. For ^{222}Rn, the decay mode and energy accounted for the ionising capacity conversion are listed in Table 1. The minor gamma fraction from the ^{222}Rn decay was assumed to be detectable by the gamma spectrometer. Therefore, the data obtained by the gamma spectrometer could be considered to represent the total gamma radiation, including the terrestrial fraction, the cosmic fraction and the fraction from radon decay. In addition, the gamma spectrometer also accounts ionising energy from muons.

Table 1. Decay modes and energy of ^{222}Rn and its short-lived progeny taken into account in the ionising capacity determination. Decay partitioning is accounted in defining the weighted average decay energy. The data are extracted from the National Nuclear Data Centre of Brookhaven National Laboratory (http://www.nndc.bnl.gov/chart/).

Nuclide	Decay mode	Weighted average decay energy (keV)
^{222}Rn	α (100 %)	5589
^{218}Po	α (99.98 %)	6001
^{214}Pb	β^- (100 %)	225
^{214}Bi	β^- (100 %)	642
^{214}Po	α (100 %)	7687

The conversion from the activity concentration (Bq m^{-3}) to the ionising capacity (cm^{-3} s^{-1}) is straightforward, when the amount of energy released during the radioactive decay is known. The conversion from total dose rate (DR, µSv h^{-1}) to the ionising capacity (cm^{-3} s^{-1}) is described by the following equation:

$$Q_\gamma = \frac{\mathrm{DR} \cdot \rho_{\mathrm{air}}}{W}, \quad (1)$$

where W is the amount of energy needed for the generation of an ion pair in the air (assumed to be 34 eV) and ρ_{air} is the density of air, which can be derived from the ideal gas law.

For conciseness and clarity, hereafter the ionising capacity results from the alpha and beta decay of ^{222}Rn and its short-lived daughter nuclides is denoted as the radon ionising capacity (Q_{Rn}) and the ionising capacity from total dose rates recorded by the gamma spectrometer as the gamma ionising capacity (Q_γ).

3 Results and discussions

3.1 Seasonal and diurnal patterns in the natural ionising capacity

The natural ionising capacity has generally the same dynamical variations as ionising radiation, from which the ionising capacity was derived. A decline in the gamma ionising capacity was seen in the seasonal profile prior to the lowest value (4.5 cm^{-3} s^{-1}) reached in March (Fig. 2), which corresponded typically to the maximum accumulation of snow on the ground. After a rapid recovery in April, the median gamma ionising capacity fluctuated at around 9.5 cm^{-3} s^{-1} during the rest of the year. The median radon ionising capacity varied in the range of 0.3–4.1 cm^{-3} s^{-1} and showed a seasonal behaviour very different from that of the gamma radiation. The minimum radon ionising capacity appeared in late spring after a gradual decrease since February. It climbed slowly back in summer and remained at a relatively moderate

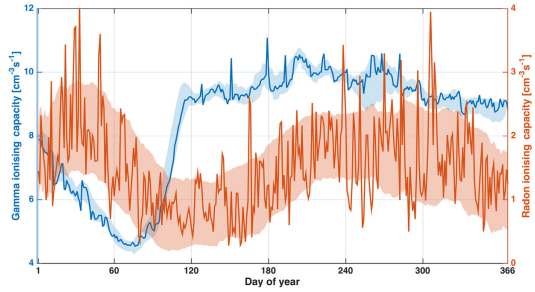

Figure 2. Seasonal patterns of radon and gamma ionising capacities as a function of day-of-year over the years 2003–2006. The radon ionising capacity was determined from the alpha and beta radioactivity associated with ^{222}Rn decay and the gamma ionising capacity from total gamma radiation. The data are presented as daily medians. Shaded bands are dedicated to outline the variabilities, expressed by standard deviations, of the data around their means determined using the moving average method.

level of around 1.7 cm^{-3} s^{-1} through autumn until the end of December.

The diurnal cycle in the ionising capacity originated mainly from the radon component and followed variations in the radon activity concentration presented by Chen et al. (2016), which was attributed to the mixing layer development. However, the contribution by gamma radiation shifted the relative levels of the ionising capacity from the seasonal pattern of the radon activity concentration shown by Chen et al. (2016). A clear diurnal cycle was observed in both spring and summer, with high ionising capacities found in the morning and low ones in the afternoon (Fig. 3). The ionising capacity was generally high in summer and autumn and low in spring and winter, with the median values being 8.9, 11.2, 11.3 and 8.7 cm^{-3} s^{-1} in spring (March–May), summer (June–August), autumn (September–November) and winter (December–February), respectively.

The share of radon ionising capacity in the total ionising capacity was in the range of 10–20 % (Fig. 4), with the lowest fraction obtained in spring and a progressive increase through the year reaching the highest share in winter. Interestingly, when separating the data according to the classification of NPF events defined by Dal Maso et al. (2005), low radon ionising capacities were found in association with NPF events. The statistical contribution of radon in ion pair production was below 10 % on NPF days in all seasons (Fig. 4) and the median radon ionising capacities on NPF event days were typically one-third to half of those on non-event days (Supplement Fig. S1 and Table 2). This observation is likely related to the fact that marine air masses from Arctic and North Atlantic oceans, which favour NPF (Nilsson et al., 2001), typically have a low radon content (Chen et al., 2016). Radon comes from the radioactive decay of radium. Since marine surface water has a significantly lower

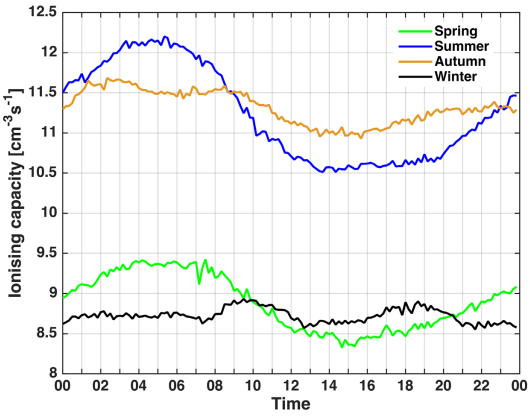

Figure 3. Diurnal cycles of the total ionising capacity presented as medians in different seasons in the years 2003–2006. Spring: March–May; summer: June–August; autumn: September–November; winter: December–February.

Table 2. Median radon ionising capacity in cm^{-3} s^{-1} on new particle formation (NPF) event and non-event days in different seasons over 2003–2006.

NPF classification	Event	Non-event
Spring	0.68	1.31
Summer	0.90	1.74
Autumn	0.99	1.8
Winter	0.56	1.96

radium content than the continental surface layer (Wilkening and Clements, 1975), only minor amount of radon can be collected by air masses traversing over the ocean. Of the airborne ^{222}Rn, 99 % originates from land and only 1 % from the sea (Baskaran et al., 1993). In addition to the air mass aspect, the MLH might also play a role in bringing about the observation of low radon ionising capacities on NPF days as NPF typically occurs on warm and sunny days with clear skies, whereas non-event days are usually associated with the presence of clouds (Nieminen et al., 2015). Mixing reaches the top of a boundary layer on sunny and clear days, diluting atmospheric radon concentrations and resulting in a lower radon ionising capacity. On cloudy days, attenuated solar radiation enervates the convective development of the boundary layer, leading to the formation of a smaller mixing volume and thereby a higher radon ionising capacity. A statistical summary of the radon and gamma ionising capacities as well as the energy deposited by ionising radiation in the air is presented in Table 3.

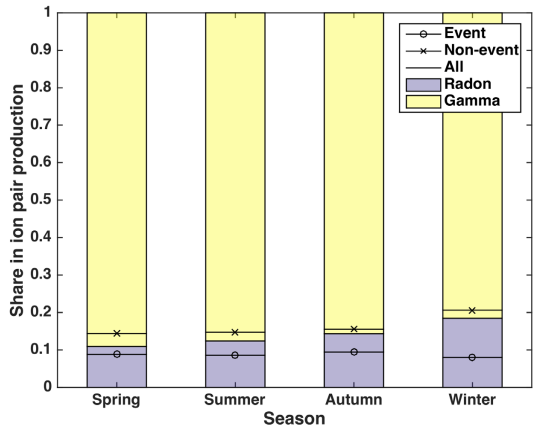

Figure 4. The relative importance of alpha and beta activities from ^{222}Rn and its short-lived daughter nuclides as well as total gamma radiation in air ion production. The division of the share between radon and gamma fractions on all days is indicated by a plain line, on new particle formation (NPF) event days by a line with an open circle and on non-event days by a line with a cross.

3.2 Factors causing variability in the ionising capacity

The seasonal and diurnal variations in the ionising capacity originate from features in ionising radiation, i.e. the atmospheric radon concentration and environmental gamma radiation. Presumably, the seasonality of the ionising capacity comes from both of the gamma and radon components, whereas the diurnal feature is primarily related to the dynamical response of radon as a result of the mixing layer evolution.

3.2.1 Factors affecting the radon ionising capacity

The atmospheric radon concentration, and consequently the derived radon ionising capacity, is affected by mixing layer dynamics, soil type, soil and meteorological conditions, long-distance transportation, etc. The atmospheric radon concentration is generally related to the mixing layer depth, which is also influenced by varying atmospheric conditions, in terms of the air temperature, wind speed, intensity of solar radiation, etc. These connections are further complicated by the arrival of continental air masses at the measurement site, which brings extra radon in addition to the local sources exhaled from the ground. Such aspects have been discussed in our earlier work (Chen et al., 2016).

Radon exhalation from the ground typically depends on the availability of ^{226}Ra – the parent nuclide of ^{222}Rn – the internal structure of mineral grains containing ^{226}Ra, soil type, moisture condition, temperature and ambient pressure (Ashok et al., 2011; Lewis et al., 1987; Nazaroff, 1992; Stranden et al., 1984). ^{226}Ra typically decays into ^{222}Rn in-

Table 3. Energy in eV m^{-3} s^{-1} deposited in the air by total environmental gamma radiation ($E\gamma$) and by alpha and beta activities from ^{222}Rn decay (ERn) based on the 2003–2006 data. The gamma and radon ionising capacities ($Q\gamma$ and Q_{Rn}) in cm^{-3} s^{-1} were derived from the deposited energy assuming 34 eV for the generation of one ion pair in the air. The statistical features of these data are presented by the five-number summary with two additional measures, the mean and standard deviation (SD).

	Min	25th percentile	50th percentile	75th percentile	Max	Mean	SD
$E\gamma$	0.769	242	314	338	544	295	72.3
E_{Rn} (α and β)	0.145	28.6	50.3	79.5	284	58.1	38.8
Q_γ	4.34	6.70	9.09	9.34	11.6	8.14	1.80
Q_{Rn}	0.00427	0.84	1.48	2.34	8.35	1.71	1.14

side mineral grains. The release of these bonded radon atoms into pores among soil grains has been found favoured by the presence of some amount of water (Stranden et al., 1984). Nonetheless, a high moisture content in the soil can block the subsequent radon migration through soil pores into the atmosphere (Nazaroff, 1992). The radon's diffusion within and exhalation from the soil have a clear temperature dependency, as demonstrated by Chen et al. (2016). A similar relationship was also seen between the radon ionising capacity derived from the atmospheric radon concentration and the soil temperature: the radon ionising capacity increased with an increasing soil temperature (Fig. 5). A shallow mixing layer permits a small mixing volume, leading to a high radon ionising capacity, whereas a deep mixing layer promotes dilution. Accordingly, the lowest radon ionising capacities were observed in the highest MLH range. High radon ionising capacities, calculated as medians in 1 °C soil temperature bins, were found at sub-zero soil temperatures with low MLHs, which are likely related to the reduced clogging by liquid water due to soil freezing and suppressed atmospheric mixing. Liquid water can remain in a frozen soil as thin films adsorbed on soil particles or in crevices and pores well below the freezing point (e.g. Spaans and Baker, 1996), which may still encourage the emanation of radon from soil grains. A further exhalation of radon into the atmosphere is probably achieved via frost-induced cracks.

In order to examine the impact of SWC on the radon ionising capacity, a soil temperature window ($T_{soil} > 14$ °C) was selected when the MLH was restricted in the range of 1000–1500 m, where the influence of soil temperature on the radon ionising capacity could be considered negligible (Fig. 6a). By zooming into this part of the data, there seemingly existed an effect of SWC, with the highest radon ionising capacity occurring at SWCs of around 0.20–0.25 m^3 m^{-3} (Fig. 6b). This observation is consistent with the findings by Stranden et al. (1984), who showed that the presence of about 25 % of water exerted the biggest enhancement in the exhalation rate of radon from soil samples. Further analysis into the SWC effect was performed by normalising the radon ionising capacity with proxies derived from MLH, soil temperatures and wind direction to minimise the influences of these

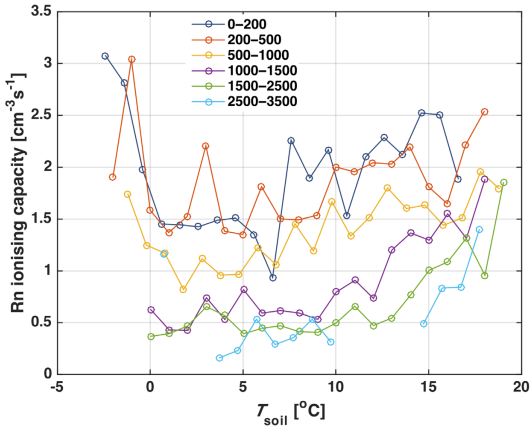

Figure 5. The median radon ionising capacity as a function of the soil temperature in 1 °C bins. Lines are colour-coded by mixing layer height (MLH) intervals.

factors. However, no systemic pattern was isolated between the radon ionising capacity and SWC for a supportive interpretation to be drawn upon. Besides, although RH has been reported as an influencing factor for radon exhalation (Ashok et al., 2011), no clear correlation between the radon ionising capacity and RH was found based on our dataset after ruling out the variability in the radon ionising capacity brought by MLH, temperature and wind.

3.2.2 Factors affecting the gamma ionising capacity

In comparison with the radon ionising capacity accounting for alpha and beta emissions of radon decay, the gamma ionising capacity exhibits a simpler pattern. Little diurnal variations exist in the total gamma radiation and therefore in the derived gamma ionising capacity. However, occasionally high gamma radiation is perceivable during rain events on a temporary basis, generally of about 2 h. Such observations are typically ascribed to gamma emissions of the washed-out short-lived progeny of radon (Brunetti et al., 2000; Dwyer

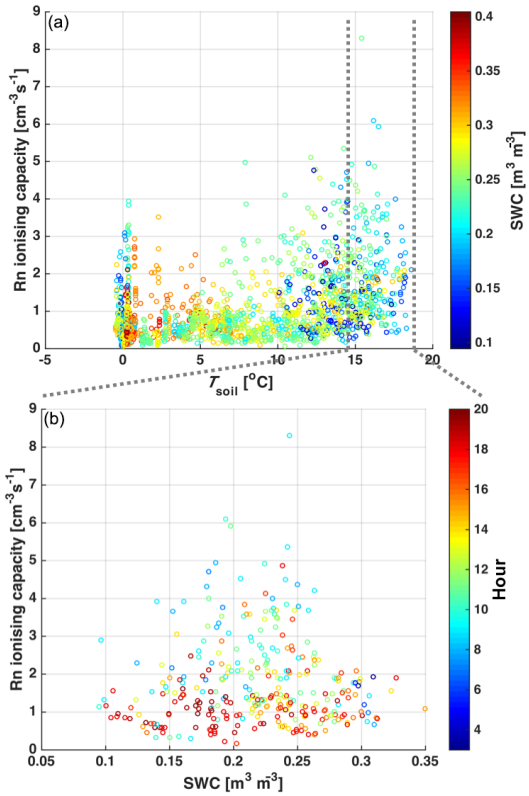

Figure 6. The effect of soil conditions on the radon ionising capacity. **(a)** Radon ionising capacities vs. soil temperatures (T_{soil}) in the MLH range of 1000–1500 m with soil water content (SWC) shown on the colour scale. Hourly data are presented for 2003–2006 with data in 2004 excluded. According to Ilvesniemi et al. (2010), the quality of SWC data in 2004 was not acceptable. **(b)** Radon ionising capacities vs. SWCs for soil temperatures larger than 14 °C.

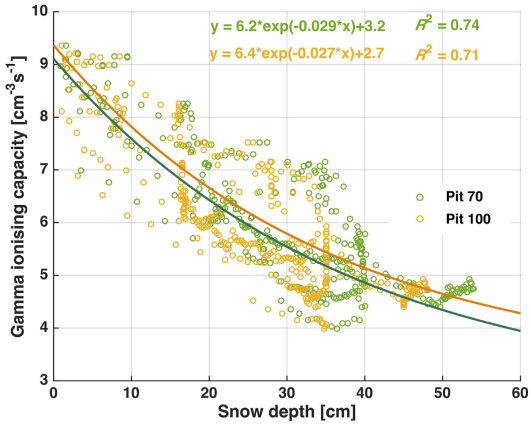

Figure 7. The attenuation effect of total gamma radiation by snow cover for the years 2003–2006. Pit 70 and 100 are two measurement points of snow cover depth. Exponential fittings were made with the goodness of fit denoted as R^2. The 95 % confidence bounds for the constant term are [2.2 4.1] and [1.3 4.0] for pit 70 and pit 100, respectively.

et al., 2012; Paatero and Hatakka, 1999). As for the seasonal cycle, the low gamma ionising capacity in winter results from the attenuation effect of snow cover on the terrestrial fraction of gamma radiation. An exponential reduction was typically seen in the gamma ionising capacity along with snow cover thickening (Fig. 7). A similar feature has been reported on the relationship between snow water equivalents and gamma dose rates for two other Finnish measurement sites in Sodankylä (67°22′ N, 26°39′ E) and Tikkakoski (62°24′ N, 25°40′ E) (Hatakka et al., 1998; Paatero et al., 2005). According to Paatero et al. (2005), the constant term in the exponential fitting to the measured snow depth data, which is about 3 cm^{-3} s^{-1}, could represent an approximation of the contribution by cosmic radiation to the ionising capacity. A rate of 2 cm^{-3} s^{-1} has been generally accepted as the ionisation rate of cosmic radiation for the production of small ions at sea level (Hensen and van der Hage, 1994). The cosmic radiation contribution to the ionising capacity determined from our measured total dose rates with the exponential fittings was close to this value. The discrepancy comes likely from uncertainties involved in the mathematical fitting and measurement including calibration. Minor contribution might originate from spatial variations in the cosmic radiation ionisation rate and solar activity influence.

3.3 Ionising radiation and observed air ions

Cluster ions are produced from primary and more complex molecular ions via their attachment to pre-existing small neutral clusters and the growth by vapour uptake. Molecular ions include both primary ions and those originating from the fraction of primary ions that have survived from the recombination or other sinks, and they are therefore in a close linkage with the ionising capacity. However, due to technical limitations, no reliable measurement can be carried out to acquire the concentration of molecular ions. Ions in the cluster size range (0.8–1.7 nm) are the smallest detectable air ion group based on the current counting technology. Since the formation of these ions are directly related to the dynamics of molecular ions and, to certain extent, to the ionising capacity, the focus in this section is the analysis of variations in the air ion concentration of the cluster size range in association with the ionising capacity.

3.3.1 Patterns in the ionising capacity and cluster ion concentration

The cluster ion concentration exhibited some degree of association with the ionising capacity (Fig. 8). The median cluster ion concentration showed little diurnal variations during the cold months: from January to March, it remained at a low level (Fig. 8a), with a median of 513 cm^{-3}. Clear diurnal cycles were discernible between April and October in cluster ions, while simultaneously the magnitude of diurnal variations in the median ionising capacity became distinguishable. On average, cluster ion concentrations were high during darker hours and low during brighter hours, which were aligned with the general feature seen in the ionising capacity (Figs. 3 and 8b), especially during the growth season of vegetation (May–August).

The enrichment in the median cluster ion concentration in the evening between May and August occurred typically a few hours ahead of the recovery of the median ionising capacity (Fig. 8). Such increases in cluster ion concentrations could result from either an augmentation in the production or a recession in the consumption or sink of these ions. In the former case, a balance between electric charge production and acquisition is re-established towards a higher production of cluster ions. Typically, this can be achieved via either a promotion in the production of electric charges or an enhancement in the charge acquisition. However, since no remarkable increase in the ionising capacity was observed, when cluster ion concentrations started to increase (Fig. 8), the production of cluster ions could be attributed to an enhancement in the charge acquisition. For the formation of cluster ions, the charge acquisition may occur at three stages: (a) prior to clustering via the formation of molecular ions from primary ions, (b) during the actual clustering process from both primary ions and molecular ions and (c) after clustering via the charge uptake from both primary ions and molecular ions. Recombination consumes part of these acquired charges, leaving the rest retained eventually in the form of cluster ions. In the latter case, certain removal processes of ions from the cluster size range are inhibited, which can be either the growth of cluster ions to sizes bigger than 1.7 nm or the loss of cluster ions by the attachment to bigger particles. All of these mechanisms, however, are manipulated primarily by atmospheric conditions. Atmospheric conditions, such as the temperature and relative humidity, can directly influence the rate of clustering and growth. Nonetheless, they also modify atmospheric compositions via the production of functional vapours involved in clustering or growth and via altering the availability of precursor gases of these vapours. As a consequence, these phenomena, seen in Fig. 8, are likely brought by a synergy of complicated atmospheric dynamic processes.

Although high ionising capacities were found in the morning, on average the morning cluster ion concentration was not so high as the evening level during the relatively warm months between April and October (Fig. 8a). Especially in autumn months, the enhancement in air ion production from the high morning ionising capacity was not reflected in the cluster ion concentration. Such observations may result from the cluster formation process becoming inferior to the preferred particle growth due to photochemical processes, while facing the dilution led by the expansion of the mixing volume. Autumn was the second peak period for the occurrence of NPF events at the SMEAR II station after spring (Nieminen et al., 2014). The dissimilar autumn and spring patterns in the cluster ion concentration originate likely from differences in atmospheric conditions and vapour sources. For example, spring UVA radiation intensities are higher than the autumn ones, while the RH shows an opposite behaviour (Lyubovtseva et al., 2005). Biogenic VOC emissions have a strong seasonality (Hakola et al., 2012; Tarvainen et al., 2005), which is reflected in their atmospheric concentrations. Hakola et al. (2012) demonstrated that monoterpenes tend to dominate VOCs in late summer and autumn, while aromatic hydrocarbons dominate in spring and early summer. Sesquiterpene emissions and concentrations were found to be high in late summer and autumn (Hakola et al., 2012; Tarvainen et al., 2005, 2007).

3.3.2 Variations in cluster ion concentrations in sub-size ranges

Ion concentrations in different sub-size ranges (0.8–1, 1–1.2 and 1.2–1.7 nm) of cluster sizes showed distinct patterns (Fig. 9). While the positive polarity dominated the overall cluster ion concentration, more negative ions were seen in the first two sub-size ranges (0.8–1 and 1–1.2 nm). The former results from the electrode effect of the negatively charged Earth surface, which repels negative ions in its vicinity, and it is a well-known phenomenon in the atmospheric electricity community (Harrison and Carslaw, 2003; Israël, 1970; Tinsley, 2008; Wilson, 1921). The latter agrees with observations that generally negative ions possess higher mean mobility than positive ions (Dhanorkar and Kamra, 1992; Hõrrak, 2001; Israël, 1970); i.e. on average, negative ions are of smaller sizes than positive ions. Ion concentrations of 0.8–1 nm were found to be the lowest (around 100 cm^{-3}) in all seasons. There was a difference of 150–200 cm^{-3} between the concentrations of 0.8–1 nm ions and 1–1.2 nm ions through all seasons in both polarities, with a larger difference observed in summer and smaller in winter. A more pronounced seasonality was observed for 1.2–1.7 nm ions, with the summer concentrations being the highest and winter concentrations being the lowest.

Slight diurnal patterns were found in 0.8–1 and 1–1.2 nm ions. The 0.8–1 nm ion concentration showed features similar to those in the ionising capacity (Figs. 9 and 3), being high in the morning and low in the afternoon. This observation possibly indicates that the dominant population in the size range of 0.8–1 nm are molecular ions, which have not

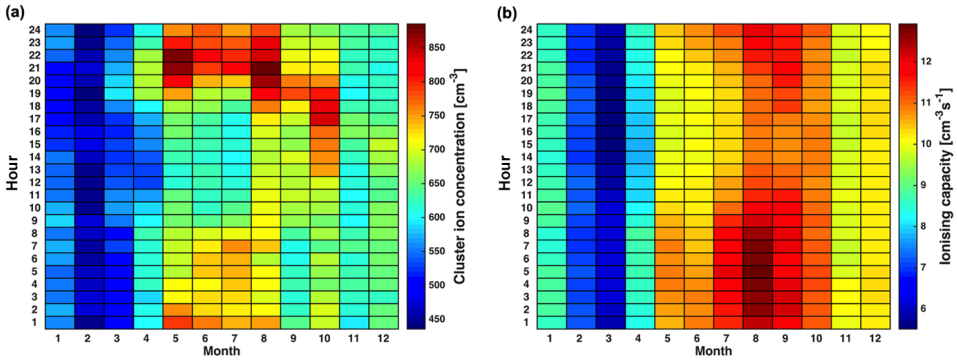

Figure 8. Median variations in **(a)** the mean cluster (0.8–1.7 nm) ion concentrations of negative and positive polarities measured by a balanced scanning mobility analyser (BSMA) and **(b)** the total ionising capacity over the years 2003–2006. Hourly medians were calculated for the whole measurement period from the 10 min measurement data prior to the processing of median values for each month as a vector of hour-of-day.

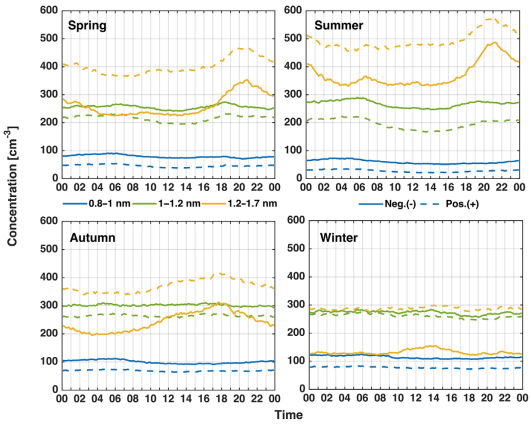

Figure 9. Median seasonality of the cluster ion concentration in 0.8–1, 1–1.2 and 1.2–1.7 nm ranges over the years 2003–2006. Negative ion concentrations are depicted by the solid line and positive ion concentrations by the dash line.

been heavily influenced by dynamical processes of cluster formation and therefore retained the characteristics of primary ions. The seasonal pattern of 1–1.2 nm ions was inconsistent with that of the ionising capacity. Two bumps existed in the concentration of 1–1.2 nm ions in spring and summer; they were found more separated in summer than in spring. However, no identifiable diurnal variation in the 1–1.2 nm ion concentration was seen in autumn; in winter, the 1–1.2 nm ion concentration showed only a small valley in the late afternoon. For 1.2–1.7 nm, which usually is the size range of critical clusters (Kulmala et al., 2012, 2013; Lange et al., 1996; Sipilä et al., 2010), clearer variations could be identified. In all the seasons, a peak close to the sunset, evolving from noon in winter to late evening (21:00) in summer, was observed.

3.3.3 Ionising capacities vs. 0.8–1 nm ions

The ionising capacity contains radon and gamma fractions, both of which were observed to have the capability to promote the production of 0.8–1 nm ions (Fig. 10). The radon ionising capacity showed a slightly better correlation with the negative 0.8–1 nm ion concentration than with the positive polarity. Along with the increase in the radon ionising capacity, more of the 0.8–1 nm ions were detected, but the degree of dispersion intensified in the correlation plots (Figs. 10a and S2). This dispersion could come from a joint effect of the temperature (T), moisture and background aerosol scavenging. Higher 0.8–1 nm ion concentrations were typically observed during darker hours (Fig. 8a) when the mixing layer is thin and photochemical processes restricted, possibly because the freshly formed 0.8–1 nm ions are confined in a smaller mixing volume and the production of vapours capable of growing small clusters becomes insufficient to support the growth of these ions out of the size range in question. According to Duplissy et al. (2016) and Kirkby et al. (2011), lower temperatures favour cluster formation in the atmosphere. However, since dark conditions prohibit the further growth of the newly formed clusters, a build-up of 0.8–1 nm ions during the darker hours is likely enabled at low temperatures, resulting in the highest 0.8–1 nm ion concentrations at the lowest air temperatures in Fig. S2c and d.

At high radon ionising capacities, the 0.8–1 nm ion concentration, especially in the positive polarity, dropped to a medium level in winter months under moist conditions (Fig. 10a–d). This observation might be related to the proton affinity of water molecules (H_2O), which assigns H_2O the

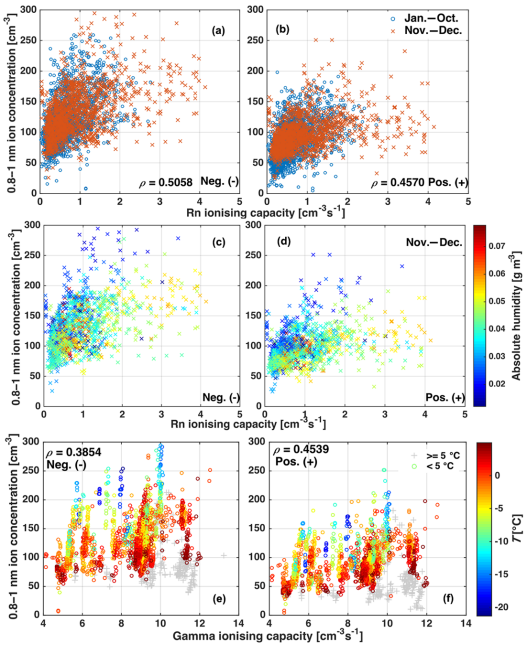

Figure 10. Relationship between the hourly ionising capacity and the 0.8–1 nm ion concentration when the condensation sink (CS) is below 0.001 s^{-1}. Upper panels **(a, b)**: radon ionising capacities vs. 0.8–1 nm ion concentrations for January–October (circle) and for November–December (cross). Middle panels **(c, d)**: radon ionising capacities vs. 0.8–1 nm ion concentrations with absolute humidity on the colour scale for November–December. Lower panel: gamma ionising capacities vs. 0.8–1 nm ion concentrations with air temperature (T) on the colour scale. The Spearman's rank correlation coefficients (ρ) in the upper panel were determined using all available data and those in the lower panel were determined between the gamma ionising capacity and the 0.8–1 nm ion concentration, when the T was below 5 °C.

ability to bind positive charges. The formed cations may constitute a portion of hydronium ions (H_3O^+), which are too small to be detected by the BSMA, resulting in the flattening-out of the 0.8–1 nm ion concentration. However, further experimental investigations are needed for the verification of this mechanism and quantification of its significance. As the CS can provide a measure of the condensational loss rate onto aerosol particles, the relatively high CS, as seen in Fig. S2e and f, could be an additional reason for the lower 0.8–1 nm ion production at high radon ionising capacities. For the negative polarity, a weak positive correlation between the radon ionising capacity and the 0.8–1 nm ion concentration was still perceptible at high radon ionising capacities, which may result from the ability of H_2O to accommodate negative charges via the formation of clusters, even though it has negative electron affinity (Jalbout and Adamowicz, 2001; Rienstra-Kiracofe et al., 2002). However, in addition to the CS effect, such dispersion could also originate from the variability in the stability of the anion clusters that is influenced, for example, by the geometric configuration of the cluster components as well as dipole properties of them.

The relationship between the gamma ionising capacity and 0.8–1 nm ion production was temperature dependent (Fig. 10e and f). When the T was below 5 °C, the 0.8–1 nm ion concentration showed a linear relation with the gamma ionising capacity. In addition, more 0.8–1 nm ions also tended to appear at lower temperatures, similar to the temperature effect seen on the relationship between the 0.8–1 nm ion concentration and the radon ionising capacity. A slightly higher correlation coefficient was found between the 0.8–1 nm ion concentration and the gamma ionising capacity in the positive polarity than that in the negative polarity (Fig. 10e and f). However, when the T was above 5 °C, the linear relationship between the 0.8–1 nm ion concentration and the gamma ionising capacity was no longer identifiable: 0.8–1 nm ion concentrations remained at the lowest around 70 cm^{-3} in the negative polarity and 30 cm^{-3} in the positive polarity, regardless of the increase in the gamma ionising capacity.

The connections between the overall ionising capacity and the 0.8–1 nm ion concentration are reflected in their diurnal behaviour, with minor dissimilarities associated with varying atmospheric conditions and dynamical processes. The median diurnal variation of the 0.8–1 nm ion concentration was very similar to that of the ionising capacity in spring, summer and autumn: both the lowest median 0.8–1 nm ion concentration and the ionising capacity occurred typically at 14:00 when the mixing layer was fully developed (Fig. 11). In comparison with the ionising capacity, however, the 0.8–1 nm ion concentration seemed to follow more instantly the changes in the MLH. The reason behind this observation may be related to the fact that the diurnal variation in the ionising capacity is primarily contributed by radon decay emissions; for example, Chen et al. (2016) showed that the atmospheric radon concentration at near ground level does not respond immediately to mixing layer expansion or shrinkage. In contrast, 0.8–1 nm ion concentrations are related, in addition to the ionising capacity, to photochemical processes and availability of nucleating vapours influenced by solar intensity and atmospheric conditions.

In summer and spring, the median 0.8–1 nm ion concentration built up with the increase in the ionising capacity in the early morning before the solar irradiance started to intensify and the mixing layer to grow. The turbulence introduced by mixing layer development may assist the production of vapours for nucleation and growth from photochemical reactions, possibly initiating the growth of these 0.8–1 nm ions. As can be seen from Figs. 9 and S3, peak concentrations in the 1–1.2 nm size range occurred typically later than those in the 0.8–1 nm size range. Also, tiny bumps in 1.2–1.7 nm

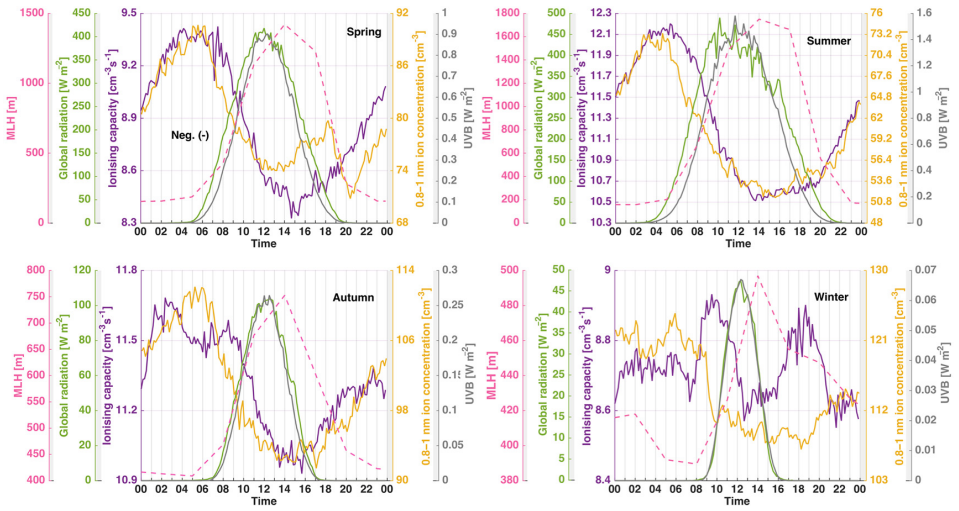

Figure 11. Diurnal patterns in median 0.8–1 nm negative and positive ion concentrations, ionising capacities, global and UVB radiation intensities as well as modelled mixing layer heights (MLH) in different seasons over 2003–2006.

ion concentrations could be discerned with some time lag at around 08:00–12:00 in spring and 05:00–07:00 in summer.

After the mixing layer had fully developed in spring, summer and autumn, there could be observed a transient boost in the 0.8–1 nm ion production (especially of the positive polarity) along with the shrinkage of the mixing layer, even prior to a clear recovery of the ionising capacity (Fig. 11). This observation may be attributed to the production of certain vapours that compete with the recombination process and other sink mechanisms for electric charges either via clustering or simple charge binding. Ionising radiation can potentially free a large number of electric charges, which would "sacrifice" themselves mostly in recombination, if not otherwise become detectable air ions. The survived electric charges take part in the formation of 0.8–1 nm ions mainly in the form of primary ions and molecular ions. Certain vapours can cluster among themselves around primary ions to form 0.8–1 nm ions. Charge-binding vapours, however, are able to take over charges from primary ions to form molecular ions. This charge transfer process may occur either via charge exchange ionisation or via chemical reactions between the vapour molecules and primary ions. Some of the molecular ions are possibly born with a size falling in the 0.8–1 nm size range. Ions in the 0.8–1 nm size range may additionally originate from (a) further growth of molecular ions via chemical reactions, (b) clustering of primary ions or molecular ions with nucleating vapours or among themselves or (c) charge uptake by small neutral clusters. Accordingly, the enhanced production of 0.8–1 nm ions after the complete development of the mixing layer, seen in Fig. 11, may be related to changes in the availability of nucleating or charge-binding vapours, altered likely by atmospheric conditions and mixing volume reduction.

Although the ionising capacity continued to increase ever since the recovery in the late afternoon, the enrichment of the 0.8–1 nm ion population ceased typically when little solar radiation was left (Fig. 11). At the same time, bursts in 1–1.2 nm ion concentrations and subsequently in 1.2–1.7 nm ion concentrations were seen (Figs. 9 and S3), which were probably linked to the nocturnal cluster formation events (Ehn et al., 2010; Lehtipalo et al., 2011; Mazon et al., 2016). The emergence of this phenomenon lies at the basis that the production rate of 0.8–1 nm ions by clustering or charge binding is overtaken by the consumption rate of them via either coagulation or condensational growth. The 1.2–1.7 nm ion concentration typically peaked nearly right after the die-out of photochemical reactions when dark hours came (Fig. S3). Concurrently, the 0.8–1 nm ion concentration started to increase again, as the ionising capacity intensified (Fig. 11).

3.3.4 Role of ionising radiation in cluster ion formation

There existed a weak relation between the total ionising capacity and the ion concentration of the whole cluster size (0.8–1.7 nm) range (Fig. 12). On NPF event days, the cluster ion concentration showed a relatively clear increase with the intensification of the ionising capacity (Fig. 12a and b). However, since the cluster ions are very small, they can preserve some properties of gaseous molecules and therefore may sink onto bigger particles. Consequently, corresponding to an ionising capacity value, the cluster ion concentration

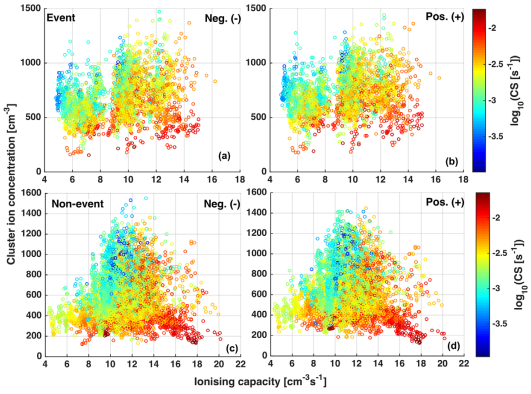

Figure 12. The 1 h cluster (0.8–1.7 nm) ion concentration as a function of the total ionising capacity on new particle formation event days (upper panel) and non-event days (lower panel), with the condensation sink (CS) indicated on the colour scale.

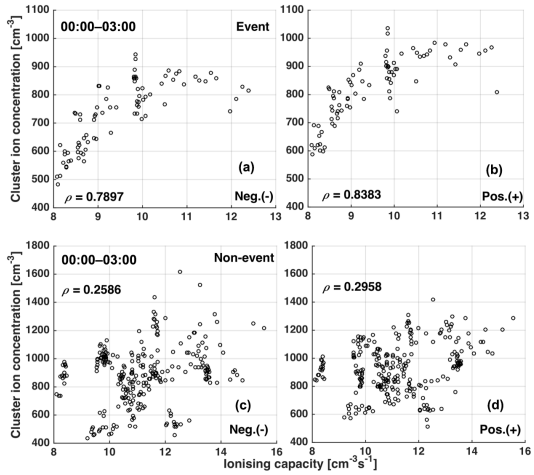

Figure 13. The cluster (0.8–1.7 nm) ion concentration as a function of the ionising capacity (radon ionising capacity + gamma ionising capacity) for selected data in the years 2003–2006, with Spearman's rank correlation coefficient (ρ). The data were constrained on **(a, b)** event days and **(c, d)** non-event days in September–December between 00:00 and 03:00 with the wind direction between 280 and 30° and the condensation sink (CS) below 0.002 s^{-1}. No dependence of the cluster ion concentration on the CS or hour-of-day was identified. Also the snow season was screened out. The negative polarity is shown in **(a, c)** and the positive in **(b, d)**.

spanned over a wide range, with high cluster ion concentrations occurring at low CSs. On non-event days, however, the connection between the ionising capacity and the cluster ion concentration became even less identifiable, probably due to the fact that CSs on non-event days are typically higher than those on event days by a factor of 3.6 on average (Dal Maso et al., 2005). In addition to this, meteorological and atmospheric conditions are also more versatile on non-event days than on event days, because NPF events are usually localised in spring, but non-events are spread all over the year (Dal Maso et al., 2005; Nieminen et al., 2014).

By carefully setting constraints to focus on data obtained under relatively uniform conditions, it was possible to observe a clear relationship between the total ionising capacity and the whole cluster population (Fig. 13). A time window between 00:00 and 03:00 was selected to minimise the effect of diurnal variations. Since the value of CS is typically largest during night-time (Kulmala et al., 2013), the constraint on the CS was set to be below 0.002 s^{-1}, instead of 0.001 s^{-1}, in Fig. 13. No dependency of the cluster ion concentration on the CS or on the hour of the day was identified. As can be seen in Fig. 2, generally little variations in both radon and gamma ionising capacities existed between September and December, which therefore was chosen as the time window for the analysis. Furthermore, the wind direction was restricted between 280 and 30° to shield the effect of radon transported from continental sources.

On both NPF event (Fig. 13a and b) and non-event (Fig. 13c and d) days, the cluster ion concentration grew with an increase in the ionising capacity. The dependency of the cluster ion concentration on the ionising capacity was weaker on non-event days than that on NPF event days. Higher ionising capacities were seen on non-event days, and correspondingly more cluster ions were detected on such days than on event days. The cluster ion concentration tended to level out on event days at high ionising capacities for both polarities ($\geq$ 10.5 cm^{-3} s^{-1}) (Fig. 13a and b), implying that the formation process of cluster ions was not efficient enough to rescue charges from recombination. However, such a feature showed no trace on non-event days and also the cluster ion concentration was more dispersed as a function of the ionising capacity. The reason for these observations may be owing to the fact that NPF occurs on days with some certain combination of atmospheric conditions as well as physical and chemical processes, but high variability is involved in these parameters on non-event days. In addition, the better dependency of the cluster ion concentration on the ionising capacity observed on NPF event days than on non-event days may also imply that charges, after being produced via ionisation by ionising radiation, on NPF event days did not undergo significant transformations to become cluster ions. Therefore, the linkage between the cluster ion concentration and ionising capacity was traceable statistically. However, this connection was very poorly preserved on non-event days, possibly because, after being created, charges went through a too complicated series of modifications before reaching the cluster sizes. These observations may also provide some indirect measure of the relative duration of dynamic processes faced by newly formed charges before they become cluster ions

under different atmospheric conditions: it might suggest that charges became cluster ions in a shorter timescale on NPF event days than on non-event days and, as a consequence, the cluster ions on NPF event days are enabled to retain some features in connection to ionising radiation.

4 Conclusions

In this work, diurnal and seasonal cycles in ionising radiation were presented and key influencing factors responsible for these features were overviewed in order to investigate how observed air ions respond to these variations and to improve our understanding on air ion formation. To assist the analysis, a term, ionising capacity, was introduced to capture patterns in ionising radiation. The ionising capacity was determined theoretically as the potential maximum production rate of ion pairs in the atmosphere by ionising radiation, based on the assumption that an ion pair is produced upon every 34 eV energy dissipation of ionising radiation. The data used in this study were collected from ambient measurements from a boreal forest site in southern Finland during 2003–2006. In our analysis, the accounted ionising radiation is composed of energy from alpha and beta decays of ^{222}Rn and accompanying gamma radiation, energy contained in the gamma radiation from terrestrial origins as well as gamma radiation and muons released from the interactions between cosmic rays and air molecules. However, a portion of high-energy cosmic ray muons may be missing from our scope. Variations in the ionising capacity were primarily related to boundary layer development, soil conditions, snow accumulation and the origin of air masses.

Although ionising radiation is known to be responsible for air ion production, patterns in the measured air ion concentration in the cluster size range (0.8–1.7 nm) did not exhibit a highly comparability to those in the ionising capacity due to modifications of air ion properties exerted by different dynamical processes and chemical reactions during the evolution of charges in the atmosphere. Nevertheless, the connection of air ions to ionising radiation was seen for air ions detected in the lowest detected size band (0.8–1 nm) of the cluster size range (0.8–1.7 nm). The evolvement of these 0.8–1 nm ions with time to larger sizes in the cluster size band was also identified, affirming the primary role of ionising radiation in the production of air ions in the lower atmosphere. However, atmospheric conditions, such as temperature, humidity and pre-existing aerosol particles, brought complications into this relationship. By carefully constraining data to conditions of a similar meteorology, seasonality, diurnality and amount of background aerosol particles, a strong dependency of total cluster ion concentrations on the ionising capacity was identified on NPF days. However, the linkage was not visible on non-event days. These observations may suggest that charges, after being born, underwent different processes on NPF days and non-event days and possibly indicate also that the transformation of newly formed charges to cluster ions occurred faster on NPF days than on non-event days. These results could help to advance our understanding on the role of ions in atmospheric new particle formation.

However, to obtain further insights into the fate of charges created by ionising radiation in the atmosphere, i.e. ion balance, and into the role of air ions in the atmospheric new particle formation process, it is crucial to understand the transformation process of electric charges into detectable air ions. For this purpose, knowledge on the number size distribution of air ions smaller than 0.8 nm is of necessity. Additionally, theoretical understanding on the formation mechanisms of cluster ions from molecular ions needs to be deepened. Conjointly, also advancing instrumental development for the detection of sub-0.8 nm ions could be worth being brought onto the agenda.

5 Data availability

The aerosol particle and meteorological data used in this work are publicly accessible on the SmartSmear website (http://avaa.tdata.fi/web/smart/smear/) (SMEAR, 2016). The air ion and ionising radiation data are in the process to be implemented in the SmartSmear system. The MLH data were extracted from the European Centre for Medium-Range Weather Forecasts (ECMWF) Meteorological Archival and Retrieval System (MARS), Reading, UK (www.ecmwf.int) (ECMWF, 2016). All the data are also available upon direct request to the corresponding author.

The Supplement related to this article is available online at doi:10.5194/acp-16-14297-2016-supplement.

Acknowledgements. This work received funding support from the Academy of Finland Centre of Excellence (project no. 272041 and 1118615), European Union's Horizon 2020 research and innovation programme under grant agreement no. 654109 (ACTRIS-2) as well as the European Union Seventh Framework Programme (FP7/2007-2013 ACTRIS) under grant agreement no. 262254. Also the CRyosphere-Atmosphere Interactions in a Changing arctic Climate (CRAICC) project of the Nordic Centre of Excellence is acknowledged. The authors appreciate the valuable communication with Jaana Bäck, Pasi Kolari, Anne Hirsikko and Juha Hatakka.

Edited by: D. Spracklen
Reviewed by: two anonymous referees

References

Aalto, P., Hämeri, K., Becker, E., Weber, R., Salm, J., MäKelä, J. M., Hoell, C., O'Dowd, C. D., Karlsson, H., Hansson, H.-C., VäKevä, M., Koponen, I. K., Buzorius, G., and Kulmala, M.: Physical characterization of aerosol particles during nucleation events, Tellus, 53B, 344–358, 2001.

Aplin, K. L. and Harrison, R. G.: A computer-controlled Gerdien atmospheric ion counter, Rev. Sci. Instrum., 71, 3037, doi:10.1063/1.1305511, 2000.

Ashok, G. V., Nagaiah, N., Shiva Prasad, N. G., and Ambika, M. R.: Study of radon exhalation rate from soil, Bangalore, south India, Radiat. Protect. Environ., 34, 235–239, 2011.

Baskaran, M., Coleman, C. H., and Santschi, P. H.: Atmospheric depositional fluxes of ^{7}Be and ^{210}Pb at Galveston and College Station, Texas, J. Geophys. Res., 98, 20555, doi:10.1029/93jd02182, 1993.

Bennett, A. J. and Harrison, R. G.: Atmospheric electricity in different weather conditions, Weather, 62, 277–283, 2007.

Brunetti, M., Cecchini, S., Galli, M., Giovannini, G., and Pagliarin, A.: Gamma-ray bursts of atmospheric origin in the MeV energy range, Geophys. Res. Lett., 27, 1599–1602, doi:10.1029/2000gl003750, 2000.

Canton, J.: Electrical Experiments, with an Attempt to Account for Their Several Phaenomena; Together with Some Observations on Thunder-Clouds, Phil. Trans., 48, 350–358, 1753a.

Canton, J.: A letter to the right honourable the earl of macclesfield, president of the royal society, concerning some new electrical experiments, Phil. Trans., 48, 780–785, 1753b.

Carlson, P. and De Angelis, A.: Nationalism and internationalism in science: the case of the discovery of cosmic rays, Eur. Phys. J. H, 35, 309–329, doi:10.1140/epjh/e2011-10033-6, 2011.

Chen, X., Paatero, J., Kerminen, V.-M., Riuttanen, L., Hatakka, J., Hiltunen, V., Paasonen, P., Hirsikko, A., Franchin, A., Manninen, H. E., Petäjä, T., Viisanen, Y., and Kulmala, M.: Responses of the atmospheric concentration of radon-222 to the vertical mixing and spatial transportation, Boreal Environ. Res., 21, 299–318, 2016.

Crookes, W.: On Electrical Insulation in High Vacua, P. R. Soc. London, 28, 347–352, 1878.

Cumeras, R., Figueras, E., Davis, C. E., Baumbach, J. I., and Gracia, I.: Review on ion mobility spectrometry. Part 1: current instrumentation, Analyst, 140, 1376–1390, doi:10.1039/c4an01100g, 2015.

Dal Maso, M., Kulmala, M., Riipinen, I., Wagner, R., Hussein, T., Aalto, P. P., and Lehtinen, K. E. J.: Formation and growth of fresh atmospheric aerosols: eight years of aerosol size distribution data from SMEAR II, Hyytiälä, Finland, Boreal Environ. Res., 10, 323–336, 2005.

De Angelis, A.: Atmospheric ionization and cosmic rays: studies and measurements before 1912, Astropart. Phys., 53, 19–26, doi:10.1016/j.astropartphys.2013.05.010, 2014.

Dhanorkar, S. and Kamra, A. K.: Relation between electrical conductivity and small ions in the presence of intermediate and large ions in the lower atmosphere, J. Geophys. Res., 97, 20345–20360, 1992.

Duplissy, J., Merikanto, J., Franchin, A., Tsagkogeorgas, G., Kangasluoma, J., Wimmer, D., Vuollekoski, H., Schobesberger, S., Lehtipalo, K., Flagan, R. C., Brus, D., Donahue, N. M., Vehkamäki, H., Almeida, J., Amorim, A., Barmet, P., Bianchi, F., Breitenlechner, M., Dunne, E. M., Guida, R., Henschel, H., Junninen, H., Kirkby, J., Kürten, A., Kupc, A., Mättänen, A., Makhmutov, V., Mathot, S., Nieminen, T., Onnela, A., Praplan, A. P., Riccobono, F., Rondo, L., Steiner, G., Tome, A., Walther, H., Baltensperger, U., Carslaw, K. S., Dommen, J., Hansel, A., Petäjä, T., Sipilä, M., Stratmann, F., Vrtala, A., Wagner, P. E., Worsnop, D. R., Curtius, J., and Kulmala, M.: Effect of ions on sulfuric acid-water binary particle formation: 2. Experimental data and comparison with QC-normalized classical nucleation theory, J. Geophys. Res.-Atmos., 121, 1752–1775, doi:10.1002/2015JD023539, 2016.

Dwyer, J. R., Schaal, M. M., Cramer, E., Arabshahi, S., Liu, N., Rassoul, H. K., Hill, J. D., Jordan, D. M., and Uman, M. A.: Observation of a gamma-ray flash at ground level in association with a cloud-to-ground lightning return stroke, J. Geophys. Res., 117, A10303, doi:10.1029/2012ja017810, 2012.

ECMWF: Boundary layer heights from the operative forecast model in use at the time by the European Centre for Medium-Range Weather Forecasts (ECMWF), available at: http://www.ecmwf.int/en/forecasts/datasets, last access: 14 November 2016.

Ehn, M., Junninen, H., Petäjä, T., Kurtén, T., Kerminen, V.-M., Schobesberger, S., Manninen, H. E., Ortega, I. K., Vehkamäki, H., Kulmala, M., and Worsnop, D. R.: Composition and temporal behavior of ambient ions in the boreal forest, Atmos. Chem. Phys., 10, 8513–8530, doi:10.5194/acp-10-8513-2010, 2010.

Ehn, M., Junninen, H., Schobesberger, S., Manninen, H. E., Franchin, A., Sipilä, M., Petäjä, T., Kerminen, V.-M., Tammet, H., Mirme, A., Mirme, S., Hõrrak, U., Kulmala, M., and Worsnop, D.: An instrumental comparison of mobility and mass measurements of atmospheric small ions, Aerosol Sci. Tech., 45, 522–532, doi:10.1080/02786826.2010.547890, 2011.

Fernandez-Garcia, J. and Fernandez de la Mora, J.: Measuring the effect of ion-induced drift-gas polarization on the electrical mobilities of multiply-charged ionic liquid nanodrops in air, J. Am. Soc. Mass Spectr., 24, 1872–1889, doi:10.1007/s13361-013-0702-1, 2013.

Flagan, R. C.: History of electrical aerosol measurements, Aerosol Sci. Tech., 28, 301–380, doi:10.1080/02786829808965530, 1998.

Franklin, B.: A Letter of Benjamin Franklin, Esq; to Mr. Peter Collinson, F. R. S. concerning an Electrical Kite, Phil. Trans., 47, 565–567, 1751.

Gerdien, H.: Die absolute messung der specifischen leitfähigkeit und der dichte des verticalen leitungsstromes in der atmosphäre, Terrestrial Magnetism and Atmospheric Electricity, 10, 65–74, 1905.

Goldhagen, P.: Overview of aircraft radiation exposure and recent ER-2 measurements, Health Phys., 79, 526–544, 2000.

Hakola, H., Hellén, H., Hemmilä, M., Rinne, J., and Kulmala, M.: In situ measurements of volatile organic compounds in a boreal forest, Atmos. Chem. Phys., 12, 11665–11678, doi:10.5194/acp-12-11665-2012, 2012.

Hari, P. and Kulmala, M.: Station for measuring ecosystem-atmosphere relations (SMEAR II), Boreal Environ. Res., 10, 315–322, 2005.

Harrison, R. G. and Carslaw, K. S.: Ion-aerosol-cloud processes in the lower atmosphere, Rev. Geophys., 41, 1012, doi:10.1029/2002rg000114, 2003.

Hatakka, J., Paatero, J., Viisanen, Y., and Mattsson, R.: Variations of external radiation due to meteorological and hydrological factors in central Finland, Radiochemistry, 40, 534–538, 1998.

Hensen, A. and van der Hage, J. C. H.: Parameterisation of cosmic radiation at sea level, J. Geophys. Res., 99, 10693–10695, 1994.

Herbert, K. B. H.: John Canton – Pioneer investigator of atmospheric electricity, Weather, 52, 286–290, 1997.

Hewitt, G. W.: The charging of small particles for electrostatic precipitation, Trans. Am. Inst. Elect. Engr., 76, 300–306, 1957.

Hinds, W. C.: Aerosol technology: Properties, behavior, and measurement of airborne particles, 2 Edn., Wiley-Interscience, New York, 1999.

Hirsikko, A., Paatero, J., Hatakka, J., and Kulmala, M.: The ^{222}Rn activity concentration, external radiation dose and air ion production rates in a boreal forest in Finalnd between March 2000 and June 2006, Boreal Environ. Res., 12, 265–278, 2007.

Hirsikko, A., Nieminen, T., Gagné, S., Lehtipalo, K., Manninen, H. E., Ehn, M., Hõrrak, U., Kerminen, V.-M., Laakso, L., McMurry, P. H., Mirme, A., Mirme, S., Petäjä, T., Tammet, H., Vakkari, V., Vana, M., and Kulmala, M.: Atmospheric ions and nucleation: a review of observations, Atmos. Chem. Phys., 11, 767–798, doi:10.5194/acp-11-767-2011, 2011.

Hogg, A. R.: The intermediate ions of the atmosphere, Proc. Phys. Soc., 51, 1014–1027, 1939.

Hõrrak, U.: Air ion mobility spectrum at a rural area, PhD, Institute of Environmental Physics, University of Tartu, Tartu, Estonia, 81 pp., 2001.

Ilvesniemi, H., Pumpanen, J., Duursma, R., Hari, P., Keronen, P., Kolari, P., Kulmala, M., Mammarella, I., Nikinmaa, E., Rannik, U. L., Pohja, T., Siivola, E., and Vesala, T.: Water balance of a boreal scots pine forest, Boreal Environ. Res., 15, 375–396, 2010.

Israël, H.: Atmospheric electricity, Vol. I, Israel Program for Scientific Translations, Jerusalem, 1970.

Jalbout, A. F. and Adamowicz, L.: Dipole-Bound Anions of Adenine-Water Clusters. Ab Initio Study, J. Phys. Chem. A, 105, 1033–1038, 2001.

Jesse, W. and Sadaukis, J.: Absolute energy to produce an ion pair by beta particles from S^{35}, Phys. Rev., 107, 766–771, doi:10.1103/PhysRev.107.766, 1957.

Junninen, H., Ehn, M., Petäjä, T., Luosujärvi, L., Kotiaho, T., Kostiainen, R., Rohner, U., Gonin, M., Fuhrer, K., Kulmala, M., and Worsnop, D. R.: A high-resolution mass spectrometer to measure atmospheric ion composition, Atmos. Meas. Tech., 3, 1039–1053, doi:10.5194/amt-3-1039-2010, 2010.

Junninen, H., Duplissy, J., Ehn, M., Sipilä, M., Kangasluoma, J., Franchin, A., Petäjä, T., Manninen, H. E., Kerminen, V.-M., Worsnop, D., and Kulmala, M.: Measuring atmospheric ion bursts and their dynamics using mass spectrometry, Boreal Env. Res., 21, 207–220, 2016.

Kirkby, J., Curtius, J., Almeida, J., Dunne, E., Duplissy, J., Ehrhart, S., Franchin, A., Gagne, S., Ickes, L., Kurten, A., Kupc, A., Metzger, A., Riccobono, F., Rondo, L., Schobesberger, S., Tsagkogeorgas, G., Wimmer, D., Amorim, A., Bianchi, F., Breitenlechner, M., David, A., Dommen, J., Downard, A., Ehn, M., Flagan, R. C., Haider, S., Hansel, A., Hauser, D., Jud, W., Junninen, H., Kreissl, F., Kvashin, A., Laaksonen, A., Lehtipalo, K., Lima, J., Lovejoy, E. R., Makhmutov, V., Mathot, S., Mikkila, J., Minginette, P., Mogo, S., Nieminen, T., Onnela, A., Pereira, P., Petaja, T., Schnitzhofer, R., Seinfeld, J. H., Sipila, M., Stozhkov, Y., Stratmann, F., Tome, A., Vanhanen, J., Viisanen, Y., Vrtala, A., Wagner, P. E., Walther, H., Weingartner, E., Wex, H., Winkler, P. M., Carslaw, K. S., Worsnop, D. R., Baltensperger, U., and Kulmala, M.: Role of sulphuric acid, ammonia and galactic cosmic rays in atmospheric aerosol nucleation, Nature, 476, 429–433, doi:10.1038/nature10343, 2011.

Krause, S., Clark, H. M., Ferris, J. P., and Strong, R. L.: Chemistry of the environment, Elsevier Science & Technology Books, 2002.

Kruis, F. E., Fissan, H., and Peled, A.: Synthesis of nanoparticles in the gas phase for electronic, optical and magnetic applications – a review, J. Aerosol Sci., 29, 511–535, 1998.

Ku, B. K. and Fernández de la Mora, J.: Relation between electrical mobility, mass, and size for nanodrops 1–6.5 nm in diameter in air, Aerosol Sci. Tech., 43, 241–249, doi:10.1080/02786820802590510, 2009.

Kulmala, M., Maso, M. D., Mäkelä, J. M., L. Pirjola, Väkevä, M., P. Aalto, Miikkulainen, P., Hämeri, K., and O'Dowd, C. D.: On the formation, growth and composition of nucleation mode particles, Tellus, 53B, 479–490, 2001.

Kulmala, M., Riipinen, I., Sipila, M., Manninen, H. E., Petaja, T., Junninen, H., Maso, M. D., Mordas, G., Mirme, A., Vana, M., Hirsikko, A., Laakso, L., Harrison, R. M., Hanson, I., Leung, C., Lehtinen, K. E., and Kerminen, V.-M.: Toward direct measurement of atmospheric nucleation, Science, 318, 89–92, doi:10.1126/science.1144124, 2007.

Kulmala, M., Petaja, T., Nieminen, T., Sipila, M., Manninen, H. E., Lehtipalo, K., Maso, M. D., Aalto, P. P., Junninen, H., Paasonen, P., Riipinen, I., Lehtinen, K. E., Laaksonen, A., and Kerminen, V.-M.: Measurement of the nucleation of atmospheric aerosol particles, Nat. Protoc., 7, 1651–1667, doi:10.1038/nprot.2012.091, 2012.

Kulmala, M., Kontkanen, J., Junninen, H., Lehtipalo, K., Manninen, H. E., Nieminen, T., Petaja, T., Sipila, M., Schobesberger, S., Rantala, P., Franchin, A., Jokinen, T., Jarvinen, E., Aijala, M., Kangasluoma, J., Hakala, J., Aalto, P. P., Paasonen, P., Mikkila, J., Vanhanen, J., Aalto, J., Hakola, H., Makkonen, U., Ruuskanen, T., Mauldin, R. L., 3rd, Duplissy, J., Vehkamaki, H., Back, J., Kortelainen, A., Riipinen, I., Kurten, T., Johnston, M. V., Smith, J. N., Ehn, M., Mentel, T. F., Lehtinen, K. E., Laaksonen, A., Kerminen, V.-M., and Worsnop, D. R.: Direct observations of atmospheric aerosol nucleation, Science, 339, 943–946, doi:10.1126/science.1227385, 2013.

Kulmala, M., Hõrrak, U., Manninen, H. E., Mirme, S., Noppel, M., Lehtipalo, K., Junninen, H., Vehkamäki, H., Kerminen, V.-M., Noe, S. M., and Tammet, H.: The legacy of Finnish–Estonian air ion and aerosol workshops, Boreal Environ. Res., 21, 181–206, 2016.

Laakso, L., Petäjä, T., Lehtinen, K. E. J., Kulmala, M., Paatero, J., Hõrrak, U., Tammet, H., and Joutsensaari, J.: Ion production rate in a boreal forest based on ion, particle and radiation measurements, Atmos. Chem. Phys., 4, 1933–1943, doi:10.5194/acp-4-1933-2004, 2004.

Lange, R., Fissan, H., and Schmidt-Ott, A.: Determination of equivalent diameters of agglomerates, J. Aerosol Sci., 29, S417–S418, 1996.

Laskin, A., Laskin, J., and Nizkorodov, S. A.: Mass spectrometric approaches for chemical characterisation of atmospheric

aerosols: critical review of the most recent advances, Environ. Chem., 9, 163–189, doi:10.1071/en12052, 2012.

Lehtipalo, K., Sipilä, M., Junninen, H., Ehn, M., Berndt, T., Majos, M. K., Worsnop, D. R., Petäjä, T., and Kulmala, M.: Observations of nano-CN in the nocturnal boreal forest, Aerosol Sci. Tech., 45, 499–509, doi:10.1080/02786826.2010.547537, 2011.

Lewis, C., Hopke, P. K., and Stukelt, J. J.: Solubility of radon in selected perfluorocarbon compounds and water, Ind. Eng. Chem. Res., 26, 356–359, 1987.

Lyubovtseva, Y. S., Sogacheva, L., Maso, M. D., Bonn, B., Keronen, P., and Kulmala, M.: Seasonal variations of trace gases, meteorological parameters, and formation of aerosols in boreal forests, Boreal Environ. Res., 10, 493–510, 2005.

Mäkelä, J. M., Riihelä, M., Ukkonen, A., Jokinen, V., and Keskinen, J.: Comparison of mobility equivalent diameter with Kelvin – Thomson diameter using ion mobility data, J. Chem. Phys., 105, 1562–1571, doi:10.1063/1.472017, 1996.

Manninen, H. E., Petäjä, T., Asmi, E., Riipinen, I., Niemnen, T., Mikkilä, J., Hõrrak, U., Mirme, A., Mirme, S., Laakso, L., Kerminen, V.-M., and Kulmala, M.: Long-time field measurements of charged and neutral clusters using Neutral cluster and Air Ion Spectrometer (NAIS), Boreal Environ. Res., 14, 591–605, 2009.

Manninen, H. E., Mirme, S., Mirme, A., Petäjä, T., and Kulmala, M.: How to reliably detect molecular clusters and nucleation mode particles with Neutral cluster and Air Ion Spectrometer (NAIS), Atmos. Meas. Tech., 9, 3577–3605, doi:10.5194/amt-9-3577-2016, 2016.

Mason, E. A. and McDaniel, E. W.: Transport properties of ions in gases, John Wiley & Sons, New York, Chichester, Brisbane, Toronto, Singapore, 1988.

Mattsson, R., Paatero, J., and Hatakka, J.: Automatic alpha/beta analyser for air filter samples – absolute determination of radon progeny by pseudo-coincidence techniques, Radiat. Prot. Dosim., 63, 133–139, 1996.

Mazon, S. B., Kontkanen, J., Manninen, H. E., Nieminen, T., Kerminen, V.-M., and Kulmala, M.: Cluster events in a boreal forest: comparing night-time with day-time ion clusters in 2003–2013, Boreal Environ. Res., 21, 242–261, 2016.

Millikan, R. A.: The general law of fall of a small spherical body through a gas, and its bearing upon the nature of molecular reflection from surfaces, Phys. Rev., 22, 1–23, doi:10.1103/PhysRev.22.1, 1923.

Mirme, A., Tamm, E., Mordas, G., Vana, M., Uin, H., Mirme, S., Bernotas, T., Laakso, L., Hirsikko, A., and Kulmala, M.: A wide-range multi-channel Air Ion Spectrometer, Boreal Environ. Res., 12, 247–264, 2007.

Mirme, S. and Mirme, A.: The mathematical principles and design of the NAIS – a spectrometer for the measurement of cluster ion and nanometer aerosol size distributions, Atmos. Meas. Tech., 6, 1061–1071, doi:10.5194/amt-6-1061-2013, 2013.

Nazaroff, W. W.: Radon transport from soil to air, Rev. Geophys., 30, 137–160, 1992.

Nieminen, T., Asmi, A., Maso, M. D., Aalto, P. P., Keronen, P., Petäjä, T., Kulmala, M., and Kerminen, V.-M.: Trends in atmospheric new-particle formation: 16 years of observations in a boreal-forest environment, Boreal Environ. Res., 19, 191–214, 2014.

Nieminen, T., Yli-Juuti, T., Manninen, H. E., Petäjä, T., Kerminen, V.-M., and Kulmala, M.: Technical note: New particle formation event forecasts during PEGASOS-Zeppelin Northern mission 2013 in Hyytiälä, Finland, Atmos. Chem. Phys., 15, 12385–12396, doi:10.5194/acp-15-12385-2015, 2015.

Nilsson, E., Paatero, J., and Boy, M.: Effects of air masses and synoptic weather on aerosol formation in the continental boundary layer, Tellus, 52B, 462–478, 2001.

Nolan, J. J.: The constitution of gaseous ions, Phys. Rev., 24, 16–30, doi:10.1103/PhysRev.24.16, 1924.

Paatero, J. and Hatakka, J.: Wet deposition efficiency of short-lived radon-222 progeny in central Finland, Boreal Environ. Res., 4, 285–293, 1999.

Paatero, J., Hatakka, J., Mattsson, R., and Lehtinen, I.: A comprehensive station for monitoring atmospheric radioactivity, Radiat. Prot. Dosim., 54, 33–39, 1994.

Paatero, J., Kyrö, E., Hatakka, J., Aaltonen, V., and Viisanen, Y.: Measurement of snow cover based on external radiation, Seventh International Symposium on The Natural Radiation Environment (NRE-VII), Rhodes, Greece, 20–24 May 2005.

Pumpanen, J., Ilvesniemi, H., Perämäki, M., and Hari, P.: Seasonal patterns of soil CO_2 efflux and soil air CO_2 concentration in a Scots pine forest: comparison of two chamber techniques, Glob. Change Biol., 9, 371–382, 2003.

Read, J.: A Meteorological Journal, Principally Relating to Atmospherical Electricity; Kept at Knightsbridge, from the 9th of May, 1790, to the 8th of May, Philos. T. R. Soc. Lond., 82, 225–256, 1792.

Reischl, G. P.: Measurement of ambient aerosols by the differential mobility analyzer method: concepts and realization criteria for the size range between 2 and 500 nm, Aerosol Sci. Tech., 14, 5–24, doi:10.1080/02786829108959467, 1991.

Rienstra-Kiracofe, J. C., Tschumper, G. S., and Schaefer, H. F.: Atomic and Molecular Electron Affinities: Photoelectron Experiments and Theoretical Computations, Chem. Rev., 102, 231–282, 2002.

Robotti, N.: J. J. Thomson at the cavendish laboratory: The history of an electric charge measurement, Ann. Sci., 52, 265–284, doi:10.1080/00033799500200231, 2006.

Rosell-Llompart, J. and Fernández de la Mora, J.: Minimization of the diffusive broadening of ultrafine particles in differential mobility analysers, Synthesis and measurement of ultrafine particles, Delft, 1993.

Sipilä, M., Berndt, T., Petaja, T., Brus, D., Vanhanen, J., Stratmann, F., Patokoski, J., Mauldin III, R. L., Hyvarinen, A. P., Lihavainen, H., and Kulmala, M.: The role of sulfuric acid in atmospheric nucleation, Science, 327, 1243–1246, doi:10.1126/science.1180315, 2010.

SMEAR: Aerosol and meteorological data at SMEAR II Hyytiälä forest station, Atmospheric Sciences/University of Helsinki (UHEL), available at: http://avaa.tdata.fi/web/smart/smear/, last access: 14 November 2016.

Spaans, E. J. A. and Baker, J. M.: The soil freezing characteristic: its measurement and similarity to the soil moisture characteristic, Soil Sci. Soc. Am. J., 60, 13–19, 1996.

Stranden, E., Kolstad, A. K., and Lind, B.: The influence of moisture and temperature on radon exhalation, Radiat. Prot. Dosim., 7, 55–58, 1984.

Tammet, H.: The aspiration method for the determination of atmospheric-ion spectra, Israel Program for Scientific Translations, Jerusalem, 1970.

Tammet, H.: Size and mobility of nanometer particles, clusters and ions, J. Aerosol Sci., 26, 459–475, 1995.

Tammet, H.: Continuous scanning of the mobility and size distribution of charged clusters and nanometer particles in atmospheric air and the Balanced Scanning Mobility Analyzer BSMA, Atmos. Res., 82, 523–535, doi:10.1016/j.atmosres.2006.02.009, 2006.

Tammet, H.: Symmetric Inclined Grid Mobility Analyzer for the measurement of charged clusters and fine nanoparticles in atmospheric air, Aerosol Sci. Tech., 45, 468–479, doi:10.1080/02786826.2010.546818, 2011.

Tammet, H.: the function-updated millikan model: a tool for nanometer particle size-mobility conversions, Aerosol Sci. Tech., 46, i–iv, doi:10.1080/02786826.2012.700740, 2012.

Tarvainen, V., Hakola, H., Hellén, H., Bäck, J., Hari, P., and Kulmala, M.: Temperature and light dependence of the VOC emissions of Scots pine, Atmos. Chem. Phys., 5, 989–998, doi:10.5194/acp-5-989-2005, 2005.

Tarvainen, V., Hakola, H., Rinne, J., Hellén, H., and Haapanala, S.: Towards a comprehensive emission inventory of terpenoids from boreal ecosystems, Tellus B, 59, 526–534, doi:10.1111/j.1600-0889.2007.00263.x, 2007.

Tinsley, B. A.: The global atmospheric electric circuit and its effects on cloud microphysics, Rep. Prog. Phys., 71, 066801, doi:10.1088/0034-4885/71/6/066801, 2008.

Vehkamäki, H.: Classical nucleation theory in multicomponent systems, Springer, Berlin, Heidelberg, New York, 2006.

Vojtek, T., Skoupil, T., Fiala, P., and Bartušek, K.: Accuracy of air ion field measurement, Electromagnetics Research Symposium, Cambridge, USA, 26–29 March 2006.

Walter, M.: From the discovery of radioactivity to the first accelerator experiments, in: From Ultra Rays to Astroparticles. A Historical Introduction to Astroparticle Physics, edited by: Falkenburg, B. and Rhode, W., Springer, 17–47, 2012.

Wiedensohler, A., Birmili, W., Nowak, A., Sonntag, A., Weinhold, K., Merkel, M., Wehner, B., Tuch, T., Pfeifer, S., Fiebig, M., Fjäraa, A. M., Asmi, E., Sellegri, K., Depuy, R., Venzac, H., Villani, P., Laj, P., Aalto, P., Ogren, J. A., Swietlicki, E., Williams, P., Roldin, P., Quincey, P., Hüglin, C., Fierz-Schmidhauser, R., Gysel, M., Weingartner, E., Riccobono, F., Santos, S., Grüning, C., Faloon, K., Beddows, D., Harrison, R., Monahan, C., Jennings, S. G., O'Dowd, C. D., Marinoni, A., Horn, H.-G., Keck, L., Jiang, J., Scheckman, J., McMurry, P. H., Deng, Z., Zhao, C. S., Moerman, M., Henzing, B., de Leeuw, G., Löschau, G., and Bastian, S.: Mobility particle size spectrometers: harmonization of technical standards and data structure to facilitate high quality long-term observations of atmospheric particle number size distributions, Atmos. Meas. Tech., 5, 657–685, doi:10.5194/amt-5-657-2012, 2012.

Wilkening, M. H. and Clements, W. E.: Radon 222 from the ocean surface, J. Geophys. Res., 80, 3828–3830, doi:10.1029/JC080i027p03828, 1975.

Wilkening, M. H.: Radon in atmospheric studies: a review, Second special symposium, Bhabha atomic reseach center, Bomday, India, 1981.

Wilson, C. T. R.: The effect of rontgen's rays on cloudy condensation, P. R. Soc. Lond., 59, 338–339, 1895.

Wilson, C. T. R.: On the condensation nuclei produced in gases by the action of rontgen rays, uranium rays, ultra-violet light, and other agents, Philos. T. R. Soc. Lond., 192, 403–453, 1899.

Wilson, C. T. R.: Investigations on lightning discharges and on the electric field of thunderstorms, Philos. T. R. Soc. Lond., 221, 73–115, 1921.

Supplement of Atmos. Chem. Phys., 16, 14297–14315, 2016
http://www.atmos-chem-phys.net/16/14297/2016/
doi:10.5194/acp-16-14297-2016-supplement

Atmospheric Chemistry and Physics Open Access EGU

Supplement of

How do air ions reflect variations in ionising radiation in the lower atmosphere in a boreal forest?

Xuemeng Chen et al.

Correspondence to: Xuemeng Chen (xuemeng.chen@helsinki.fi)

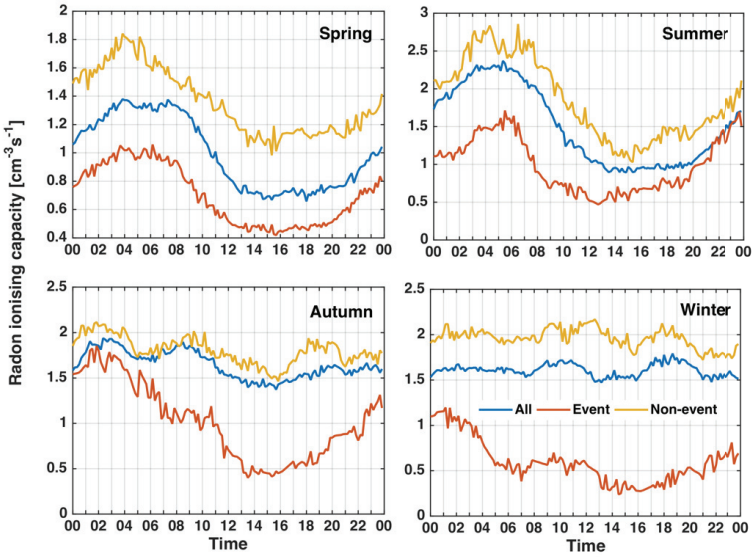

Figure S1. 10-min median radon ionising capacities on event and non-event days in different seasons over 2003-2006.

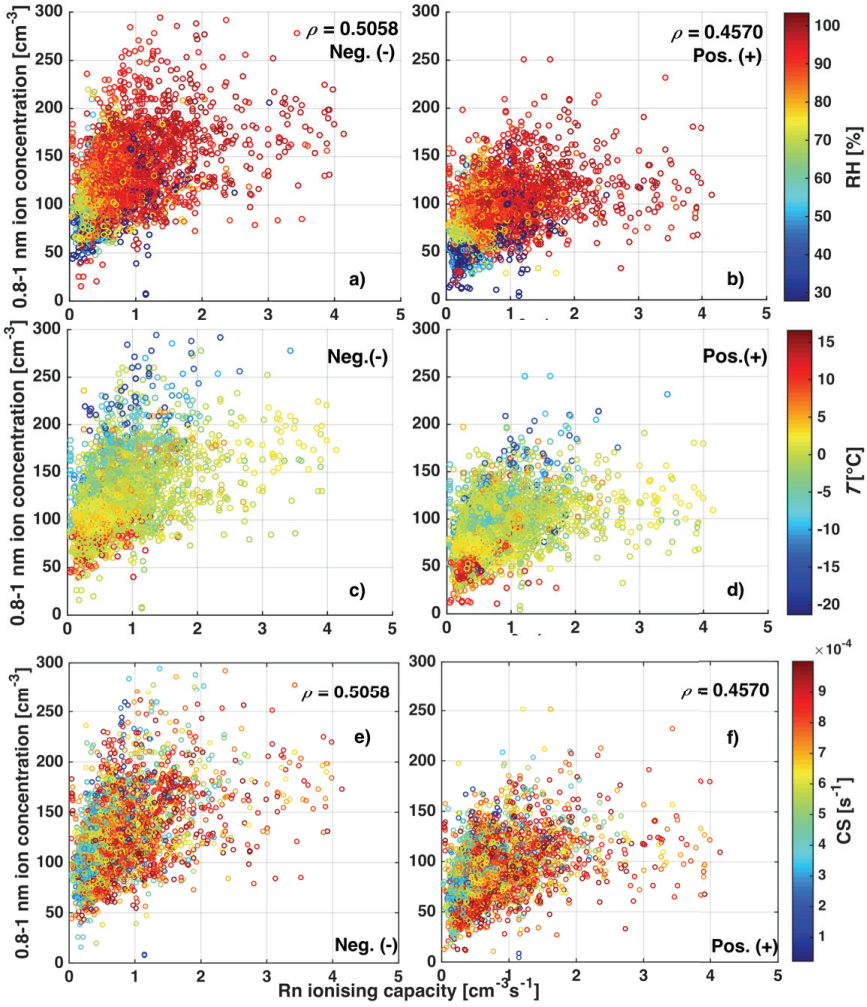

Figure S2. Relationship between the hourly ionising capacity and the 0.8-1 nm ion concentration with Spearman's rank correlation coefficients (ρ) when the condensation sink (CS) is below 0.001 s^{-1}. Upper panel: with relative humidity (RH) on the colour scale. Middle panel: with air temperature (T) on the colour scale. Lower panel: with condensational sink (CS) on the colour scale.

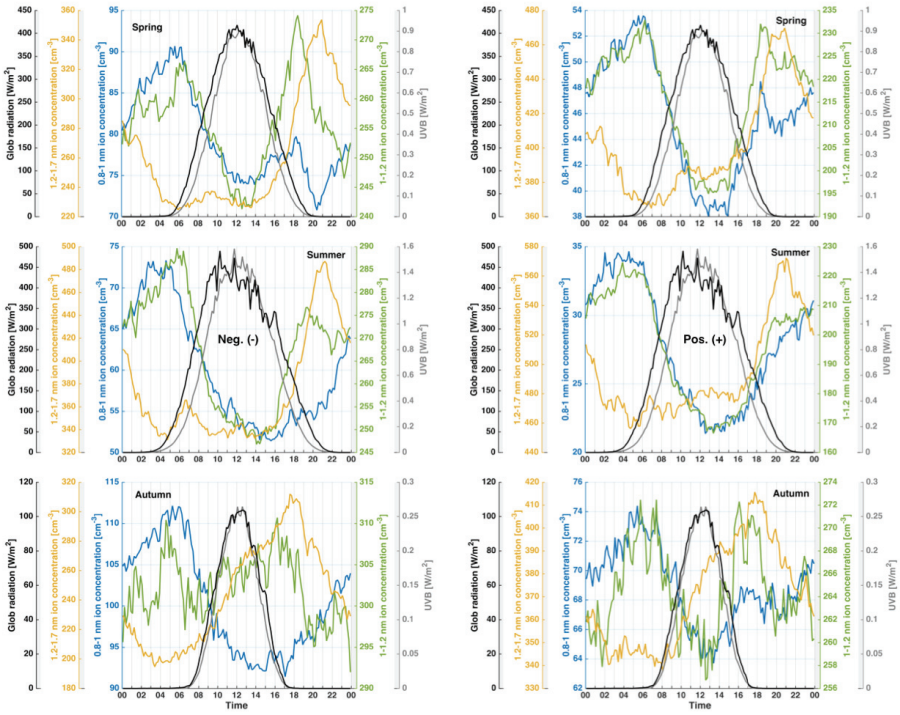

Figure S3. Diurnal relationship between median solar radiation intensities and ion concentrations in 0.8-1 nm, 1-1.2 nm and 1.2-1.7 nm sub-cluster size ranges in different seasons over 2003-2006.

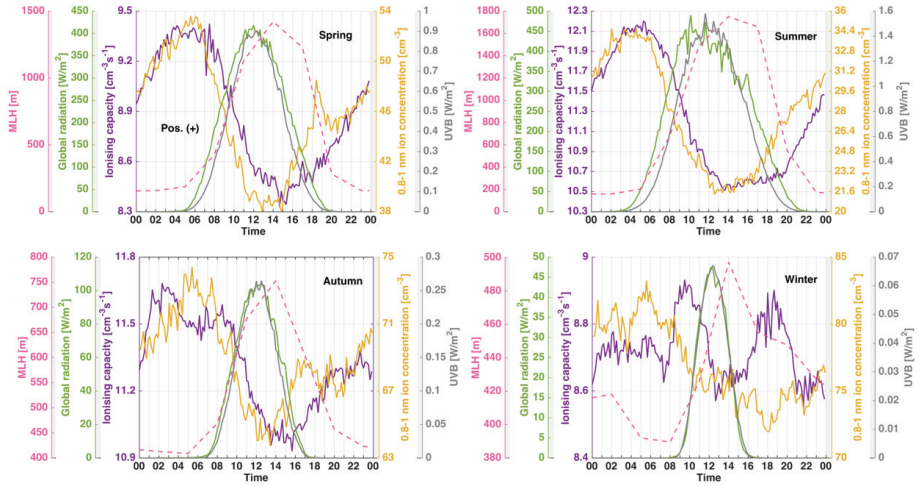

Figure S4. Diurnal patterns in median 0.8-1 nm positive ion concentrations, ionising capacities, global and UVB radiation intensities as well as modelled mixing layer heights (MLH) in different seasons over 2003-2006.